

Technische Universität Dresden

Energy Harvesting for Tire Pressure Monitoring Systems

Dipl.-Ing.

Sebastian Maxim Germer

der Fakultät Elektrotechnik und Informationstechnik
der Technischen Universität Dresden

zur Erlangung des akademischen Grades

Doktoringenieur

(Dr.-Ing.)

genehmigte Dissertation

Vorsitzender	Prof. Dr.-Ing. habil. Gerald Gerlach
Gutachter	Prof. Dr.-Ing. habil. Uwe Marschner Prof. Christopher Rhys Bowen, Ph.D.

Eingereicht am: 24.01.2023

Verteidigt am: 15.09.2023

Danksagung

An dieser Stelle möchte ich mich bei all denjenigen bedanken, die mich während der Anfertigung meiner Dissertation intensiv unterstützt sowie wissenschaftlich, fachlich und mental begleitet haben.

Besonderer Dank gilt Prof. Dr.-Ing. Uwe Marschner für die umfangreiche Betreuung, seine fachliche Unterstützung, die zahlreichen inspirierenden Diskussionen, seine motivierenden Worte und die Zeit und Mühe, die er auch außerhalb seiner Arbeitszeit aufopferte, obgleich nachts oder am Wochenende. Ferner bedanke ich mich bei Prof. Dr.-Ing. Andreas Richter, der mir als von Continental geförderter Stipendiat an seiner Professur die Forschung ermöglichte und mit Rat und Tat zur Seite stand.

Großer Dank gilt ebenso dem Automobilzulieferer und Reifenhersteller Continental und dessen Mitarbeitern. Insbesondere ist Tobias Huber zu nennen, der in den ersten zwei Jahren mich fachlich auf Unternehmensseite betreute und mit wichtigen Mitarbeitern vernetzte. Ohne sein Engagement wäre die Promotion gar nicht möglich gewesen. Den Kollegen Martin Kurz, Ingo Paul, Marian Rostek, Joachim Busche sowie Nicolas Guinart danke ich besonders für ihre konstruktiven Ideen und Kommentare in den zahllosen Videokonferenzen. Ohne ihre Expertise und ihr Engagement hätten die notwendigen Experimente am Fahrzeugreifen gar nicht stattfinden können.

Aurélien Bachmann und Dominik Stösser sei herzlich gedankt für ihre Anmerkungen und sprachlichen Korrekturen.

Bedanken möchte ich mich weiterhin bei meinem Zimmerkollegen Anthony Beck; bei René Körbitz, Andreas Voigt, Petko Barkadjiev, Philipp Mehner, Konrad Henkel, Stefan Grünzner und vielen anderen für die endlosen Diskussionen, den Meinungs austausch, die technische Unterstützung bei IT-Fragen sowie für die äußerst angenehme Arbeitsatmosphäre, die eine hervorragende Grundlage für die kontinuierliche Arbeit an dieser Dissertation bildete.

Abschließend gilt mein herzlichster Dank meinen Eltern und meinen beiden Geschwistern die stets liebevoll, unterstützend und motivierend auf mich positiven Einfluss nahmen und nehmen.

Kurzfassung

Reifendruckkontrollsysteme (RDKS) detektieren zu hohen und niedrigen Reifendruck und alarmieren den Fahrer in kritischen Situation. Heutige RDKS sind batteriebetrieben und besitzen eine begrenzte Lebensdauer. Neue Sensorfunktionen wie das Erkennen von Aquaplaning erfordern mehr Energie und würden die Lebensdauer des RDKS erheblich verkürzen. Energy Harvesting im Fahrzeugreifen gilt als vielversprechende Alternative und ermöglicht Energieautarkie. Entsprechend besteht das Ziel dieser Doktorarbeit darin, verschiedene elektromechanische Energiewandler zu entwickeln, die den Energieanforderungen des RDKS genügen und gleichzeitig robust sind.

Im Mittelpunkt stehen dabei piezoelektrische und elektromagnetische Wandler. Im Gegensatz zu vorangegangenen Arbeiten auf diesem Gebiet konzentriert sich diese Arbeit ganzheitlich auf die Bereiche Energieerzeugung, Energiewandlung, Schnittstellenschaltungen sowie Energiespeicherung und deren gegenseitige Beeinflussung. Völlig neu sind auch Untersuchungen zur Effizienz von Schnittstellenschaltungen in Abhängigkeit von der Spannung des Speichermediums. Die Analyse zeigt, dass piezoelektrischen Systeme in Kombination mit Synchronous Electric Charge Extraction (SECE)-Schaltungen den Wirkungsgrad um ein Vielfaches gegenüber konventionellen Schaltungen erhöhen.

Ferner wird eine neue Signaldarstellung eingeführt, die darauf abzielt, die Energiemenge eines elektromagnetischen Wandlers oberhalb einer bestimmten Spannung zu charakterisieren, die z. B. durch Gleichrichterdiolen erzeugt wird. Diese Signaldarstellung erweitert die typische Darstellung im Zeit- und Frequenzbereich und ermöglicht eine intuitive Erfassung von Informationen über die Energieverteilung in Abhängigkeit von der Spannungsamplitude. Sie erleichtert den Vergleich verschiedener Energy Harvester Systeme allein auf der Grundlage der Leerlaufspannung.

Während Zweiwege-Gleichrichter bei niedrigen Spannungen zu hohen Verlusten führen und die Spannung verringern, erfüllt ein Spannungsverdreifacher in Verbindung mit einem elektromagnetischen Harvester die gewünschten energetischen Anforderungen an RDKS. Um sowohl höhere als auch lastunabhängige Wirkungsgrade zu erzielen, wird ein neues, durch einen Schalter gesteuertes Aufwärtswandlersystem allgemein mathematisch beschrieben. Bemerkenswert ist, dass das optimale Tastverhältnis allein vom Verhältnis der Induktivität zum parasitären Widerstand des elektromagnetischen Energiewandlers abhängt. Mit dem optimalen Tastverhältnis werden Wirkungsgrade von mehr als 80 % erreicht.

Versuche auf einem Reifenprüfstand zeigen das Verhalten verschiedener Prototypen bei verschiedenen Geschwindigkeiten (20 km/h - 200 km/h) und Lasten (1000 N - 90000 N). Sowohl die Kombination dehnungsbasierter piezoelektrischer Generatoren mit einer SECE-Schaltung als auch Zentrifugalbeschleunigungsbasierte elektromagnetische Wandler mit Spannungsverdreifacher erweisen sich nicht nur als robust, sondern übertreffen alle bisher veröffentlichten Ergebnisse zur Energieerzeugung um bis zu 1500 %

Abstract

Tire pressure monitoring systems (TPMSs) predict over- and underinflated tires, and warn immediately the driver about the tire pressure in a critical situation. Today, battery powered TPMSs suffer from limited energy. New sensor features such as friction determination or aquaplaning detection require more energy and would significantly decrease the TPMS lifetime.

Harvesting electrical energy inside the tire of a vehicle has been considered as a promising alternative to overcome the limited lifetime of a battery. This work aims at developing different electromechanical energy transducers that meet the energy requirements of the TPMS while being simultaneously robust.

Piezoelectric and electromagnetic transducers are focused. In contrast to former work, this work considers the complete energy harvesting chain, starting from the mechanical energy across the transducer system, the interface circuit to the storage medium. Entirely novel are the investigations of the efficiency of interface circuits as a function of the storage voltage. It turns out that the studied piezoelectric systems combined with Synchronous Electric Charge Extraction (SECE) circuits increase the efficiency by many times compared to conventional Standard Energy Harvesting (SEH) and Synchronous Switch Harvesting on Inductor (SSHI). In addition, it is demonstrated that a well-selected energy storage can reduced the demands on the energy.

A new signal representation is introduced and aims at characterizing the amount of energy of an electromagnetic transducer above a specific voltage, imposed by e.g. rectifying diodes. The innovative signal representation extends the typical representation in time-domain and frequency-domain, and enables an intuitive acquisition of information on the energy distribution depending on the amplitude. It facilitates the comparison of different transducer systems, solely based on the open-circuit voltage.

While two-way rectifiers lead to high losses at low voltages and as they decrease the incoming voltage, a voltage tripler connected to an electromagnetic harvester meets the desired energetic requirements of TPMSs. In order to achieve both higher and converter-independent efficiencies, a new step-up converter system, controlled by a switch, is generally described mathematically. An astonishing outcome of the analysis is, that the optimal timing depends solely on the inherent inductor of the electromagnetic energy harvester. With the optimal timing, efficiencies of more than 80 % are reached.

Tests on a tire test rig of different combinations of assembled energy harvesting prototype and interface circuit are conducted to evaluate the electrical energy and the reliability at different vehicle speeds (20 km/h - 200 km/h) and tire loads (1000 N - 90000 N). Both the combination of strain-based piezoelectric generators with SECE circuits and centrifugal acceleration-based electromagnetic converters with voltage triplers are not only robust, but also surpass all previously published values of energy generation in the literature by up to 1500 %.

Table of Contents

- 1 Introduction** **1**

- 2 Energy Harvesting Inside the Tire** **7**
 - 2.1 The Wheel as a Source of Energy 7
 - 2.1.1 The Gravitational Acceleration at the Rim 8
 - 2.1.2 The Centrifugal Acceleration at the Tire Inner Liner 9
 - 2.1.3 The Tire Strain at the Tire Inner Liner 10
 - 2.2 Energy Requirements 11
 - 2.2.1 Effective Energy of a Coin Cell Battery 11
 - 2.2.2 Energy Consumption of Tire Pressure Monitoring Systems 12
 - 2.3 Summary 18

- 3 Electromechanical Transducers** **19**
 - 3.1 Electrical Transducers 20
 - 3.1.1 Piezoelectric Transducer 20
 - 3.1.2 Electrostatic Transducer 23
 - 3.1.3 Ferroelectret Transducer 25
 - 3.1.4 Triboelectric Transducer 26
 - 3.2 Magnetic Transducers 27
 - 3.2.1 Electrodynamic Transducer 28
 - 3.2.2 Piezomagnetic Transducer 30
 - 3.3 Summary 31

- 4 State of the Art of TPMS Energy Harvesters** **33**
 - 4.1 Rim Wave Based Systems 33
 - 4.2 Tire Wave Based Systems 34
 - 4.3 Strain Based Systems 37
 - 4.4 Overview 39
 - 4.5 Consequences for the Energy Harvester Design 43
 - 4.5.1 Rim Wave Based Systems 43
 - 4.5.2 Tire Wave Based Systems 43
 - 4.5.3 Strain Based Systems 45
 - 4.6 Summary 46

5	Piezoelectric Energy Harvesting	47
5.1	Piezoelectric System Description	47
5.2	Tire Wave Based Piezoelectric Energy Harvester	48
5.2.1	Preliminary Energy Considerations	48
5.2.2	Piezoelectric Energy Harvester System Design	51
5.3	Strain Based Piezoelectric Energy Harvester	57
5.3.1	Material Selection	59
5.3.2	Experimental Characterization on an Electrodynamical Shaker . . .	60
5.3.3	Network Parameter Prediction	64
5.3.4	Network Simulation	66
5.4	Summary	69
6	Piezoelectric Energy Harvester Interface Circuits	71
6.1	Energy and Charge of a Piezoelectric Transducer	73
6.2	Standard Energy Harvesting - SEH	76
6.3	Switch only Rectifier - SOR	78
6.4	Synchronized Switch Harvesting on Inductor - SSHI	79
6.5	Synchronous Electric Charge Extraction - SECE	83
6.5.1	Energy Transfer from the Capacitance C_p to the Inductance L . . .	85
6.5.2	Energy Transfer from the Inductance L to the Storage C_s	86
6.6	Numerical Validation	89
6.7	Summary	92
7	Electromagnetic Energy Harvesting	93
7.1	Linear Electromagnetic System Description	94
7.2	Nonlinear Electromagnetic System Description	97
7.3	Preliminary Energy Considerations	97
7.4	Numerically Parameter Determination	99
7.4.1	Finite Element Analysis of the Magnetic Field	99
7.4.2	Coil Setup and Electromagnetic Transducer Coefficient	103
7.4.3	Repulsive Magnetic Force and Fixed Magnet	105
7.5	Experimental Parameters	107
7.5.1	Electromagnetic Energy Harvester Prototypes	107
7.5.2	Electromagnetic Transducer Coefficient	108
7.5.3	Damping Coefficient	108
7.5.4	Repulsive Magnetic Force	109
7.5.5	Elastic Bumper Force	111
7.6	Network Simulation	112
7.7	Summary	118

8	Electromagnetic Energy Harvesting Interface Circuits	119
8.1	Standard Energy Harvesting and Stochastic Signal Analysis	120
8.2	Voltage Multipliers	126
8.3	Synchronized Magnetic Flux Extraction (SMFE)	128
8.4	Energizing and Transferring Circuit – EaT	134
8.4.1	Discontinuous Current Mode – DCM	136
8.4.2	Continuous Current Mode – CCM	138
8.4.3	Transferring Phase	140
8.4.4	Simulation and System Performance	142
8.5	Numerical Validation	144
8.6	Summary	145
9	Tire Prototype Testing and Experimental Results	147
9.1	Experimental Setup	148
9.2	Tire Wave Based Piezoelectric Energy Harvester	151
9.2.1	Open-Circuit Voltage and Corresponding Energy	151
9.2.2	Robustness	153
9.3	Strain Based Energy Harvesters	154
9.3.1	Velocity Dependency	155
9.3.2	Orientation Dependency	157
9.3.3	Tire Force Dependency	158
9.3.4	Robustness	159
9.3.5	Interface Circuits and Harvested Energy	162
9.3.6	Summary	164
9.4	Centrifugal Acceleration Based Electromagnetic Energy Harvester	166
9.4.1	Velocity Dependency	169
9.4.2	Tire Force Dependency	172
9.4.3	Interface Circuits and Harvested Energy	174
9.4.4	Robustness	178
9.4.5	Optimization	179
9.5	Summary	180
10	Conclusions	181
	Appendices	184
A	Voltage-Current-Relation of a Piezoelectric Transducer	185
B	SSHI - Parasitic Effect	187
C	Average Efficiency of Piezoelectric Interface Circuits	188
D	SECE Efficiency Calculation	192
E	Electromagnetic Energy Harvester Simulation Parameters	194
F	Energizing and Transferring Circuit - Efficiency Calculation	194

G	Strain Based Energy Harvester Results	196
Bibliography		196
List of Acronyms		229
List of Symbols		229
List of Figures		235
List of Tables		241
List of Publications		243

1 Introduction

Harvesting energy describes the process of transforming a small amount of ambient energy into electrical energy to power small autonomous systems [1]. It has been the intense focus of research for more than two decades. It is still an emergent topic due to the massive growth of microsystems and their entrance in our today's life to measure and monitor environmental data and to alert in case of emergency. Typically, microsystems get their energy from small batteries, which suffer from a limited lifetime. Their replacement is either time and money consuming or not accessible in hostile environments. Energy harvesting powered systems promise a longer lifetime since they transduce ambient energy into electrical energy from an energy reservoir, which can be considered as endless compared to the battery energy. One of these promising application fields is the tire of a vehicle, in which accelerations with amplitudes of up to $20,000 \text{ m/s}^2$ occur.

The tire of a vehicle is the only connection point between the road surface and the vehicle. A well positioned sensor system inside the tire is able to detect and monitor fundamental tire data and to analyze road surface conditions. Nowadays, tire pressure monitoring systems (TPMSs) measure the tire pressure p , the temperature T and the centrifugal acceleration a_c and communicate these data to the engine control unit (ECU) of the vehicle. Already in 2008, the National Highway Traffic Safety Administration (NHTSA) obliged car companies to integrate TPMSs in newly registered vehicles as a consequence of high tire failures during the Firestone and Ford tire controversy [2]. In 2014, the European Union followed and made TPMSs mandatory for newly registered vehicles, too [3]. Besides the most important fact of reducing safety issues, the TPMS detects underinflated and overinflated tires, enables reducing tire wear and fuel consumption.

One vision is, that next generation tires with direct TPMSs¹ will determine additionally important parameters as friction, tread depth, strain, contact pressure, vehicle load, surface conditions, tire cracks, will raise the tire "intelligence" to a next level [4–6] and contribute to reducing the number of accidents. In 2019, more than 36,000 and 22,700 people died in the US and in the EU due to fatal motor vehicle crashes with many hundreds of thousands others injured. More than 20 % of the accidents are due to adverse weather conditions, mainly wet road conditions [7–9]. Current technologies and algorithms enable to detect critical road conditions such as aquaplaning [10], potholes or black ice and give

¹A direct TPMS uses pressure sensors that regularly measure the pressure precisely. Contrary, an indirect TPMS uses the sensors of already available systems, e.g. ABS or ESC and computes relative pressure differences between the tires based on the tire rolling circumference.

hope to further decrease the number of accidents and fatalities. These data are not only useful for the vehicle associated with the tire. The communication between the vehicles and the Internet of Vehicles (IoV) will enable to exchange information about forthcoming road conditions and lead to a new paradigm of driving, based on information exchange, e.g. in smart cities [11]. Subsequent vehicles can be warned early enough in case of emergency, as illustrated in Fig. 1.1, so that they have enough time to take appropriate measures automatically to avoid the danger.

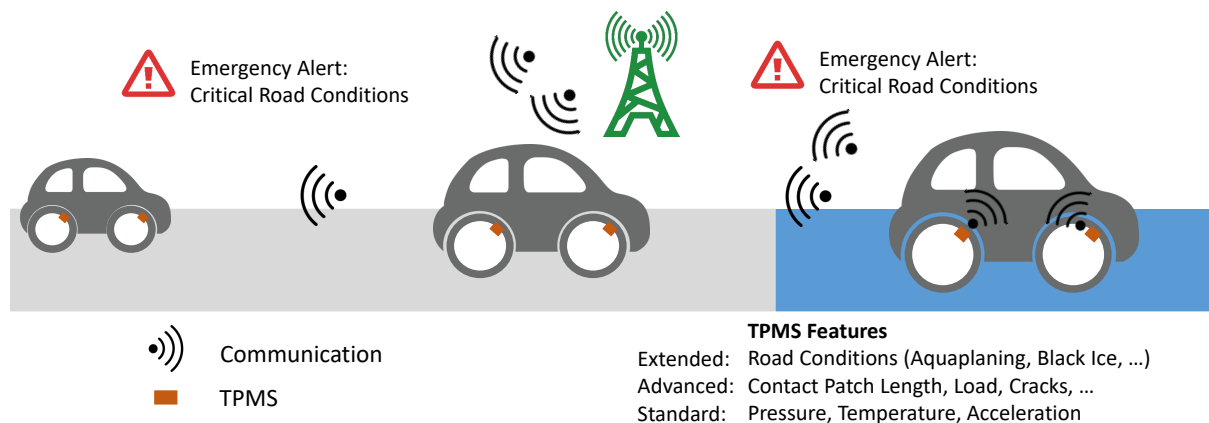


Figure 1.1: Smart tire pressure monitoring systems will improve the intelligence of the tire and will provide new features for the Internet of Vehicles

Data of the monitored tire also render possible maintenance on time, extend the tire lifetime, improve the fleet management and improve the vehicle-as-a-service model. Autonomous vehicles equipped with intelligent tires, being a part of smart transportation systems [12], will know accurately the tire wear and tire tread depth, predict the time to change the tire and inform the fleet manager about appropriate measures. Beyond that, intelligent tires will help to estimate the severity of accidents and will provide data for vehicle accident detection systems [13]. In case of a severe accident, the vehicle will initiate automatically an emergency call.

To enable this vision of intelligent and connected tires, the sensor systems will require more energy than today's systems. Nowadays, typical CR2032 button cell batteries are widely spread for the energy supply, but have a limited lifetime and due to the manifold requirements in a tire, they are hermetically encapsulated in the TPMS and are not designed for replacement. The rising demand of energy for the next generation of TPMSs is worsening the situation. Originally, only a progressive add-on, now the car holder has to renew the entire sensor system, if the battery runs out of energy, rendering the otherwise perfectly working TPMS obsolete.

From this consideration, the demand arises to implement an autonomous, self-sustaining system in order to reduce electronic waste and maintenance, to assure an up-to-the-minute information in the context of Age of Information [14], to save time and money.

The idea of harvesting energy from ambient sources has been considered as a promising alternative to overcome the detriment of limited battery lifetime and to provide the neces-

sary energy for more functionalities in today’s TPMSs. In the last twenty years, scientists have been mostly working on systems generating electrical energy from tire vibrations, wheel vibrations or tire deformations. However, to the knowledge of the author, all commercially available TPMSs depend on a battery and are not self-sufficient. Therefore, this work intends to identify reasons, why energy harvesters for TPMSs have not reached the breakthrough, yet. The hostile conditions of the automotive sector are one apparent and challenging reason. They are presented with other boundary conditions in Chapter 2. Furthermore, an energy harvester has to compete in terms of energy with low-cost and widely-spread coin cell batteries which serve as a benchmark.

Successful energy harvesting comprises studying the energy source, the design of the energy harvester system, the selection of well suited interface circuits and temporary energy storages. Fig. 1.2 illustrates the complete energy harvesting chain.

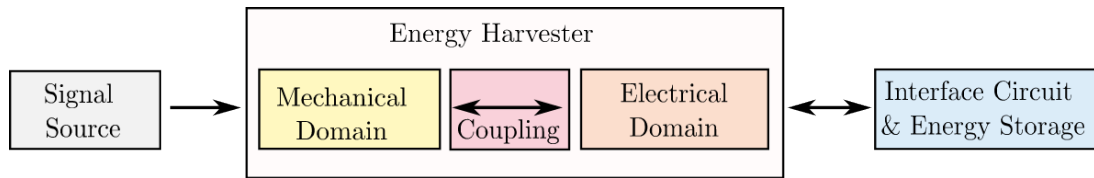


Figure 1.2: Energy harvesting chain - from the source to the storage

The possible signal sources entering the energy harvester in Fig. 1.2 are surveyed in Sec. 2.1. To determine suitable transducer systems for TPMS, this work summarizes state-of-the-art energy conversion mechanisms in Chapter 3.

Former scientific activities focused solely on the energy harvester, which is framed in Fig. 1.2. This thesis expands the focus to the entire energy harvesting chain and incorporates suitable interface circuits in the system concept.

Different system concepts based on electromagnetic and piezoelectric harvesting principles are the foundation of this work. A mathematical description with coupled differential equations, presented in Chapter 5 and Chapter 7, helps to describe, analyze, simulate the system concepts and to identify well-suited parameters in order to build energy harvester prototypes for the tire.

The tire as source of vibration differs tremendously in signal from a harmonic vibration source. The frequency spectrum depends on the vehicle’s velocity and is shifted towards higher frequencies with increasing velocity, whereas the signal amplitude increases quadratically. Under these circumstances, the problem has to be addressed whether a commonly used linear system is suitable to harvest energy from a quadratically increasing vibrational amplitude.

A formulation of an upper bound of the energy is deduced and merges mechanical system characteristics with the input signal. The amount of the generated electrical energy of linear systems is estimated and reveals the systems’ limitations.

In response to the nonlinear vibrational signal sources, nonlinear energy harvesters are studied. The efficient combination of computer aided engineering (CAE) tools to

describe these nonlinear systems is one key element of this thesis. The output of the energy harvester, excited by nonlinear signals exhibits a high nonlinearity, too. Mostly, recent works considered a rectifier circuit with an optimal load resistance to estimate the generated energy by integrating the power across the load resistance over time, irrespective whether voltage, current or energy level are sufficient for the following TPMS stage. A temporary buffer, which enables energy accumulation during many tire revolutions, was generously neglected within the past analysis.

Interface circuits with a connected storage are studied in Chapter 6 and Chapter 8 with respect to their efficiencies. They add further nonlinearities to the system and make the system description more complex. Furthermore, the voltage level of the energy buffer has a significant impact on the transferred energy. Analytical expressions and numerical methods are used to quantify the efficiency of selected interface circuits, such as a standard interface circuits, voltage multipliers, synchronized extraction circuits and boost circuits.

Stochastic methods are applied to analyze the non-harmonic voltage signal of the harvester output to establish an essential and innovative data representation. This representation permits quick comparisons between different systems and easy evaluations whether the energy harvester meets the imposed energy requirements.

Subsequently, different energy harvesting circuits are both implemented in the simulation kit and evaluated. Promising and easily realizable circuits are connected to different energy harvesting prototypes and tested within experimental studies with approximately 1200 data sets, including different energy harvesters, varying velocities and tire loads. The results are shown and evaluated in Chapter 9.

At the end of this thesis, an overview of performance data of the best energy harvesting system is provided with focus on the electrical energy generation and compared to the energy supply of a coin cell battery.

An overview of the key aspects of this thesis are visualized in Fig. 1.3. The definition of the efficiency of the energy harvester, interface circuit and the total system are used when it comes to the characterization of the systems.

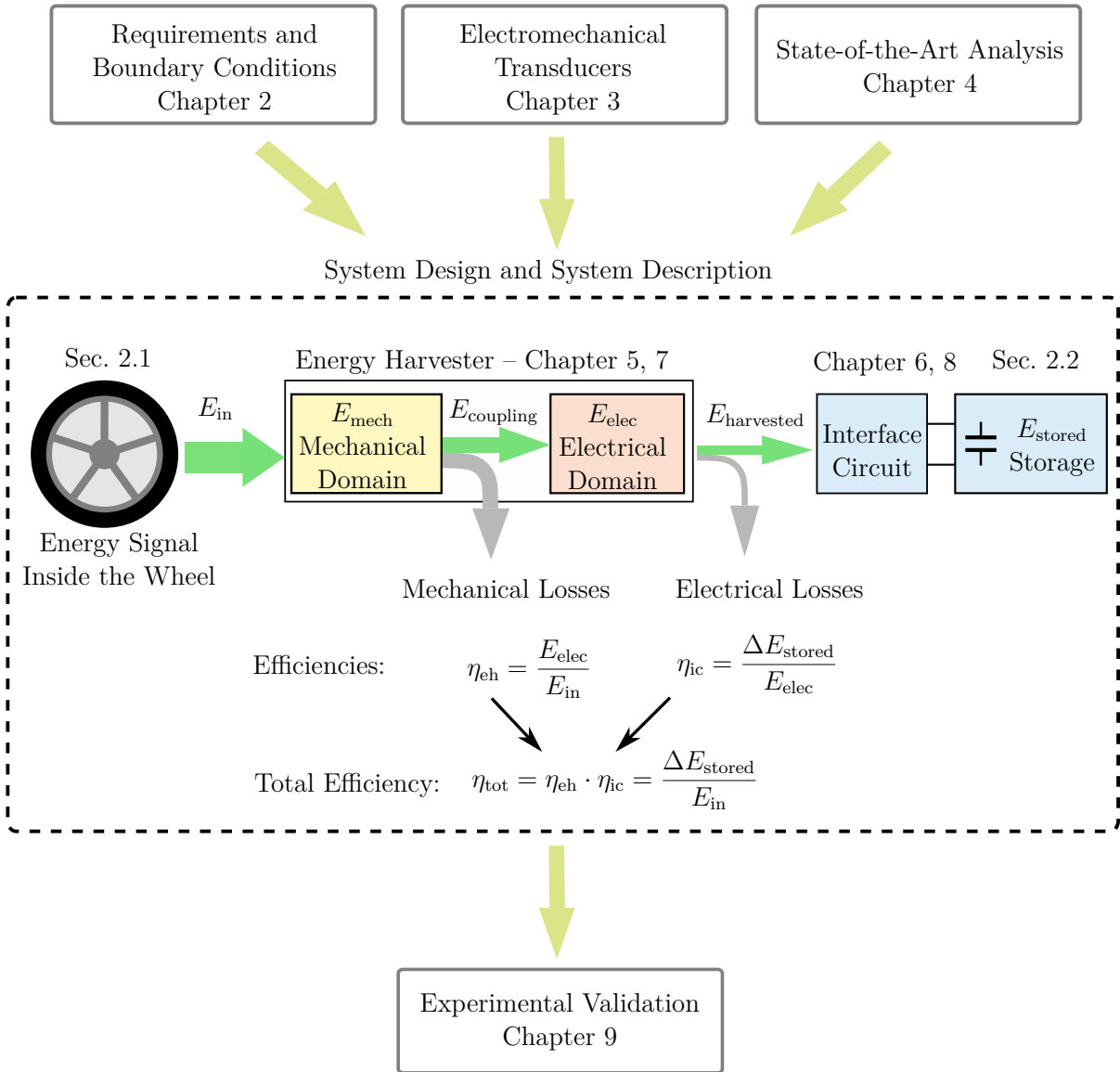


Figure 1.3: Visualization of the structure of this thesis

2 Energy Harvesting Inside the Tire

This chapter presents first different ways how to extract mechanical energy from a wheel and second analyzes the required amount of energy to replace the current energy supply, which is a CR2032 coin cell battery. The content of this chapter was presented at [15] and published in [16].

2.1 The Wheel as a Source of Energy

The mechanical energy E_{in} , entering an energy harvesting system, is generally described by the mechanical work, defined as

$$E_{\text{in}} = \int_{z(t=0)}^{z(t)} F_{\text{ex}} dz, \quad (2.1)$$

where z and F_{ex} are the position and the applied excitation force, respectively. The rotating wheel provides two different acceleration signals $a(t)$, one at the rim and one at tire inner liner, which is the inner rubber layer that prevents airflow between the air inside the tire and the environment. For a given acceleration, the force is expressed as

$$F_{\text{ex}} = m \cdot a(t) = m \cdot \ddot{z} \quad (2.2)$$

where m is the seismic mass of the system. Then, the energy E_{in} rewritten as

$$E_{\text{in}} = \int_{z(t=0)}^{z(t)} m \cdot a(t) dz. \quad (2.3)$$

Typically two acceleration signals can be used to excite vibrational energy harvesters with an inertia mass. A third source of energy is related to the tire rolling behavior in the area of ground contact. In this area the tire is strongly deformed. The corresponding deformation energy of a cuboid with cross section A and length l , and strained by the strain $S = \Delta z/l$, is given by Hooke's law as

$$E_{\text{in}} = \frac{1}{2} Y \cdot A \cdot l \cdot S^2. \quad (2.4)$$

The specific position inside the wheel influences the experienced by the mounted energy harvester. The three signals are presented subsequently. Hereinafter, the stationary case

is considered, in which the wheel's rotational velocity is constant.

2.1.1 The Gravitational Acceleration at the Rim

A device mounted at the rim experiences an acceleration $a(t)$, which is split into a constant part, the centrifugal acceleration a_c and a time-varying part $a_g(t)$, the change of gravitational acceleration, when the device orientation is changed from upside-down to downside-up and vice versa as shown in Fig. 2.1. For harvesting energy, only the change of gravitational acceleration is significant. The acceleration $a(t)$ is described by

$$a(t) = a_g(t) + a_c \quad \text{with} \quad (2.5)$$

$$a_g(t) = g \cdot \sin(\omega t), \quad (2.6)$$

$$a_c = \omega^2 R_r, \quad (2.7)$$

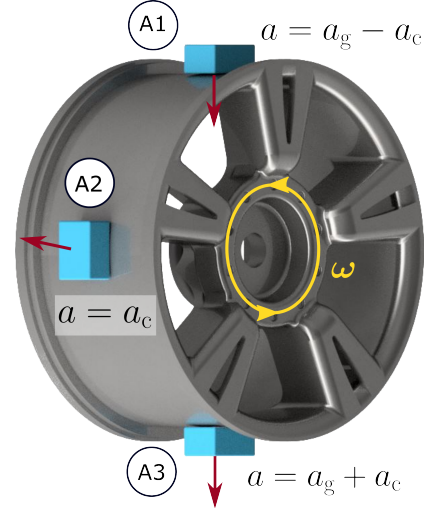


Figure 2.1: Rim mounted energy harvester

where g , ω and R_r are the gravitational acceleration, angular velocity and rim radius, respectively, follows

$$a(t) = g \cdot \sin(\omega t) + \omega^2 R_r. \quad (2.8)$$

The angular velocity is determined by $\omega = v/R$, where v and R are vehicle velocity and tire radius. Then, Eqn. 2.8 is rewritten to

$$a(t) = g \cdot \sin(\omega t) + \left(\frac{v}{R}\right)^2 R_r. \quad (2.9)$$

The corresponding waveform of the total acceleration $a(t)$, here named as "rim wave", is illustrated in Fig. 2.2. The rim wave signal goes from $a_c + g$ to $a_c - g$ and its amplitude is $1g$, irrespective of the vehicle velocity. Already at moderate velocities and especially at high velocities, the centrifugal acceleration is about 40 times larger at 50 km/h and 260 times larger at 130 km/h than the gravity, if a typical rim radius $R_r = 0.2$ m and a tire radius $R = 0.32$ m are assumed. Thus, the effect of gravity decreases with higher velocities, leading to difficulties as explained later in Sec. 4.1.

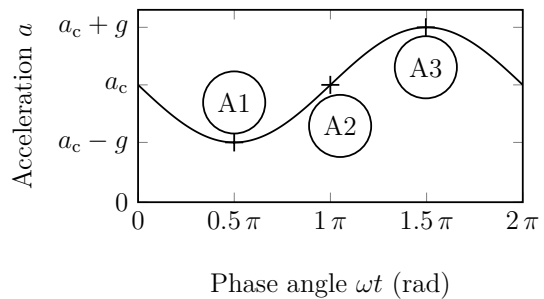


Figure 2.2: Rim wave signal for one tire revolution at constant velocity

2.1.2 The Centrifugal Acceleration at the Tire Inner Liner

In contrast to the former signal, much higher signal amplitudes can be observed at the tire inner liner. Due to tire deformations, which are illustrated in Fig. 2.3, the acceleration signal $a(t)$ fluctuates significantly and a so-called "tire wave" is formed. The time-varying component is mainly $a_c(t)$, which is superimposed by $a_g(t)$ as

$$a(t) = a_c(t) + a_g(t). \quad (2.10)$$

The corresponding acceleration signal is depicted in Fig. 2.4.

There are three main areas: The area B1, in which the acceleration is constant, as long as the tire has not contacted the ground. If the tire contacts the ground - termed the contact patch - it lies flat and the local tire radius tends towards infinity while the centrifugal acceleration vanishes (B2). Before entering and after leaving the contact patch, the acceleration signal reaches a peak value as a consequence of smoothed tire deformation. In the context of vibrational energy harvesting, the signal can be interpreted as a step function excitation, followed by a free oscillation during the time of ground contact. Both tire pressure and tire load, which characterizes the force with which the tire is pressed against the road, determine the area of ground contact. From [17], the ground contact length is estimated to be one tenth of the circumference.

As depicted in Fig. 2.5a, with increasing velocity, the time of ground contact decreases linearly, e.g. from 29 ms at 25 km/h to 14.5 ms at 50 km/h. Similarly, the number of free oscillations of an energy harvester during this time decreases, if the oscillation frequency of the transducer ω remains almost constant. Simultaneously, the vibration amplitude increases quadratically with the velocity, leading to a greater oscillation amplitude. The quadratic relation between velocity v and centrifugal acceleration a_c is presented in Fig. 2.5b. When the acceleration dependent velocity increases to a few thousand g and drops immediately to zero, system reliability has to be faced since system robustness is a concern.

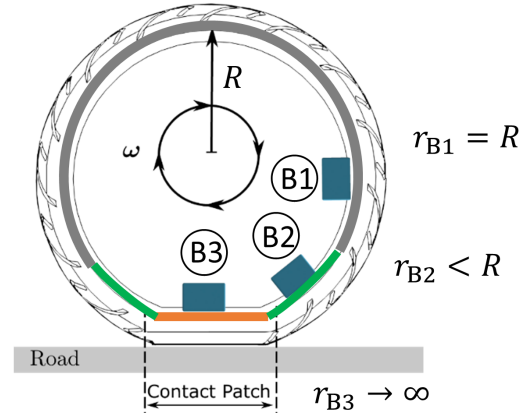


Figure 2.3: Tire inner liner mounted energy harvester

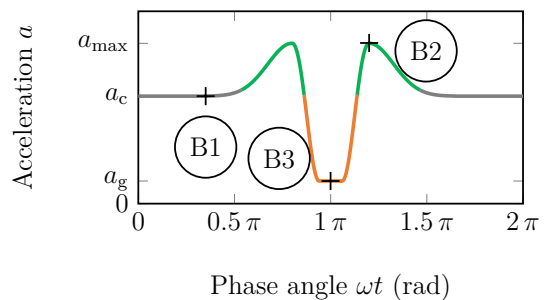


Figure 2.4: Tire wave signal for one tire revolution at constant velocity

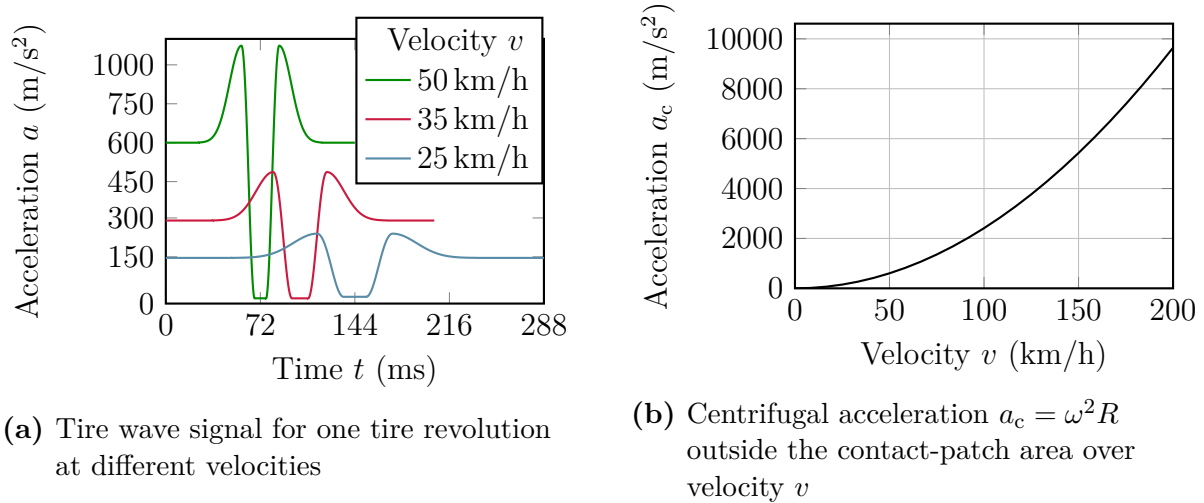


Figure 2.5: Tire wave signal for different velocities and related centrifugal accelerations

2.1.3 The Tire Strain at the Tire Inner Liner

The tire deformations in proximity of the area of ground contact do not only constitute a vibration source, but also a strain source. In order to lie flat on the ground, the round tire is stretched. Before and after the contact patch area, the tire is compressed. Smart transducer materials directly attached to the tire, such as piezoelectrics or triboelectrics, transform a part of this strain energy into electrical energy. Referring to [17, 18], the tire strain ranges from -0.3% to 0.7% . The strain deformation of the tire and the waveform are illustrated in Figs. 2.6a and 2.6b. In contrast to the vibrational sources, the strain is mostly velocity independent since the ground contact length remains unaffected [19].

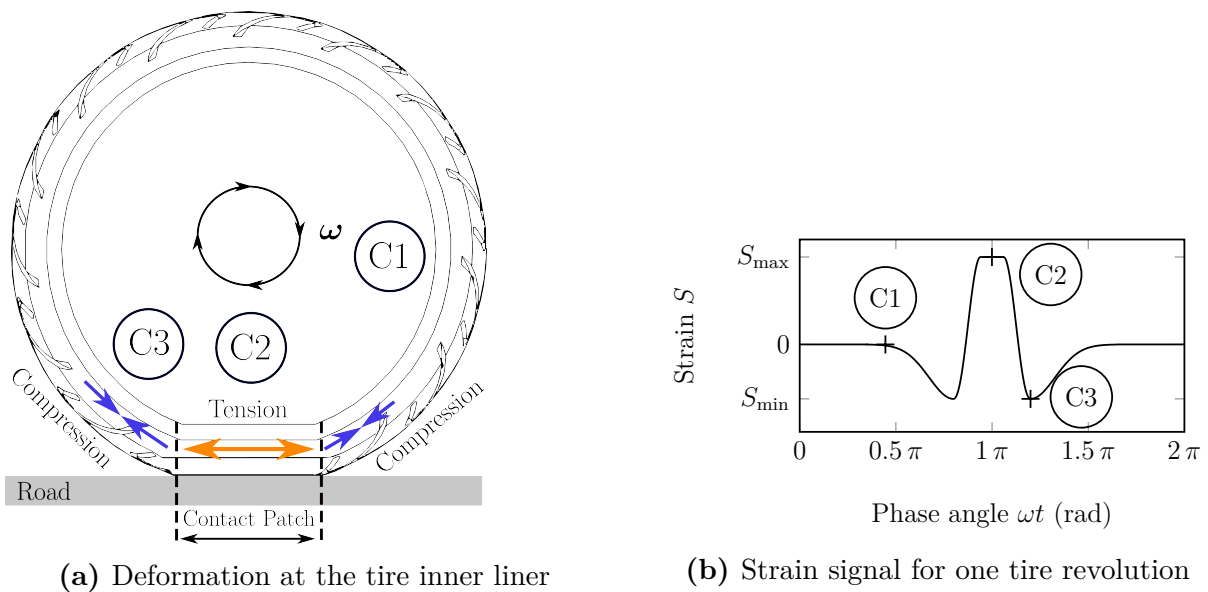


Figure 2.6: Tire deformation at the tire inner liner and corresponding strain wave signal

2.2 Energy Requirements

Before one of the former presented signal sources is chosen to develop a system, the amount of energy of today's TPMS needs to be estimated, pursuing two paths:

First, the energy harvester has to reach the set standards of a CR2032 battery, typically used in common TPMS and second, the energy harvester needs to provide enough energy within a given time for the TPMS data transfer. As shown subsequently, both approaches will lead to similar energy demands.

2.2.1 Effective Energy of a Coin Cell Battery

The CR2032 battery is cheap, has a nominal voltage of 3V, and a nominal capacity Q_{bat} of 200mAh to 250mAh. Only 70% of the usable capacity can be approximately used in the operating temperature range of -40°C up to 125°C [20]. In addition not the entire 70% of the capacity can be directly used for data measurement and transmission. The ISO 21750:2006 implies a TPMS lifetime of at least 6 years or 100,000 km [21]. An average yearly self discharge of 1%, referring to the nominal capacity, reduces the amount of capacity by 6%. In TPMSs about half of the available capacity is reserved for the stationary sleep or power-down mode, when the vehicle is parking. Finally, about 27% of the nominal capacity, equivalent to a charge of 61mAh, are effectively available for measurement and communication. The capacity proportions are presented in Fig. 2.7.

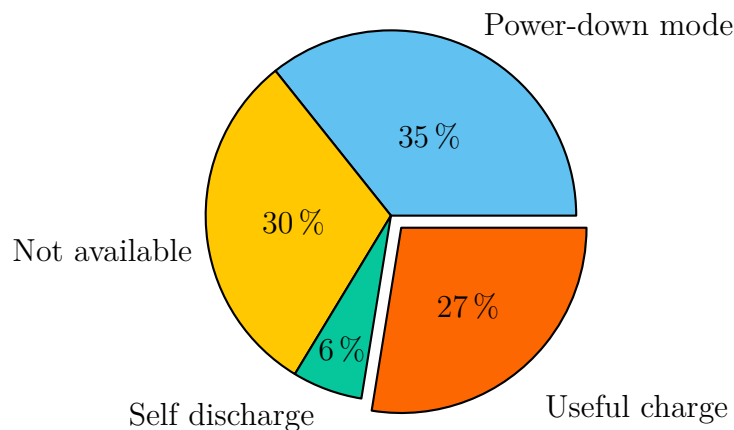


Figure 2.7: Distribution of the available capacity of a CR2032 battery in a TPMS

To obtain the available energy E_{bat} , delivered to the TPMS, the battery capacity Q_{bat} is multiplied with the voltage u and leads to

$$E_{\text{bat}} = u \cdot \int i dt = u \cdot Q_{\text{bat}}. \quad (2.11)$$

Since low efficient power converters such as linear regulators are used to convert the battery voltage of 3V to the application specific integrated circuit (ASIC) voltage, $u_{\text{asic}} = 2.5\text{V}$, the nominal capacity is multiplied with 2.5V, resulting in $E_{\text{bat}} = 550\text{J}$.

The imposed distance of 100,000 km by the ISO21750:2006 corresponds to 50 million tire turns with the tire radius of $R = 0.32$ m. To normalize the energy E (which can be either the battery energy E_{bat} or the required energy, being deduced in Sec. 2.2.2) to the number of tire revolutions N , the energy per revolution E_{rev} is introduced as

$$E_{\text{rev}} = \frac{E}{N}. \quad (2.12)$$

Due to the normalization of the energy E to one revolution rather than to the period T of one revolution (which leads to the average power $\bar{P} = E/T$), the parameter energy per revolution is less affected by the velocity, and allows both comparisons between different systems and for one system at various velocities. Hereinafter, the energy per revolution is considered as the most suitable benchmark for TPMS energy harvesting systems. The provided battery energy, split on a single revolution over the whole lifetime is

$$E_{\text{rev,bat}} = \frac{550 \text{ J}}{50 \cdot 10^6} = 11 \text{ } \mu\text{J}. \quad (2.13)$$

As in most scientific papers the average electrical power \bar{P} was used as a benchmark, the following relation converts the average power to the energy per revolution by

$$E_{\text{rev}} = \frac{\int_0^T P(t) \cdot dt}{\int_0^T v(t) \cdot dt} = \frac{T \cdot \bar{P}}{T \cdot \bar{v}} = 2\pi R \frac{\bar{P}}{\bar{v}}. \quad (2.14)$$

where \bar{v} is the average velocity. Since the energy per revolution is stated for one specific velocity $v(t) = \text{const.}$, the momentary velocity $v = v(t)$ is used instead of the average velocity \bar{v} , subsequently. With $R = 0.32$ m, \bar{P} in μW and v in km/h follows

$$\frac{E_{\text{rev}}}{\mu\text{J}} = 7.2 \frac{\bar{P}/\mu\text{W}}{v/\text{km/h}}. \quad (2.15)$$

The advantage of an energy transducer powered system compared to a battery powered system is that the standby mode is not required. However, when the vehicle stands still, an energy transducer will not provide any energy. In addition, the self discharge of a intermediate storage capacitor is much higher than that of the coin cell battery and the storage capacitor will be discharged after a comparably small amount of time. Consequently, a transducer system needs to be designed to provide sufficient energy, quickly after the vehicle started moving. Then, the TPMS has the ability to immediately start measuring and transmitting data.

2.2.2 Energy Consumption of Tire Pressure Monitoring Systems

The second approach to find out how much energy is needed is based on the current consumption of a tire pressure monitoring system at the constant ASIC voltage u_{asic} . In

Fig. 2.8 the current of different tasks such as standby/leakage, measurement and data transmission during a measurement and transmission cycle is shown. Most of the time, when the system is in standby, a very low current of a few hundred nanoamperes is needed. During a few milliseconds a current of coarsely 1 mA is required for wake-up and measurements. The highest current has to be supplied for the data transfer, which can last from a few milliseconds to several hundred milliseconds. The corresponding charge Q_d for measuring and transmitting data is

$$Q_d = \int_{t_1}^{t_3} i_d(t) dt. \quad (2.16)$$

The specific current levels and time intervals depend on the specific ASIC and the utilized

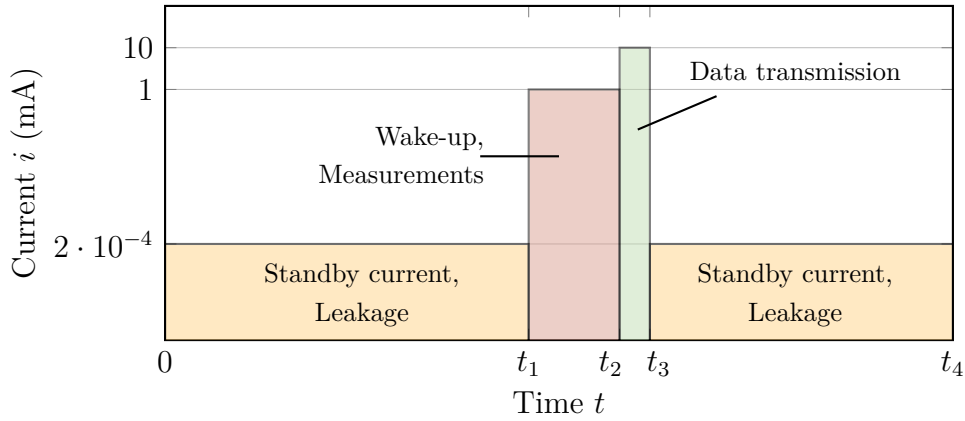


Figure 2.8: Current consumption of typical TPMS tasks

electronic components. During the last years, different current levels, mainly depending on the data length and ASIC voltage, were reported and are summarized in Tab. 2.1.

Mostly, the energy E_{asic} and either the minimal ASIC voltage u_{asic} or the charge Q_d were published, supposing an ideal voltage source. The missing quantity was added in Tab. 2.1 and estimated based on the relation of a battery as

$$E_{\text{asic}} = \int u_{\text{asic}} \cdot i_d dt = u_{\text{asic}} \cdot \int i_d dt = u_{\text{asic}} \cdot Q_d. \quad (2.17)$$

In [26, 32] a large capacitor was used instead of a battery. The minimal voltage u_{asic} and the required energy E_{asic} were reported. From both quantities, the charge Q_d can be calculated as explained below. The capacitor initially contains the charge Q_0 , which is reduced by the charge Q_d after one measurement and transmission cycle. The corresponding energy E_{asic} is

$$E_{\text{asic}} = \frac{Q_0^2 - (Q_0 - Q_d)^2}{2 C_s} \quad (2.18)$$

$$E_{\text{asic}} = \frac{2 Q_0 Q_d - Q_d^2}{2 C_s} = \frac{Q_d}{2 C_s} \cdot (2 Q_0 - Q_d). \quad (2.19)$$

Table 2.1: Overview of published data concerning the energy consumption of a TPMS for one measuring and transmission cycle

Year	Author	E_{asic} (μJ)	u_{asic} (V)	Q_d (μC)	Comments
2003	Roundy [22]				– Transmission: 120 bits/rev – Consumption: 1.3 μJ /rev
2007	Löhndorf et al. [23]	200 - 250	2 - 3.6	70 - 100 ¹	– Datagram length: 100 bits – Data rate: 10 kbits/s
2008	Roundy [24]	1175	3	375	– Datagram length: 12 - 90 bits – Data rate: 4.2 - 9.6 kbit/s – Transmission period: 60 s
2011	Herndl [25]	45 ¹	1.8	25	– 5 mA necessary over 5 ms – Data rate: 50 kbits/s – Frequency: 2.4 GHz – Storage capacitor: 200 μF
2012	Zimmermann et al. [26]	742	2.3	320	– Storage capacitor: 2.35 mF – Transmission period: 80 s
2012	Wang [27]	6100	3.6	1690	– OrangeP409S TPMS
2013	Frey [28]	180	1.5	120 ¹	– Transmission period: 60 s
2013	Schajjk [29]	210			– Transmission period: 30 s – Frequency: 2.4 GHz
2014	Elfrink et al.	240	2.2	110 ¹	– Transmission period: 30 s – Frequency: 2.4 GHz
2014	Kubba et al. [30]	450			
2014	Roundy [31]	375			– Transmission period: 60 s – Storage capacitor: 40 μF
2018	Guo et al. [32]	1215	3.9	310 ¹	– Storage capacitor: 1 mF

¹ This quantity was approximated based on the relation $E_{\text{asic}} = Q_d \cdot u_{\text{asic}}$.

If the charge Q_d is much smaller than Q_0 , the energy can be approximated by

$$E_{\text{asic}} \approx \frac{Q_d}{2C_s} \cdot 2Q_0. \quad (2.20)$$

With $Q_0 = C_s \cdot u_{\text{asic}}$ follows

$$E_{\text{asic}} \approx Q_d \cdot u_{\text{asic}}, \quad (2.21)$$

which is similar to Eqn. 2.17. Accordingly, the charge Q_d in [26, 32] was calculated.

The energy E_{asic} in Tab. 2.1 varies from 45 μJ up to 6,100 μJ . Most published data are in the range of 200 μJ to 400 μJ . One reason for the strong variations rely on the transmission frequency. Some prototypes were evaluated with 2.4 GHz transmitters, whilst typical TPMSs transmit their data at 315 MHz or at 434 MHz (Europe) [23] and require more transmission time and consequently more energy.

With the knowledge of the required energy, voltage and charge, the energy storage is studied. In general, a large energy storage, being initially charged, provides energy in standby mode for several hours up to a few days and enables measuring and transmitting

data immediately when the vehicle starts driving. While driving, the energy harvester generates electrical energy and charges the storage. Supercapacitors and rechargeable batteries are well-known candidates for this task. However, they do not meet the requirements of many hundreds of thousands of charge cycles. Furthermore, they would suffer from aging, caused by elevated temperatures in the tire. Quite recently, the company Thinika has presented a thin film energy storage device that fulfills these requirements, operating up to 150 °C and guaranteeing more than 100,000 charge cycles [33, 34]. The energy density per area is specified as 10–17 $\mu\text{Ah}/\text{cm}^2$ [34, 35]. The capacity of this thin film storage with an area of a 1 cm^2 would hold between 2 days to 4 days in parking mode, where the TPMS is in standby. However, the main problem arises after a long parking period of more than a couple of days. In this case, the energy storage is discharged, which leads to a voltage drop below u_{asic} . As a consequence, the energy harvester has to generate electrical energy for the signal transmission at the start of the journey on the one hand, and raise the battery level to u_{asic} on the other hand. The latter process depends on the actual voltage level of the partially discharged storage and may take more than a few minutes, which is critical.

Alternatively, a small sized capacitor needs less energy to reach the voltage u_{asic} and can be charged quickly. If an energy harvester is able to provide both sufficient energy to precharge the capacitor to the voltage u_{asic} and additional energy to measure and transmit a signal at the minimum velocity in a specific time, it will always meet the energy requirements. The ISO 21750:2006 defines the minimal velocity and transmission period to be 25 km/h, and 3 mins, respectively. Original equipment manufacturers (OEMs) further confine the signal transmission time to 60 s at most [23].

Commonly used tantalum capacitors with a capacitance of a few hundred microfarads work at operating temperatures of 125 °C. In addition, tantalum capacitors are widely spread, versatilely tested and appropriate for automotive applications. As tantalum capacitors are typically available in a wide range, the appropriate capacitance is determined, subsequently, respecting the E-series of electronic components.

The storage capacitance C_s impacts the amount of energy to precharge the capacitor to the minimal voltage u_{asic} , which is

$$E_{\text{asic}} = \frac{C_s \cdot u_{\text{asic}}^2}{2}. \quad (2.22)$$

Adding the charge Q_d to the precharged capacitor increases the voltage to u_{charged}

$$u_{\text{charged}} = u_{\text{asic}} + Q_d/C_s. \quad (2.23)$$

Accordingly, the total energy E_{charged} is

$$E_{\text{charged}} = \frac{1}{2}C_s u_{\text{charged}}^2 = \frac{1}{2}C_s \cdot (u_{\text{asic}} + Q_d/C_s)^2. \quad (2.24)$$

The energy E_{add} , corresponding to the added charge Q_d , is determined by

$$E_{\text{add}} = E_{\text{charged}} - E_{\text{asic}} = \frac{C_s u_{\text{charged}}^2 - C_s u_{\text{asic}}^2}{2}. \quad (2.25)$$

Replacing u_{charged} from Eqn. 2.23 in Eqn. 2.25 results in

$$E_{\text{add}} = u_{\text{asic}} Q_d + \frac{Q_d^2}{2C_s}. \quad (2.26)$$

With respect to the charge Q_d , listed in Tab. 2.1, a charge $Q_d = 300 \mu\text{C}$ and a voltage $u_{\text{asic}} = 2.5 \text{ V}$ are assumed in this thesis and outlined in Tab. 2.2.

Table 2.2: Charge and ASIC voltage supposed in this thesis

Charge Q_d	300	μC
ASIC voltage u_{asic}	2.5	V

To see the impact of the capacitance C_s on the energy, the charge-voltage relation of the capacitances $C_s = 100 \mu\text{F}$, $220 \mu\text{F}$ and $330 \mu\text{F}$ (E6-series) is illustrated in Fig. 2.9. The red and yellow areas correspond to the energy E_{asic} and E_{add} , respectively.

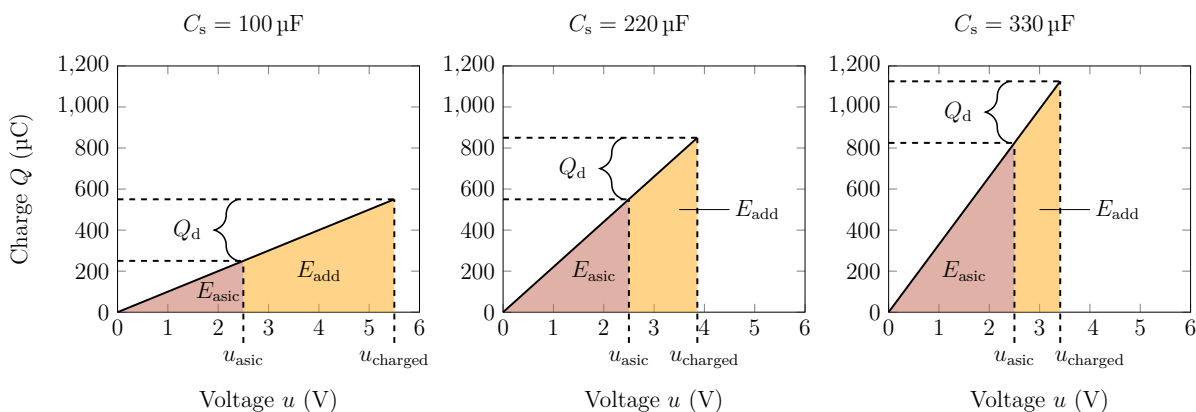


Figure 2.9: Charge Q that a capacitor C_s must store to provide the charge Q_d above the ASIC voltage u_{asic} . The red area represents the energy E_{asic} . The yellow area represents the energy E_{add} to store the charge Q_d on the precharged capacitor.

While a small capacitor requires only little energy E_{asic} and a large amount of added energy E_{add} to store the charge Q_d , the added energy E_{add} decreases with increasing capacitance, whereas the energy E_{asic} raises proportional. The corresponding optimization problem is visualized in Fig. 2.10, where the voltage u_{charged} , the energies E_{asic} , E_{add} and E_{charged} are depicted and additionally quantified in Tab. 2.3.

The total energy E_{charged} in Fig. 2.10 is the superposition of the linear function $E_{\text{asic}}(C_s)$ and the hyperbolic function $E_{\text{add}}(C_s)$ with a minimum at $C_{s,\text{min}} = Q_d/u_{\text{asic}} = 300 \mu\text{C}/2.5 \text{ V} = 120 \mu\text{F}$. The voltage-capacitance relation is purely hyperbolic and decreases with increasing capacitance. While a $100 \mu\text{F}$ capacitor stores sufficient energy when it is charged up to

5.8 V, the capacitors with 220 μF and 330 μF need to be charged to only 3.9 V and 3.4 V, respectively. As commonly known and as it will be shown later in Sec. 7, high voltages are difficult to obtain with electromagnetic energy harvester (EMEH). As a consequence, the capacitance $C_s = 220 \mu\text{F}$ is a good tradeoff between voltage u_{charged} , component size and the required energies E_{add} and E_{charged} .

Table 2.3: Capacitances and corresponding energies normalized to 208 revolutions to be precharged to the voltage u_{asic} , to provide the charge Q_d above the voltage u_{asic} and to be entirely charged to measure and transmit a signal

C_s	u_{asic}	u_{charged}	E_{asic}	E_{add}	E_{charged}	$E_{\text{rev,add}}$	$E_{\text{rev,charged}}$
100 μF	2.5 V	5.50 V	310 μJ	1200 μJ	1510 μJ	5.8 μJ	7.3 μJ
150 μF	2.5 V	4.50 V	470 μJ	1050 μJ	1520 μJ	5.0 μJ	7.3 μJ
220 μF	2.5 V	3.86 V	690 μJ	950 μJ	1640 μJ	4.6 μJ	7.9 μJ
330 μF	2.5 V	3.41 V	1030 μJ	890 μJ	1920 μJ	4.3 μJ	9.2 μJ

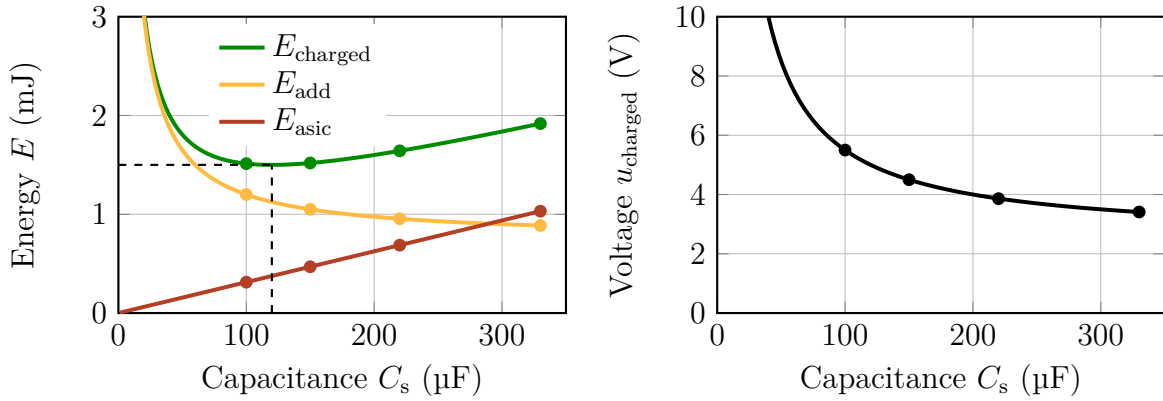


Figure 2.10: Energy E_{asic} , energy E_{add} and their sum E_{charged} as a function of capacitance C_s . The energy E_{charged} corresponds to the voltage u_{charged} of the capacitor C_s . The marks and the dashed lines designate selected capacitances of the E6-series and the minimum of E_{charged} , respectively.

Finally, the required energy is $E_{\text{rev}} = 7.9 \mu\text{J}$ to charge a 220 μF capacitor from 0 V to 3.9 V within 60 s at 25 km/h. The energy matches well with the normalized energy of a coin cell battery $E_{\text{rev,bat}} = 11 \mu\text{J}$ from Sec. 2.2.1. Hence, if a system is able to provide on average $7.9 \mu\text{J}/\text{rev}$, it provides enough energy for a cold start and generates even more energy than required, once it has left the parking mode, and once it is continuously moving. In this case only $E_{\text{rev,add}} = 4.6 \mu\text{J}/\text{rev}$ will be required to maintain the data transmission once a minute. The energy surplus of $7.9 \mu\text{J}/\text{rev} - 4.6 \mu\text{J}/\text{rev} = 3.3 \mu\text{J}/\text{rev}$ can be used for new, energy-hungry algorithms with higher sensor data rates or for a higher data transmission rate while driving. Focusing on both values $E_{\text{rev,add}} = 4.6 \mu\text{J}$ and $E_{\text{rev,charged}} = 7.9 \mu\text{J}$, innovative TPMS energy transducer systems from the literature will be analyzed in detail and compared in Chapter 4.

2.3 Summary

Energy Sources

The most common mechanical excitations sources of the wheel are:

Source	Location	Characteristics
Gravitational acceleration	Rim	<ul style="list-style-type: none"> Vibration amplitude 1 g $a_c \gg g$ for $v \geq 50$ km/h Harmonic excitations with DC bias
Centrifugal acceleration	Tire	<ul style="list-style-type: none"> Large acceleration amplitudes $a_c \propto v^2$ Periodic, non-harmonic excitations
Strain	Tire	<ul style="list-style-type: none"> $-0.3\% < S < 0.7\%$ Velocity independent Periodic, non-harmonic excitations



Requirements

The TPMS energy harvester has to be designed for the following boundary conditions:

Parameter	Symbol	Unit	Value
Operating temperature	T	°C	$-40 < T < 125$
Lifetime	t	a	6
Life span	x_{life}	km	100,000
Signal transmission after	x	m	417
Signal transmission at	v_{min}	m/s	25

From the boundary conditions the following energy specifications were derived:

Parameter	Symbol	Unit	Value
Storage capacitance	C_s	μF	220
Minimal ASIC voltage	u_{asic}	V	2.5
Charged capacitor voltage	u_{charged}	V	3.9
Energy per revolution to charge C_s from 2.5 V to 3.9 V	$E_{\text{rev,add}}$	μJ	4.6
Energy per revolution to charge C_s from 0 V to 3.9 V	$E_{\text{rev,charged}}$	μJ	7.9



3 Electromechanical Transducers

There are manifold electromechanical transducers transforming vibrational energy or strain energy into electrical energy. In this chapter, the most common principles studied for energy harvesting will be presented and are classified according to their physics in electrical and magnetic transducers, as depicted in Fig. 3.1.

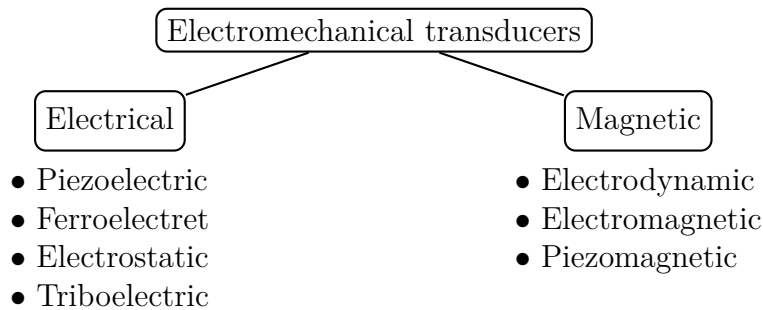


Figure 3.1: Overview of common electromechanical transducers for energy harvesting

For each transducer the energy density w will be derived as a figure of merit to decide which transducer is suitable for harvesting energy for TPMSs. The results will extend the outcomes, presented in [36]. The energy density w is defined as

$$w = \frac{dE}{dV}. \tag{3.1}$$

and describes how much energy E a system can store per volumetric unit V . The quantity is deduced for each transducer and represents an upper limit.

In 2005 [37], an overview of the electrical power density, normalized to the surface area of different ultra-low energy conversion mechanisms was presented. Although this overview is helpful, it has two drawbacks: first, the overview was fed with data from experimentally validated systems. Therefore, it depends on the specific system, even if not optimally designed. Second, both peak-power and the effective power depend strongly on the excitation frequency and are only meaningful for harmonic excitations. For impulse-driven excitations the average power $\bar{P} = 1/T \int_0^T P(t)dt$ is more of interest. The multiplication of the average power \bar{P} with the period T results in the energy. Considering the energy density instead of the power density as an upper bound has the advantage to be independent from both the system design and the excitation signal.

3.1 Electrical Transducers

The first group to be studied are energy transducers made of dielectric materials. Dielectric materials are insulators, which can exhibit polarization in the presence of an electric field \vec{E} [38]. The polarization leads to a displacement of electric charges Q , as described by Gauss's law

$$\oiint \vec{D} \, d\vec{A} = Q \quad (3.2)$$

where \vec{D} , ε and \vec{A} are electric displacement field, permittivity and oriented area, respectively. The electric field is linked to the electric displacement by

$$\vec{D} = \varepsilon \vec{E}. \quad (3.3)$$

The origin of the displacement of the electric charge depends on the transducer and will be described subsequently.

3.1.1 Piezoelectric Transducer

Piezoelectricity describes the phenomena of certain materials to polarize and consequently accumulate electric charge while being mechanically stressed [39]. The effect is also called direct piezoelectric effect. It is reversible and the inverse piezoelectric effect characterizes the opposite behavior of being deformed while an electric field is applied [40]. Piezoelectricity is strongly related to the crystal symmetries. Only crystals with a lack of inversion symmetry (point symmetry) can exhibit piezoelectric behavior, which is illustrated in Fig. 3.2. In the uncompressed state (a) the centers of charge of the positive and negative charged particles balance each other. If the crystal lattice is deformed mechanically (b), the centers of charge of the positive and negative charged particles are displaced and do not balance each other anymore. They form microscopic dipoles within the crystal – proportional to the applied stress. Macroscopically, the volumetric integral of the dipoles creates an electric field, measurable as a voltage.

The macroscopic material behavior is generally described as a tensor. In the following, only the effects are of interest in which the mechanically field direction and the electric field direction are either parallel or orthogonal, commonly known as "33-effect" and "31-effect", respectively. The simplified governing equations are

$$\begin{aligned} D &= d \cdot T + \varepsilon^T \cdot E \\ S &= s^E \cdot T + d \cdot E \end{aligned} \quad (3.4)$$

where D , T , E , S , d , ε^T , s^T are the electric displacement field, stress, electric field, strain, piezoelectric stress constant, elastic constant and dielectric permittivity when the stress $T = 0$, expressed by the superscript. The transition from the field quantities to quantities

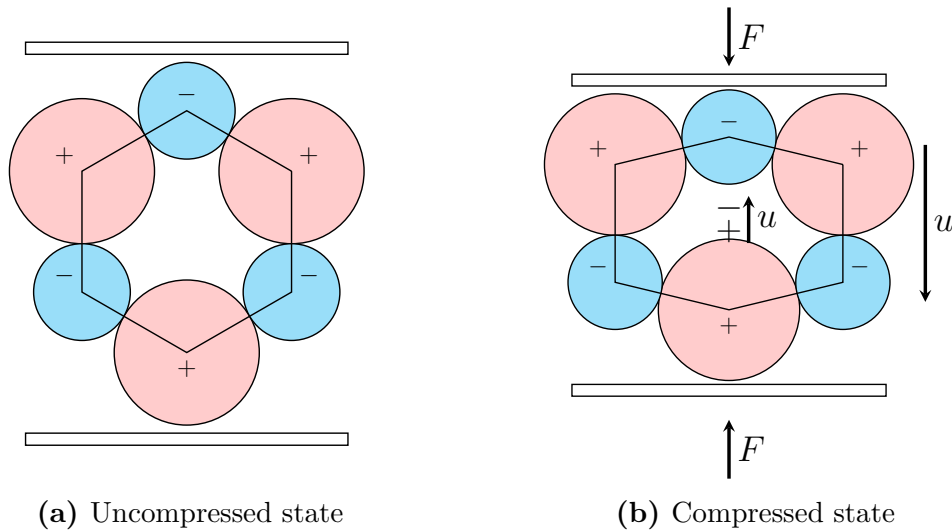


Figure 3.2: Simplified two-dimensional crystal lattice structure without point symmetry. A force F deforms the crystal lattice and forms electrical dipoles, which create an electric field, measurable as a voltage u .

of an electromechanical network is explained in [40] and leads to the network model shown in Fig. 3.3 with the transducer coefficient α , the compliance n_{sc} , which is obtained when the electrical domain is short-circuited ($u = 0$) and with the piezoelectric capacitance C_p , which can be determined when the mechanical domain is short-circuited ($v = 0$).

Worthwhile mentioning is the big advantage of a network model description: Electrical networks are used to simulate complex electrical circuits. With the help of optimized algorithms, the electrical network quantities voltage and current are rapidly calculated in every single node and across every component, respectively, either in time or frequency domain. As other physical domains, such as thermodynamics or mechanics underlie isomorphic mathematical descriptions, namely differential equations, their systems can be described similarly and interpreted as a network with electrical symbols. For example, the mechanical quantities force and velocity correspond to the electrical quantities current and voltage in the so-called 2nd analogy and represent flow and across quantities, respectively. The mechanical element mass, described by the relation between force and velocity

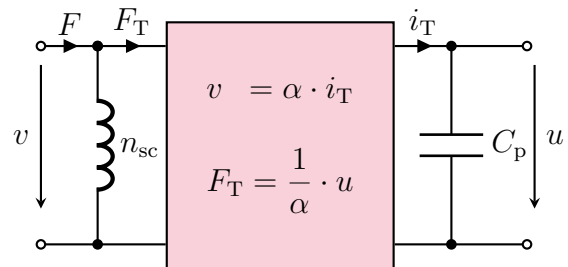


Figure 3.3: Transducer element of a piezoelectric material

$$F = m \cdot a = m \cdot \frac{dv}{dt} \quad (3.5)$$

and the mechanical element compliance, expressed as

$$F = \frac{z}{n} = \frac{1}{n} \int v dt \quad (3.6)$$

are represented by the symbol of a capacitor and of an inductance, respectively, in an electromechanical network. More isomorphic structures are deduced and listed in [41].

When a piezoelectric materials is strained, it transforms mechanical energy into electrical energy. The mechanical energy density w_{mech} is expressed as

$$w_{\text{mech}} = \frac{Y S^2}{2} \quad (3.7)$$

with S and Y are strain and Young's modulus. Multiplying the mechanical energy density with the material specific squared electromechanical coupling coefficient defined by

$$k = \sqrt{\frac{E_{\text{el}}}{E_{\text{mech}}}} \quad (3.8)$$

leads to the electrical energy density

$$w_{\text{el}} = k^2 \cdot w_{\text{mech}}. \quad (3.9)$$

Lead zirconate titanate (PZT) compounds are used as piezoelectric materials with high piezoelectric constants and with high electromechanical coupling. However, PZT ceramics are brittle. This drawback has already been counteracted in the past: Macro Fiber Composite (MFC) [42, 43], which consists of piezo-ceramic fibers embedded in a polymer matrix, are a good tradeoff between flexibility and energy density. The material properties of PZT ceramics can be modified through doping. A selection of PZT ceramics of different manufactures are characterized and opposed to the more elastic piezoelectric material polyvinylidene fluoride (PVDF) in Tab. 3.1.

Based on Eqns. 3.7, 3.8, the electrical and mechanical energy density can be approximated and are listed in Tab. 3.2. A strain S of 0.1% and 2% is supposed for the piezo-ceramics and for PVDF, respectively. The strain limit includes the minimum of the tensile strength of the piezoelectric material and the non-negligible depolarization which in the case of PZT-5A already occurs at a compressive strain of 0.15% [49].

Temperature stability inside the tire is demanded for temperatures up to 125 °C. Since the Curie temperature is defined as temperature at which all ferroelectric or ferromagnetic properties entirely disappear, the depolarization starts at lower temperatures. Therefore, the Curie temperature of the material should be largely above 125 °C. A rule of thumbs is that the Curie temperature of the desired material should be twice the operation temperature in °C. PVDF materials do not fulfill this requirement. Furthermore, the system design should take into account that piezo-ceramics have a much larger compressive strength σ_c than tensile strength σ_t .

Table 3.1: Properties of selected piezoelectric materials

Parameter	Unit	PZT-5A [40, 44]	PIC 252/255 [45]	M1100 [46]	PVDF [47, 48]
d_{33}	pC/N	374	400	640	-27
d_{31}	pC/N	-171	-180	-315	20
s_{33}	10^{-12} m ² /N	18.8	19	20.6	400
s_{11}	10^{-12} m ² /N	16.4	15	14.2	400
ε_{33}	ε_0	1730	1750	4500	12
ε_{11}	ε_0	1700	1650	4750	12
k_{33}	1	0.71	0.69	0.71	0.2
k_{31}	1	0.34	0.35	0.42	0.15
T_{Curie}	°C	365	350	177	80
σ_c	MPa	>520	> 600	> 600	60
σ_t	MPa	75-80		80	35-50

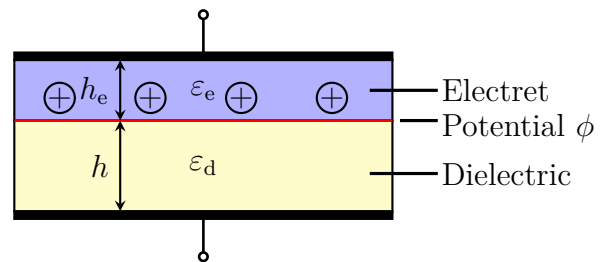
Table 3.2: Maximal strain and calculated mechanical energy density of selected piezoelectric materials

Parameter	Unit	PZT-5A	PIC 252/255	M1100	PVDF
S_{max}	%	0.1	0.1	0.1	2
w_{mech}	mJ/cm ³	31	33	35	500
$w_{\text{el},33}$	mJ/cm ³	15	16	18	20
$w_{\text{el},31}$	mJ/cm ³	3.6	4.1	6.2	11

3.1.2 Electrostatic Transducer

Electrostatic systems convert mechanical energy into electrical energy by a capacitor whose capacitance is modified: Mechanical work is responsible for changing the distance between the capacitor electrodes, which surround a dielectric with relative permittivity ε_d , while either the charge or the voltage is kept constant. Today, two conversion principles exist: the electret-free and the electret-based transduction.

An electret is a dielectric materials, which preserve electric charges for a long period [50]. The electret-free conversion requires an additional source (e.g. a battery) and is not considered as a solution for a self-sufficient energy harvesting system. The electret-based electrostatic converter uses an electret, that exhibits the constant electric potential ϕ at the surface between dielectric and electret as illustrated in Fig. 3.4. The

**Figure 3.4:** Schematic of an electret-based electrostatic transducer

voltage potential is derived from Gauss's law as

$$\varepsilon_e \varepsilon_0 E = \sigma, \quad (3.10)$$

where ε_0 , ε_e , E and σ are the vacuum permittivity, the relative permittivity, the electric field and the surface charge density of the electret, respectively. Supposing a homogeneous electric field distribution across the dielectric, then the electric potential ϕ is

$$\phi = \frac{\sigma h_e}{\varepsilon_0 \varepsilon_e}, \quad (3.11)$$

where h_e is the electret height [51]. Table 3.3 lists the parameters of common electret materials to calculate the surface potential. Although environmental conditions such as temperature and humidity have an impact on the surface charge density, the temperature stability of the listed electrets is given for temperatures up to 150 °C [52–54]. Applying

Table 3.3: Properties of common electrets [51]

Electret	Maximal height h_e (μm)	Relative permittivity ε_e (1)	Surface charge density σ (mC/m ²)
PTFE/FEP	100	2.1	0.1 - 0.25
SiO ₂	< 3	4	5 - 10
Parylene	20	3	0.5 - 1

Eqn. 3.11 on the listed parameters in Tab. 3.3, voltages of many hundred volts can be obtained. Air at ambient pressure is typically used as dielectric material for electrostatic transducers. The electrical energy density of the system is approximated by

$$w_{\text{el}} = \frac{1}{2} \varepsilon E^2, \quad (3.12)$$

with E the electric field strengths. The electric field strength in air is limited by the breakdown field strength E_b , which is related to the breakdown voltage u_b and the distance h between two electrodes by $E_b = u_b/h$. The breakdown voltage is a function of pressure p and electrode distance h and described by Paschen's law. For air at room temperature the voltage has the minimum $u_b \approx 340$ V at $p \cdot h_{\text{min}} = 7.3$ bar· μm [55]. The minimum breakdown voltage corresponds to the breakdown field strength $E_b = 480$ MV/m. In [36], a much smaller field strength of 30 MV/m was assumed as more probable to obtain, leading to the electrical energy density of

$$w_{\text{el}} \leq 4 \frac{\text{mJ}}{\text{cm}^3}. \quad (3.13)$$

3.1.3 Ferroelectret Transducer

Another interesting material type are ferroelectrets. A ferroelectret consists of a non-polar polymer foam, which encapsulates artificial air voids. These voids are used to trap and store charges quasi-permanently. A strong electrical field is applied to the material. When the electric field strength in the air voids reaches the Paschen breakdown field strength, the process of ionization starts in the air cavities and charges of opposite polarity are separated [56]. When the electric field is removed, the separated charges form a macroscopic dipole, as shown in Fig. 3.5a. The fabricated material behaves similar to a ferroelectric material: One can observe a permanent dipole polarization and hysteresis of that polarization in response to a periodic electric field [57]. As depicted in Fig. 3.5b, an applied force compresses the polymer and the air cavities. The macroscopic dipole moments are reduced and consequently the charge, too. If both two electrodes are connected, the change in charge results in a measurable electric current.

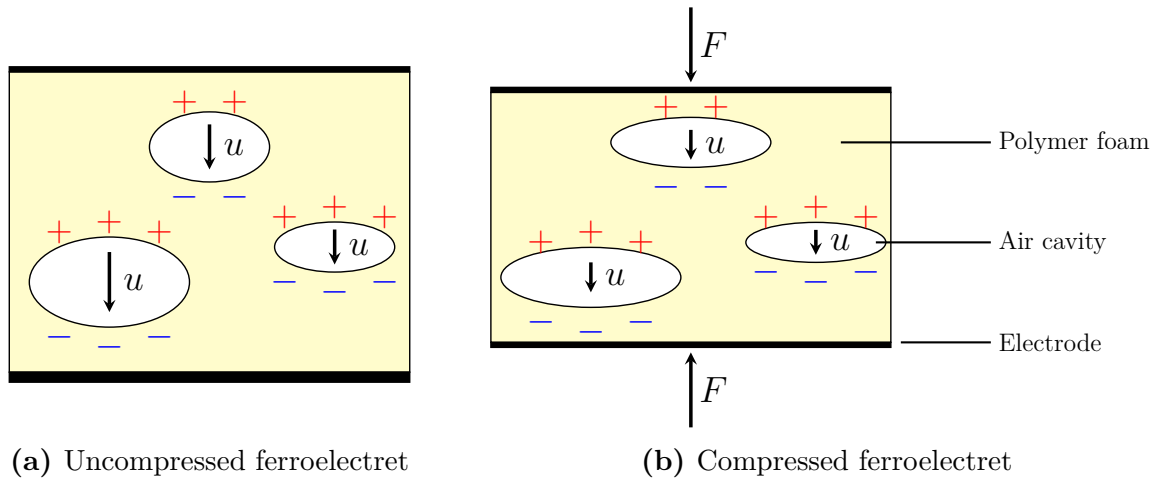


Figure 3.5: Schematic of a ferroelectret transducer with polarized air cavities in (a) and altered center of charge due to an external force F in (b)

Ferroelectrets are approximately 10^5 times more compliant compared to their piezoceramic pendant. Their Young's modulus is in the range of a few megapascal [57]. Due to their softness, the piezoelectric constant d_{33} is in the range of the one of PZT or higher [58, 59], as listed in Tab. 3.4. However, most trapped charge voids suffer from a significant discharge at temperatures elevated above 70°C [59, 60]. Recently, a few polymer materials based on fluoropolymers, like PTFE and FEP were established and work at higher operation temperatures. They were evaluated at temperatures of 120°C and above without a significant decrease in piezoelectricity up to 120°C [61–63].

In contrast to the high longitudinal piezoelectric coefficient of ferroelectrets, the transverse coefficient is typically in the range of 2 pC/N . Quite recently, Zhang et al. [58, 65] developed a tubular FEP based ferroelectret energy harvester with relatively high transverse activity and stated a piezoelectric coefficient of 32 pC/N . Their material data are listed in Tab. 3.5.

Table 3.4: Properties of ferroelectret with large direct effect [64]

Modified Young's modulus	Y_{11}	1-6	MPa
Relative permittivity	ε	2 - 2.1	
Piezoelectric coefficient	d_{33}	200-1200	pC/N

Table 3.5: Properties of ferroelectret with large transverse effect [65]

Height	h	25 - 300	μm
Modified Young's modulus	$Y_{11} \cdot h$	60	N/m
Relative permittivity	ε	1.2	
Piezoelectric coefficient	d_{31}	32	pC/N

Supposing that the trapped charge voids fill the whole space between the electrodes, the system resembles a capacitor. Since the voids are in the range of a few tens to hundreds of micrometers, the same field strength as for electrostatic transducers is supposed. Applying Eqn. 3.12 with $E = 30 \text{ MV/m}$ leads to the electrical energy density

$$w_{\text{el}} \leq 4 \text{ mJ/cm}^3, \quad (3.14)$$

independently of the polymer foam, of the applicable strain and of the charge density.

3.1.4 Triboelectric Transducer

The triboelectric effect describes the phenomena, that a certain material becomes electrically charged after being separated from a different material. The effect often appears in our normal life, when the hair is combed, while walking with shoes in a room with carpeting or while sliding down the slide. Even if the effect has been known for centuries, only a few years ago, the first triboelectric nanogenerator was presented in [66]. One well known mechanism is the contact electrification, in which two different materials are brought together to be in contact. Due to different electronegativities of the materials, surface charge transfer occurs at the intersection. When the materials are separated, each material has a net charge that can be measured as the voltage across the electrodes [67]. The principle is illustrated in Fig. 3.6.

Nanomaterials play an important role, as they increase the surface area and thereby the triboelectric effect. The vision described in [68] is to use triboelectric nanogenerators to generate energy from ocean waves on a large scale. However, triboelectric nanogenerators are an emerging technology and a nearly constant power generation at temperatures up to 125°C is still a problem [69, 70]. The nanogenerators mostly exhibit very high open-circuit voltages in the range of $100 \text{ V} - 1000 \text{ V}$ but very low short currents in the range of $1 \text{ nA} - 1 \mu\text{A}$. Consequently, the accumulated charge is only in the range of 100 nC [71–73].

Triboelectric generators are comparable with electrostatic generators with the differ-

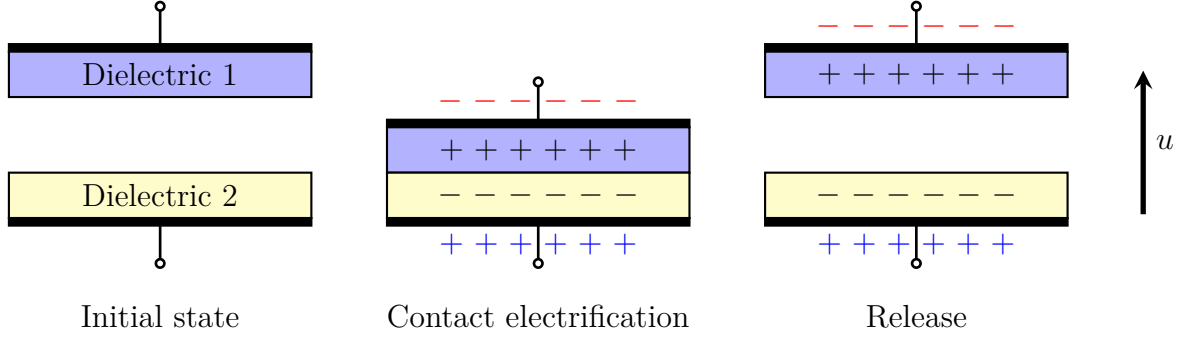


Figure 3.6: Schematic of the triboelectric transducer principle

ence, that the contact electrification generates charges. For a typical contact electrification as depicted in Fig. 3.6, the energy density is limited by the energy of the electric field, as deduced in Sec. 3.1.2 and stated in Eqn. 3.13. Under ambient air conditions, it is

$$w_{el} \leq 4 \frac{\text{mJ}}{\text{cm}^3}. \quad (3.15)$$

3.2 Magnetic Transducers

The second main transducer group bases on effects related to the magnetic field. One effect is the electromagnetic induction inside an electric conductor when the magnetic flux density \vec{B} is varied. The phenomenon is formalized by the Maxwell-Faraday equation as

$$u = \oint \vec{E} d\vec{s} = - \iint \frac{\partial \vec{B}}{\partial t} d\vec{A}, \quad (3.16)$$

where u , \vec{E} , \vec{s} , t , \vec{A} are induce voltage, electric field, oriented integration path, time and oriented cross-section, respectively. When the conductor is connected to a load, a current flows and creates a magnetic field which is oppositely directed to the original magnetic field. The effect is described by the Lorentz force \vec{F}_1 as

$$\vec{F}_1 = i \cdot \int d\vec{l} \times \vec{B}. \quad (3.17)$$

Both equations are governing for both electrodynamic and piezomagnetic transducers.

Not only is the electromagnetic induction fundamental to characterizing the energy conversion, but also Ampère's circuital law which describes the magnetic flux density around a closed loop that is related to the current flowing through this closed loop. It is known as

$$\oint \vec{B} \cdot d\vec{s} = -\mu_0 \cdot i. \quad (3.18)$$

In an magnetic circuit with a small air gap, the magnetic flux density can be considered

constant. If the length of the air gap is modified and leads to a change of the magnetic energy. The relation between force and magnetic flux is calculated according to the principle of virtual work [74] and leads after linearization to

$$\vec{F}_{\text{mag}} = \frac{\vec{B}^2}{2\mu_0} \vec{A}. \quad (3.19)$$

With the magnetic flux $\Phi = \vec{B}\vec{A}$ follows

$$\vec{F}_{\text{mag}} = \frac{\Phi^2}{2A\mu_0} e_{\vec{A}}, \quad (3.20)$$

where $e_{\vec{A}}$ is the unit vector in the direction of the oriented area \vec{A} . Equations 3.18 and 3.20 are governing for the electromagnetic transducer, presented in [74]. Electromagnetic transducers are typically driven by an electromagnet and require an additional energy supply that is not self-sufficient. Therefore, only electrodynamic and piezomagnetic transducers will be presented in detail, subsequently.

Since electromagnetic transducers according to the definition of [74] are not considered further, the strict distinction between electromagnetic and electrodynamic transducers is neglected in the following chapters and both terms electromagnetic energy harvester (EMEH) and electromagnetic transducer are used synonymously for electrodynamic transducers.

3.2.1 Electrodynamic Transducer

The magnetic flux density of an electromagnetic transducer can be created either by a permanent magnet or by an electromagnet. Permanent magnets exhibit permanently a magnetic field, which make them appropriate candidates for energy harvesting, compared to electromagnets which require an external energy source and which are not self-sufficient. The relative movement of a permanent magnet with respect to a conductor as depicted in Fig. 3.7 leads to an electromagnetic induction at the terminals of the coil according to Eqn. 3.17.

The corresponding network model of the ideal electrodynamic transducer is depicted in Fig. 3.8, where n_{oc} and L_c are the compliance under electrical open-circuit condition and the inductance of the ideal coil, re-

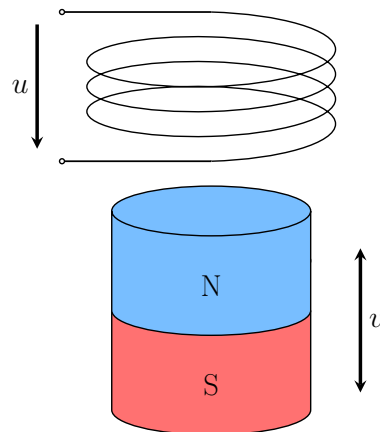


Figure 3.7: Electromagnetic induction caused by the relative motion between permanent magnet and coil

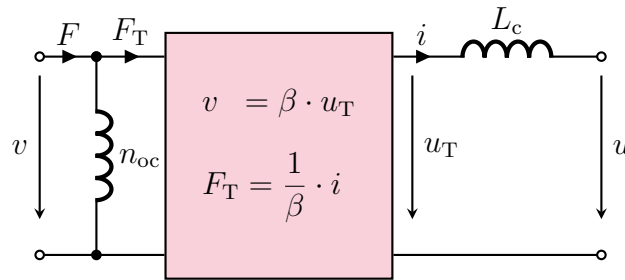


Figure 3.8: Electrodynamic transducer element

spectively. As demonstrated in [40, 75], the network coordinates (u_T, i) and (v, F_T) are coupled by the transducer coefficient, here denoted β , which depends on the magnetic field and the system geometry. The coefficient β can be considered constant for small displacements of the permanent magnet with respect to the coil length. Otherwise, the inhomogeneous magnetic field provokes a position dependent transducer coefficient.

The higher the magnetic field \vec{B} of the permanent magnet, the higher the induced voltage and the higher the portion of mechanical energy is which is transformed into electrical energy. Important characteristics of permanent magnets are the energy product BH , representing the total stored field energy, the Curie temperature T_{curie} and the permeability μ . Ferrite and neodymium are two typical materials to manufacture permanent magnets. Their important material properties are contrasted in Tab. 3.6.

Neodymium (NdFeB) magnets are well known for their high energy product. The grade of a neodymium magnet corresponds to the energy product, given in the centimeter-gram-second (CGS) unit MGOe (Mega Gauss Oersted), where $1 \text{ MGOe} = 7.96 \text{ mJ/cm}^3$. Today, these magnets exhibit the highest magnetic field among the commercially available permanent magnets. Depending on the material composition, their maximal operation temperature varies between 80°C and 200°C . The ratio of the magnet surface area to the height has an influence on the operation temperature. The smaller the ratio is, the higher the operation temperature is. Ferrite magnets loose a part of their magnetization below -40°C [76], whereas this temperature is not critical for neodymium magnets.

Table 3.6: Properties of selected magnetic materials

Parameter	Symbol	Unit	Ferrite [76, 77]	Neodymium [78, 79]
Energy product	BH	mJ/cm^3	30 – 45	240 – 430
Rel. permeability	μ_r	1	1.05 – 1.1	1.05
Curie temp.	T_{curie}	$^\circ\text{C}$	460	310 – 380
Operation temp.	T_{op}	$^\circ\text{C}$	$-40 < T_{\text{op}} < 250$	$< 80 - 200$

3.2.2 Piezomagnetic Transducer

In 1842 James Prescott Joule observed a length change in iron when a magnetic field was applied [80], today known as magnetostriction. A few years later, the Italian scientist Villari discovered the inverse effect, that the permeability of a material is changed while being stressed [81]. All ferromagnetic materials possess these properties. The effect is highly nonlinear. When linearized around an operating point, where only first-order effects appear, the term piezomagnetism is used [82]. The explanation of magnetostriction relies on quantum physical spin-orbit coupling. Macroscopically, the phenomena can be simplified by an alignment of magnetic domains, which causes a strain. Widely known magnetostrictive materials with a high magnetostriction are Terfenol-D and Galfenol. Both materials have high coupling coefficients and the Curie temperature is sufficiently high for tire energy harvesting application. Their material properties are summarized in Tab. 3.7.

Table 3.7: Properties of magnetostrictive materials

Parameter	Symbol	Unit	Terfenol-D [83]	Galfenol [84]
Young's modulus	Y	GPa	18 – 55	40 – 60
Tensile strength	σ_t	MPa	28 - 40	350
Compressive strength	σ_c	MPa	300 - 880	-
Curie temperature	T_{curie}	°C	380	670
Relative permeability	μ_r	1	2 – 10	75 – 100
Piezomagnetic constant	d_{33}	nm/A	6 – 10	20 – 30
Magnetomechanical coupling	k_{33}	1	0.7 – 0.8	0.6 – 0.7

Based on the tensile strength and Young's modulus, the employable strain is estimated and both the maximal mechanical and maximal magnetic energy density are calculated applying Eqn. 3.7 and Eqn. 3.9, respectively. The results are listed in Tab. 3.8.

Table 3.8: Calculated mechanical energy density of selected piezoelectric materials

Parameter	Unit	Terfenol-D	Galfenol
S_{max}	%	0.1	0.7
w_{mech}	mJ/cm ³	19	1200
w_{mag}	mJ/cm ³	11	510

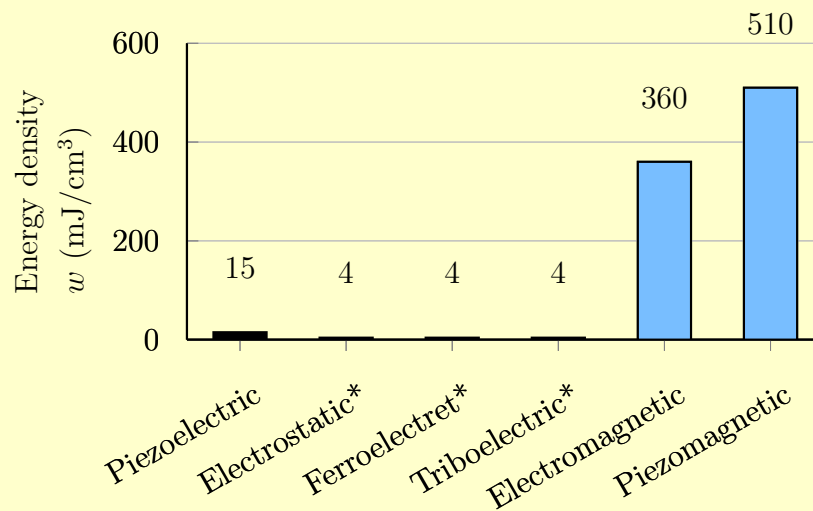
According to Tab. 3.8, the magnetic energy density is high. However, further losses occur, as the magnetic energy needs to be converted into electrical energy. Therefore, a well positioned coil on a piezomagnetic system transduces the magnetic energy into electrical energy [85, 86]. For a high transducer coefficient a biasing magnet is typically employed and sets the operating point. Compared to piezoelectric transducers, piezomagnetic transducers have a similar mechanical setup, including clamping and a beam structure, but need additional components which make them bulky [86–88].

3.3 Summary

Electromechanical Transducers

Various transducers have been presented and are summarized below, wherein the most suitable material has been selected as a representative of its category. With respect to Paschen's law, a breakdown field strength in air of $E_b = 30 \text{ MV/m}$ was assumed for the calculation of the electrical energy density of the electrical transducers with *. The notation "new" in the table below indicates, that these transducers are relatively new and require further fundamental research.

Transducer	w_{el} or w_{mag} (mJ/cm ³)	$T_{\text{op}} \geq 125 \text{ }^\circ\text{C}$	Comment
Piezoelectric	15	yes	brittle
Electrostatic*	4	yes	typically miniaturized
Ferroelectret*	4	yes	soft, new
Triboelectric*	4	not yet	nanomaterials, new
Electrodynamic	360	yes	low voltage
Piezomagnetic	510	yes	very low voltage, bulky



Magnetic transducers exhibit the highest energy density among the transducers. The electrical energy density is actually lower because an additional step is necessary to convert the magnetic energy into electrical energy. Since piezomagnetic systems are bulky, electrodynamic transducers are more suitable.

Among the electric transducers, piezoelectric systems have the highest energy density. The brittleness of PZT can be overcome if it is embedded in a polymer matrix. Consequently, **piezoelectric** and **electrodynamic transducers** are regarded as **appropriate candidates** for TPMS energy harvesting.



4 State of the Art of TPMS Energy Harvesters

This chapter presents recently developed and studied energy harvesters specifically designed to harvest energy inside the wheel. A throughout comparison between different TPMS transducers is presented and overviews the state-of-the-art comprehensively. Typical TPMS energy harvesters are summarized and common problems are outlined, focusing on the transducer mechanism, interface circuit and energy generation. Pros and cons of different energy transducer principles for their operation inside the tire are balanced. Focusing on reliability and on normalized energy generation, this chapter highlights potent energy harvesters for system enhancement and creates the basis of own energy harvester prototyping. This chapter is part of the article published in [16].

4.1 Rim Wave Based Systems

In 2009, Zheng et al. [89] presented a rim-based piezoelectric cantilever. They designed an asymmetric air spaced system to take advantage of the much higher compressive strength of a piezo-ceramic compared to its tensile strength. A diode bridge rectified the signal and a 32 μF capacitor was used to store the energy. At about 80 km/h, the system with a seismic mass of 21.6 g was able to provide a power of 47 μW , equivalent to 4 $\mu\text{J}/\text{rev}$ applying Eqn. 2.15.

Roundy and Tola presented an innovative piezoelectric system, driven by the gravitational change at the rim in 2013 [90] and 2014 [31]. Their system contained two piezoelectric beams, lying flat on the top and bottom side of a metallic housing, as shown in Fig. 4.1. In the inner part of the housing, a 6.8 g heavy ball was placed, which moved in the direction of z from one end to the other and backwards within one tire revolution.

Two holes were drilled in the housing, one at the bottom and one at the top side. Two steel balls, one in each hole, formed with the piezoelectric beams a spring. The setup enabled to transform the movement in the z -plane into a perpendicular movement of the two piezoelectric beams. While the heavy ball passed the center, the two piezoelectric beams were deflected and generated energy. Highly advantageously, both the beam deflection amplitude and the provided piezoelectric energy per revolution were constant and independent of the velocity. During tests, the scientists connected a rectifier between the harvester and a 40 μF capacitor. Applying Eqn. 2.15 on the published data, an energy

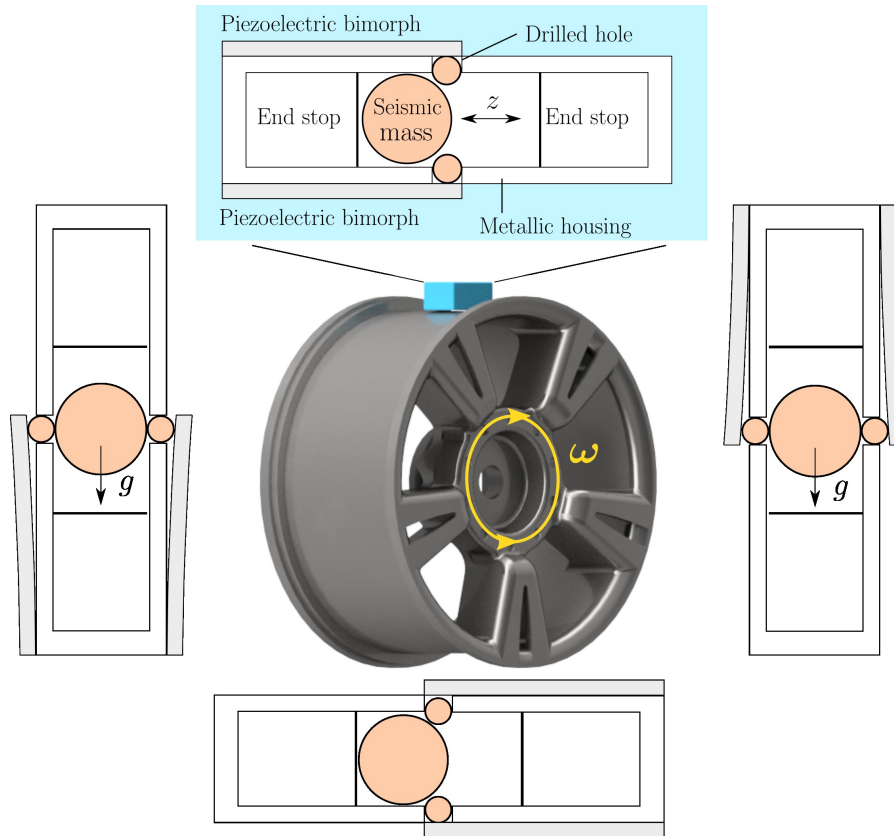


Figure 4.1: Schematic of the rim based piezoelectric energy harvester from Roundy et al. [31]. During one tire revolution, the seismic mass rolls between the two end stops and causes a deflection of the piezoelectric bimorphs

per revolution of $6 \mu\text{J}$ over a wide range of velocities up to 155 km/h can be estimated. At velocities above, measurements revealed system problems and the good performance collapsed rapidly because of the increasing rolling friction.

4.2 Tire Wave Based Systems

Years earlier, in 2003, Roundy dedicated a chapter of his PhD thesis to use the energy of an automobile tire with a piezoelectric bimorph converter [22]. He designed a transducer, consisting of a one sided clamped beam on whose end he attached a seismic mass¹. The system is illustrated in Fig. 4.2. A vivid analysis of such a system is given in [41] and [74]. As the proof mass spanned the majority of the beam, it performed simultaneously a limit

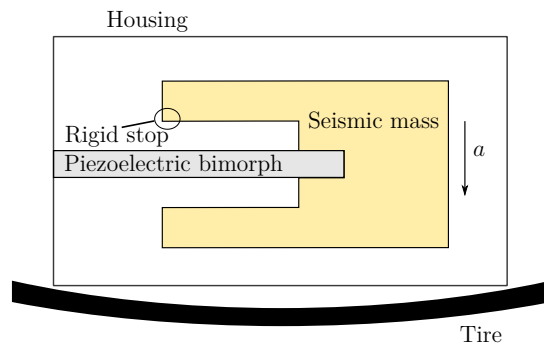


Figure 4.2: Clamped piezoelectric bimorph converter with seismic mass and rigid stoppers

¹Proof mass, tip mass and seismic mass are synonymously used.

stop and restrained the beam deflection. Roundy simulated the system response for a $300\text{ k}\Omega$ resistive load connected to a full-wave rectifier at 20 km/h , 60 km/h and 100 km/h and obtained an energy per revolution of $2\text{ }\mu\text{J}$, $5\text{ }\mu\text{J}$ and $6\text{ }\mu\text{J}$, respectively.

Four years later, Keck [91] studied a piezoelectric PZT-steel unimorph, connected to a 1.1 g seismic mass at the center as depicted in Fig. 4.3. Pin supports at both ends guaranteed a smaller stiffness compared to the fixed-fixed support. Asymmetrically arranged rigid motion stops were used to limit the strain and to account for the different tensile and compressive strength of a piezo-ceramic. However, the author reported robustness issues at high speeds. A full-wave rectifier with a capacitor was used to store the harvested energy. In the range between 40 km/h and 80 km/h the system was able to provide more than $6\text{ }\mu\text{J/rev}$, whereas at other velocities the energy was smaller.

A few years later, the research group around Frey, Kühne et al. [28, 92–95] studied a MEMS piezoelectric unimorph. In contrast to a commonly used rectangular beam, they designed a triangular shaped mechanical oscillator with a thin film piezoelectric layer deposited on a substrate layer, optimized for a constant stress distribution in the material. A combination of passive and active full-wave rectifier and a capacitor were connected to the piezoelectric transducer. However, an experimental verification inside the tire was missing [26].

A different idea to the former piezoelectric system came from Renaud, Fujita et al. [96–100]. They presented a $\text{SiO}_2\text{-Si}_3\text{N}_4$ electret-based electrostatic energy harvester, actually using the change in tangential acceleration. They considered the independent design of the system components as a big advantage compared to piezoelectric systems, where the properties, such as electromechanical coupling and compliance, are interconnected and rely on the chosen piezoelectric material. The $1\text{ }\mu\text{m}$ thick SiO_2 and $0.15\text{ }\mu\text{m}$ thick Si_3N_4 stacked electret was treated by Corona discharge which led to a surface potential of 120 V . According to both Eqn. 3.11 and the data in presented in Tab. 3.3, the voltage refers to a surface charge density of 4.25 mC/m^2 . In practical tire tests, the authors measured an average power of $15\text{ }\mu\text{W}$ with a matched resistance at 50 km/h , corresponding to an energy of $2.2\text{ }\mu\text{J/rev}$. Furthermore, they suggested to connect a DC-DC buck converter to charge a storage capacitor, working in discontinuous conduction mode, if supplied at least with a voltage of 2.2 V . At lower voltages a direct charge mechanism, presumably a full-wave rectifier, was used to charge the storage capacitor.

Being aware of the huge shock impacts, the authors investigated the system reliability

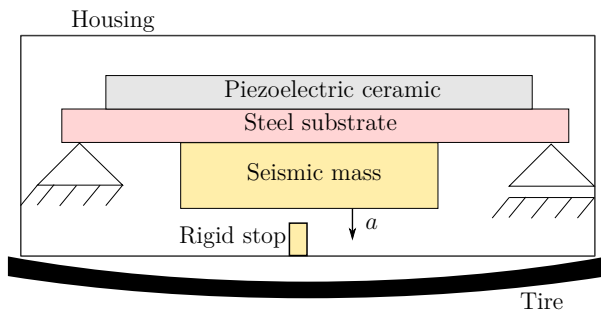


Figure 4.3: Piezoelectric unimorph with asymmetric motion stops and seismic mass

in four scenarios. They added hard stoppers, parylene based soft stoppers and flexible stoppers for a silicon only solution and compared them with the unmodified system. Between 26 and 28 samples were tested in each category. While systems without stoppers and with rigid stopper developed cracks at the minimal shock amplitude of 400 g (≈ 125 km/h), only one sample out of 27 failed with the soft parylene stopper at 2500 g (≈ 310 km/h). Two of 27 samples with flexible stoppers failed at 1750 g (≈ 260 km/h). The author further observed, the more flexible the stoppers are, the higher the crackless impact can be.

From 2010 to 2012, Tornincasa, Bonisoli et al. [101–103] analyzed an electromagnetic energy harvester, depicted in Fig. 4.4. They placed a freely movable permanent magnet inside a cylindrical tube. A magnet with opposite magnetic field with respect to the movable magnet was embedded at the bottom of the tube. Both magnets formed a nonlinear magneto-mechanical spring due to the nonlinear repulsive magnetic force. In addition, elastic bumpers were attached, one at each cylinder end. Two coils wound around the cylinder generated a voltage according to Faraday’s law, whenever the magnetic field changed. Within one tire rotation, the movable magnet is pressed towards the fixed magnet.

However, the centrifugal force is released in the area of tire ground contact and the movable magnet starts oscillating and creates a changing magnetic field, pervading the coils. The authors simulated the system behavior inside a Simulink environment at different velocities and tested the performance on a shaker at 40 km/h and 60 km/h, reproducing the recorded tire acceleration signal without the mean value. To establish the mean acceleration component a_c as introduced in Sec. 2.1.2, they added a second fixed magnet at the upper lid.

A combined finite element method (FEM) and network simulation of the nonlinear system was provided by Germer et al. in [75]. A full-wave bridge rectified the AC signal. To imitate the constant centripetal force appearing outside the contact patch, the inventors added a second fixed magnet with repulsive force with respect to the floating magnet. In which way this magnet represents a centrifugal force of a tire has not been stated. As the fixed magnet adds a high position dependent nonlinear force, its comparison with the centrifugal acceleration is very restricted. In addition, the centrifugal force at different velocities cannot be reconstructed by one single fixed magnet.

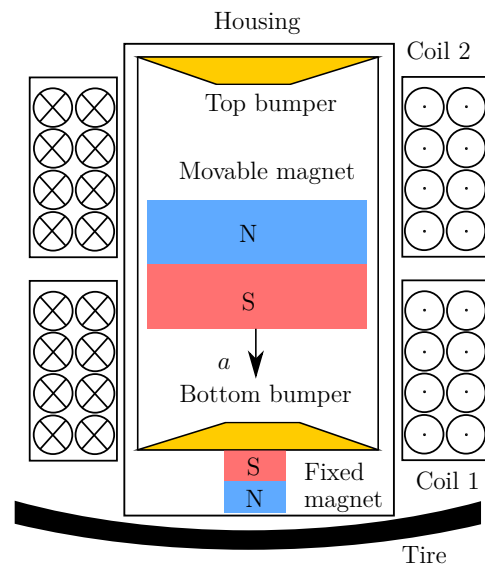


Figure 4.4: Nonlinear cylindrical electromagnetic energy harvester [75]

A huge advantage of the transducer system consists of its compact and robust structure. The movable magnet is robust and the high impact at both cylinder ends will be converted in an elastic rebound, produced by the interplay of movable magnet and elastic bumper. Although this electromagnetic system seems to be very promising, the published data cannot be easily compared to other systems in terms of energy, due to different data representation and due to a lack of information. Power values of a few milliwatt were published, but cannot neither consistently linked to the peak power nor to the average power of the presented system data.

4.3 Strain Based Systems

In 2012, van den Ende et al. [104, 105] studied strain based energy harvesters and compared different self built ceramic-polymer composites, containing PZT particles, with commercial available PVDF and MFC. Hereinafter, of greater interest are the results of PVDF and MFC, as they had the highest piezoelectric response among the studied materials. The research group estimated an energy per revolution of $54 \mu\text{J}$ and $5.2 \mu\text{J}$ normalized to 1 cm^2 active piezoelectric area for MFC and PVDF, respectively, based on charge measurements under optimal capacitive load conditions.

The authors studied the influence of elevated temperatures and strains on the piezoelectric response. They reported a significant irreversible decrease of the piezoelectric coefficient of PVDF above 60°C due to the low Curie temperature of about 100°C . For MFC, a slight performance decrease was observed at temperatures above 100°C . However, the manufacturer Smart Materials GmbH delivers MFCs by default with a maximum operating temperature $T \leq 85^\circ\text{C}$ which explains the observed performance decrease. However, a high temperature variant of MFC with an operating temperature $T \leq 130^\circ\text{C}$ is available and needs to be addressed explicitly when ordering. Consequently the question arises, how a high temperature MFC would behave. Further, van den Ende et al. used a tensile test machine to detect any degradation caused by high strains. PVDF was strained up to 2% and a slight increase of the piezoelectric coefficient was measured. For MFCs, the piezoelectric coefficient increased at first, and decreased irreversibly to $4.8 \mu\text{J}/\text{rev}/\text{cm}^2$ above 0.22% strain, which is consistent with the observations made in [106, 107]. Own simulations and experiments of the MFC-type 1 material, exploiting the 33-effect, are presented in Sec. 5.3.2 and show that this material exhibits very high voltages of more than 105 V at strains above 0.22%. As it will be shown in Sec. 6.2, efficient energy transfer from a sinusoidal voltage source to a capacitor connected to a full-wave rectifier, which is also known as Standard Energy Harvesting (SEH), is limited to 25% at most and necessitates a normalized voltage

$$\frac{u_{s,0}}{u_0} = 0.5, \quad (4.1)$$

where $u_{s,0}$ is the initial storage capacitor voltage and u_0 the maximal voltage of the piezoelectric transducer under open-circuit conditions. According to Tab. 2.3 the targeted capacitor voltage level ranges between 2.5 V and 3.9 V. Consequently, the normalized voltage $u_{s,0}/u_0$ ranges between 0.02 and 0.08 and is much smaller than the optimal ratio. The momentary efficiency of a standard interface circuit η_{SEH} with imposed strain is determined in Sec. 6.2 and expressed as

$$\eta_{SEH} = 2 \frac{u_{s,0}}{u_0} \cdot \left(1 - 2 \frac{u_{s,0}}{u_0} \right). \quad (4.2)$$

The equation is valid for the case that the storage capacitor is much larger than the piezo-electric capacitance $C_s \gg C_p$, which renders true for energy harvesters with connected storage.

Similar to the former presented system, Lee et al. [17] studied a self-built piezoelectric fiber composite with interdigital electrodes to take advantage of the higher piezoelectric 33-effect compared to the 31-effect. The system resembled the former mentioned MFC type 1 transducer. Lee et al. measured the tire strain using an elastic strain gauge with an operational range of up to 15 % elongation. They obtained a strain range of $-0.25 \% < S < 0.35 \%$ at a load of $F = 700 \text{ kgf}$ (6864 N) on the tire inner liner. They further reported, that the tire strain is velocity independent [19]. The group attached their 60 mm x 10 mm x 0.3 mm long piezoelectric composite to an epoxy substrate which was bonded to the tire. The system was tested both on a tire test rig and on a passenger vehicle at 30 km/h with 300 kgf (2942 N) and at 60 km/h with 450 kgf (4413 N). A bridge rectifier and a two stage storage were used to save the energy temporarily. Lee et al. measured an energy per revolution before rectification and storage of 200 μJ at 30 km/h and both 380 μJ and 354 μJ at 60 km/h on the test rig and on the passenger, respectively. The effective energy at 60 km/h decreased to 34.5 $\mu\text{J}/\text{rev}$ and to 32.2 $\mu\text{J}/\text{rev}$, being equivalent to 5.8 $\mu\text{J}/\text{rev}/\text{cm}^2$ and 5.4 $\mu\text{J}/\text{rev}/\text{cm}^2$, after rectification and storage, while a capacitor was charged from 3 V to 3.25 V. Due to their inefficient interface circuit, they estimated that 90.1 % of the electrical energy were being lost. The authors explained this variation between energy measurements on a test rig and in a car tire with the small test rig curvature radius of 0.3 m compared to the flat road surface. With a relative variation of 7 %, the strain overestimation due to the test rig is not significant compared to vehicle conditions.

Kubba et al. [30] also studied a similar system and observed a slight velocity dependent energy generation during test rig experiments at a much smaller tire load of 1500 N for 30 km/h, 40 km/h and 50 km/h. In that work, a LTC-3588 circuit from Linear Technology with bridge rectifier and buck operation was used for the power management. However, the generated energy per revolution was only 3 $\mu\text{J}/\text{cm}^2$.

Because of the thin transducer structure, the presented direct strain energy harvester prototypes are very compact and light compared to the tire wave based and rim wave

based systems. Advantageously, the transducer size can be adapted easily in order to produce more energy. It simply suffices to enlarge the area of the transducer linearly with the desired amount of energy. Contrary, the stated conversion losses of 90.1 % by Lee et al.[19] are unsatisfying, but show the great potential linked to the improvement of the interface circuit.

The topic of piezoelectric interface circuits is vast and will be discussed in Chapter 6.

4.4 Overview

The aforementioned systems already represent a typical selection of TPMS harvesters with a large variety of different approaches, facing this challenging engineering problem. Most research problems of low power TPMS energy harvesters have been revealed in these examples. In addition, most promising transducer designs, incorporating widely studied techniques such as electrostatic, piezoelectric and electromagnetic conversion, have been described. Magnetostrictive transducer systems as referred to [85, 86, 108, 109] have not been studied yet as they are bulky and provide a relatively low open-circuit voltage. In addition to this selection, Tabs. 4.1 and 4.2 give an overview of the majority of the reported systems, specifically designed for TPMS harvesting. Both tables list the signal source, the type of energy harvester, the applied transducer material, the interface circuit and if and how the system was verified experimentally. The proof mass corresponding to each system is listed and was deduced, if not stated in the publication, based on the volume and material information. The beam mass and especially the mass of the housing were been incorporated. The volume V and the area A characterize the size of the system for voluminous and thin transducers, respectively.

For a compact overview, the following abbreviations are used: PE - piezoelectric, EM - electromagnetic, TE - triboelectric, FWR - full-wave rectifier, C_s - storage capacitor, SC - short-circuit, OC - open-circuit. Two devices used the relative movement between the wheel and a fixed area as signal source, abbreviated by "rel. mov."

From the given overview, the following general conclusions can be drawn. First, more tire wave based system were studied than gravitation based and strain based systems. Piezoelectricity was widely the preferred transducer mechanism, far ahead of electromagnetism. Less than a handful of electrostatic and triboelectric systems were built. The majority of these systems possessed a linear elastic force and rigid limit stops, leading to cracks and reliability issues. While centrifugal acceleration based and strain based systems usually did not exceed the mass limitation of a few grams, the gravitation based systems widely did. Most systems used the connection of a full-wave rectifier and a capacitor to store the energy, however, inefficiently. Especially, piezoelectric energy harvesters suffer from small efficiencies as low as 25 % and lower according to Eqn. 4.2, even if the diode forward voltage is negligible. As the capacitor voltage of a few volts is far below the piezoelectric voltage of a few tens of volts, the efficiency is poor and optimization is

Table 4.1: TPMS energy harvesters - state of the art overview. A comparison according to the amount of provided energy is given in Figs. 4.5a- 4.5c.

Year	Source	Vibration	Method	Restor. Force	Limit Stops	Material	Proof Mass (g)	V [mm ³] or A (mm ²)
2003	Roundy [22]	centrifugal	PE	linear	proof mass,rigid	PZT-5H	0.7	5 x 5 x 5
2007	Keck [91]	centrifugal	PE	linear	asymmetr., rigid	PZT	1.1	10 x 10 x 2
2009	Zheng [89]	gravitational	PE	linear	no	PZT 5A	21.6	20 x 6 x 46
2009	Hatipoglu [110]	tangential	EM	linear	one sided,rigid	NdFeB	4	50 x 30 x 10
2009	Manla [111–113]	gravitational	PE	nonlinear	flexible	Thunder	20.76	17.7 cm ³
2010	Bonisoli [101–103]	centrifugal	EM	nonlinear	flexible bumpers	NdFeB	-	-
2010	Elfrink [114–116]	centrifugal	PE	linear	rigid package	AlN	0.006	10 x 10 x 0.06
2011	Hu [117]	strain	TE	linear	no	ZnO	-	∅ 15mm x 5
2011	Makki [118, 119]	strain	PE	linear	no	PZT	-	∅ 2 x 0.3 mm
2011	Frey [26, 94, 95]	centrifugal	PE	linear	rigid package	PZT	-	A < 100mm ²
2012	Singh [120]	centrifugal	PE	linear	flexible beams	PZTZNN	11.45	25 x 5 x 0.85
2012	Westby [121]	centrifugal	ES	linear	rigid package	Electret	0.015	3.8 x 4.34 x 0.4
2012	Mak [122, 123]	centrifugal	PE	linear	rigid & flexible	PZT 5A	0.97	11 x 5 x 0.46
2012	Gu [124]	gravitational	PE	linear	one sided	PZT	0.4	25 x 20 x 20
2012	Wang [125]	gravitational	EM	linear	no	NdFeB	45	∅ 26 x 7
2012	Ende [104, 105]	strain	PE	-	no	MFC, PVDF	-	-
2012	Tang [126]	gravitational	PE	nonlinear	rigid housing	NdFeB	4.6	∅ 6 x 30
2013	Lee [127]	rel. mov.	EM	linear	no	NdFeB	246	102 x 25 x 13
2013	Renaud [96, 98, 99]	tangential	ES	linear	hard & soft	SiO ₂ /Si ₃ N ₄	0.15	10 x 10 x 0.65
2014	Trabaldo [128]	centrifugal	PE	linear	rigid package	PIC 255	0.009	9 x 5 x 0.16
2014	Roundy [31]	gravitational	PE	nonlinear	rigid wall	PZT	6.8	-
2014	Wu [129]	gravitational	PE	nonlinear	no	PVDF	5.8	25 x 16 x 5
2014	Kubba [30]	strain	PE	linear	no	PFC	-	132 x 10 x 0.375
2014	Lee [17, 19]	strain	PE	linear	no	PZT	-	60 x 14 x 0.8
2015	Wang [130]	gravitational	EM	nonlinear	rigid housing	NdFeB	10	44 x 12 x 12
2016	Jousimaa [131]	centrifugal	PE	linear	rigid housing	THUNDER	65	30.6 cm ³
2017	Yu-Jen [132]	gravitational	PE	nonlinear	no	PVDF	24.3	-
2018	Guo [32]	strain	TE	linear	no	FEP, Cu, PI	-	-
2018	Deng [133]	centrifugal	PE	linear	rigid housing	AlN	-	∅ 25 x 1.5
2018	Liu [134]	rel. mov.	EM	linear	no	NdFeB	350	10 x ∅ 25 x 200
2019	Esmaeeli [135]	strain	PE	linear	no	PZT-5H	-	11 x 5 x 4.3

not only recommendable but mandatory to harvest sufficient energy for TPMS.

On the one hand, the piezoelectric material can be tuned. Instead of a piezoelectric plate with the height $h = h_0$, two plates with $h = h_0/2$ can be used and, if appropriately stacked, quadruple the piezoelectric capacitance. An example for this approach is the piezoelectric transducer DuraAct Power from PI Ceramic as presented in [136]. On the other hand, buck-boost converter principles such as Synchronous Electric Charge Extraction (SECE) or Synchronous Switch Harvesting on Inductor (SSHI) increase the efficiency significantly and are introduced and evaluated in Chapter 6.

To compare the TPMS energy harvesting systems from an energy point of view, the harvested energy per revolution E_{rev} has been calculated with respect to the reported data and is illustrated for rim wave based, tire wave based and strain based systems on a semi-logarithmic scale in Figs. 4.5a, 4.5b and 4.5c, respectively. Only those publications were considered, if one of the following criteria could be applied on the reported data. They were

1. simulated with a tire signal, similar to the one described in Sec. 2.1.
2. tested on a rotating wheel (for rim based energy harvester).
3. tested on a tire test rig.
4. tested on a passenger vehicle.

The required energy was derived in Sec. 2.2 and is represented by gray dashed and dotted lines. They correspond to $E_{rev,charged} = 7.9 \mu\text{J}/\text{rev}$ and $E_{rev,add} = 4.6 \mu\text{J}$ if the initial

Table 4.2: TPMS energy harvesters - state of the art overview (contd.)

Year	Source	Circuit	Simulation	Test System
2003	Roundy [22]	FWR + C_s	tire wave signal	shaker
2007	Keck [91]	FWR + C_s	tire wave signal	vehicle
2009	Zheng [89]	FWR + C_s	frequency sweep	vehicle
2009	Hatipoglu [110]	load resistor	square wave excitation	shaker
2009	Manla [111–113]	matching resistor	rim wave signal	rotating wheel
2010	Bonisoli [101–103]	FWR + RC load	tire wave signal	shaker + magnetic offset
2010	Elfrink [114–116]	FWR + power management + C_s	square shaped shock	tire
2011	Hu [117]	OC, SC	no	bicycle tire squeezing
2011	Makki [118, 119]	FWR + C_s	-	tire test rig (flat track)
2011	Frey [26, 94, 95]	FWR (passive & active)	-	pulsed excitation
2012	Singh [120]	FWR + buck boost switch converter	tire wave signal	tire test rig
2012	Westby [121]	matching resistor	colored noised	-
2012	Mak [122, 123]	matching resistor	tire wave signal	-
2012	Gu [124]	matching resistor	rim wave signal	rotating fan
2012	Wang [125]	matching resistor	harmonic signal	rotating wheel
2012	Ende [104, 105]	FWR + C_s	no	deflated tire on flat track
2012	Tang [126]	matching resistor	harmonic signal	-
2013	Lee [127]	OC	-	bicycle test
2013	Renaud [96, 98, 99]	FWR + buck DCM converter	-	shock test, drop machine
2014	Trabaldo [128]	matching resistor	ideal TWS	-
2014	Roundy [31]	FWR + C_s	rim wave signal	rotating rim, vehicle
2014	Wu [129]	matching resistor	rim wave signal	rotating plastic arm
2014	Kubba [30]	LTC3588 + C_s	FE rotation	tire test rig
2014	Lee [17, 19]	FWR + C_s	strain wave	tire test rig, vehicle
2015	Wang [130]	rotating plate	rotating plate	-
2016	Jousimaa [131]	VD + boost charger BQ25504	pulse excitation	tire test rig
2017	Yu-Jen [132]	matching resistor	rim wave signal	rotating plate
2018	Guo [32]	FWR + C_s	no	-
2018	Deng [133]	matching resistor	half sine signal	-
2018	Liu [134]	FWR + boost + C_s	not precised	electric motor with cam
2019	Esmaeeli [135]	load resistor (not matching)	strain wave	-

voltage of a 220 μ F capacitor is $u_s = 0$ V and $u_s = 2.5$ V, respectively.

In general, rim wave based systems provide a velocity independent amount of energy per revolution, since the change in gravitational acceleration is not affected by the velocity. Identically, strain based systems provide a constant amount of energy over a wide range of velocities, because the tire deformation is not influenced by the velocity, neither. The few data points from Kubba et al. [30] can be extrapolated to be on a constant line.

Contrarily, tire wave based systems are excited by a quadratically increasing centrifugal acceleration, whereas the tire contact time (the time in which the tire is in contact with the ground) decreases linearly with the velocity, as already explained in Sec. 2.1.2. Since the tire contact time does not affect the very first deflection of the oscillating transducer, but some of the following ones, which contain less energy due to damping, the energy per revolution effectively increases more than linearly. The energy increase is visible in Fig. 4.5b only at small and medium velocities, because motion stops limit the deformation of the piezoelectric transducers at higher velocities. If the deflection is limited, the energy per revolution decreases above a specific velocity with increasing velocities due to the further linear decrease in tire contact time.

Among the rim wave based systems, the system from Roundy et al [31] fulfills widely the imposed energy conditions. However, the 6.8 g seismic mass already made the overall system too heavy, irrespective of the housing mass and the spring mass. The performance of other plotted rim wave based systems is not sufficient.

Analyzing the tire wave based systems shows that just a few systems were tested at manifold velocities but not over a wide range. Even if the system from Keck [91] is

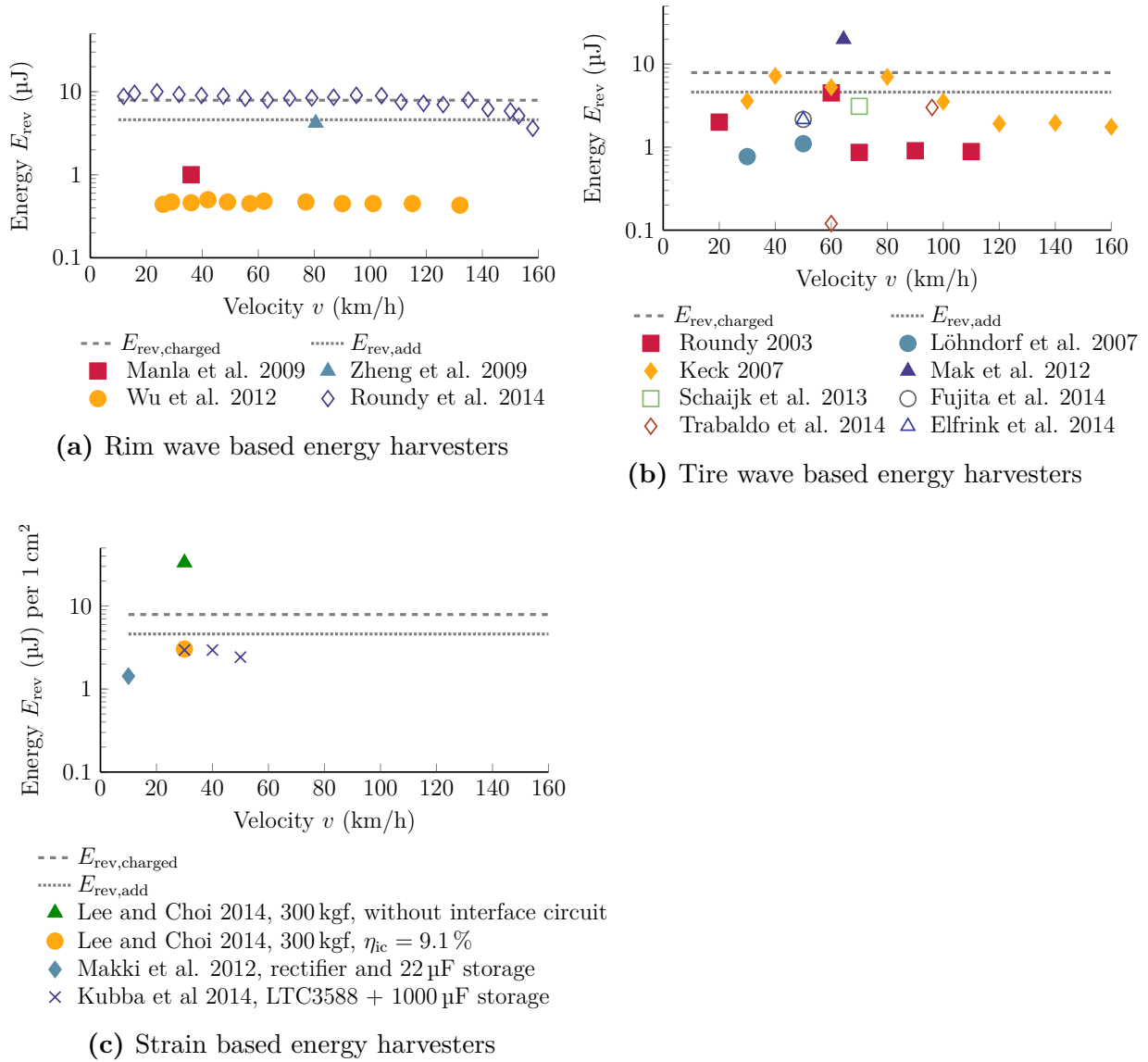


Figure 4.5: Energy per revolution of TPMS energy harvesters distinguished with respect to the energy source. The energy is velocity independent for rim wave and strain based transducers, and dependent for tire wave based systems

close to meeting the herein imposed energy requirements at 40 km/h , none of the presented systems performed sufficiently well to provide enough energy over a wide velocity range. Although the energy extraction can be tuned, using advanced interface circuits, the reliability problem at high velocities will remain.

Similarly, only one of the strain based systems generated enough energy per revolution at first sight. However, the energy has been normalized to the area of 1 cm^2 to allow a better comparison between the systems. Hence, the full size systems originally generated several times more energy. In addition, if the efficiency of the interface was reported in the corresponding papers or could be deduced from them, it has been added to the legend in Fig. 4.5c. Consequently, if a surface of a few square centimeter is covered by one of

these systems, enough energy will be generated to power TPMSs self-sufficiently.

4.5 Consequences for the Energy Harvester Design

Based on the state of the art analysis, this section summarizes the problems and reveals improvements for a successful energy harvester design inside the tire.

4.5.1 Rim Wave Based Systems

Harvesting energy at the rim while using the change in gravitational acceleration is not recommended, because the amount of energy with respect to the mass is too small. At very high velocities, the centrifugal force is dominating and presses the seismic mass against the wall. As a result, it inhibits any movement of the mass and the generation of energy.

4.5.2 Tire Wave Based Systems

Centrifugal based energy harvesters suffer from very large acceleration impulses which occur at high velocities. The general problem is, that a fragile system with a linear restoring force cannot generate enough energy at small velocities while being simultaneously robust at high velocities, because the centrifugal force increases quadratically with the velocity. The following simplified calculation underlines the problem:

Let w_{mech} be the mechanical energy density of a strained material, described as

$$w_{\text{mech}} = \frac{1}{2} Y S^2. \quad (4.3)$$

The material strain is determined by Hook's law

$$S = \frac{\sigma}{Y} = \frac{F}{Y A} \quad (4.4)$$

where σ , F , A are mechanical stress, applied force and cross section, respectively. Replacing the applied force by the centrifugal force $F_c = mv^2/R$, compressing the spring during every rotation, and inserting Eqn. 4.4 into Eqn. 4.3 leads to

$$w_{\text{mech}} = \frac{1}{2} \frac{m^2}{Y (AR)^2} v^4. \quad (4.5)$$

Equation 4.5 highlights, the mechanical energy density increases with the fourth power of the velocity. Assuming that a fixed ratio of mechanical energy is converted into electrical energy, this high nonlinear behavior makes it enormously challenging both to harvest enough energy at small velocities and to transduce energy without any damage and material fatigue at high velocities.

Supposing that a piezoelectric-ceramic with a high electromechanical coupling is used to convert the energy, e.g. PZT-5A with $Y = 60$ GPa and $S_{\max} = 0.1\%$ as given in Tabs. 3.1, 3.2, the maximal energy density is $w_{\max} = 30$ mJ/cm³. For the case that the energy harvester has to withstand velocities of 200 km/h at which the strain does not exceed S_{\max} , the quotient $m^2/(YA^2R^2)$ is determined. Consequently, the energy density decreases with the fourth power of the velocity and is stated in Tab. 4.3. To calculate the energy from the mechanical energy density, a surface of 1 cm² and a height of 200 μ m of the piezoelectric material were supposed. In addition, the squared piezoelectric 31-coupling coefficient of a perfectly, uniformly strained beam is approximated by 10%, but it is practically even smaller. Under perfect load matching conditions, only 50% of the source energy can be converted. The resulting electrical energy is listed in Tab. 4.3. Hereinafter, according to Sec. 2.1.2 it is supposed, that two step functions, one while entering and one while leaving the area of ground contact, are responsible to store mechanical energy in the piezoelectric system. Even if the harvester generates energy outside the area of ground contact, the thereby generated energy is negligible at small velocity.

Table 4.3: Energy density as a function of velocity for a PZT-5A piezoelectric energy harvester

Velocity v	Mechanical energy	Electrical energy
	density w_{mech}	$V = 1 \text{ cm}^2 \times 200 \text{ } \mu\text{m}, \eta = 5\%$
20 km/h	3 $\mu\text{J}/\text{cm}^3$	0.03 μJ
30 km/h	15 $\mu\text{J}/\text{cm}^3$	0.15 μJ
50 km/h	120 $\mu\text{J}/\text{cm}^3$	1.20 μJ
100 km/h	1,900 $\mu\text{J}/\text{cm}^3$	19.00 μJ
200 km/h	30,000 $\mu\text{J}/\text{cm}^3$	300.00 μJ

One reason, why some of the published systems generated electrical energy of in the order of microjoule both at low and high speeds are limit stops. They cause nonlinearities, restricting both the movement and the strain at high velocities. If the limit stops are only rigid packages, housings or rigid bumpers, chipping damages are produced. They lead to malfunctioning and to system destruction when continuously repeated. A better and promising approach is to use elastic and soft bumpers [98]. As proposed in [91], asymmetric motion stops take the lower tensile strength of piezoelectric ceramics into account compared to the compressive strength. In addition, triangular or trapezoidal shaped harvesters can be considered for a more uniform stress distribution. However, to provide the same compliance as a rectangular shaped beam, the length has to be increased, leading to a larger, less compact system.

For electromagnetic harvesters, the elastic energy stored also depends on the fourth power of the velocity. However, the transducer design allows to easily implement contactless nonlinear magnetomechanical springs, which is a big advantage compared to piezoelectric harvesters. Elastic bumpers, as presented in [103], add further nonlinearities,

useful at high velocities, and improve the reliability. The system of [103] has several advantages: First, the system is robust as a compact magnet moves and bumps against the elastic stoppers within a coil, where no brittle beams are overstrained. Secondly, the system is compact as the magnet partly represents at the same time the system components seismic mass, spring and electromechanical transducer element. Thirdly, no clamping is needed in contrast to piezoelectric systems in which a beam is commonly clamped at one side, a piezoelectric layer is attached to a substrate and at the beam's end a mass is fixed. The clamping of the piezoelectric material as well as the mass fixation can lead to problems at high velocities. The big disadvantage of an electromagnetic system is the relatively low generated voltage. The AC-DC rectification with a full-wave rectifier causes significant losses due to the diode forward voltage drop and requires an efficient step-up converter. Efficient AC-DC converters for electromagnetic energy harvesters are discussed in Chapter 8.

4.5.3 Strain Based Systems

Strain based energy harvesters are mainly velocity independent, because the tire strain amplitude at the contact patch is velocity independent and only depends on the tire load. The slight dependency on the tire load is not an issue, as a higher tire load at a constant pressure provokes a longer contact patch and a higher strain, resulting in more electrical energy. The theoretical amount of provided energy per 1 cm^2 is relatively high and can be increased easily, while the weight of a few grams will not be exceeded. However, the studied interface circuits suffer from poor conversion efficiencies. Appropriate interface circuits are one solution on the path to a self-sufficient TPMS breakthrough.

A main mechanical problem can consist in driving over a curb which leads to higher local deformations in the tire. This potential issue has not been investigated in the context of TPMS energy harvesting. Another disadvantage concerns the high effort to attach the piezoelectric material properly. A good electromechanical energy conversion necessitates a well established adhesive connection. When it comes to tire replacement, the TPMS can be reused, but not the piezoelectric material. From an environmental point of view, the pros and cons have to be balanced.

4.6 Summary

Relevant state-of-the-art publications have been presented and analyzed in terms of system design, generated energy at different velocities, robustness, interface circuit and system verification. Problems and opportunities are:

Problems

Common and most significant problems with TPMS energy transducers are related to robustness and energy generation:

- Robustness issues with linear centrifugal based piezoelectric transducers
- Cracks in brittle piezo-ceramics due to rigid motion stops
- Very low efficient interface circuits were widely used
- Prototype performances worse than a battery in terms of available energy
- Tire wave based linear piezoelectric transducers harvest enough energy at low velocities and are fragile at high velocities or vice versa, they harvest very low energy at low velocities and are rigid at high velocities



An intense verification under road-like conditions, not only at one but at different velocities, are missing in the majority of the studies.

Opportunities

General system improvements rely on:

- Elastic motion stops increasing system robustness
- Contactless magnetic springs decreasing rigid body impact
- Nonlinear springs encountering nonlinearly increasing centrifugal forces
- Advanced interface circuits increasing significantly the efficiency
- Employing strain based systems experiencing constant strain amplitudes



The following work is focusing on **tire wave based** and **strain based** transducers, as the ratio of the system mass to the generated energy is much more elevated than for rim wave based energy transducers.

5 Piezoelectric Energy Harvesting

The previous chapter presented a wide range of TPMS energy harvesters, and most of them based on piezoelectricity. Although piezoelectric centrifugal based systems were widely studied in the literature, they suffered from brittleness and have to be made more robust. Compared to them, only a handful of strain based harvesters were developed and successfully tested. Their stated energy per revolution normalized to 1 cm^2 was too small to replace a battery due to low efficient interface circuits. In this chapter, piezoelectric tire wave based and strain based systems are studied with the objective to generate the required energy $E_{\text{rev,charged}} = 7.9 \mu\text{J}$ during one revolution. Both an analytical description and an electromechanical network description are used to characterize the system behavior and the maximal electrical energy output. While FEM is used to estimate appropriate dimensions of the centrifugal wave based system, experimental measurements of commercially available thin piezoelectric transducers help to analyze the material and to point out differences between the transducers.

5.1 Piezoelectric System Description

A Piezoelectric energy harvester (PEH) is described by the coupled differential equations

$$m\dot{v} + cv + \frac{1}{n_{\text{sc}}} \int v dt + \alpha u = ma_{\text{ex}} \quad (5.1)$$

$$i = \alpha v - C_p \dot{u}, \quad (5.2)$$

where m , c , n_{sc} , $v = \dot{z}$, α , C_p , i , u , a_{ex} are the lumped elements mass, damping coefficient, short-circuit compliance, velocity, piezoelectric transducer coefficient, piezoelectric capacitance, current, voltage and acceleration of the excitation, respectively.

Usual piezoelectric transducers consist of a tip mass and either a unimorph or a multimorph beam. Both mechanical components can be assigned to the lumped elements of Eqns. 5.1, 5.2 as listed in Tab. 5.1 which highlights that it is difficult to modify the lumped parameters independently.

Except for the damping coefficient, all lumped parameters can be accurately predicted

Table 5.1: Piezoelectric component assignment

Parameter	Assigned component
m	tip mass, beam
c	beam, atmosphere
n_{sc}	beam, support
α	beam
C_p	beam (piezo layer)

either analytically or numerically based on geometry and material data and without experimental measurements. Numerical calculation, e.g. by means of FEM, is advantageous for complex or inhomogeneous beam structures. The damping coefficient can be estimated by comparison with similar studies if available. More precise is the experimental determination by analyzing the transient behavior of a deflected beam, as explained in [87]. The system of coupled differential equations from Eqns. 5.1, 5.2 can be represented by an electromechanical network as depicted in Fig. 5.1 [74, 137].

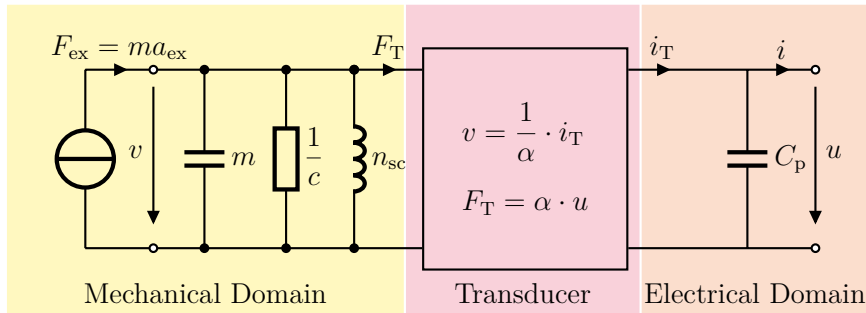


Figure 5.1: Electromechanical network model of a linear piezoelectric energy harvester

The electromechanical network model visualizes the dynamic components, the way in which mechanical and electrical domain are coupled and how the quantities force, velocity, voltage and current impact each other. Both electromechanical network and the coupled equations are used in the following to describe various piezoelectric transducers.

5.2 Tire Wave Based Piezoelectric Energy Harvester

This section deals with the design of piezoelectric inertia transducers to harvest energy from the tire wave, as introduced in Sec. 2.1.2. A system placed in the tire, as shown in Fig. 5.2, experiences the centrifugal acceleration and is pressed against the tire. In the area of ground contact, the centrifugal acceleration vanishes. The excitation signal can be interpreted as a step function, which occurs both when entering and leaving the area of ground contact.

5.2.1 Preliminary Energy Considerations

To find suitable parameters such as mass and optimal beam configurations of the piezoelectric transducer that fulfill the energy requirements, the generable energy per revolution will be coarsely approximated. It is assumed, that mainly the step function of the centrifugal force, while entering and leaving the contact patch, is responsible for the production of electrical energy. Supposing that the mechanical domain only effects the electrical domain and that the impact of the electrical domain on the mechanical domain is negligible

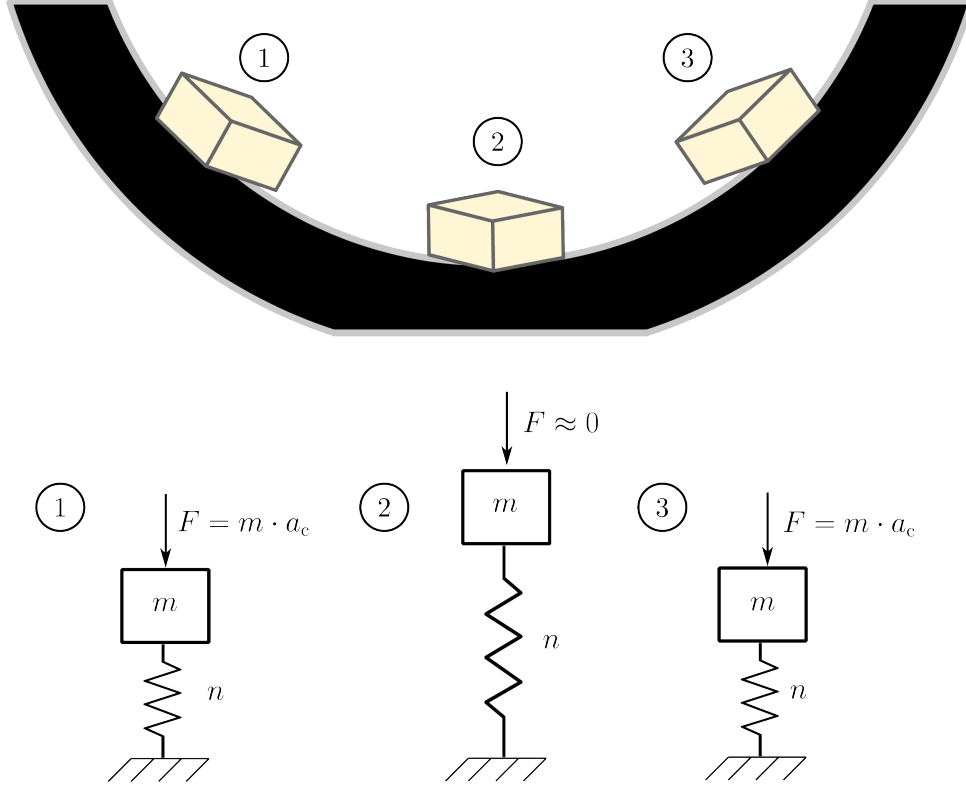


Figure 5.2: Mass-spring system inside the tire

for the strike of the step function, the electrical energy of one strike is

$$E_{1,\text{strike}} = \frac{1}{2} C_p u^2. \quad (5.3)$$

As mentioned, the step function appears twice and the harvestable energy is doubled

$$E_{2,\text{strikes}} = 2 \cdot E_{1,\text{strike}} = C_p u^2. \quad (5.4)$$

The piezoelectric voltage is determined under open-circuit conditions ($i = 0$) and is according to Eqn. 5.2

$$0 = \alpha \cdot \dot{z} - C_p \cdot \dot{u}. \quad (5.5)$$

The time integral in the interval $[t_0, t]$ leads to

$$C_p \int_{t_0}^t \dot{u}(t) dt = \alpha \int_{t_0}^t \dot{z}(t) dt, \quad (5.6)$$

$$u(t) - u(t_0) = \frac{\alpha}{C_p} [z(t) - z(t_0)]. \quad (5.7)$$

The continuous discharge of the piezoelectric transducer once it has been prestrained leads to the initial voltage $u(t_0) = 0$. The initial deflection $z(t_0)$ is limited by both force and

compliance n_{oc} under electrical open-circuit conditions and results in

$$z(t_0) = \hat{F}_{ex} \cdot n_{oc}, \quad (5.8)$$

where \hat{F}_{ex} is the maximal force. The compliance n_{oc} is composed of the short-circuit compliance n_{sc} and the capacitance C_p acting as parallel connected compliance C_p/α^2 as

$$n_{oc} = \frac{n_{sc} \cdot \frac{C_p}{\alpha^2}}{n_{sc} + \frac{C_p}{\alpha^2}} = \frac{n_{sc} \cdot C_p}{\alpha^2 n_{sc} + C_p}. \quad (5.9)$$

The case $n_{sc} \ll C_p/\alpha^2$ leads to the approximation $n_{oc} \approx n_{sc}$, which will be the case for the considered transducers. In the following the compliance n is used instead

$$n = n_{oc} \approx n_{sc}. \quad (5.10)$$

The maximal force is determined by the centrifugal force and approximated by

$$\hat{F}_{ex} = 1.3 m \frac{v^2}{R}, \quad (5.11)$$

where the prefactor 1.3 incorporates the smoothed tire deformation and reduction of the tire radius before entering and after leaving the contact patch, as visualized in Fig. 2.3.

Actually, the system would be deflected from $-\hat{F}_{ex} \cdot n < z < \hat{F}_{ex} \cdot n$ if damping was negligible. However, piezo-ceramics withstand much higher compressive than tensile load which is important to consider for a robust design. Accordingly, to allow only compressive loads on the piezo-ceramic, a unimorph instead of a bimorph is considered as suitable beam and necessitates a motion stop to restrict the deflection z in the interval $0 \leq z \leq \hat{F}_{ex} \cdot n$. Then, with Eqns. 5.7 and 5.8 the maximal voltage \hat{u} is

$$\hat{u} = \frac{\alpha \hat{F}_{ex} n}{C_p}. \quad (5.12)$$

Figure 5.3 depicts two arrangements of the piezoelectric material on the support material. In Fig. 5.3a the piezoelectric material experiences only a static compressive strain, which is why this is considered more suitable than the setup of Fig. 5.3b where a tensile strain occurs in the piezo-ceramic.

To estimate the energy per revolution, Eqn. 5.12 is inserted in Eqn. 5.4 and results in

$$E_{2,\text{strikes}} = \frac{(\alpha n)^2}{C_p} \hat{F}_{ex}^2. \quad (5.13)$$

The coefficients, related to the design of the material, are summarized by the parameter

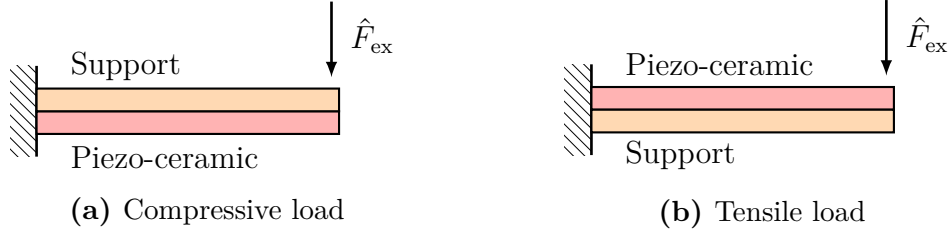


Figure 5.3: Static deflection of a piezoelectric unimorph beam as static compliance, where the piezo-ceramic experiences in (a) a compressive strain and in (b) a tensile strain due to the deflection, caused by the static force \hat{F}_{ex}

c_M with

$$c_M = \frac{(\alpha n)^2}{C_p} \quad (5.14)$$

which leads to

$$E_{2,\text{strikes}} = c_M \hat{F}_{\text{ex}}^2. \quad (5.15)$$

There are two independent ways to modify the amount of energy. First, the force $F_{\text{ex}} = m \cdot a_{\text{ex}}$ can be changed by the tip mass m . Second, the parameter c_M can be modified by the parameters α , C_p and n . These parameters are modified by the beam length, cross-section and selected material. However, referring to Tab. 5.1, changing the transducer geometry does not only change one parameter, e.g. the capacitance but also the compliance and the piezoelectric coefficient.

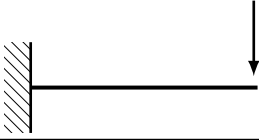
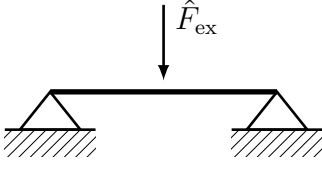
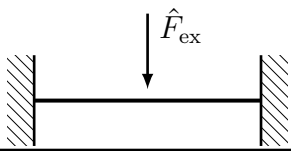
Generally, the compliance n_{sc} of a beam is given by the boundary conditions. Common setups of a homogeneous beam with rectangular cross-section are illustrated and characterized in Tab. 5.2 [138]. In all cases, the compliance is a function of beam length l , Young's modulus Y and second moment of inertia I , with $I = w \cdot h^3/12$ for a rectangular cross section, where w and h are the beam width and height, respectively. As it can be deduced from the Tab. 5.2, the one-sided clamped beam with applied force at the tip has the highest compliance for a constant beam geometry. Compared to one-sided clamped rectangular beams, both trapezoidal and triangular beams allow a more homogeneous stress distribution [139], but need a larger beam width at the clamping to have the same compliance. Similarly, circular diaphragms as described in [140] are compact but much stiffer than rectangular shaped beams.

In the following, the objective is to choose the system parameters of a compact system, which provide at least an energy of $7.9 \mu\text{J}/\text{rev}$.

5.2.2 Piezoelectric Energy Harvester System Design

Based on the results of the previous subsection, the parameters of the energy harvester are studied, subsequently. The energy harvester system to be developed bases on a unimorph

Table 5.2: Selected boundary conditions of a beam and corresponding compliances for a beam with a rectangular cross section

Beam type	Schematic	Compliance n_{sc}
One-sided clamped beam with force at the beam tip		$\frac{l^3}{3YI}$
Two-side supported beam with force at the beam center		$\frac{l^3}{48YI}$
Two-sided clamped beam with force at the beam center		$\frac{l^3}{192YI}$

beam structure with proof mass and elastic motions stops to prevent tensile overload. The soft piezoelectric material M1100 with a height of 260 μm provided by the company JohnsonMatthey was used for the following investigations and cut with a wafer dicing saw in rectangular samples. The properties of M1100 are listed in Tab. 3.1.

The piezo-ceramic needs to be attached on a substrate with a high tensile strength and with a Young's modulus which has the same order of magnitude and which is commercially available in thickness of a few hundred micrometer. Furthermore, it is advantageous if a solder connection can be easily established on the substrate.¹ Among various metals, the brass alloy CuZn37 - CW508L (MS63) R350 (F37) semi-hard EN 1652 fulfilled these demands. Especially, a wire connection via soldering is very easy to establish on brass, compared to aluminum or titanium sheets. The mechanical properties of the brass alloy are listed in Tab. 5.3.

Table 5.3: Material properties of brass as substrate layer [141]

Young's modulus	E_{11}	110	GPa
Poisson's rate	n_{xy}	0.34	
Relative permittivity	ε_r	2	
Tensile strength	σ_T	300 – 370	MPa
0.2 % Yield strength	$\sigma_{0.2}$	<180	MPa
Height	h	300	μm

The geometry, especially the unimorph length is imposed by rubber containers, provided by Continental, which embed the TPMS for passenger cars and trucks on the tire inner

¹In retrospective, a solder connection of the substrate metal is not mandatory. As the unimorph is clamped at one side, a thin wire being also clamped can establish an electrical connection, too.

liner. The container for passenger cars is circular cylindrical with a diameter of 22 mm, whereas the container for truck TPMS is an elliptical shaped cylinder with the main axis and minor axis of 37 mm x 28 mm and a height of 19 mm. The effective cuboid dimensions inside this cylinder are 32 mm x 14 mm x 19 mm ($l \times w \times h$).

A static finite element analysis was performed in ANSYS Workbench to determine appropriate beam dimensions. In general, the case where the substrate and piezoelectric layer were of different lengths and deflected by a constant force was investigated. If the piezoelectric layer is shorter than the substrate layer, the beam is more compliant which results in a larger beam deflection. Thus, more bending stress is applied to the piezoelectric substrate, resulting in a higher piezoelectric voltage. Since the stress is the highest at the clamping and decreases linearly with increasing distance from the clamping, the piezoelectric material near the tip, where the stress is zero, does not contribute significantly to the piezoelectric voltage. If the piezoelectric substrate is too short, less material is stressed, a lower voltage is generated and less electrical energy can be provided.

Consequently, there is an optimal length ratio between substrate and piezoelectric layer that results in the highest amount of energy being stored in the material while it is deflected with the static force \hat{F}_{ex} , as shown in Fig. 5.4. The indices p and s correspond to the piezoelectric and substrate layer, respectively. In the FEM, according to Fig. 5.4, the top surface of the piezoelectric layer (blue line) is defined as the electrical reference potential $u = 0$ (electrical ground), while the nodes of the bottom surface (green line) are electrically coupled in the FEM to account for the electrical coating of the piezo-ceramic.

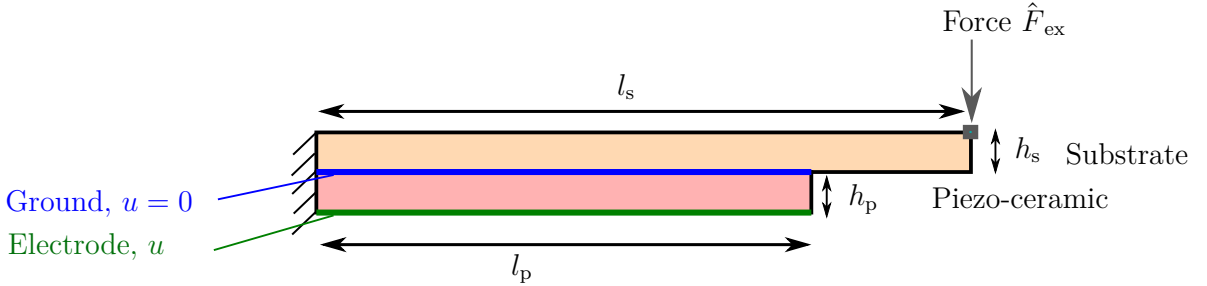


Figure 5.4: Electrical and mechanical boundary conditions of the piezoelectric one-sided clamped beam with different substrate and piezo-ceramic length

For a given force \hat{F}_{ex} , substrate length l_s , substrate height $h_s = 300 \mu\text{m}$ and piezo-layer height $h_p = 260 \mu\text{m}$, the coefficient c_M is used as a figure of merit (FOM) to study the optimal length ratio between substrate length l_s and piezo-ceramic length l_p . The static force \hat{F}_{ex} results in a beam deflection, that creates stress in the material such that charges are accumulated, measurable as an open-circuit voltage u . The coefficient c_M is calculated according to Eqn. 5.14, normalized to its maximum and illustrated in Fig. 5.5. The parameters n_{sc} , C_p and α were calculated in ANSYS Workbench for the static case according to Eqn. 5.8 and Eqn. 5.12, respectively.

Analyzing the function in Fig. 5.5 reveals an increasing FOM c_M with increasing length

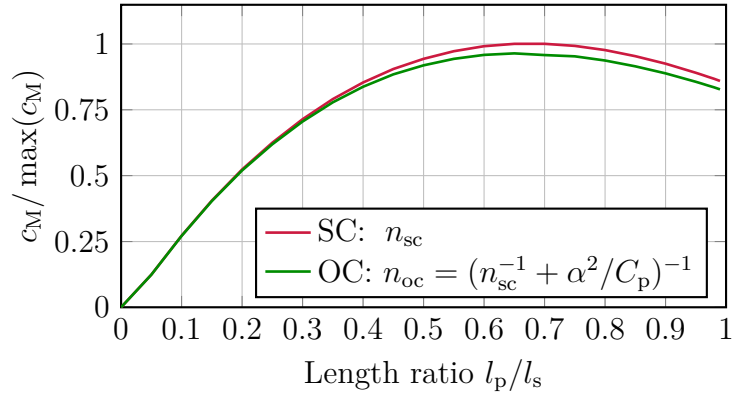


Figure 5.5: Coefficient c_M as a function of beam length ratio l_p/l_s . The optimal length ratio results mainly from the trade-off between compliance n , deflection $z = \hat{F}_{ex}/n$ and piezoelectric capacitance $C_p = \epsilon l_p \cdot w/h_p$

ratio until $l_p/l_s \approx 0.7$ and $l_p/l_s \approx 0.65$, where the maximum is reached for the short-circuit and open-circuit case, respectively. Similar results can be deduced from [142] where a piezoelectric unimorph beam with different length ratios was studied analytically. From the analytical results an optimal length ratio of 0.67 mm can be deduced which is in very good accordance with the numerical results. To account for the size of the TPMS truck reservoir, the length of the piezoelectric layer and of the substrate layer were chosen to be $l_p = 13$ mm and $l_s = 18$ mm, respectively, and led to a length ratio of 0.7.

Both, tip mass m and vehicle velocity v determine the maximal centrifugal force with respect to Eqn. 5.11. In addition, the beam width w impacts the compliance, the beam deflection and the electrical energy to be supplied. Based on Eqn. 5.13, various parameter combinations m, v, w were studied which provide the minimal energy $E_{2,strikes} = 7.9 \mu\text{J}$. They are shown in Fig. 5.6.

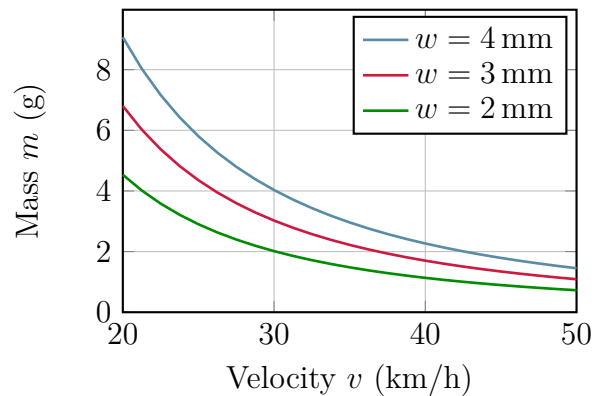


Figure 5.6: Relation between mass m and velocity v and beam width w to generate at least $E_{2,strikes} = 7.9 \mu\text{J}$

For a given velocity, a narrow beam is more compliant and requires a smaller tip mass compared to a wide beam. However, at higher velocities, the beam would be stronger deflected, such that the beam is more strained and strain limits are reached earlier, com-

pared to systems with a wide beam width. A wide beam width can generate more energy, because higher forces can be applied, leading to higher deflections and higher strains.

To reach more energy than the minimum of $7.9 \mu\text{J}$ at low velocities, high forces are required which correspond to high tip masses. For example already the static beam deflection at 1 N corresponds to the mass, velocity pairs $(1 \text{ g}, 55 \text{ km/h})$, $(2 \text{ g}, 40 \text{ km/h})$, $(3 \text{ g}, 30 \text{ km/h})$, $(5 \text{ g}, 25 \text{ km/h})$. To reduce reliability issues and unbalanced wheels, only masses of 2 g and 3 g are selected to be combined with unimorph beams of 3 mm and 4 mm width.

A general schematic of the prototype is illustrated in Fig. 5.7 and consists of a one-side clamped brass-piezo-ceramic unimorph with a length ratio of 0.7 mm and an attached tip mass. The corresponding geometry parameters are listed in Tab. 5.4. Bumpers are placed, glued to the housing and are used to avoid long-term depolarization due to large compressive overstrain, and destruction due to tensile overload. To incorporate the promising results from Renaud et al. [98], elastic motion stops² were installed, ensuring a free deflection in the range of $0 \text{ mm} < z < -1 \text{ mm}$. A feedthrough enables an electrical connection through the housing.

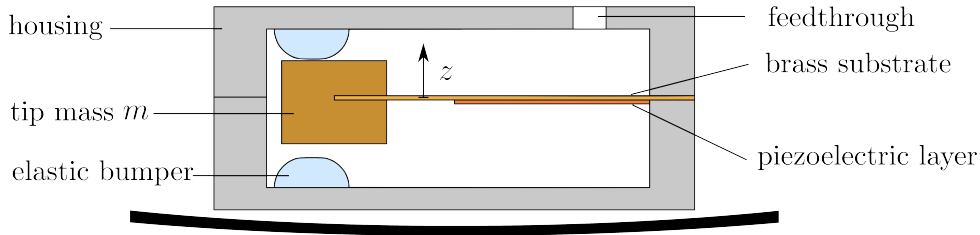


Figure 5.7: Schematic of the tire wave based piezoelectric energy harvester prototype

Table 5.4: Geometry parameters of the inertia piezoelectric systems

Parameter	Value	Unit
Substrate length	l_s	19 mm
Piezo-ceramic length	l_p	13 mm
Substrate height	h_s	300 μm
Piezo-ceramic height	h_p	260 μm
Unimorph width	w	[3, 4] mm
Mass	m	[2, 3] g

The extractable energy, based on the two-strikes assumption, is depicted in Fig. 5.8 for a 3 mm and 4 mm wide beam. The deflection of -1 mm already corresponds to a compressive strain of 3000 ppm and 2200 ppm for the 3 mm and 4 mm wide samples, respectively, but referring to Tab. 3.1 this strain is much smaller than the limit resulting from the compressive strength and the compliance. When the deflection exceeds 1 mm , the elastic bumper restricts further deflections, with the consequence of a limited

²Elastic bumpers from 3M Electronics were used with diameter $d = 5 \text{ mm}$ and a height $h = 2 \text{ mm}$.

energy generation. Different beam eigenmodes than the first beam eigenmode were not considered, because the elastic bumper restricts the deflection of the beam tip where the seismic mass is located and where most of the centrifugal force is applied compared to a thin light-weight beam. The piezoelectric open-circuit voltage, related to the deflection $z = 1$ mm is $\hat{u} = 80$ V in the static case.

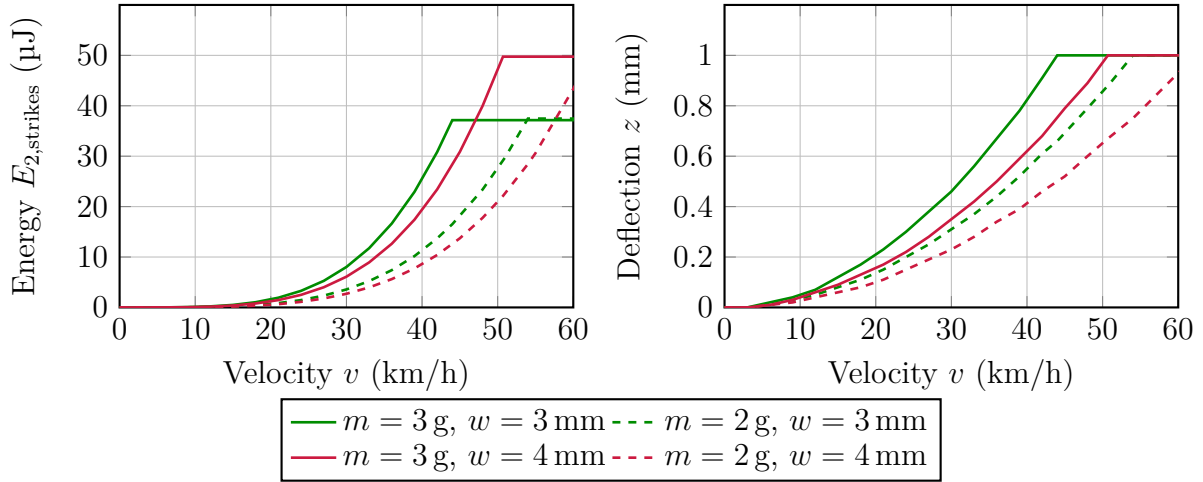


Figure 5.8: Harvestable energy $E_{2,strikes}$ and deflection z for two beam widths w for two tip masses m . Due to the deflection limits at $z = 1$ mm, the energy $E_{2,strikes}$ is restricted.

Eight samples, two of each combination of tip mass (2 g, 3 g) and width (3 mm, 4 mm) were manufactured and are depicted in Fig. 5.9. Their effective length is 18 mm. Extensions of 2 mm and 4 mm are used for the clamping and mass attachment, respectively, resulting in a total beam length of 24 mm. The system parameters calculated from the FEM simulation for $l_p = 13$ mm and $l_s = 18$ mm are listed in Tab. 5.5. A piezoelectric inertia energy harvester embedded in a metal housing is shown in Fig. 5.10. Experimental results will be presented in Sec. 9.2.

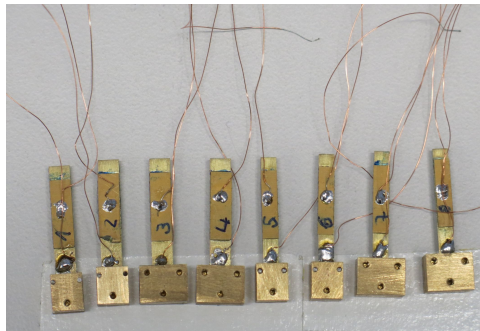
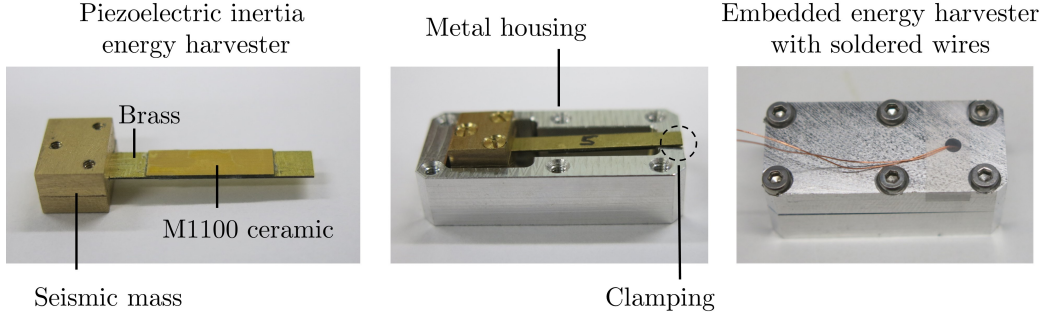


Figure 5.9: Piezoelectric inertia energy harvester samples

Table 5.5: Calculated system parameters of inertia based piezoelectric system deduced from ANSYS FEM simulations

w (mm)	α ($\mu\text{C}/\text{m}$)	n_{sc} (mm/N)	C_p (nF)
3	474	0.53	6
4	632	0.40	8


Figure 5.10: Piezoelectric inertia energy harvester and metal housing

5.3 Strain Based Piezoelectric Energy Harvester

Producing electrical energy when the tire rotates but regardless of fast it rotates is the main property assigned to direct strain based piezoelectric transducers [19], because the tire strain amplitude remains unaffected by the vehicle velocity. The system description is similar to the one presented in Fig. 5.1, whereas the input source is different. While in the previous case the centrifugal acceleration acts on the movable mass and constitutes a mechanical force source for an inertia based system, both the tire dynamics and the tire strain remain almost unaffected by a thin transducer. The rotating tire can be considered as a strain source and imposes the displacement $\xi(t)$ as a function of time. The displacement, defined as

$$\xi = \int_0^l S(x)dx, \quad (5.16)$$

can be expressed as the product of material length l and average strain \bar{S}

$$\xi = l \cdot \bar{S}. \quad (5.17)$$

Since the velocity is the derivative of the displacement with respect to time, it can be expressed as follows

$$v(t) = l \cdot \frac{d\bar{S}(t)}{dt}. \quad (5.18)$$

Supposing, that a thin piezoelectric patch influences neither the tire rolling behavior nor the tire strain noticeably, the mechanical network components mass m , damping c and

short-circuit compliance n_{sc} can be neglected for the dynamic behavior. The general network model of a strain based piezoelectric transducer is presented in Fig. 5.11. When the velocity source is transformed to the electrical domain with the relation

$$i_T = \alpha v = \alpha \cdot l \cdot \frac{d\bar{S}(t)}{dt}, \quad (5.19)$$

the network can be further simplified to the network as depicted in Fig. 5.12.

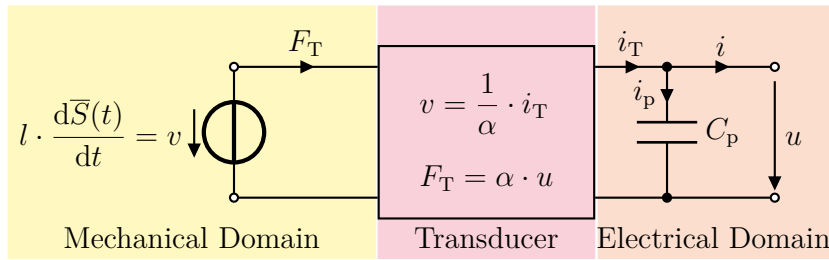


Figure 5.11: Network model of a piezoelectric strain energy harvester

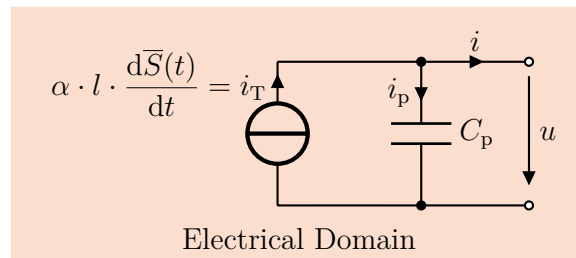


Figure 5.12: Network model of a piezoelectric strain energy harvester after transformation

Thin piezoelectric transducers hardly affect the tire strain. However, the transducer composition and the elastic modulus determine how much strain the transducer experiences. The numerical quantification of the experienced strain inside the tire is challenging. To predict how strong a piezoelectric sample will be deformed in a tire and how much electrical energy can be generated, Continental carried out a FEM simulation of a 10 mm x 10 mm x 0.5 mm specimen with an average Young's modulus of 18.3 GPa attached to the inner liner of a 205 x 55 R 16 tire both in circumferential and in tangential direction. The boundary conditions were $p = 2.1$ bar and $F = 6033$ N, where F is the force, pressing the tire against the ground. While the tire strain reached 30.000 ppm (3%) in the area of ground contact, the specimen experienced a strain of approximately 10 ppm. According to the simulation, such a device would not generate more than a few tens of nanojoule per revolution. However, practical tests stated in the literature, demonstrated different behaviors.

Lee et al. [17] measured tire strains in the range of a few thousands of parts per million with a Y11-FA strain gauge. How much a significantly stiffer material, attached to the tire inner liner, will be strained is difficult to predict, since it is assumed, that the average

tire strain is uniformly applied on the piezoelectric transducer. While the assumption is valid for thin materials, the thicker the material and the higher the Young's modulus is, the stiffer the material and the less valid this assumption is. In the same work, Lee et al. developed a thin energy transducer. They determined the strain, applying the bending beam theory and stated that the strain experienced by their energy harvester is reduced to 25% of the tire strain, leading to a maximal tensile strain of 800 ppm and a compressive strain of 500 ppm. On the one hand, only a part of the deformation energy can be effectively used. On the other hand, if the tensile strain was much larger, it would result in long-term depolarization of the piezoelectric patch [49]. That is why the strain reduction is advantageous and not a problem.

In the following, selected commercially available materials will be studied for strain based energy harvesting. The samples were characterized in preliminary experiments. The electromechanical network model can be fed with the results and is used to estimate the amount of electrical energy per tire revolution.

5.3.1 Material Selection

Piezoelectric materials suffer generally from brittleness. To overcome the limitation imposed by the brittleness, a couple of innovative thin transducers were developed in the past, are shortly presented and their specialties are highlighted. The National Aeronautics and Space Administration (NASA) invented a flexible and durable piezoelectric fiber composite, called Macro Fiber Composite (MFC), which was awarded in 2000 as one of the 100 most significant technical products of that year [42]. The spin-off companies Smart Materials Corporation, located in Sarasota (Florida, USA) and Smart Materials GmbH, located in Dresden (Saxony, Germany) licenced this technology.

An MFC consists of piezoelectric rectangular rods, embedded in an epoxy matrix and sandwiched by adhesive layers of interdigitated electrodes and polyimide on the top and bottom side [143]. The structure allows high bending compared to usual piezoelectric materials, as demonstrated by the manufacturer in Fig. 5.13.

Two main types of MFCs are available. The P2 type is a typical thin transducer that builds on the less efficient 31-piezoelectric effect. While the positive and negative electrodes of the P2 type are established on the top and bottom side, respectively, the interdigitated electrodes of the P1 type change their polarities from positive to negative to positive and so forth on each side and enable an electrical field in rod direction. Because the electric field and mechanical field direction are in parallel, the more efficient 33-effect is exploited. However, the electric field distribution between the interdigitated



Figure 5.13: Flexibility test of an MFC by the manufacturer [42]

electrodes is strongly inhomogeneous. To maintain a high conversion efficiency, the ratio between electrode distance and material depth is imposed and leads to a small capacitance per area [144].

The capacitance ratio between a P2 to P1 type material with the same area is about 26 which results in an at least 5 times larger open-circuit voltage of the P1 type compared to the P2 type when being excited. High voltages of several hundred volts necessitate careful electronic circuit design with components of bigger size, which might be detrimental for a compact system. For later material characterization, the samples M2807-P1 and M2807-P2 were chosen with an active area of 28 mm x 7 mm and a thickness of 300 μm , whereas the piezoelectric material is 180 μm thin.

The company PI Ceramic GmbH manufactures comparable commercially available piezoelectric composites. It also offers two different thin transducers, building on both piezoelectric effects. The systems P878.SP1 and the P878.A1 were selected and cover an active area of 15 mm x 5 mm and 10 mm x 10 mm, and exhibit the 31-effect and the 33-effect, respectively [145]. Both materials have a soft piezoelectric ceramic core, embedded in an epoxy matrix. While the P876.SP1 transducer has electrodes on the top and bottom, the P878.A1 is similar in structure to a stack actuator with 0.2 mm thin ceramic slices separated by electrodes.

The stacked structure enables a homogeneous electric field between the electrodes, contrary to the inhomogeneous field of the MFC-P1 transducer [146]. The creation of a homogeneous electric field as illustrated in Fig. 5.14 leads to higher conversion efficiency while being deformed compared to inhomogeneous 33-transducers. The capacitance and the output voltage can be theoretically adjusted by the length of the ceramic slices, but requires a change in the production line of PI Ceramic. Relevant material and geometry data are listed in Tab. 5.6 and Tab. 5.7, respectively.

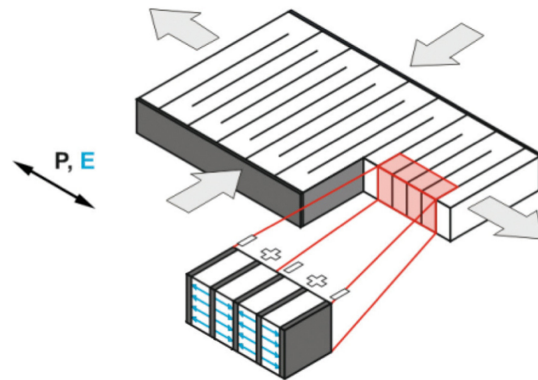


Figure 5.14: Structure of the thin stacked transducer P878.A1 [136]

5.3.2 Experimental Characterization on an Electrodynamical Shaker

The electrical response of the different transducers is characterized subsequently: One sample of each product was attached to a 130 mm x 20 mm x 2 mm long one-side clamped-free-end aluminum beam as depicted in Fig. 5.15. At a distance of 10 mm from the beam clamping, the much thinner samples were glued with cyanoacrylate. The beams were mounted on an electro-dynamical shaker that excited the specimens harmonically in

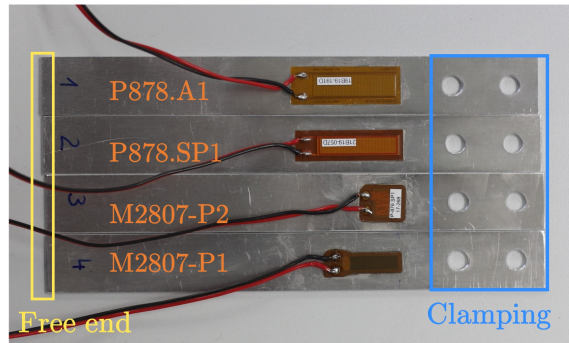
Table 5.6: Properties of commercially piezoelectric thin transducers

Parameter	Symbol	Unit	M2807-P1	M2807-P2	P876.SP1	P878.A1
Piezoelectric const.	d	pC/N	400 to 460	-170 to -210	-	-
Rel. permittivity	ε_{11}^T	1	1600	1600	1750	1750
Capacitance	C_p	nF	0.59	15.3	8	100
Young's modulus	Y	GPa	30	30	40 [147]	40 [147]
Maximal strain	S_{\max}	ppm	4500	4500	1300	-
Curie temperature	T_{curie}	°C	370	370	350	350

Table 5.7: Geometry data of piezoelectric thin transducers

Material			M2807-P1	M2807-P2	P876.SP1	P878.A1
Piezomaterial			PZT 5A1	PZT 5A1	PIC 255	PIC 252
Composite	length	l (mm)	28	28	10	15
	width	w (mm)	7	7	10	5.4
	thickness	t (mm)	0.18	0.18	0.2	0.3
Total geometry	length	l (mm)	37	38	16	27
	width	w (mm)	10	13	13	9.4
	thickness	t (mm)	0.3	0.3	0.5	0.6

proximity of beams first eigenfrequency at 97 Hz. A laser displacement sensor measured the beam deflection. The base excitation of the electrodynamic shaker was adapted such that the measured deflection amplitude of the aluminum beam remained constant. The experimental setup is shown in Fig. 5.16.


Figure 5.15: Flexible piezoelectric transducers attached to a 130 mm x 20 mm x 2 mm aluminum beam for material characterization on an electrodynamic shaker

Since the beam's tip deflection amplitude was maintained constant, the network quantity velocity v is imposed and the equivalent circuit, depicted in Fig. 5.17, is used to describe the electrical part of the piezoelectric transducers. Different, purposely selected resistors R_L were connected to the output of the piezoelectric samples. The voltage-

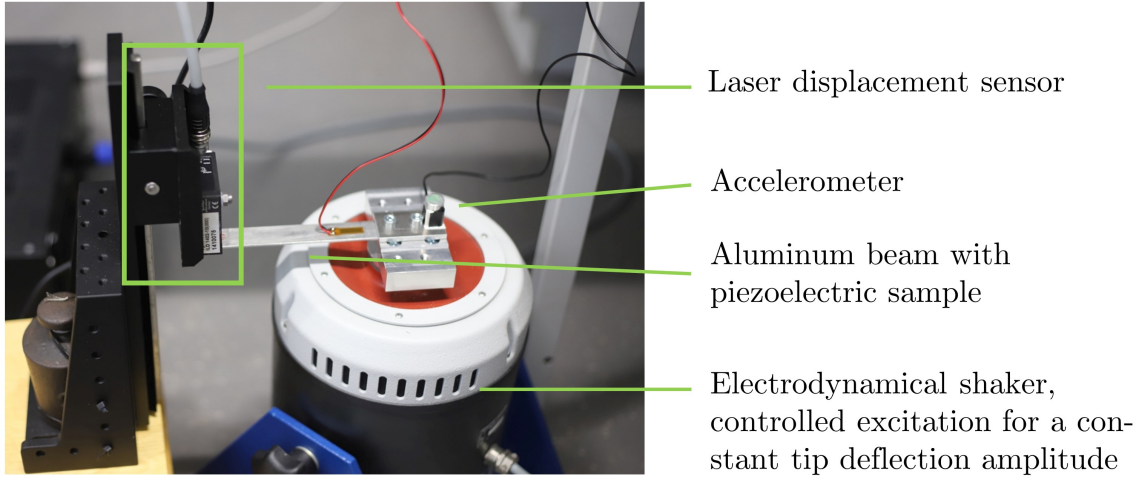


Figure 5.16: Experimental setup of the clamped-free-end aluminum beam with attached piezoelectric sample mounted on an electrodynamic shaker. The excitation amplitude of the shaker was adapted so that the deflection amplitude of the beam's tip remained constant.

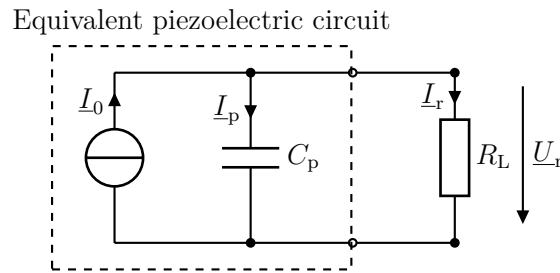


Figure 5.17: Equivalent piezoelectric circuit with a piezoelectric current source and a connected resistance R_L

current relation of a resistive load connected to the electrical terminals of a piezoelectric transducer, driven by a current source, is derived in App. A. The voltage amplitude U_r and the current amplitude I_r obey an elliptical law, which results from the phase shift between voltage and current as a function of the complex current divider

$$\frac{I_r}{I_0} = \frac{j\omega C_p}{j\omega C_p + R_L}. \quad (5.20)$$

The relation between voltage and current is

$$\left(\frac{I_r}{I_0}\right)^2 + \left(\frac{U_r}{I_p/(\omega C_p)}\right)^2 = 1, \quad (5.21)$$

where U_r and I_r are the absolute values of the complex voltage \underline{U}_r and current \underline{I}_r , respec-

tively. Equation 5.21 describes the standard ellipse of the form

$$(x/a)^2 + (y/b)^2 = 1 \quad (5.22)$$

with $x = I_r$, $y = U_r$ and $a = I_0$, $b = I_0/(\omega C_p)$,

centered at the origin. The load resistances R_L were chosen such that the first quadrant of the ellipse is divided into n similar angles φ . Details about the calculation of the corresponding load resistances can be found in Tab. A.1. Six beam tip deflection amplitudes $\hat{z} = [0.5, 1, 1.5, 2, 2.5, 3]$ mm were selected to characterize the voltage amplitude \hat{U}_r and current amplitude \hat{I}_r and to deduce the piezoelectric transducer coefficient α . The voltage-current relations of the four thin transducers connected to various load resistances are depicted in Fig. 5.18.

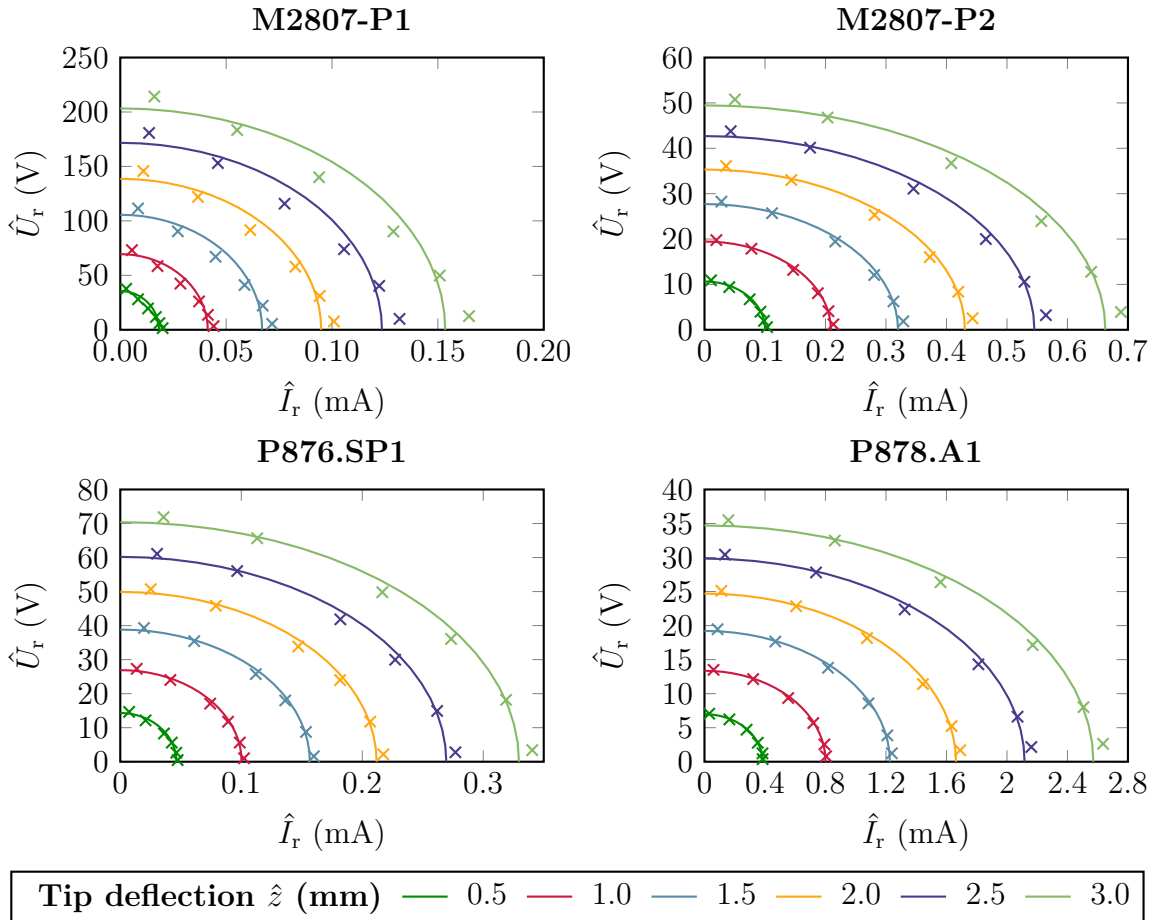


Figure 5.18: Relation between voltage amplitude \hat{U}_r and current amplitude \hat{I}_r for four different piezoelectric transducers for different tip deflection amplitudes. Marks and solid lines represent measured and approximated data, respectively.

In Fig. 5.18, the sample M2807-P1 exhibits the highest voltage among the samples, as expected, paired with the lowest current due to the smallest capacitance. The samples M2807-P2 and P876.SP1 exhibit open electric voltages of a few tens of volts. The short-circuit of the M2807-P2 is twice as high as the P876.SP1 current for the same deflection,

which is presumably caused as a result of the twice as large piezo-ceramic area. The P878.A1 sample provides 4 times higher short-circuit currents than the M2807-P2 sample, whereas the open-circuit voltage is 1.5 times smaller.

The measured data points follow the elliptical voltage-current relationship of Eqn. 5.21. The ideal ellipses (solid lines) are calculated by means of the least square method of the measured data. At small tip deflections up to 2 mm, the measured data points lie on the elliptical curves within a very good accordance, except the data-points of the M2807-P1. Increasing mechanical nonlinearities coupled with increasing inhomogeneous field distribution between the electrodes of the M2807-P1 sample led to non-harmonic voltages signals and to a stronger variation.

Based on the measured data, network parameters are predicted as shown below.

5.3.3 Network Parameter Prediction

To simulate the electrical behavior during one tire revolution, relevant network parameters are required. From the aforementioned measurements, the open-circuit voltage amplitude of the piezoelectric transducer will be linked to the amplitude of the time dependent average strain $\bar{S}(t)$. Therefore, the strain of the transducer, being attached on the aluminum beam, has to be determined. A FEM simulation in ANSYS was conducted to link the average strain to the known deflection of the beam's tip, as illustrated in Fig. 5.19. In the simulation, homogeneous mechanical material properties are assumed and listed in Tab. 5.6. The simulated strain, corresponding to the deflection amplitude $\hat{z} = 1$ mm, is listed in Tab. 5.8.

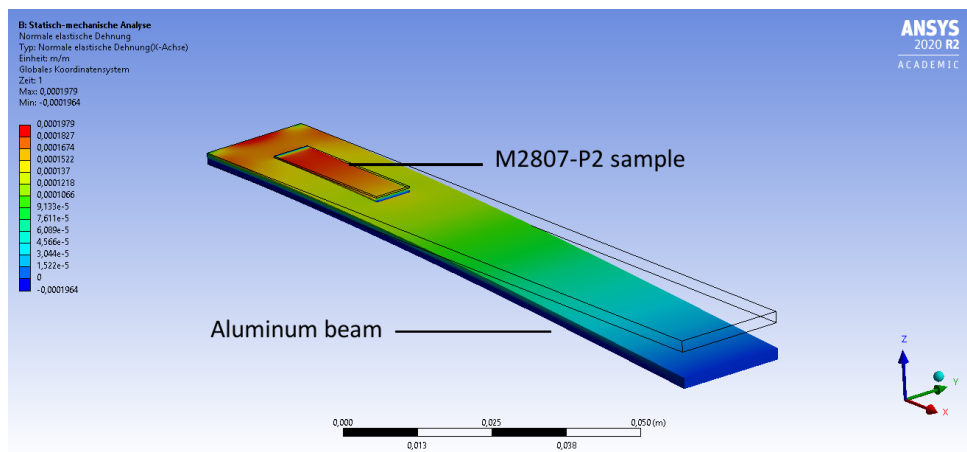


Figure 5.19: ANSYS static structural analysis of an aluminum beam with attached M2807-P2 piezoelectric sample. From the FE simulation, the average strain inside the piezoelectric sample can be deduced as a function of displacement z .

With the assumption, that the thin piezoelectric patches do not affect the tire strain, the strain and the transducer current i_T under short-circuit conditions ($u = 0$) can be

Table 5.8: Simulated average strain corresponding to a tip deflection $\hat{z} = 1$ mm for studied piezoelectric samples

Sample	\bar{S} (ppm) for $\hat{z} = 1$ mm
M2807-P1	180
M2807-P2	180
P876.SP1	150
P878.A1	180

used to estimate the piezoelectric coefficient α according to Eqn. 5.19 as

$$\alpha = \frac{i_T}{l \frac{d\bar{S}(t)}{dt}}. \quad (5.23)$$

Since the excitation was sinusoidal, the average strain is sinusoidal with $\bar{S}(t) = \hat{S} \sin(\omega t)$, too. Consequently, under short-circuit conditions the piezoelectric transducer coefficient can be calculated by

$$\alpha = \frac{\hat{i}_T}{l\omega\hat{S}}, \quad (5.24)$$

or with the relation $u = 1/C_p \int i_T dt$, the coefficient is expressed under open-circuit conditions $\hat{u}_{oc} = \hat{U}_r|_{\hat{i}_r=0}$ as

$$\alpha = \frac{C_p \hat{u}_{oc}}{l\hat{S}}. \quad (5.25)$$

The piezoelectric transducer coefficient α was calculated based on the open-circuit condition $\hat{U}_r|_{\hat{i}_r=0}$ for the measured data of Fig. 5.18 for deflection $\hat{z} = 3$ mm and with the base excitation $f_0 = 97$ Hz. The deduced transducer coefficient α , the capacitance C_p and the effective piezoelectric length l are summarized in Tab. 5.9.

Table 5.9: Network parameter estimation of strain based transducers

Sample	Type	l (mm)	C_p (nF)	α (mC/m)
M2807-P1	longitudinal	28	0.6	8
M2807-P2	transversal	28	15	50
P876.SP1	transversal	10	7	110
P878.A1	longitudinal	15	100	430

To deduce which of the four materials provides the most energy once being deflected, the energy stored in the piezoelectric material in the open-circuit case is determined by

$$E_p = \frac{C_p}{2} \hat{u}_{oc}^2. \quad (5.26)$$

As it will be shown in Sec. 6.5, this energy can be harvested twice. Therefore, the maximal available energy can be estimated by

$$E_{\max} = 2 \cdot E_p = C_p \hat{u}_{oc}^2. \quad (5.27)$$

The energy as a function of deflection \hat{z} is shown in Fig. 5.20. The dashed line illustrates the minimal energy per revolution of 7.9 μJ . Although the sample P878.A1 has the low-

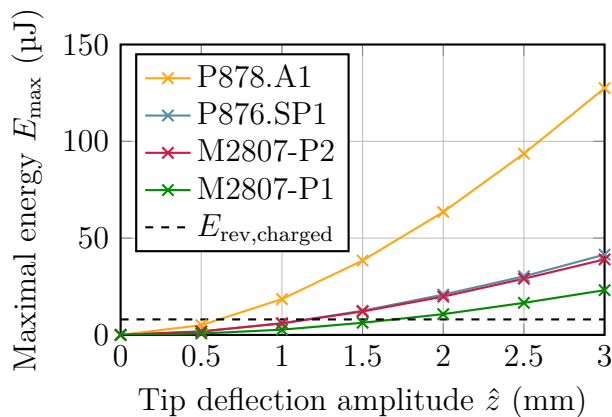


Figure 5.20: Maximal energy E_{\max} for different samples as a function of tip deflection amplitude

est open-circuit voltage, it has the highest energy, because it exploits the piezoelectric 33-effect and because of its high capacitance. The sample M2807-P1 also exploits the 33-effect, however, it has the worst energy performance among the four samples. Due to the lowest energy output and due to the very high open-circuit voltages, sample M2807-P1 was not considered for further investigations inside the tire. The remaining transducers, namely the M2807-P2 and the P876.SP1 perform similarly well. But if the energy is normalized to the effective piezoelectric surface, the smaller P876.SP1 transducer generates almost twice as much energy as the M2807-P2. If the strain corresponding to the deflection of 2 mm is applied in the tire (average strain is in the range of 300 ppm and 360 ppm) and if the piezoelectric energy can be efficiently transferred to an energy storage, the energy per revolution will be enough for the energy supply of TPMS.

5.3.4 Network Simulation

Based on the parameters listed in Tab. 5.9, the open-circuit voltage, the total charge as integrated short-circuit current and the momentary available energy were simulated in LTspice applying the electromechanical network as presented in Fig. 5.11. The work from Lee et al. [17] provided preliminary strain data for the simulation input. The reconstructed signal is illustrated in Fig. 5.21. To be in line with Lee et al., 25% of the strain are supposed to be transferred to each piezoelectric transducer in the network model. According to Eqn. 5.19, the transducer current was deduced. The current can be described

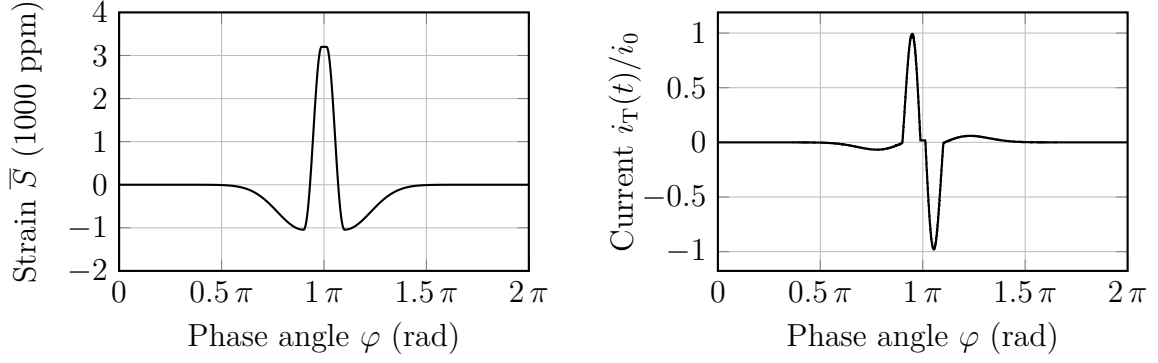


Figure 5.21: Strain signal and deduced transducer current according to Eqn. 5.19 for one tire revolution used as input for the electromechanical network simulation. Only 25% of the strain are supposed to be transferred to the piezoelectric samples.

by harmonic half waves with low amplitude and low frequency, and two half waves with high amplitude and slightly higher frequency.

The simulation results are depicted in Fig. 5.22 for the samples M2807-P2, P876.SP1 and P876.A1 for one tire revolution. Figure 5.22 illustrates the voltage $u = u_{oc}$ under open-circuit conditions, the accumulated charge³ ΔQ with

$$\Delta Q(t) = \int_{t'=0}^t |i_p(t')| dt' \quad (5.28)$$

and the energy E_p corresponding to the piezoelectric capacitor voltage u with

$$E_p(t) = \frac{1}{2} C_p u^2(t). \quad (5.29)$$

Among the studied systems, the sample P878.A1 would provide the most energy. The transducer M2807-P2 and P876.SP1 would provide a similar amount of energy in the range of $45 \mu\text{J}$. This energy is available while being strained from 0 to \hat{S} and again while being released from \hat{S} to 0, so there is actually twice as much energy available ($2 \cdot 45 \mu\text{J}$). The predicted amount of energy is much higher than the desired minimal energy of $7.9 \mu\text{J}$. Since the electrical energy generation is not impacted by the velocity, strain based systems are promising candidates for harvesting energy inside the tire.

In Sec. 9.3, experimental data measured in the tire will be used to verify whether the transducers generate the predicted amount of electrical energy. Furthermore, the experimental data will highlight which sample is the most appropriate for TPMS energy harvesting among the strain based systems.

³The accumulated charge ΔQ per tire revolution is considered as a figure of merit of a strain based energy harvester. As it will be shown in Sec. 6.2, a full-wave rectifier is an appropriate interface circuit to measure the amount of charges, generated by a piezoelectric transducer.

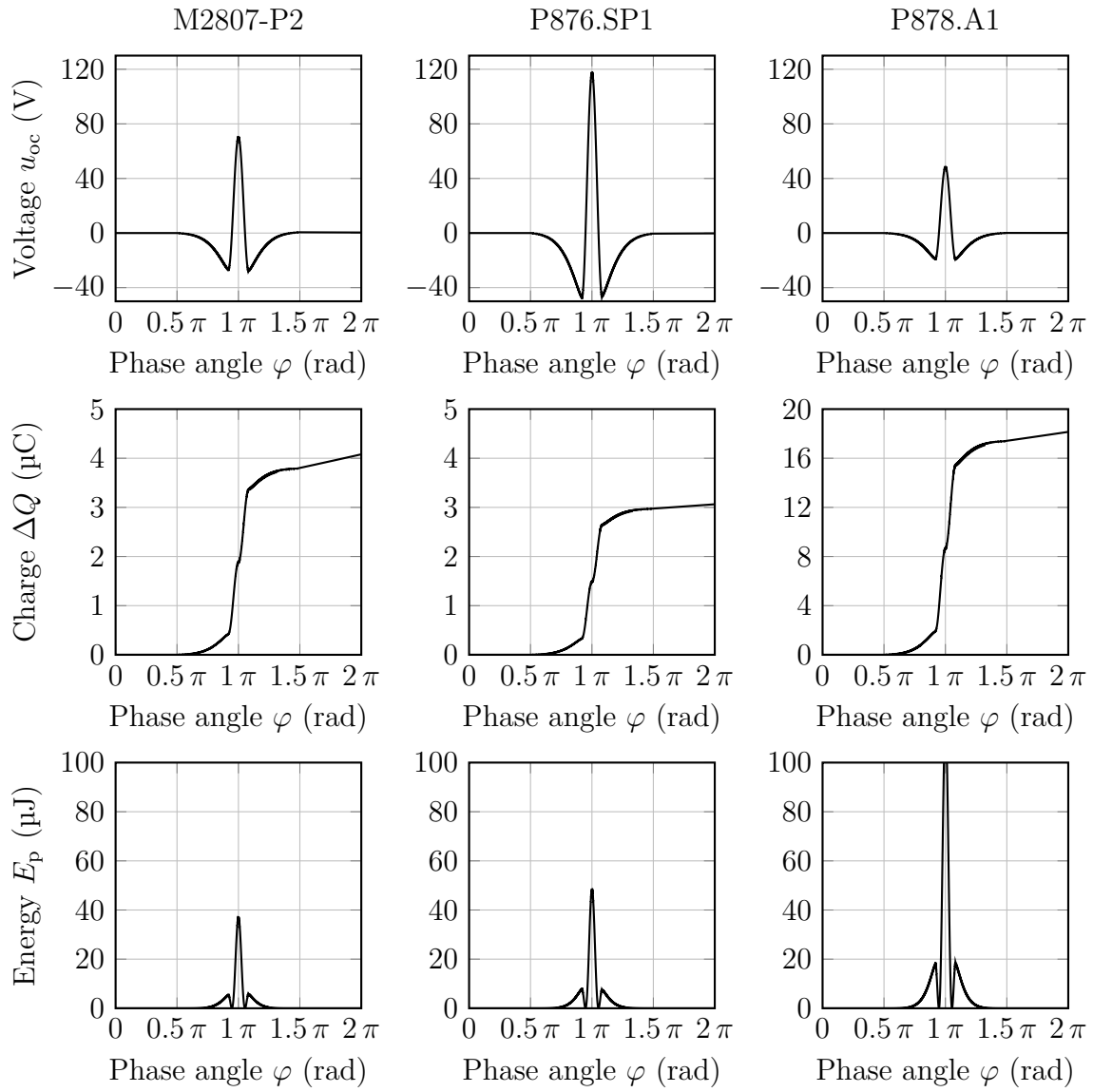


Figure 5.22: Strain PEH prototype simulations - open-circuit voltage $u = u_{oc}$, accumulated charge ΔQ and momentary piezoelectric energy E_p for one tire revolution.

5.4 Summary

Tire Wave Based Piezoelectric Energy Harvesters

System

- Unimorph (brass/M1100) as compliance with tip mass m
- Dimensions: 18 mm x [3, 4] mm x 0.57 mm ($l \times w \times h$)
- Tip mass: $m = [2, 3]$ g

Features

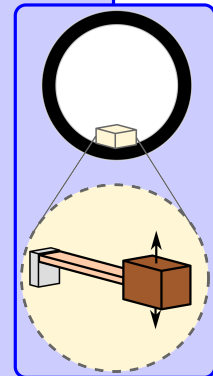
- Elastic bumpers as flexible limit stops
- Overload protection of PE layer against too high strains
- Optimal length ratio l_p/l_s of 0.7 between PE and brass layer

Advantage

- System reusability

Disadvantages

- Very low energy output at 25 km/h
- Total system mass of a few grams leads to an unbalanced tire



Strain Based Piezoelectric Energy Harvesters

System

- Thin piezoelectric fiber composites
- Dimensions: 28 mm x 7 mm x 0.3 mm (M2807-P2),
10 mm x 10 mm x 0.4 mm (P876.SP1),
15 mm x 5 mm x 0.5 mm (P878.A1)
- Total mass $m < 1$ g

Features

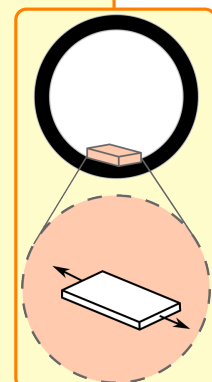
- Flexible materials

Advantages

- Scalable energy generation by modifying the area
- Negligible impact of the prototypes on tire mass distribution
- Durable as only a fraction of the tire strain is applied

Disadvantages

- Reusability is difficult due to glued attachment



6 Piezoelectric Energy Harvester Interface Circuits

Piezoelectric transducers can generate high voltages of a few tens to hundreds of volts inside the wheel and have a high ohmic output impedance. The generated piezoelectric current is alternating. Due to the disparity between generated electrical energy and power on the one hand and required energy and power on the other hand, the accumulated energy has to be stored on a capacitor until sufficient energy has been gathered, before enough power can be supplied to the TPMS for a specific time interval. Referring to Fig. 1.3, the amount of added energy to the capacitor is mainly affected by the efficiency of the interface circuit η_{ic} , which has been defined as

$$\eta_{ic} = \frac{\Delta E_{\text{stored}}}{E_{\text{elec}}}. \quad (6.1)$$

The main objective of this chapter is to select a suitable interface circuit for the previous presented piezoelectric systems in order to fulfill the energy requirements. In Fig. 6.1 the electrical domain of a piezoelectric transducer is shown and connected to an interface circuit and storage capacitor. Four common and basic interface circuits for piezoelectric

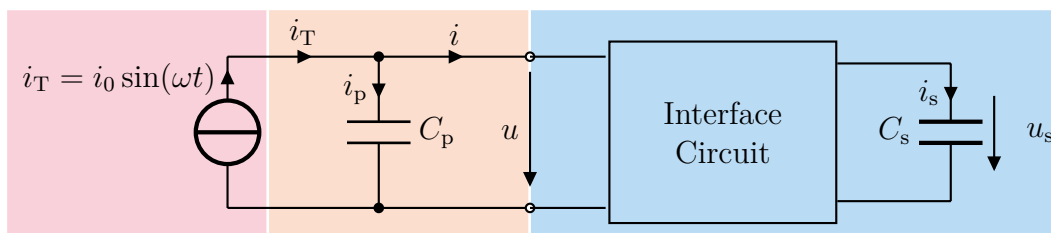


Figure 6.1: Equivalent circuit of the piezoelectric transducer in the electrical domain with interface circuit and storage capacitor C_s . A constant amplitude i_0 is assumed, which imposes a constant strain amplitude in the mechanical domain

energy harvesting, specifically Standard Energy Harvesting (SEH), Switch-Only Rectifier (SOR), Synchronous Switch Harvesting on Inductor (SSHI) and Synchronous Electric Charge Extraction (SECE) are described and analyzed, hereinafter. In [148, 149], they were studied generally with respect to the normalized delivered power as a function of the product of squared coupling coefficient k^2 and mechanical quality Q_m , but an energy storage, connected to the interface circuit with optimal voltage, was always supposed. With

respect to Fig. 6.1, the authors of the cited publications always considered the voltage u_s to be optimal in their analysis. However, the assumption of an optimal voltage is not applicable in this thesis, because the capacitor voltage u_s varies from 0 V, and 2.5 when it is empty and precharged, respectively, to at least 3.9 V, when enough energy is available for the TPMS to transmit a signal. Furthermore, in [148–150] an acceleration signal with constant amplitude was assumed, which is meaningful for inertia based piezoelectric energy harvesters being harmonically excited. For inertia based piezoelectric energy harvesters being excited by a step-function, this assumption is not meaningful. In contrast to the assumption of a constant acceleration amplitude, strain based energy harvesters are driven by a strain signal with constant amplitude, as demonstrated in Sec. 5.3. As mentioned in the previous chapter, the mechanical network components mass, damping and compliance can be neglected for the dynamic behavior for strain based systems.

In [151], the basic interface circuits SEH, SOR SSHI were studied for a comparable unidirectionally coupled piezoelectric system, which was excited by a harmonic signal. In that work, the electrical energy and power as functions of the storage capacitor voltage u_s was provided for each interface circuit. The scientists stated a strong dependency of the transferred energy from the voltage u_s for all circuits. Especially at a low voltage u_s , the transferred energy was similarly small for all three circuits. To reduce the dependency on the connected load, the circuit SECE was developed. While in [152] the transferred energy was studied as a function of load resistance, in a recent study from 2020 [153], the output of an SECE was connected to a capacitor and the limit of the maximal output power was provided. However, this limit did not incorporate relevant losses during the energy transfer to the capacitor. Similarly in 2021, the power of a the SECE was studied in [154], whereas the charging losses of the storage capacitor were neglected, too.

Although there are manifold studies and advancements of efficient interface circuit, different mechanical boundary conditions (harmonic vs. non-harmonic input signal, displacement signal with constant amplitude vs. acceleration signal with constant amplitude) and electrical boundary conditions (resistive load vs. capacitive load, varying capacitor voltages vs. optimal capacitor voltage) were supposed. Therefore, this chapter aims at providing an understanding of the four interface circuits in their basic form. With respect to the strain based energy harvesters, a strain signal with constant amplitude is supposed as mechanical excitation, which is why, the transducer systems are considered to be unidirectionally coupled. For a comprehensive understanding, a harmonic excitation signal is supposed, leading to a harmonic current signal. Even if the current signal of the strain energy harvester, depicted in Fig. 5.21 is not perfectly harmonic, the following general analysis and the consequences can be applied to it without any restrictions. While the analysis of the transferred energy as a function of storage voltage of SEH, SOR and SSHI represents a generalization of already published findings, the one of the SECE is new.

6.1 Energy and Charge of a Piezoelectric Transducer

To compare the interface circuits, the maximal output voltage u_0 and the maximal available electrical energy E_0 , being stored on the piezoelectric capacitance of the simplified transducers of Fig. 6.2, are deduced. The harmonic transducer current is expressed as

$$i_T(t) = i_0 \sin(\omega t). \quad (6.2)$$

Every half wave the charge Q_0 can be accumulated with

$$Q_0 = \int_{t=0}^{T/2} i_T(t) dt \quad (6.3)$$

$$Q_0 = \frac{2i_0}{\omega}. \quad (6.4)$$

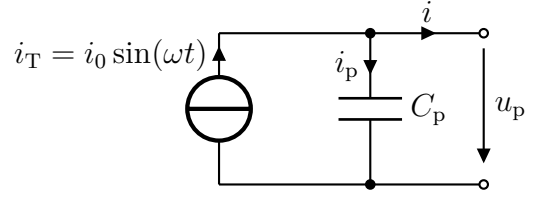


Figure 6.2: Equivalent circuit of the piezoelectric transducer

This is the maximal amount of charge of the same polarity. Under open-circuit conditions, all charges are stored on the piezoelectric capacitance C_p , leading to the maximal piezoelectric voltage

$$u_0 = \frac{Q_0}{C_p} = \frac{2i_0}{\omega C_p}. \quad (6.5)$$

The corresponding electrical energy, stored on the piezoelectric capacitance is

$$E_0 = \frac{Q_0^2}{2C_p} = \frac{C_p u_0^2}{2}. \quad (6.6)$$

This is the energy maximum only under open-circuit conditions. The transferred energy of the interface circuits will be normalized to this energy. As it will be shown in the following, the interface circuits SEH, SOR and SSHI transfer charges from the piezoelectric transducer to the storage capacitor, which results in a small efficiency when the capacitor voltage u_s is very small compared to the open-circuit voltage u_0 of the piezoelectric transducer. A general explanation, why the efficiency is low, will be given and implies the subsequent assumptions:

1. A storage capacitor C_s and an ideal diode (forward voltage drop $u_d = 0$) is connected to the piezoelectric capacitance C_p as depicted in Fig. 6.3. The diode avoids any discharge of the capacitor C_s .
2. The capacitor C_s is generally precharged, with the initial charge $Q_s(t = 0) = Q_{s,0}$.
3. The capacitance C_p is generally precharged, with the initial charge $Q_p(t = 0) = Q_{p,0}$.
4. The capacitance C_s is much greater than the capacitance C_p , which is fulfilled for the studied transducers, since $C_s = 220 \mu\text{F}$ and $C_p \leq 100 \text{ nF}$.

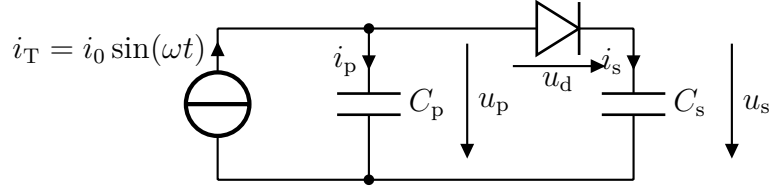


Figure 6.3: Piezoelectric transducer with connected capacitor C_s

With respect to Fig. 6.3, the total charge Q_0 will be divided into the charge ΔQ_p added to the capacitor C_p and the charge ΔQ_s added to the precharged capacitor C_s with initial charge $Q_{s,0}$. This is expressed by

$$Q_0 = \Delta Q_p + \Delta Q_s. \quad (6.7)$$

According to Kirchhoff's law, the charge Q_0 is divided such that the capacitor voltages are equal ($u_p = u_s + u_d$ with $u_d = 0$). Consequently

$$u_p = u_s \quad (6.8)$$

$$\frac{\Delta Q_p + Q_{p,0}}{C_p} = \frac{\Delta Q_s + Q_{s,0}}{C_s} \quad (6.9)$$

$$\Delta Q_p = \frac{C_p}{C_s} \cdot (\Delta Q_s + Q_{s,0}) - Q_{p,0} \quad (6.10)$$

Replacing ΔQ_p in Eqn. 6.10 by Eqn. 6.7 results in

$$Q_0 - \Delta Q_s = \frac{C_p}{C_s} (\Delta Q_s + Q_{s,0}) - Q_{p,0} \quad (6.11)$$

$$\Delta Q_s \left(1 + \frac{C_p}{C_s}\right) = Q_0 - \frac{C_p}{C_s} Q_{s,0} - Q_{p,0}. \quad (6.12)$$

With $C_p \ll C_s$, $Q_{s,0} = C_s \cdot u_{s,0}$ and $Q_{p,0} = C_p \cdot u_{p,0}$ follows

$$\Delta Q_s = Q_0 - C_p \cdot u_{s,0} + C_p \cdot u_{p,0}. \quad (6.13)$$

Normalizing the charge ΔQ_s to the available charge $Q_0 = C_p \cdot u_0$ finally leads to

$$\boxed{\frac{\Delta Q_s}{Q_0} = 1 - \frac{u_{s,0}}{u_0} + \frac{u_{p,0}}{u_0}}. \quad (6.14)$$

Equation 6.14 highlights that the transferred charge depends on the ratio of the initial voltages $u_{s,0}$ and $u_{p,0}$ to the maximal piezoelectric voltage u_0 . The charge ΔQ_s decreases linearly with increasing voltage $u_{s,0}$ and with decreasing voltage $u_{p,0}$.

Based on the transferred charge, the added energy ΔE_{stored} can be deduced. It is generally the difference between the capacitor energy E_s and $E_{s,0}$ after and before the

charge transfer, respectively. The added energy $\Delta E_{\text{stored}} = \Delta E$ is described by

$$\Delta E = E_s - E_{s,0} \quad (6.15)$$

$$\Delta E = \frac{(Q_{s,0} + \Delta Q_s)^2}{2C_s} - \frac{Q_{s,0}^2}{2C_s} \quad (6.16)$$

$$\Delta E = \frac{2\Delta Q_s Q_{s,0} + \Delta Q_s^2}{2C_s} \quad (6.17)$$

Normalizing the energy ΔE to the energy E_0 from Eqn. 6.6 results in the efficiency η

$$\eta = \frac{\Delta E}{E_0} = \frac{C_p}{C_s} \frac{\Delta Q_s}{Q_0} \left(2 \frac{Q_{s,0}}{Q_0} + \frac{\Delta Q_s}{Q_0} \right) \quad (6.18)$$

Replacing $\Delta Q_s/Q_0$ by Eqn. 6.14, $Q_{s,0}$ by $Q_{s,0} = C_s \cdot u_{s,0}$ and $Q_0 = C_p \cdot u_0$ leads to

$$\eta = \frac{C_p}{C_s} \left(1 - \frac{u_{s,0}}{u_0} + \frac{u_{p,0}}{u_0} \right) \left(2 \frac{C_s u_{s,0}}{C_p u_0} + \left(1 - \frac{u_{s,0}}{u_0} + \frac{u_{p,0}}{u_0} \right) \right) \quad (6.19)$$

$$\eta = \left(1 - \frac{u_{s,0}}{u_0} + \frac{u_{p,0}}{u_0} \right) \left(2 \frac{u_{s,0}}{u_0} + \frac{C_p}{C_s} \left(1 - \frac{u_{s,0}}{u_0} + \frac{u_{p,0}}{u_0} \right) \right). \quad (6.20)$$

If the capacitor C_s is entirely empty ($u_{s,0}$), the efficiency can be approximated as

$$\eta(u_{s,0} = 0) = \frac{C_p}{C_s} \left(1 + \frac{u_{p,0}}{u_0} \right)^2. \quad (6.21)$$

Since the capacitor voltage $C_p \ll C_s$ is very small, the efficiency is $\eta(u_{s,0} = 0)$ is very small, too. Already at voltages $u_{s,0} \gg C_p/C_s$ the efficiency from Eqn. 6.20 can be finally rewritten with $C_p \ll C_s$ to

$$\boxed{\eta = \frac{\Delta E}{E_0} = 2 \frac{u_{s,0}}{u_0} \left(1 - \frac{u_{s,0}}{u_0} + \frac{u_{p,0}}{u_0} \right)}. \quad (6.22)$$

The efficiency is a function of normalized initial capacitor voltages $u_{s,0}/u_0$ and $u_{p,0}/u_0$. Both normalized charge and efficiency as a function of normalized voltage are depicted in Fig. 6.4 for the case $u_{p,0} = 0$. While the charge ΔQ_s is maximal at the voltage $u_{s,0} = 0$, the electrical field of the capacitor is minimal. Adding a charge to the discharged capacitor only leads to a small voltage increase and the corresponding field energy is low. The higher the voltage $u_{s,0}$ the higher the electrical field energy is, but the smaller the added charge is. In the considered example, at $u_{s,0} = u_0/2$, the transferred energy is maximal and decreases, until all charge is required to rise the voltage of C_p from 0 V to $u_{s,0} = u_0$. Then, no charge will be transferred to the storage and the added energy is $\Delta E = 0$.

The three interface circuits SEH, SOR and SSHI imposes different initial charge conditions $Q_{p,0}$, leading to different behaviors, which are analyzed in the next subsections.

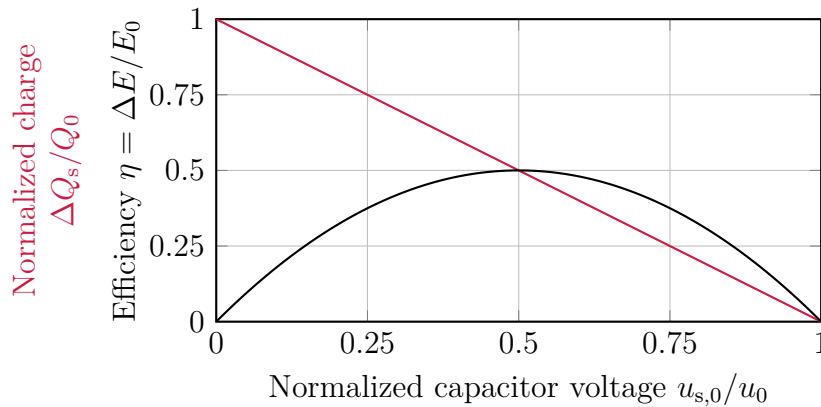


Figure 6.4: Normalized charge and efficiency as functions of normalized capacitor voltage for an initially empty capacitance C_p with $u_{p,0} = 0$. An increasing voltage $u_{s,0}$ leads to a smaller charge ΔQ_s .

6.2 Standard Energy Harvesting - SEH

One of the simplest ways to charge a storage capacitor with the alternating current from a piezoelectric transducer is to use a full-wave rectifier connected between the transducer and the storage. The circuit is depicted in Fig. 6.5. The corresponding waveforms are shown in Fig. 6.6. In steady-state at each beginning of a half wave as depicted in Fig. 6.6

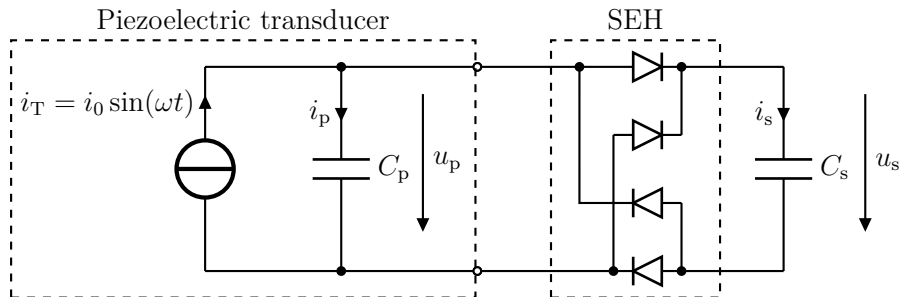


Figure 6.5: SEH interface circuit with storage capacitor

the piezoelectric capacitance has been precharged to the storage voltage $u_{s,0}$. Since the current i_T of the former half wave was negative, the actual piezoelectric voltage is negative with $u_{p,0} = -u_{s,0}$. Therefore, all diodes are reverse-biased and the current $i_T(t)$ first compensates the oppositely charged capacitor with charge $Q_{p,0} = -C_p \cdot u_{s,0}$, until the piezoelectric capacitance has the same voltage as the storage capacitance ($|u_p| = u_s$). Then, two diodes are conductive and both capacitors are charged equally. In that case, a much higher charge is needed to raise the voltage of C_s to the same level as C_p . Corresponding to the current divider

$$\frac{i_p}{i_T} = \frac{C_p}{C_p + C_s}. \quad (6.23)$$

and with $C_p \ll C_s$ the current i_p in Fig. 6.6 drops almost down to zero when the current i_s is approximately equal to the source current i_T ($i_s \approx i_T$). Due to the rectification of the positive and negative half waves of the current signal, it suffices to study the energy transfer during one half wave - the positive half wave. With the initial condition

$$u_{p,0} = -u_{s,0}, \quad (6.24)$$

the charge relation of Eqn. 6.14 is rewritten to

$$\frac{\Delta Q_s}{Q_0} = 1 - 2 \frac{u_{s,0}}{u_0}. \quad (6.25)$$

The energy relation of Eqn. 6.22 is then

$$\eta_{\text{SEH}} = \frac{\Delta E}{E_0} = 2 \frac{u_{s,0}}{u_0} \left(1 - 2 \frac{u_{s,0}}{u_0} \right). \quad (6.26)$$

Both normalized charge and efficiency are shown in Fig. 6.7. The efficiency is additionally shown and compared with other interface circuits in Fig. 6.21a. With respect to Eqn. 6.26, the efficiency is maximal if the voltage ratio is $u_{s,0}/u_0 = 0.25$ and equals 25%.

A significant amount of energy is lost, because a part of the piezoelectric current $i(t)$ is used to discharge the oppositely charged piezoelectric capacitances. Periodic, impulse driven energy harvesters (shoe, pacemaker, tire) with a SEH interface behave slightly differently. The impulse causes a mechanical oscillation with exponential decay. Due to the piezoelectric capacitance self-discharges between the impulses it is almost empty when the next impulse appears. Higher efficiencies are the result. For harmonic excitations, this beneficial discharge is provoked on purpose, leading to the next circuit, the SOR.

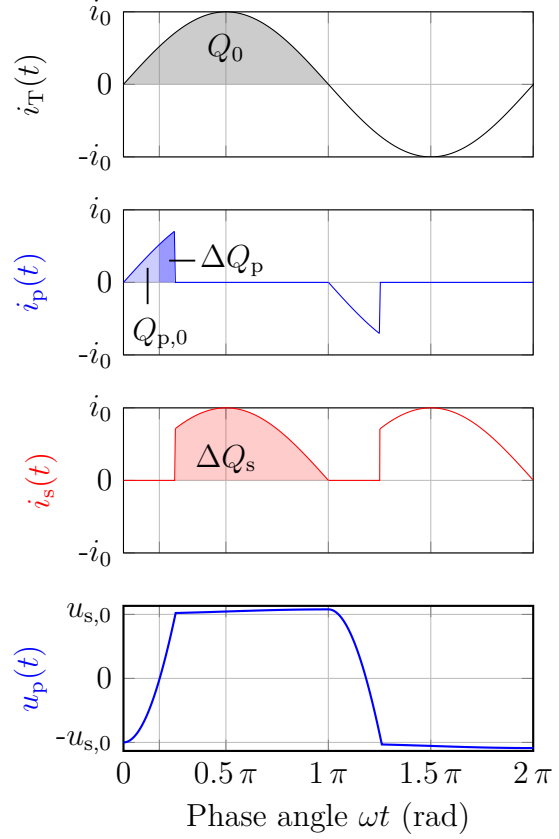


Figure 6.6: Simulated SEH source current i_T , piezoelectric current i_p , capacitor current i_s and piezoelectric voltage u_p for one period corresponding to Fig. 6.5 with $C_s \gg C_p$. The current i_p first flows into C_p until $|u_p| = u_s$ is reached.¹

¹For a compact overview, only the bottom plot possess an x-axis. It is the same for all three plots.

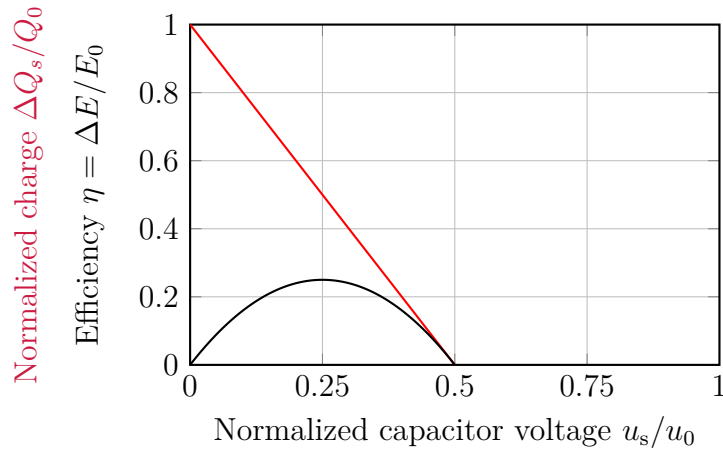


Figure 6.7: SEH - normalized charge and efficiency as functions of normalized capacitor voltage for an initially precharged capacitance C_p with $u_{p,0} = -u_{s,0}$. Due to the charge and discharge of the piezoelectric capacitance C_p every half wave, a charge ΔQ_s can be transferred if the voltage is $u_{s,0} < u_0/4$.

6.3 Switch only Rectifier - SOR

A switch is added in parallel between the piezoelectric circuit and the SEH circuit as presented in Fig. 6.5. Usually, the switch $S1$ is open. It closes and short-circuits the piezoelectric harvester when the polarity of the current $i_T(t)$ reverses, measurable by a decrease of the voltage u_p . While being short-circuited, the residual charge on the capacitance C_p is removed, appearing as a large, short-circuit current peak i_p at multiples of half of the period $t = n \cdot T/2$, $n \in \mathbb{N}$. A zero crossing of the piezoelectric voltage u_p indicates that all charge has been removed. This is the moment when the switch is opened again. The circuit, also known as Switch-Only Rectifier (SOR), is depicted in Fig. 6.8 [151]. Due to the discharge, the initial condition is

$$u_{p,0} = 0. \quad (6.27)$$

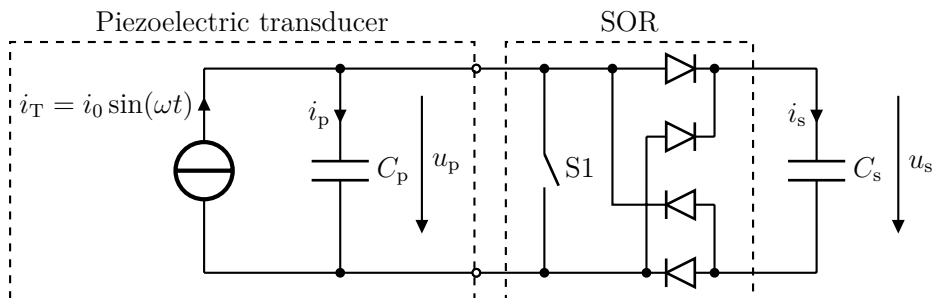


Figure 6.8: SOR interface circuit with storage capacitor. The switch $S1$ is closed every half-wave, when the current i_T changes the polarity which leads to a discharge of the precharged capacitance C_p .

Then, the charge relation of Eqn. 6.14 is rewritten to

$$\frac{\Delta Q_s}{Q_0} = 1 - \frac{u_{s,0}}{u_0}. \quad (6.28)$$

The efficiency of Eqn. 6.22 is then

$$\eta_{\text{SOR}} = \frac{\Delta E}{E_0} = 2 \frac{u_{s,0}}{u_0} \left(1 - \frac{u_{s,0}}{u_0} \right). \quad (6.29)$$

The efficiency η_{SOR} is limited by 50% and is reached when $u_{s,0}/u_0 = 0.5$. Both normalized charge and efficiency are plotted in Fig. 6.10 and compared with other interface circuits in Fig. 6.21a. Implemented as an electrical circuit, this concept requires a peak detector and a zero-crossing detector of the voltage signal $u_p(t)$ to determine the moment when the switch S1 must be closed and opened.

Even if the efficiency is doubled compared to the SEH, at least half of the energy is lost as heat due to the short-circuit of the piezoelectric capacitor. To further improve the efficiency, the piezoelectric capacitor is not discharged, but the polarity of the charge is inverted. This approach leads to the Synchronous Switch Harvesting on Inductor (SSHI) circuit.

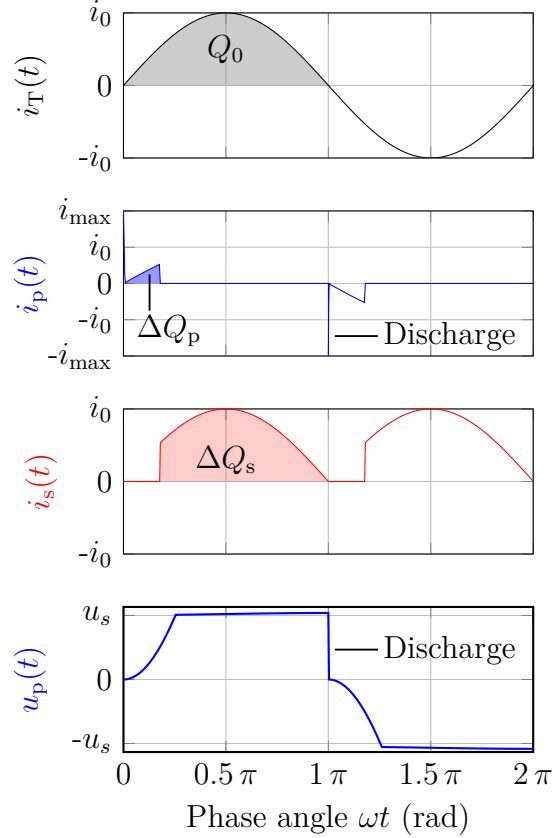


Figure 6.9: SOR source current i_T , piezoelectric current i_p , capacitor current i_s and piezoelectric voltage u_p for one period corresponding to Fig. 6.8 with $C_s \gg C_p$. At $\omega t = 0$ and $\omega t = \pi$, the capacitance C_p is discharged.

6.4 Synchronized Switch Harvesting on Inductor - SSHI

The principal Synchronous Switch Harvesting on Inductor (SSHI) circuit is depicted in Fig. 6.11, where an inductor L is connected to the switch S1 and forms together with the capacitance C_p an electrical resonator when the switch is short-circuited. In this case, the piezoelectric energy is transduced into magnetic energy of the inductor during $n \cdot T/2 < t < n \cdot T/2 + T_{LC}/2$ with T_{LC} the period of the LC_p resonator, which is in the order of microseconds. At $T_{LC}/2$ the energy is removed from the inductor and entirely stored again on the piezoelectric capacitance, with the important difference that

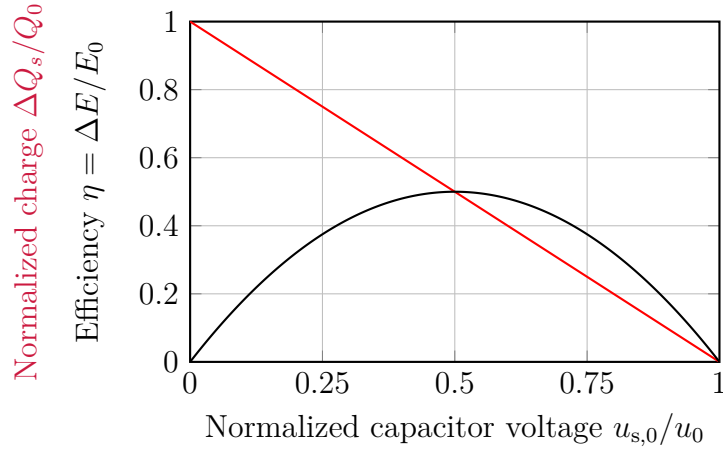


Figure 6.10: SOR - normalized charge and efficiency as functions of normalized capacitor voltage $u_{s,0}/u_0$. Due to the short-circuited piezoelectric transducer after each half wave the piezoelectric capacitance C_p is discharged ($u_{p,0} = 0$).

the charge polarity has been inverted. Simultaneously, the switch has to be opened at $t = n \cdot T/2 + T_{LC}/2$ to avoid the piezoelectric charge being inverted again.

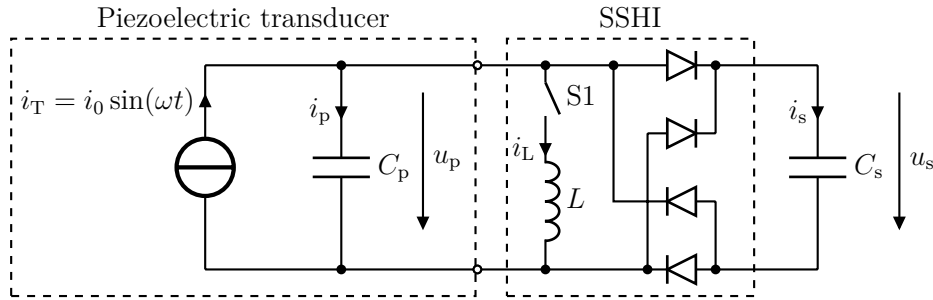


Figure 6.11: Parallel-SSHI circuit with storage capacitor. The inductor L builds an resonating circuit with the piezoelectric capacitance C_p when the switch $S1$ is closed. If switch $S1$ is timed appropriate, all piezoelectric charge $Q_{p,0}$ is inverted.

Depending on whether the inductor and the switch are connected in series or in parallel, the two main methods Series-SSHI and Parallel-SSHI are differentiated. Hereinafter, the focus relies on the Parallel-SSHI, depicted in Fig. 6.11. Figure 6.12 shows the current and voltage evolution for one period. The current inversion is visible as current peak $i_p(t)$ at $t = n \cdot T/2 + T_{LC}/2$, where all charge $Q_{p,0}$ is inverted, leading to the initially condition

$$u_{p,0} = u_{s,0}. \quad (6.30)$$

Then, the charge relation of Eqn. 6.14, can be rewritten to

$$\boxed{\frac{\Delta Q_s}{Q_0} = 1.} \quad (6.31)$$

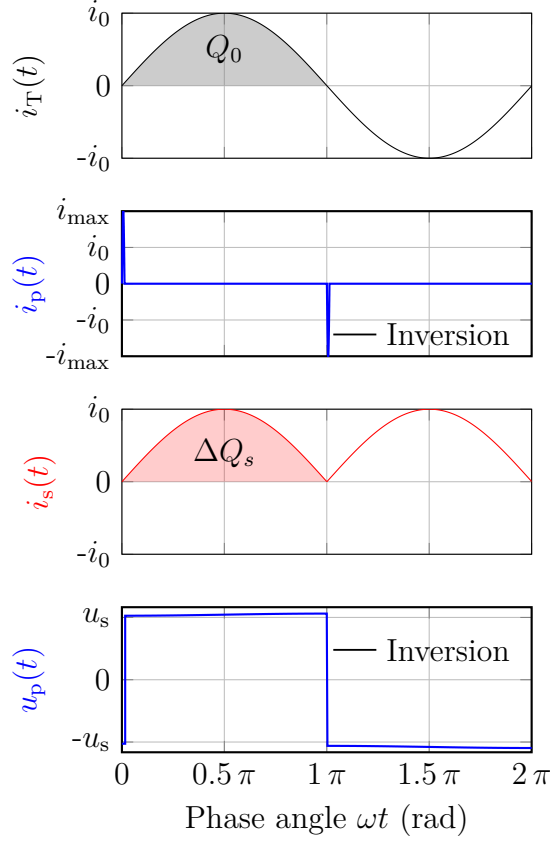


Figure 6.12: SSHI source current i_T , piezoelectric current i_p , capacitor current i_s and piezoelectric voltage u_p for one period corresponding to Fig. 6.11 with $C_s \gg C_p$. Due to the charge inversion, appearing as a short peak current i_p after each half wave, the capacitance C_p is inversely charged to $Q_{p,0}$ and the charge $\Delta Q_s = Q_0$ is added to the capacitor C_s with initial voltage $u_{s,0}$

The efficiency of Eqn. 6.22 is then

$$\eta_{\text{SSHI}} = \frac{\Delta E}{E_0} = 2 \frac{u_{s,0}}{u_0}. \quad (6.32)$$

Every half wave half the entire charge $\Delta Q_s = Q_0$ can be added to the capacitor C_s and the efficiency η_{SSHI} depends solely on the initial capacitor voltage $u_{s,0}$.

Both the charge and the efficiency are plotted in Fig. 6.13. Already for voltage ratios $u_{s,0}/u_0 = 0.5$ the efficiency would be higher than 100% due to the definition of η in Eqn. 6.22. However, two phenomena limit the efficiency η_{SSHI} . First, a parasitic piezoelectric resistance limits the piezoelectric voltage u_p . It is analyzed in App. B. Due to the parasitic resistance, the storage voltage is limited by

$$u_{s,\text{max}} = R_p \cdot \overline{i_T}(t), \quad (6.33)$$

where $\overline{i_T}(t)$ is the average current. Both the parasitic resistance and the average source current determine the maximal voltage u_s . Real diodes further decrease the maximal voltage $u_{s,\text{max}}$. If the resistance R_p is large, this effect plays a subordinated role.

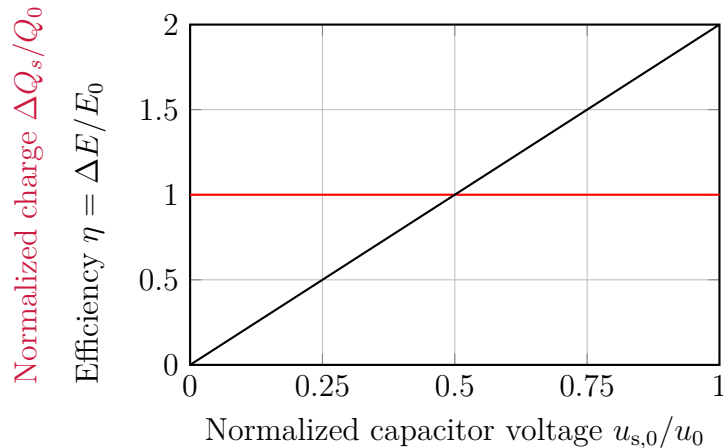


Figure 6.13: SSHI - normalized charge and efficiency as functions of voltage ratio $u_{s,0}/u_0$. The initial precharge of the capacitance C_p with $u_{p,0} = u_{s,0}$ leads both to a constant charge ΔQ_s being added and to a linear increase of the efficiency.

Second, the non-ideal inductor creates a series resonant LCR_p circuit with a finite quality factor q

$$q = \sqrt{\frac{L}{C_p}} \cdot \frac{1}{R_L}, \quad (6.34)$$

where L , R_L are the inductance and the resistive losses related to the inductor, respectively. During the charge inversion, a part of the energy is dissipated across the resistance of the inductance R_L , characterized by the inversion coefficient γ [155, 156], It will be deduced in Sec. 6.5.1 and is

$$\gamma = \frac{E_0 - E_{\text{lost}}}{E_0} = \frac{E_{\text{inversion}}}{E_0} = \exp\left(-\frac{\pi}{2q}\right). \quad (6.35)$$

Since the capacitance C_p is very small, the quality factor q is very high and the charge inversion is not strongly affected. However, the exact inversion timing is crucial.

With respect to the studied open-circuit voltage signal of the piezoelectric transducers of Chapter 5, even under ideal conditions the voltage ratio u_s/u_0 would be small, which is the main problem. Since the voltage of the storage C_s varies typically in the tire application between 0 V and 4 V and the smallest simulated peak voltage of the strain based transducers was 50 V, the normalized voltage would be at most $u_{s,0}/u_0 < 4 \text{ V}/50 \text{ V} = 0.08$, leading to the SSHI efficiency of 16% at most. Since the SOR efficiency and the SEH efficiency at this normalized voltage are 15% and 13%, respectively, the benefit of an SSHI interface circuit is marginal.

6.5 Synchronous Electric Charge Extraction - SECE

In 2005, Lefeuvre et al. [152] proposed another interface circuit, reducing the strong load dependency between the provided power of the piezoelectric transducer and a connected load resistance (which impacts the voltage u_p). The principle circuit with a connected capacitor is illustrated in Fig. 6.14. The corresponding signal waveforms are shown in Fig. 6.15.

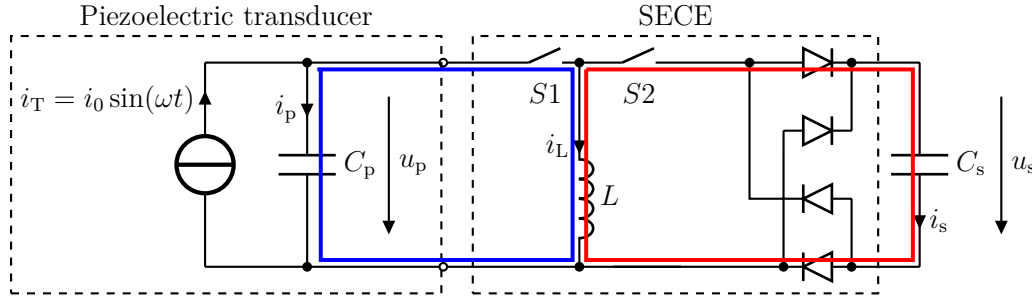


Figure 6.14: SECE circuit with storage capacitor. When switch S1 is closed and S2 is opened, the components LC_p form an electrical resonator, while when S1 is opened and S2 is closed, the components LC_s form a second resonator.

The idea was to keep the piezoelectric system open in order to accumulate charges and consequently energy (S1 open, S2 open). Similar to the SSHI scheme, a switch connects an inductor L in parallel to the terminals of the piezoelectric system. When the voltage amplitude becomes either maximal or minimal, switch S1 closes and creates a resonating RLC system, while switch S2 remains opened. When switch S1 is closed, the piezoelectric transducer energy is transformed into magnetic energy of the inductor. While switch S1 of a SSHI circuit opens the connection after $n \cdot T/2 + T_{LC_p}/2$, switch S1 has already opened and disconnected the inductor from the piezoelectric transducer after $n \cdot T/2 + T_{LC_p}/4$ when all capacitive energy has been transferred to the inductor. A zero-crossing voltage detector is used to detect this moment. Switch S1 is opened and switch S2 is closed immediately afterwards and creates a second resonance circuit to enable the energy transfer from the inductor L to the capacitor C_s . When the energy is removed from the inductor, S2 opens and waits until the next piezoelectric voltage extremum occurs.

Due to the synchronization between piezoelectric voltage, equivalent to the stored piezoelectric charges and the mechanical displacement, Lefeuvre et al. [152] called this method Synchronous Electric Charge Extraction (SECE). The two different capacitances C_s and C_p create two separate resonant circuits, whose losses are mainly determined by the resistive losses of the inductor L . Hereinafter, the electric circuit efficiency will be determined. The aforementioned phases will be quantified with respect to

1. energy transfer from the capacitance C_p to inductance L
2. energy transfer from inductance L to the storage C_s

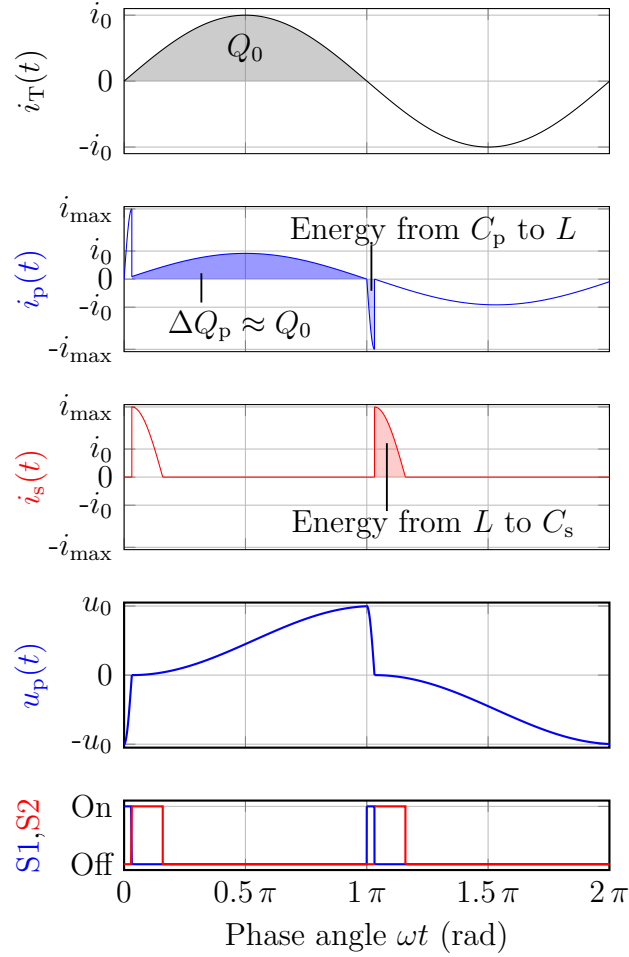


Figure 6.15: SECE currents i_T , i_p , i_s and voltage u_p for one period corresponding to Fig. 6.14. The current i_T charges the capacitance C_p , until it is maximal. Then, switch S1 is closed and the energy is transferred from C_p to L . Afterwards, switch S2 is closed and the energy is transferred from L to C_s .

Both resonators are generally described by the following second order differential equation

$$\frac{d^2i}{dt^2} + 2\delta \cdot \frac{di}{dt} + \omega_0^2 \cdot i = 0 \quad (6.36)$$

$$\text{with } \delta = \frac{R_L}{2L}, \quad \text{and } \omega_0 = \frac{1}{\sqrt{LC}}, \quad (6.37)$$

where R_L , δ , ω_0 are the parasitic resistance of the inductor, the decay rate and the natural angular frequency. If $\omega_0^2 > \delta^2$, the solution is a damped harmonic oscillation, whose solution is

$$i(t) = \exp(-\delta \cdot t) \cdot (A \cdot \sin(\omega_e t) + B \cdot \cos(\omega_e t)), \quad (6.38)$$

where A, B are constants and ω_e is the oscillation frequency of the damped system with

$$\omega_e^2 = \omega_0^2 - \delta^2. \quad (6.39)$$

6.5.1 Energy Transfer from the Capacitance C_p to the Inductance L

During each half oscillation the inductor L is empty and the piezoelectric capacitance C_p is charged. Switch S1 is open so that the total charge of the same polarity are accumulated on C_p , leading to the maximal piezoelectric voltage $u_0 = Q_0/C_p$. The initial conditions are

$$i_p(t = 0) = 0 \quad \text{and} \quad u_p(t = 0) = u_0. \quad (6.40)$$

Further, the capacitance C in Eqn. 6.37 is replaced by the piezoelectric capacitance C_p . With the relation of Eqn. 6.39, the current is

$$i_p(t) = C_p \cdot u_0 \cdot \frac{\omega_0^2}{\omega_e} \exp(-\delta t) \sin(\omega_e t). \quad (6.41)$$

All energy that is stored has been removed from the capacitance C_p when

$$i_p'(t_z) = 0 \leftrightarrow \omega_e t_z = \arctan \frac{\omega_e}{\delta}. \quad (6.42)$$

Inserting Eqn. 6.42 in Eqn. 6.41 leads to the expression of the maximal current as

$$i_{p,\max} = C_p \cdot u_0 \cdot \omega_0 \cdot \exp\left(-\frac{\delta \arctan\left(\frac{\omega_e}{\delta}\right)}{\omega_e}\right). \quad (6.43)$$

The coefficient

$$\kappa = \frac{\omega_e}{\delta} \quad (6.44)$$

is introduced. With the definition of the quality factor from Eqn. 6.34, it can be rewritten to

$$\kappa = \sqrt{4 \cdot q^2 - 1}. \quad (6.45)$$

Consequently, the maximal current is rewritten as

$$i_{p,\max} = C_p \cdot u_0 \cdot \omega_0 \cdot \exp\left(-\frac{\arctan \kappa}{\kappa}\right). \quad (6.46)$$

Then, the efficiency of the first transferring phase $\eta_{\text{SECE},1}$ is

$$\eta_{\text{SECE},1} = \frac{E_L(t_z)}{E_0} = \frac{L i_{p,\max}^2}{C_p u_0^2} = \frac{i_{p,\max}^2}{(C_p u_0)^2 \omega_0^2} \quad (6.47)$$

$$\eta_{\text{SECE},1} = \exp\left(-2 \cdot \frac{\arctan \kappa}{\kappa}\right). \quad (6.48)$$

The small piezoelectric capacitance C_p typically leads to a high quality factor q_1 of the RLC_p resonator. If the quality factor $q_1 \geq 7$, Eqn. 6.46 and Eqn. 6.48 can be simplified to

$$i_{p,\max} = C_p u_0 \omega_0 \cdot \exp\left(-\frac{\pi}{4q_1}\right) = \frac{u_0}{R_L \cdot q_1} \cdot \exp\left(-\frac{\pi}{4q_1}\right) \quad (6.49)$$

and

$$\boxed{\eta_{\text{SECE},1} = \exp\left(-\frac{\pi}{2q_1}\right)}, \quad (6.50)$$

respectively, where for $q \geq 7$ the variation from the exact solution is smaller than 1%. The efficiency is equivalent to the inversion coefficient γ , defined in the previous subsection in Eqn. 6.35. Since the quality factor is $q_1 \gg 1$, almost all energy is transferred to the inductor which will charge the capacitor C_s in the second phase.

6.5.2 Energy Transfer from the Inductance L to the Storage C_s

Immediately after reaching the current maximum, switch S1 is opened and switch S2 is closed to form the second LC circuit with $C = C_s$. The inductor has been charged, while the storage capacitor has been already precharged from former cycles. The corresponding initial conditions are

$$i_L(t=0) = i_{L,0} = i_{p,\max} \quad \text{and} \quad u_s(t=0) = u_{s,0}. \quad (6.51)$$

The constants in Eqn. 6.38 are recalculated, leading to an expression of the current as

$$i_L(t) = i_{L,0} \cdot \exp(-\delta t) \left(\cos(\omega_e t) - \frac{C_s u_{s,0} \cdot \omega_0^2 + \delta i_{L,0}}{i_{L,0} \omega_e} \sin(\omega_e t) \right). \quad (6.52)$$

Replacing $i_{L,0} = i_{p,\max}$ from Eqn. 6.49, applying Eqn. 6.45 from the first phase, introducing the phase angle $\varphi = \omega_e t$ and replacing the normalized voltage by b with

$$b = u_{s,0}/u_0 \quad (6.53)$$

results in

$$i_L(t) = i_{L,0} \cdot \exp(-\delta t) \left(\cos \varphi - \frac{2b \cdot q_1 + 1}{\sqrt{4q_2^2 - 1}} \sin \varphi \right), \quad (6.54)$$

where q_2 is the quality factor of the second resonator. All energy has been removed from the inductor when the inductor current equals zero, leading to

$$i_L(\varphi_z) = 0 \Leftrightarrow \tan \varphi_z = \frac{\sqrt{4q_2^2 - 1}}{2bq_1 + 1}. \quad (6.55)$$

As demonstrated in App. D, the angle φ_z is used to calculate the charge ΔQ_s , which is

$$\Delta Q_s = 2 \frac{i_0 \delta}{\omega_0^2} \cdot \left[-bq_1 + \sqrt{q_2^2 + (bq_1)^2 + bq_1} \cdot \exp \left(-\operatorname{atan} \left(\frac{\sqrt{4q_2^2 - 1}}{2b \cdot q_1 + 1} \right) \cdot \sqrt{4q_2^2 - 1}^{-1} \right) \right]. \quad (6.56)$$

The ratio between the energy supplied to the capacitor and the energy stored in the inductor results in the efficiency as

$$\eta_{\text{SECE},2} = \frac{E_C}{E_L} = \frac{(\Delta Q_s + Q_{s,0})^2 - Q_{s,0}^2}{LC_s \cdot i_0^2} \quad (6.57)$$

After replacing ΔQ_s by Eqn. 6.56 and after a series of reformulation steps specified in App. D, the efficiency of the second phase finally results in

$$\eta_{\text{SECE},2} = -\frac{(bq_1)^2}{q_2^2} + \left(1 + \frac{(bq_1)^2}{q_2^2} + \frac{bq_1}{q_2^2} \right) \cdot \exp \left(-2 \operatorname{atan} \left(\frac{\sqrt{4q_2^2 - 1}}{2bq_1 + 1} \right) \cdot \sqrt{4q_2^2 - 1}^{-1} \right) \quad (6.58)$$

Obviously, the efficiency $\eta_{\text{SECE},2}$ is a function of the initial voltage ratio multiplied with the quality factor of the first phase bq_1 and the quality factor of the second phase q_2 . Figure 6.16 illustrates the efficiency $\eta_{\text{SECE},2}$ as a function of the initial condition bq_1 and for different quality factors q_2 .

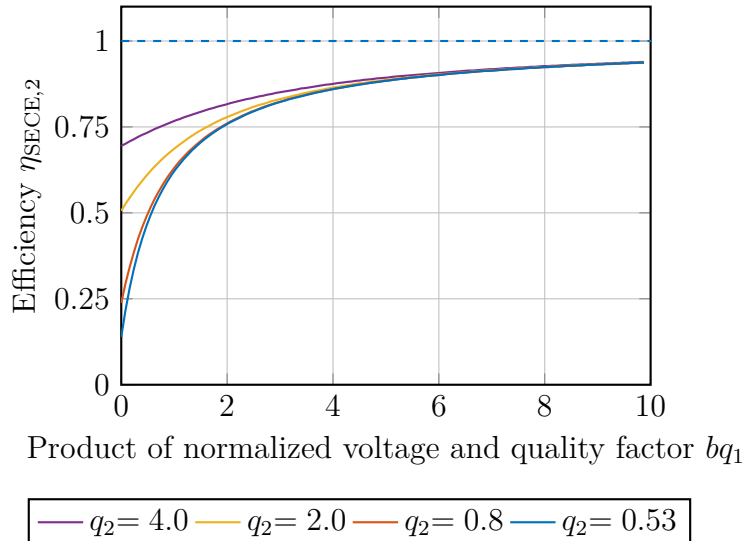


Figure 6.16: SECE efficiency as a function of product of normalized capacitor voltage and quality factor bq_1 , depicted for different quality factors q_2 corresponding to Eqn. 6.58. With increasing quality factor q_2 of the second resonator, higher interface circuit efficiencies can be also obtained for low initial voltages.

In the aperiodic borderline case of the RLC_s oscillator ($q_2 = 0.5$), the efficiency of the SECE is already at 13.5%, when $b = 0$ (discharged storage). With the data for $C_s = 220 \mu\text{F}$ and $C_p \approx 10 \text{ nF}$ from Sec. 2.2.2 and 5.3.1, respectively, and with a commercially available inductor $L = 1 \text{ mH}$ and a parasitic resistance of the inductor $R_L = 4 \Omega$, the quality factors $q_1 = 79$ and $q_2 = 0.53$ are obtained. Since $\eta_{\text{SECE},1}(q_1 = 79) = 0.98$, the total efficiency η_{SECE} with

$$\eta_{\text{SECE}} = \eta_{\text{SECE},1} \cdot \eta_{\text{SECE},2} \quad (6.59)$$

is mainly determined by the second resonator. The efficiency is illustrated for $q_1 = 79$ and $q_2 = 0.53$ in Fig. 6.17. The reason, why the efficiency increases with increasing storage capacitor voltages $u_{s,0}$ is due to the fact, that less time is required to transfer the entire energy from the inductor to a higher charged storage. Consequently, less energy is dissipated across the parasitic resistance R_L and the efficiency increases.

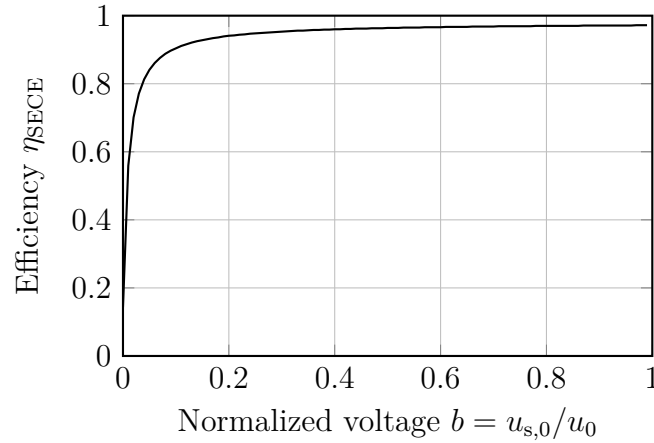


Figure 6.17: SECE - Efficiency η_{SECE} as a function of voltage ratio $b = u_{s,0}/u_0$ for the quality factors $q_1 = 79$ and $q_2 = 0.53$. The efficiency increases with increasing initial normalized voltage b .

As the lossy inductor has the strongest impact on the quality factor q_2 , the latter is investigated, subsequently. The electrical quality factor of the second resonance circuit can be rewritten as

$$q_2 = \frac{1}{R_L} \cdot \sqrt{\frac{L}{C_s}} \quad (6.60)$$

$$q_2 = \frac{\sqrt{L}}{R_L} \cdot \frac{1}{\sqrt{C_s}}, \quad (6.61)$$

and it can be divided into an inductor related part and a capacitor related part. Figure 6.18 illustrates the quotient \sqrt{L}/R_L as a function of inductance L of selected commercially available inductors of one series [157]. Since the quotient \sqrt{L}/R_L decreases with increasing inductance L , it is recommended to use smaller inductors. This outcome is in line with the results obtained in [158]. However, a smaller inductance generates

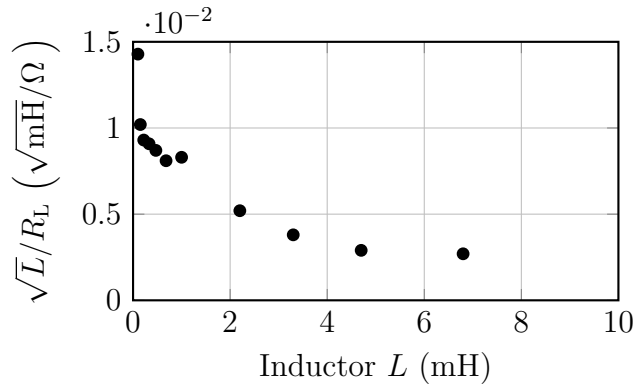


Figure 6.18: Inductor related ratio \sqrt{L}/R_L for different inductors L of a series

higher currents and might lead to an earlier saturation of the magnetic core material. To circumvent the saturation and to increase the efficiency, in [159], a way to improve the energy transfer with reduced losses from the charged piezoelectric capacitor towards the inductor via a multiple shot SECE circuit (MS-SECE) was proposed. Instead of removing the energy stored in the capacitance C_p in only one transfer, the energy is removed in multiple steps (multiple shots). Using this method applied on a 125 mm^3 sized inductor, the authors obtained an efficiency increase of typically 15 %, which can go up to 25 % compared to a normal SECE circuit.

Among the studied circuits, the SECE is supposed to provide the necessary efficiency for the considered energy harvesting problem. While a SEH circuit is easy to implement, even the implementation of a basic SECE is challenging. For minimal losses, integrated circuits with high efficiency of up to 94 % were designed and fabricated [160–162]. The design of such an integrated circuit would go far beyond the scope of this thesis. However, a comparably easy implementation of a SECE with discrete electronic components represents the Electronic Breaker (EB) [163]. It unifies envelope detection, voltage comparison and switching. It was applied to realize both SSHI [164] and SECE [165]. In contrast to the implementation in [165] where a transformer, usually bulky and lossy, was used, a compact fixed choke is better suited for energy harvesting for TPMS and has been used in this work. The modified EB circuit is depicted in Fig. 6.19.

6.6 Numerical Validation

To validate the analytical deduced results, the presented relations were studied numerically. Hereinafter, the simulation software LTspice was used to solve the network equations of the interface circuits SEH, SOR, SSHI and SECE according to Figs. 6.5, 6.8, 6.11 and 6.14, respectively. Schottky diodes (BAT54) and the network parameters, as listed in Tab. 6.1, were chosen for the simulation and run for $t = 300 \text{ s}$. State machines were programmed in LTspice and enabled the correct timing of the switches.

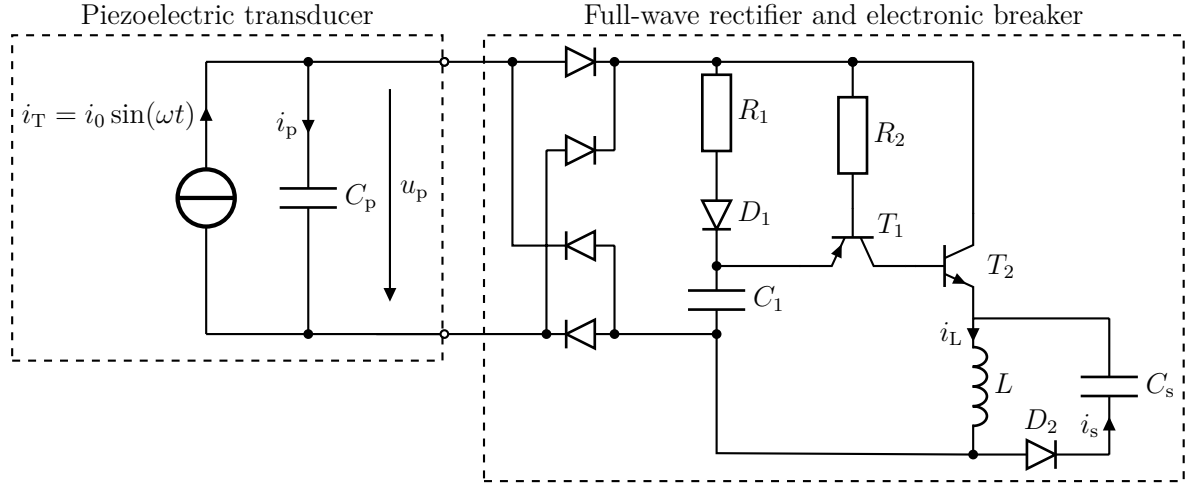


Figure 6.19: Electronic Breaker (EB) circuit as an easy implementation of the SECE principle with discrete electronic components. This circuit is supposed to provide higher efficiencies for energy harvesting for TPMS with piezoelectric transducers compared to the interface circuits SEH, SOR and SSHI.

In the numerical simulation, the capacitor energy

$$E_s = \frac{1}{2} C_s u_s^2 \quad (6.62)$$

was calculated and normalized to the energy E_0 and to the number of half waves n leading to the average efficiency $\bar{\eta}$ as

$$\bar{\eta} = \frac{E_s}{n \cdot E_0} = \frac{\frac{1}{2} C_s u_s^2}{n E_0}. \quad (6.63)$$

This ratio represents the average efficiency to charge a capacitor from 0 V to the voltage u_s . The average efficiency as a function of the normalized voltage $b = u_{s,0}/u_0$ is depicted with

Table 6.1: Parameters of the simplified electromechanical network of Fig. 6.1

Current source amplitude	i_0	100	μA
Excitation frequency	f_0	50	Hz
Piezoelectric capacitance	C_p	10	nF
Storage capacitance	C_s	220	μF
Inductor inductance	L	1	mH
Inductor resistance	R	4	Ω
Open source voltage (Eqn. 6.5)	u_0	63.7	V
Quality factor 1	q_1	79	
Quality factor 2	q_2	0.79	

solid lines in Fig. 6.20. It is opposed to the analytical results of the average efficiency (dashed lines), deduced in App. C. Both analytical and numerical results are in very good accordance. The variations from the analytical average efficiency of the SECE in Fig. 6.20 are related to the energy dissipation across the Schottky diodes. Especially

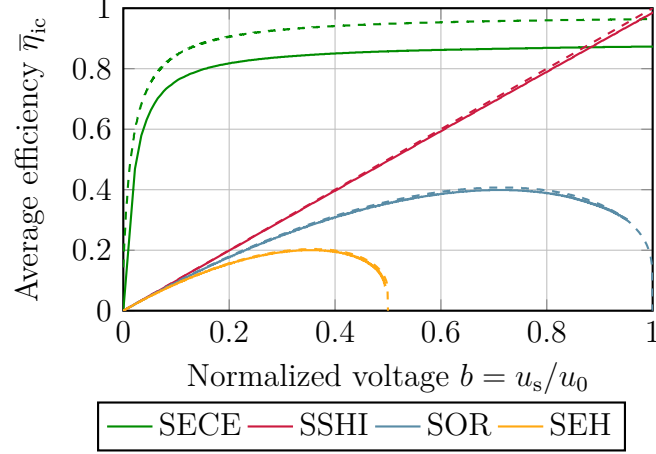


Figure 6.20: Interface circuit efficiency deduced from LTspice simulation with diode forward losses (solid lines) and from analytical results (dashed lines) of the average efficiency for the four basic interface circuits as a function of normalized output voltage. The quality factors of the SECE circuit were $q_1 = 79$ and $q_2 = 0.53$. Visibly, the SECE has the highest average efficiency. The SECE is able to charge the storage capacitor C_s to a desired voltage in the shortest amount of time.

when the energy is removed from C_p to L , a residual charge of $Q = C_p \cdot 2u_d$ remains on the piezoelectric capacitance, where u_d is the diode forward voltage. The residual charge needs to be removed within the next half wave.

Despite of diode forward losses, the numerical results confirm, that the SECE circuit should be used in combination with piezoelectric strain based energy harvesters to charge a storage capacitor. In addition, at small normalized voltage $u_{s,0}/u_0$, the interface circuits SEH, SOR and SSHI transfer energy with the similar low efficiency.

6.7 Summary

Piezoelectric Interface Circuits

Four basic interface circuits for transferring the electrical energy of the piezoelectric energy harvester to the storage capacitor have been presented. Among them, SEH, SOR, and SSHI exhibit a strong dependence on the voltage of the storage capacitor. This voltage is typically in a range of $0\text{ V} < u_s < 3.9\text{ V}$. Thus, it is much smaller than the maximum open circuit voltage of a piezoelectric device $u_0 \approx 50\text{ V}$. The corresponding voltage ratio is $b \leq 0.08$. Consequently, the SEH, SOR, and SSHI circuits would supply approximately the same energy to the capacitor, although SSHI and SOR are the successive improvement of SEH. Unlike them, the SECE interface circuit transfers energy from the electrical terminals to the storage capacitor more efficiently. This result is in contrast to the results published in [148], where it was claimed that the SECE efficiency was between that of an SEH and an SSHI. A summary of the efficiency and the average efficiency of the four circuits is visualized in Figs. 6.21a and 6.21b, respectively. Due to the superior efficiency at small voltage ratios b , the SECE circuit is well adapted for piezoelectric energy harvesting in TPMS.

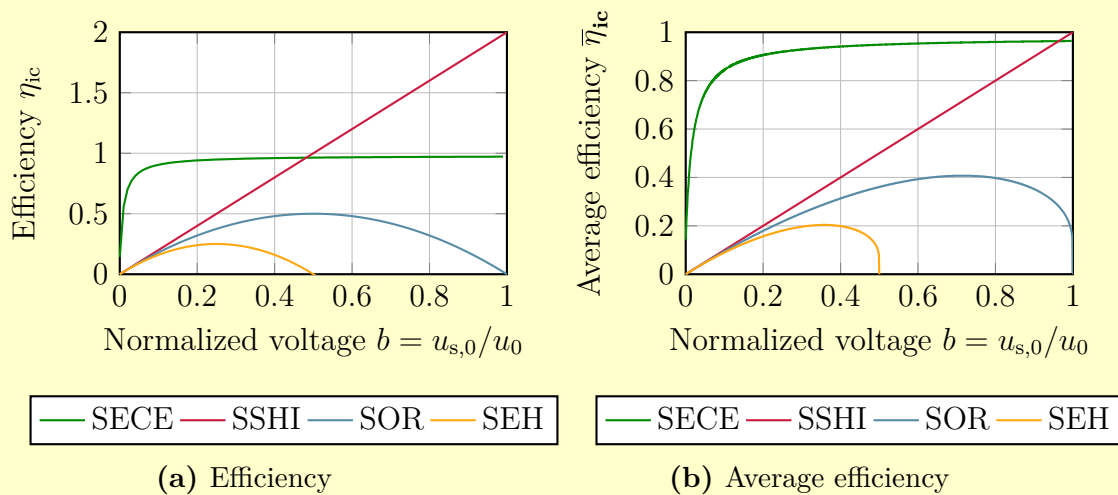


Figure 6.21: Analytical results: normalized efficiency of four basic piezoelectric interface circuits as a function of normalized voltage $b = u_{s,0}/u_0$. The efficiency of the SECE is plotted for the quality factors $q_1 = 79$ and $q_2 = 0.53$.

7 Electromagnetic Energy Harvesting

Among the previously analyzed systems of the literature in Chapter 4, only one centrifugal acceleration based energy harvester was presented that relied on electromagnetism [101–103]. Although the inventors studied the power output by means of a Matlab/Simulink model at different velocities and investigated multiple magnet and coil constellations, only voltage measurements on a shaker were presented to validate their simulations at 40 km/h and 60 km/h. The related open-circuit voltage amplitudes were 0.4 V and 1.5 V, respectively, and seem to be too low to charge a capacitor to 3.9 V. Therefore, the system parameters will be adapted in this section in order to provide a higher output voltage. In addition, an appropriate interface circuit, rather than a simple full-wave rectifier can be used to further up-convert the output voltage and to increase the efficiency to charge the storage, and is part of the next chapter.

The electromagnetic system from [101–103] is the foundation of the electromagnetic system to be designed, developed and tested in this chapter. In contrast to the former work, the design goal is that the energy harvester provides sufficient energy for TPMSs at velocities of 25 km/h and above. In distinction to the Matlab-Simulink modeling approach of the inventors, this chapter builds on the description as an electromechanical network. First, the common description of a linear electrodynamic transducer is presented. To describe the system to be studied, the transition to a nonlinear network model is necessary. Then, based on the required energy and with the help of FEM, the system components are selected. Experimentally determined parameters are used to fit the nonlinear equivalent circuit with data and to simulate the dynamic behavior in the network simulator LTspice. The final system characterization inside the tire will follow in Sec. 9.4. Parts of this chapter were published in [75].

The basic transducer has already been described in Sec. 4.2. The system consists of a permanent magnet which freely moves inside a cylindrical tube. At the bottom, which is considered as the part of the system directly attached to the tire, a fixed magnet is placed with an opposite magnetic field according to the movable magnet. The opposite orientation of the fixed and of the movable magnet creates a repulsive force and leads to a levitation of the movable magnet. The centrifugal force, caused by the rotating wheel, determines the point of equilibrium. A coil wound around the vertical center of the tube generates a voltage, when the magnetic field changes. Two elastic bumpers, one at each tube end are used to avoid hard impacts between housing and magnet. The entire system

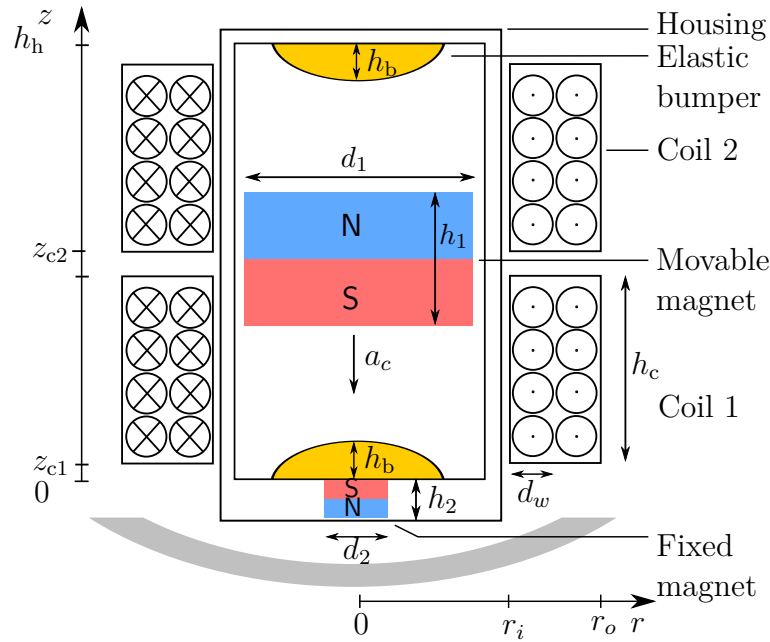


Figure 7.1: Schematic of the considered electromagnetic energy harvester

is depicted in Fig. 7.1. It is located at the tire inner liner in order to absorb the energy of the impulses while entering and leaving the area of ground contact.

7.1 Linear Electromagnetic System Description

Similar to piezoelectric systems, electromagnetic energy transducers can be described with lumped elements by coupled differential equations [74]

$$m\dot{v} + cv + \frac{1}{n_{oc}} \int v dt + \beta i = ma_{ex} \quad (7.1)$$

$$u = \beta v - R_c i - L_c \frac{di}{dt}, \quad (7.2)$$

where m , c , n_{oc} , v , β , L_c , R_c , u_T , i , a_{ex} are mass, damping coefficient, compliance at electrical open-circuit condition, velocity, electromagnetic transducer coefficient, coil inductance, coil resistance, transducer voltage, current and the acceleration of the excitation, respectively. The linear equivalent network representation is shown in Fig. 7.2.

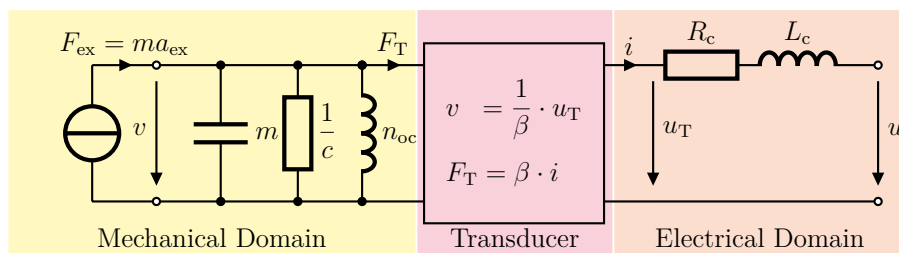


Figure 7.2: Equivalent circuit of a linear electromagnetic energy harvester

While mainly the two components beam and mass of a piezoelectric energy harvester constitute all lumped parameters (see Tab. 5.1), electromagnetic energy harvesters possess more than two degree of freedom (DOF) and enable a more independent system design. Table 7.1 assigns the lumped elements of Eqns. 7.1 and 7.2 to the system components. The magnets can be varied in material, magnetization (grade), diameter and height. The coil properties are determined by the number of turns, the wire diameter, number of coils, their arrangement and their sense of winding.

Table 7.1: Electromagnetic component assignment

Lumped element	Assigned system components
m	movable magnet volume
c	housing material, air gap
n_{oc}	movable magnet, fixed magnet
β	movable magnet, coil
R	coil
L	coil

The total magnetic field of both magnets and the coil determine the transducer coefficient β . As demonstrated in [75], the transducer coefficient can be deduced both from Faraday's law and from the Lorentz force. The vectorial Lorentz force \vec{F}_1 describes the electromagnetic feedback by

$$\vec{F}_1 = q \cdot \vec{v} \times \vec{B} = i \cdot (\vec{l} \times \vec{B}), \quad (7.3)$$

where q , i , \vec{B} and \vec{l} are the charge and current through the wire, the magnetic flux density and the directional wire length, respectively. Assuming a cylindrical wire, then the directional length \vec{l} , which determines the direction of current, is

$$\vec{l} = l \cdot \vec{e}_\varphi, \quad (7.4)$$

Then, the Lorentz force is rewritten in cylindric coordinates to

$$\vec{F}_1 = i \cdot l \cdot \vec{e}_\varphi \times (B_r \cdot \vec{e}_r + B_\varphi \cdot \vec{e}_\varphi + B_z \cdot \vec{e}_z) \quad (7.5)$$

$$\vec{F}_1 = -i \cdot l \cdot B_r \cdot \vec{e}_z + i \cdot l \cdot B_z \cdot \vec{e}_r, \quad (7.6)$$

where \vec{e}_φ , \vec{e}_r , \vec{e}_z are the unit vectors of the cylindrical coordinate system and B_φ , B_r , B_z are the corresponding magnetic flux components. Due to axis-symmetry, the component \vec{e}_r vanishes and the Lorentz force acts only in the z-direction. Then the vectorial description is replaced by the scalar description

$$F_1 = -i \cdot l \cdot B_r. \quad (7.7)$$

Comparing the coefficients of the transducer force in Fig. 7.2 with Eqn. 7.7, the transducer coefficient can be expressed by

$$\beta = -l \cdot B_r. \quad (7.8)$$

Apparently only the radial component of the magnetic flux contributes to the transducer coefficient.

The transducer coefficient is generally a nonlinear function of the position of the movable magnet z and expressed by $\beta = \beta(z)$. If not only one but many cylindrical wires form the coil, then each individual turn contributes to the electromagnetic transducer coefficient as shown in Fig. 7.3. It is the summed product of wire length $l(r)$ and position dependent radial magnetic flux $B_r(r, z)$

$$\beta(z = z_m) = \sum_{j=1}^p \sum_{k=1}^q l \left(r_i + j \cdot \frac{d_w}{2} \right) \cdot B_r \left(r_i + j \cdot \frac{d_w}{2}, z_0 + k \cdot \frac{d_w}{2} \right), \quad (7.9)$$

where p, q are the number of wire turns in r -direction and z -direction, respectively. The radius r_i and the position z_0 describe the position of closest coil layer and of the lowest coil layer, respectively. Since the circumference of each winding is only a function of radial position with $l = 2\pi r$, the transducer coefficient can be rewritten to

$$\beta(z = z_m) = 2\pi \cdot \sum_{j=1}^p \left(r_i + j \cdot \frac{d_w}{2} \right) \cdot \sum_{k=1}^q B_r \left(r_i + j \cdot \frac{d_w}{2}, z_0 + k \cdot \frac{d_w}{2} \right), \quad (7.10)$$

More details about the calculation of the transducer coefficient can be found in [75, 166].

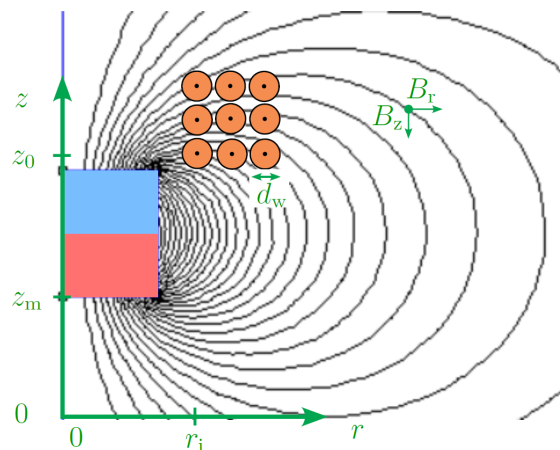


Figure 7.3: Magnetic flux lines of the movable magnet at the position $z = z_m$. Each winding with the circumference $l(r)$ experiences a radial magnetic flux component B_r and contributes to the electromagnetic transducer coefficient $\beta(z)$.

7.2 Nonlinear Electromagnetic System Description

To describe large displacements of the movable magnet, both the compliance and the transducer coefficient are nonlinear and position dependent. To incorporate these nonlinearities, a nonlinear electromechanical network is presented in Fig. 7.4. Polynomial functions are used to approximate both parameters and reduce numerical complexity while calculating the numerical solutions. The restoring force of the compliance is composed of a repulsive magnetic force over the entire range $0 < z < z_{\max}$ and a restoring bumper force at both end positions. Therefore, three position dependent force sources F_{bot} , F_{top} , F_{mag} replace the compliant network relation $F_n = z/n_{\text{oc}}$ by $F_n = F_{\text{bot}} + F_{\text{top}} + F_{\text{mag}}$ with

$$F_{\text{bot}} = f_1(z) \quad \text{for } 0 < z < z_{\text{bot}} \quad (7.11)$$

$$F_{\text{top}} = -f_2(z_{\max} - z_{\text{top}}) \quad \text{for } z_{\max} - z_{\text{top}} < z < z_{\max} \quad (7.12)$$

$$F_{\text{mag}} = f_3(z) \quad \text{for } 0 < z < z_{\max}, \quad (7.13)$$

where $f_1(z)$, $f_2(z)$ and $f_3(z)$ are polynomial approximation functions, which will be characterized in Sec. 7.5 and where z_{bot} and z_{top} stand for the position of the bottom and top bumper, respectively. A controlled source to calculate the z -position completes the equivalent network, adds the time integral of the velocity to the initial position $z_0 = z(t = 0)$ and is used to calculate the actual position $z = z(t)$ in every single iteration step.

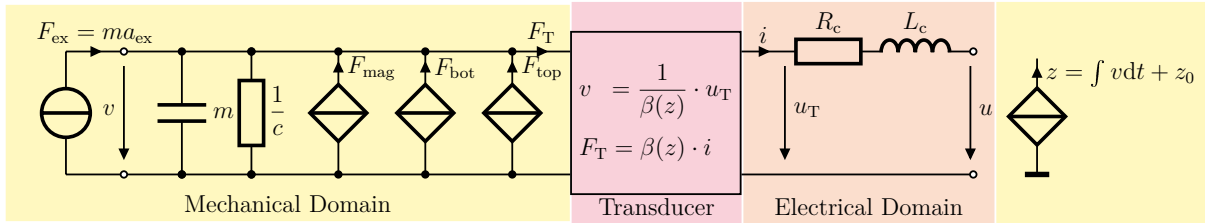


Figure 7.4: Equivalent circuit for the nonlinear electromagnetic energy harvester of Fig. 7.1 with the nonlinear electromagnetic transducer coefficient $\beta(z)$. The behavioral sources F_{mag} , F_{bot} , F_{top} represent the non-linear distance-force relations between two repulsive magnets, between movable magnet and bottom bumper, and between movable magnet and top bumper.

7.3 Preliminary Energy Considerations

The DOFs in the system design allow manifold combinations between differently sized magnets with various magnetization and diverse coil setups. From an energy point of view, the main objective is to harvest more than $E_{\text{rev,charged}} = 7.9 \mu\text{J}/\text{rev}$. Based on the desired electrical energy output, the amount of mechanical energy, which has to enter the system, can be derived. Referring to the definition stated in Fig. 1.3, the efficiency $\eta_{\text{ic}} = \Delta E_{\text{stored}}/E_{\text{elec}}$ is used to describe the interface circuit and characterizes the energy

transfer from the electrical domain to the load. Since full-wave rectifier (FWR) can reach high efficiencies, but decrease the output voltage [167], Germer et al. [168] studied the energy transfer of a boost energizing and transferring circuit and stated average efficiency of 60 % with lossy Schottky diodes. While at this stage of the work the interface circuit has not been discussed yet, and as the signal waveform is not harmonic, a more modest average interface circuit efficiency of $\eta_{ic} = 30\%$ is supposed. Further, a mechanical-to-electric efficiency of indeed $\eta_{eh} = 10\%$ is assumed and considers magnetic stray losses and mechanical damping, leading to an overall efficiency of $\eta_{tot} = 3\%$, which is in good accordance with the results of the survey study on the efficiency of energy harvesters from Blad et al. [169]. With the assumption that only 3 % of the incoming mechanical energy can be used, the system parameters are derived.

Supposing a linear restoring force F , the mechanical energy is

$$E_{\text{mech}} = \frac{1}{2}F\Delta z \quad (7.14)$$

where $F = \hat{F}_{\text{ex}}$ with

$$\hat{F}_{\text{ex}} = 1.3 \cdot \frac{mv^2}{R} \cdot \frac{\Delta}{z_0}. \quad (7.15)$$

Replacing E_{mech} and F in Eqn. 7.14 by the total efficiency $\eta_{\text{tot}} = \Delta E_{\text{stored}}/E_{\text{mech}}$ and by Eqn. 7.15, respectively, and rearranging Eqn. 7.14 to the mass m results in

$$m = \frac{\Delta E_{\text{stored}}}{\eta_{\text{tot}}} \cdot \frac{2R \cdot z_0}{1.3 \cdot \Delta z^2 \cdot v^2}. \quad (7.16)$$

The condition that the stored energy ΔE_{stored} needs to be larger than $E_{\text{rev,charged}} = 7.9 \mu\text{J}$ at $v = 25 \text{ km/h}$ forms the lower energy bound and determines the minimal mass of the movable magnet. For $\Delta z = 4 \text{ mm}$, $z_0 = 4 \text{ mm}$, the mass is

$$m \geq 0.65 \text{ g}. \quad (7.17)$$

Consequently, a magnet with a diameter $d = 6 \text{ mm}$, a height $h = 4 \text{ mm}$ and a mass $m = 0.85 \text{ g}$ has been selected.

As mentioned, a fixed magnet at the bottom of the energy harvester forms a nonlinear contactless magneto-mechanical spring with the movable magnet. Considering a housing of limited height as depicted in Fig. 7.5, a too strong magnetic force and spring would press the movable magnet against the top bumper (Fig. 7.5a) and would lead to significant displacements only at high centrifugal forces, evoked at high velocities. If the spring is too weak, the movable magnet is already pressed against the bottom at low velocities (Fig. 7.5c). The spring can absorb less mechanical energy and provides less electrical energy. In addition, more frequent and stronger impacts between the movable magnet and the bottom bumper appear, and might lead to an increased abrasion. Therefore, a

fixed magnet is necessary, which keeps the movable magnet in the center (Fig. 7.5b) at the minimal operating velocity of 25 km/h. As it will be shown in the next subsection, the transducer coefficient is maximal at the center, which leads to a higher generated energy at the center.

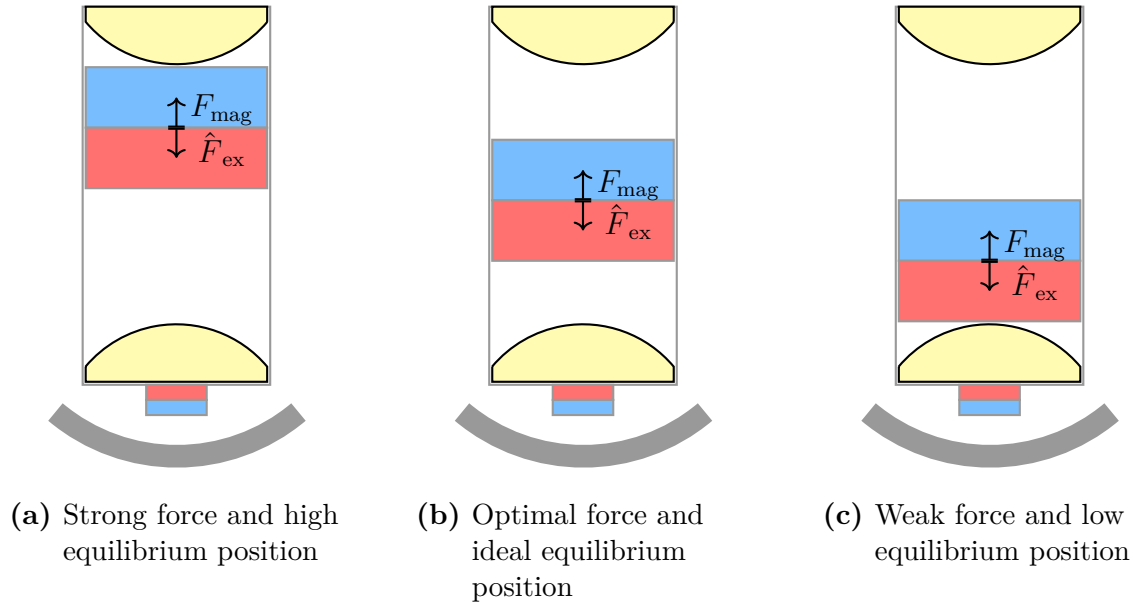


Figure 7.5: Different repulsive magnetic forces and corresponding equilibrium positions

The relation between repulsive force F_{mag} and distance z will be used to indicate which fixed magnet is suitable to align the movable magnet in the center of the housing at 25 km/h. Finite Element Modeling has been used to determine this relation, as well as to calculate the electromagnetic transducer coefficient. The modeling process is explained subsequently.

7.4 Numerically Parameter Determination

7.4.1 Finite Element Analysis of the Magnetic Field

Magnetostatic equations are used to compute the magnetic flux density of a permanent magnet. Generally in finite element (FE) modelling, the definition area Ω is defined with the boundary conditions at the border $\partial\Omega$. As only components of the magnetic flux density \vec{B} outside the permanent magnet contribute to the desired network parameters, the FE model has to replicate the stray field in the infinite air space. The analyzed setup is modeled as an open boundary problem and approximated with the Robin boundary condition [170], which is a weighted combination of Dirichlet boundary conditions and Neumann boundary conditions. The complexity and the number of elements of the three-dimensional problem can be reduced, taking into consideration the axisymmetric structure. The software FEMM was selected to create a mesh of the axisymmetric area Ω and to solve differential magnetostatic equations using cylindrical coordinates. A *lua*

script was written to automatically calculate the position-dependent magneto-mechanical force and the position-dependent transducer coefficient. Figure 7.6 depicts both – mesh and the absolute values of the magnetic flux density \vec{B} at 5 mm distance between a fixed magnet and a movable magnet.

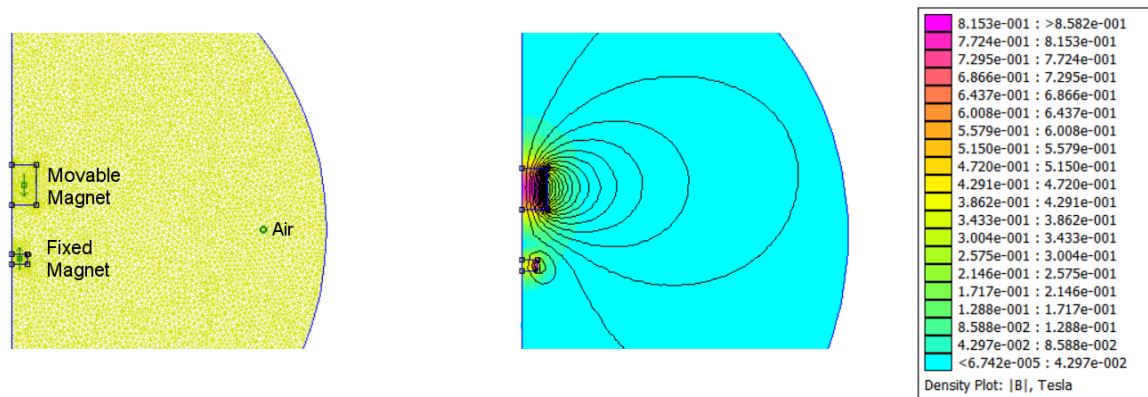


Figure 7.6: Mesh and magnetostatic FE simulation of two magnets separated by 5 mm

To determine the relevant network parameters, the most obvious way is to vary the distance z of the top magnet to the bottom magnet and to deduce $\beta(z)$ and $F_{\text{mag}}(z)$ as illustrated in Fig.7.7a. Each variation of z changes the loads in the FE model and requires a new mesh and a new simulation of the magnetic flux density \vec{B} and the magnetic field \vec{H} . An alternative way and more efficient way is depicted in Fig. 7.7b and consists in separately calculating the magnetic flux densities of both magnets \vec{B}_1 and \vec{B}_2 in the infinite air space. The magnetic quantities are extracted and each assigned to an equidistant orthogonal mesh in which the permanent magnet is at the coordinate origin. Then, both magnetic fields are superposed with varying distances z . Since this method only requires one FE-mesh and runs only one FE simulation for each magnet, it significantly reduces the simulation time to determine $\beta(z)$. It also allows one to change the coil position, the number of coils and the number of turns easily after the FE analysis as a post-processing treatment, which would otherwise require new FE simulations.

In theory, the magnetic force \vec{F}_{mag} is defined as the volume integral of the divergence of Maxwell's stress tensor, T , which can be rewritten by Gauss's law to a surface integral over a closed surface

$$\vec{F}_{\text{mag}} = \iiint \nabla \cdot T dV = \oint T \partial V. \quad (7.18)$$

As demonstrated in [171], the accuracy of numerical computation with finite elements strongly depends on the order of elements and the selected path. The developer of the software FEMM, Meeker [170], recommended calculating a weighted stress tensor volume integral, because numerical problems arise using the stress tensor surface integral over

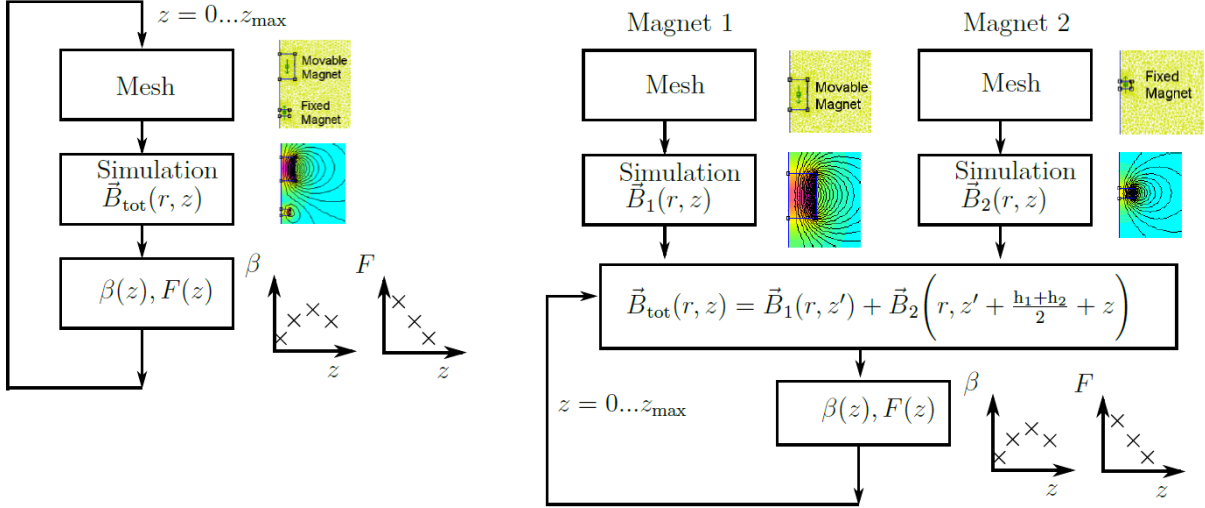


Figure 7.7: Magnetostatic parameter calculation with FEM. A common method (a) is to vary the distance z of the two magnets. Each distance requires the creation of a mesh, the calculation of the magnetic field and of the parameters β and F . More efficient (b) is to create a mesh and to calculate the magnetic field of each magnet separately and only once. By superimposing the magnetic fields at various distances, the total magnetic field is calculated and the parameters β and F are deduced much faster.

a closed surface, indiscriminately. The result is especially erroneous if the integration path is along an interface between two materials with different permeabilities. As the integral is path independent, the integration path should be a few elements away from the volume of interest, inside a volume of constant permeability. Considering this remark, the magnetic force was determined numerically for different distances with the same method as described beforehand, and compared with experimental measurements in the subsequent section.

Permanent magnets are available in different grades. They are characterized by a letter, representing the material type, e.g. N for neodymium, Y for ferrite, and a number corresponding to the maximum energy product $(B \cdot H)_{\max}$ in Mega Gauss \cdot Oersted (MGOe) and indicating the magnetic strength. For the determined geometry of the movable magnet ($d = 6$ mm, $h = 4$ mm), the strongest easily commercially available magnet was N45. As only a small selection of available permanent magnets are available in the library of the software FEMM, the grade is used to calculate the coercivity H_c with

$$\begin{aligned}
 H_c &= 2\sqrt{\frac{(B \cdot H)_{\max}}{\mu_r \mu_0}} \\
 &= 2\sqrt{\frac{10^2 \cdot B/\text{MG} \cdot 79.57 H/\text{Oe}}{\mu_r \mu_0}} \\
 &= 159155 \cdot \sqrt{\frac{\text{grade}/\text{MGOe}}{\mu_r}} \frac{\text{A}}{\text{m}},
 \end{aligned} \tag{7.19}$$

where μ_r is the relative permeability of the permanent magnet [78]. It is worthwhile noticing that in practice the coercivity H_c of a neodymium magnet with grade N48 or higher might be smaller than the coercivity of a N45 magnet, which makes linear modeling difficult [78]. Consequently, Eqn. 7.19 is only a coarse estimation. Furthermore, manufacturers classify the energy product within an interval of 2 or 3 MGOe. To reduce variations between experimental measurements and ideal simulations, the grade was reduced by 3 MGOe. To get the coercivity, which is fed to the FEM simulation, it is inserted in Eqn. 7.19 as

$$\text{grade}_{\text{sim}} = \text{grade}_{\text{datasheet}} - 3 \text{ MGOe}. \quad (7.20)$$

According to Eqn. 7.9, the transducer coefficient depends on the radial component B_r of the magnetic flux density \vec{B} of the movable permanent magnet. Therefore, the radial magnetic flux density component B_r was numerically calculated for the movable magnet centered in the cylindrical coordinate system, which is depicted in Fig. 7.8. The radial magnetic flux density is plotted both as a function of the coordinates r and z in Fig. 7.9.

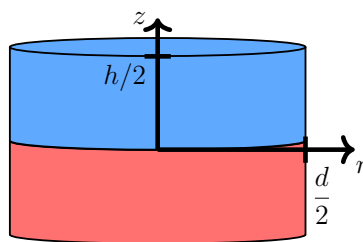


Figure 7.8: Movable magnet centered in cylindrical coordinate system

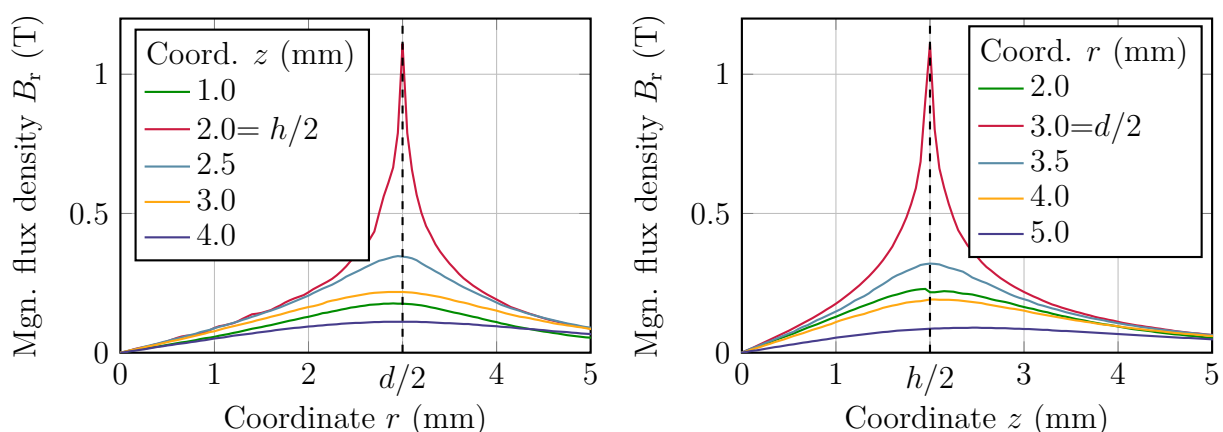


Figure 7.9: Radial magnet flux density B_r as a function of position z and radius r of the moving magnet (N45) in central position with respect to Fig. 7.8. The maximal radial magnetic field B_r is obtained at $(r, z) = (d/2, h/2) = (3 \text{ mm}, 2 \text{ mm})$ at the top edge of the cylindrical magnet.

In both figures, the radial magnetic flux increases from 0 to $z = h/2$ and $r = d/2$, when the entire volume of the permanent magnet is covered. Then, the radial magnetic flux decreases rapidly with increasing distance from the permanent magnet. The rapid decrease has a strong impact on the coil design. The closer a coil is wound with respect to the movable magnet, the higher the radial magnetic flux density is, experienced by a coil turn and the higher the overall transducer coefficient $\beta(z)$ is, according to Eqn. 7.10.

Based on both the superposition of the radial components B_r of the two permanent magnets and the relative movement to each other, the induced voltage inside the coils $u(z) = \beta(z) \cdot v(z)$ is calculated. Since electromagnetic energy harvesters typically induce small voltages, the design objective is to raise the voltage.

7.4.2 Coil Setup and Electromagnetic Transducer Coefficient

Different coil constellations and coil connections with the same and opposite sense of winding, as illustrated in Fig. 7.10, were numerically studied based on the FE simulation results. The starting point built on two coils each with 4 mm height and with the geometry data, listed in Tab. 7.2.

Wire diameter	d_w	0.1 mm
Coil height	h_c	4.0 mm
Housing height	h_{\max}	8.0 mm
Inner coil radius	r_i	3.5 mm
Outer coil radius	r_o	4.5 mm
z -position Coil 1	z_{c1}	0.0 mm
z -position Coil 2	z_{c2}	4.0 mm

Table 7.2: Coil data corresponding to the simulation of Fig. 7.11

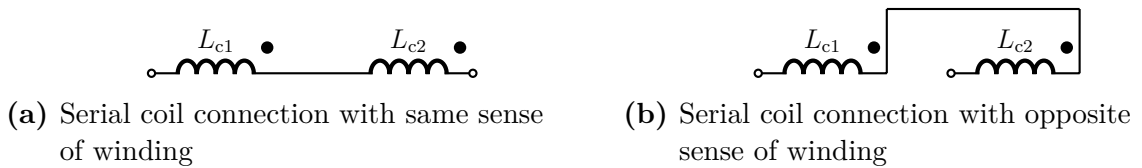


Figure 7.10: Serial coil connections with same and opposite sense of winding

The coil height coincides with the height of the magnet. The inner coil radius $r_i = 3.5$ mm is slightly larger than the radius of the movable magnet $d/2 = 3$ mm and incorporates a thickness of 0.5 mm of the coil support. A wire diameter of $d_w = 0.1$ mm leads for the listed coil geometry to 400 windings per coil.

The transducer coefficients are depicted in Fig. 7.11 for the two different series coil connection, corresponding to Fig. 7.10. Below, the position of the magnet with respect to the two coils is illustrated. When the coils are connected with the same sense of winding, the transducer coefficient vanishes at the centered position ($z = 2$ mm) of the 4 mm long magnet and is minimal/maximal at $z = -2$ mm/ $z = 2$ mm, when the magnet

is just outside the coil. Contrary, when the coils are connected with the opposite sense of winding, the transducer coefficient is maximal at the centered position.

As the velocity $v(z)$ of the movable magnet is zero at the limit stops and maximal in between, the induced voltage $u(z) = |\beta(z) \cdot v(z)|$ would be negligible at the borders (at $z = 0$ mm and at $z = 4$ mm). In contrast the velocity is maximal in the center. If the magnitude of the transducer coefficient is maximal in the center, a relatively high voltage magnitude $u(z) = |\beta(z) \cdot v(z)|$ is obtained. Consequently, the coil connection with opposite sense of winding leads to a higher output voltage and is considered as most suitable for harvesting energy in the tire.

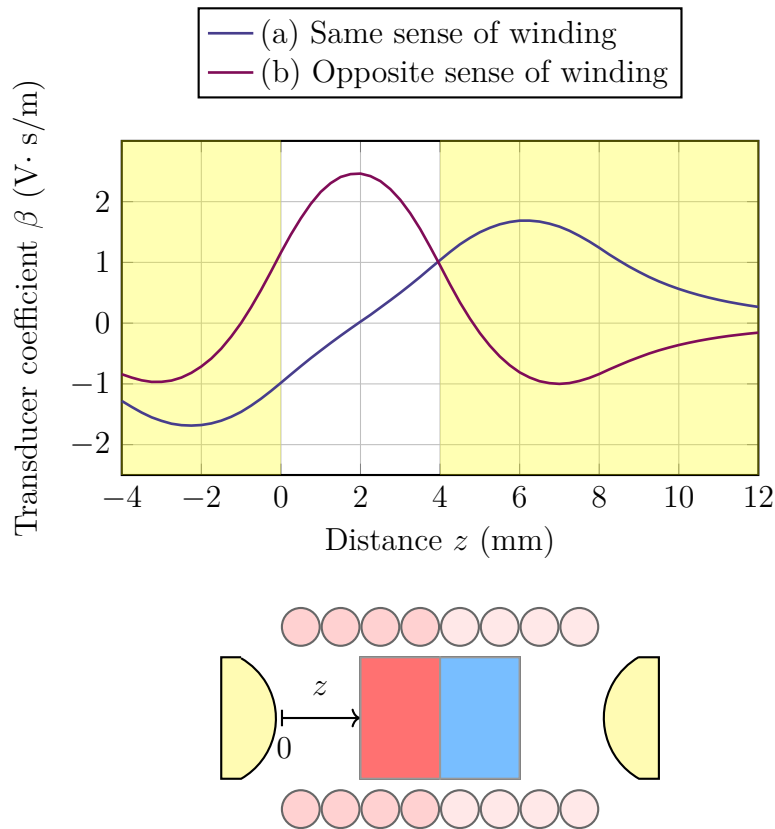


Figure 7.11: Simulated transducer coefficient as a function of distance z between the movable magnet and coil when the coils are connected in series (a) with the same sense of winding and (b) with the opposite sense of winding. The positions z represents the distance of the bottom part of the movable magnet from the coordinate origin.

FE modeling is also used to simulate the repulsive force for different constellations of fixed magnet and movable magnet, and to select a suitable fixed magnet. While in theory a housing of 8 mm is sufficient, in which the 4 mm high magnet has a range of 4 mm in which it can freely move, a larger housing is required. The reason relies on the volume of the bumpers at both tube ends and the spacers for coil winding reasons, as presented in Fig. 7.1.

Consequently, a modified housing setup is studied with 0.8 mm thick spacers between the coils. To raise the transducer coefficient, a smaller wire diameter of $d_w = 0.071$ mm is

considered and provides a transducer coefficient twice as high compared to the previously studied coils with $d_w = 0.1$ mm, while the resistance is at least four times higher, supposing that in both cases the copper volume remains constant. The final parameters are listed in Tab. 7.3. The transducer coefficients are calculated again for the modified setup which is presented in Fig. 7.12.

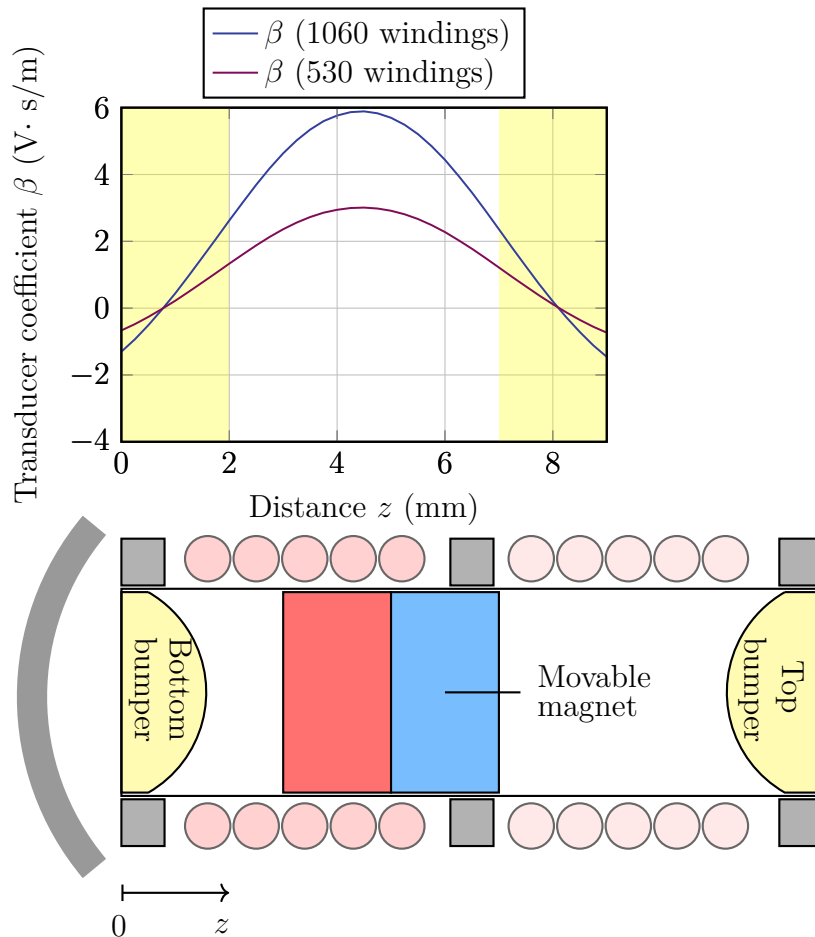


Figure 7.12: Position dependent transducer coefficient - simulation for two different wire diameters and the same copper volume, resulting in two different number of turns of each coil. The coils are connected in series with opposite winding sense according to Fig. 7.10b and with the geometry data listed in Tab. 7.3

7.4.3 Repulsive Magnetic Force and Fixed Magnet

To calculate the repulsive magnetic force, Maxwell's stress tensor of Eqn. 7.18 is used in the FE simulations. It is depicted for different fixed magnet geometries on a semi-logarithmic scale in Fig. 7.13 and opposed to the maximal force of excitation \hat{F}_{ex} at 25 km/h, 50 km/h and 70 km/h. The notation D3H1 means that diameter and height of the magnet are 3 mm and 1 mm, respectively. The yellow colored blocks in the diagram indicate the position of the elastic bumpers.

Table 7.3: Prototyping coil data for two setups with different wire diameters.

Wire diameter	d_{w1}	0.100	mm	Wire diameter	d_{w2}	0.071	mm
Turns per coil	N	530		Turns per coil	N	1060	
Coil height	h_c	5.3	mm	Coil height	h_c	5.3	mm
Housing height	h_h	13	mm	Housing height	h_h	13	mm
Inner coil radius	r_i	3.75	mm	Inner coil radius	r_i	3.75	mm
Outer coil radius	r_o	4.75	mm	Outer coil radius	r_o	4.75	mm
z -position Coil 1	z_{c1}	0.8	mm	z -position Coil 2	z_{c2}	6.9	mm
Total resistance	R_c	62	Ω	Total resistance	R_c	262	Ω
Total inductance	L_c	3.2	mH	Total inductance	L_c	13	mH

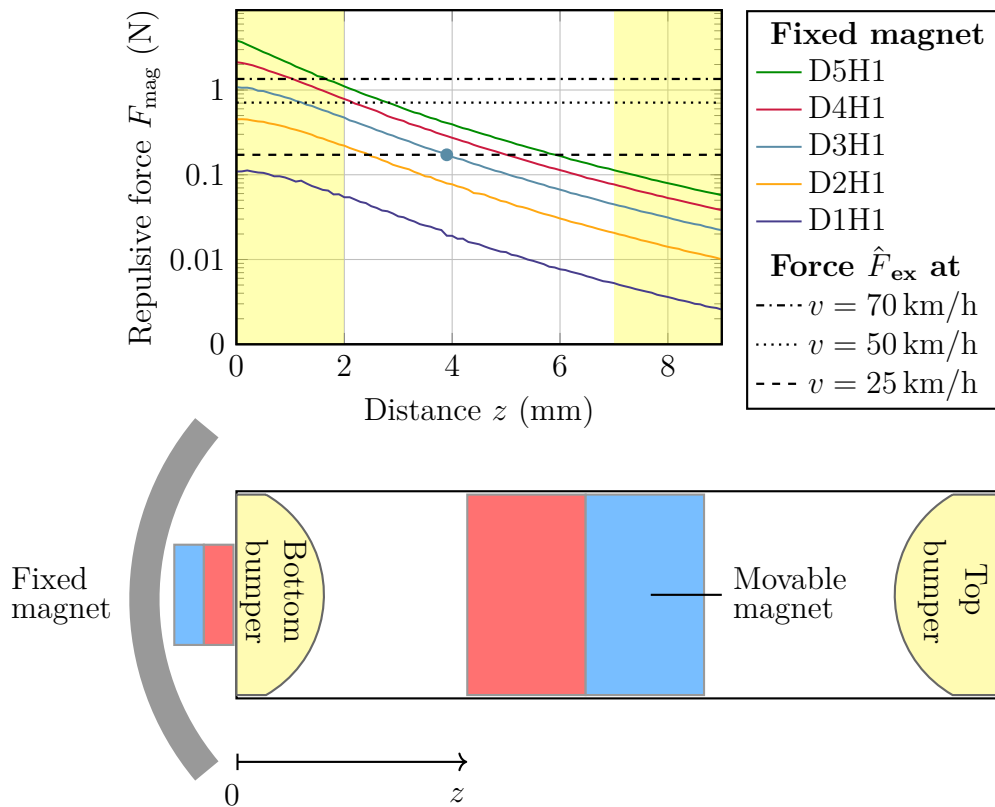


Figure 7.13: Simulated repulsive force (semi-logarithmic plot) for a N45D6H4 movable neodymium magnet and different sized fixed N48 neodymium magnets (colored lines) and maximal excitation force at 25 km/h, 50 km/h and 70 km/h (dashed, dotted, dash-dotted). At the velocity of 25 km/h, the fixed magnet D3H1 keeps the movable magnet mostly in the center between the bumpers.

The larger the magnet, the higher the repulsive force is and the more mechanical energy can be stored in the magneto-mechanical compliance but the further away the point of equilibrium is and the less the movable magnet will be deflected and the smaller the velocity of the moving magnet is, especially at vehicle speeds of 25 km/h. Referring to Fig. 7.13, magnet D1H1 is already pressed against the bottom bumper at 25 km/h, while D2H1 is close to it. Contrary, D4H1 and D5H1 cause a smaller deflection of the movable

magnet. The magnet D3H1 evokes the movable magnet to be centered in the housing at 25 km/h and seems to be a good tradeoff between deflection at 25 km/h on the one hand and contactless prestress at higher velocities on the other hand. Although the magnetic field of the fixed magnet superposes with the one of the movable magnet, the transducer coefficients remain mostly unaffected.

7.5 Experimental Parameters

7.5.1 Electromagnetic Energy Harvester Prototypes

Four prototypes, two each with 0.1 mm and 0.071 mm wire diameter windings, were manufactured. PTFE was chosen as coil support material as well as housing material due to its very low friction coefficient. Additionally, the inner cylindrical coil support was designed with a wall thickness of only 0.7 mm to enable close wire turns and to provide a high transducer coefficient. Similarly, the clearance between movable magnet and coil support was designed to be small and is in the range of 10 μm . However, when the energy harvester is encapsulated for testing as shown in Fig. 7.14b, it constitutes a fluidic system with two air chambers, separated by the movable magnet which acts as a piston. As described in [102], a low clearance leads to a high fluidic damping. To reduce this damping effect, four 0.4 mm deep and 1 mm wide air channels were milled in the inner of the cylindrical coil support and are depicted in Fig. 7.14a.

The encapsulation of the coil and magnets is designed, such that the prototype fits easily in the already existing rubber container, provided by Continental. Therefore, the encapsulation of the prototypes, presented in Fig. 7.14b, has a form of a top hat to fit in the TPMS container, shown in Fig. 7.14c.

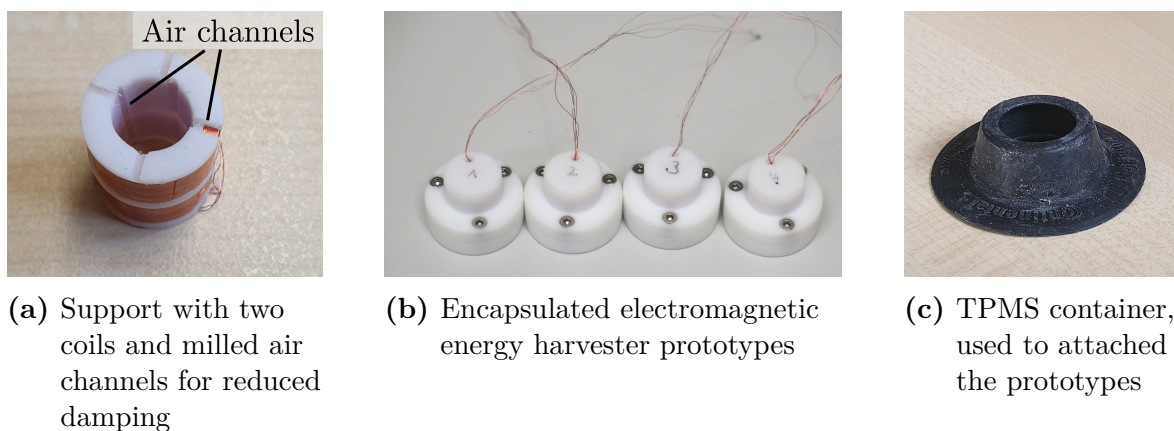


Figure 7.14: Electromagnetic energy harvester prototypes - support with coils, encapsulation and TPMS container

7.5.2 Electromagnetic Transducer Coefficient

Commonly, the transducer coefficient of a linear electromagnetic energy harvester is considered constant $\beta = \text{const.}$ In [172], different techniques to determine the transducer coefficient are described for a linear system. However, if the deflection of the magnet is too strong and nonlinearities become important as it is the case for the herein considered energy harvesters, a different measurement setup is required. The position dependent transducer coefficient $\beta(z)$ was studied experimentally by Mohammed and Germer [173]. They built an experimental setup in which the magnet, accelerated by the gravity, moved towards the coil support as shown in Fig. 7.15. During the accelerated movement, the exact position of the movable magnet was measured with a laser triangulation sensor and the open-circuit coil voltages with a voltmeter. Since the top of the magnet would be shadowed when it entered the coil leading to restricted measurements with a laser triangulation sensor, Mohammed and Germer extended the magnet upward with a plastic rod. From both the voltage-time measurements $u(t)$ and the time dependent position $z(t)$, they determined the velocity $v = \dot{z}(t)$. Based on the relationship

$$u(z) = \beta(z) \cdot \dot{z}(t), \quad (7.21)$$

the transducer coefficient was calculated. The experimental values were compared with the simulated values in Fig. 7.16. Simulation and measurement are in very good accordance.

7.5.3 Damping Coefficient

Furthermore, Mohammed and Germer studied the damping coefficient when the magnet moves inside the coil [173]. They added the fixed magnet to the previously described setup to levitate the movable magnet as shown in Fig. 7.17. To obtain the highest sensitivity, a spacer between fixed magnet and housing was used to locate the movable magnet to the position of maximal transducer coefficient in equilibrium ($g = \ddot{z} = 9.81 \text{ m/s}^2$). This position is exactly in between the two coils. The modified setup was placed on an electrodynamic shaker. The open-circuit output voltage was measured at 50 Hz excitation frequency and at a sinusoidal excitation of 50 m/s^2 . The corresponding deflection amplitude with $\hat{z} = 0.5 \text{ mm}$ is sufficiently small to linearize the transducer coefficient. Based on the newly measured output voltage, a parameter sweep analysis of the linearized system was driven in LTspice and revealed through comparison a damping coefficient of $c = 0.23 \text{ kg/s}$. At the time of the investigations, the coil did not yet have milled air channels, so a lower damping coefficient is expected with milled air channels.

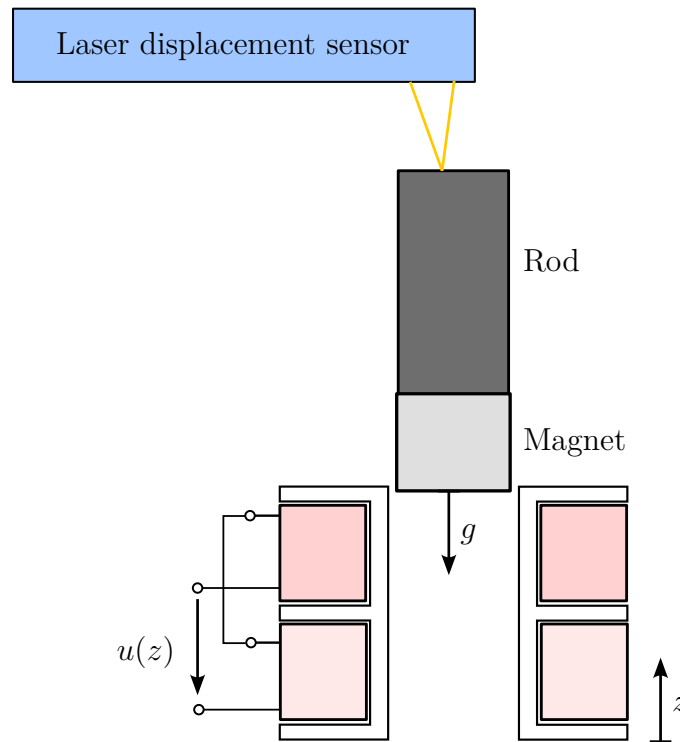


Figure 7.15: Experimental setup to determine the distance-dependent transducer coefficient $\beta(z)$. A laser displacement sensor and a voltmeter measure the distance of the magnet $z(t)$ and the voltage $u(t)$ as a function of time, respectively. The transducer coefficient is calculated from both quantities.

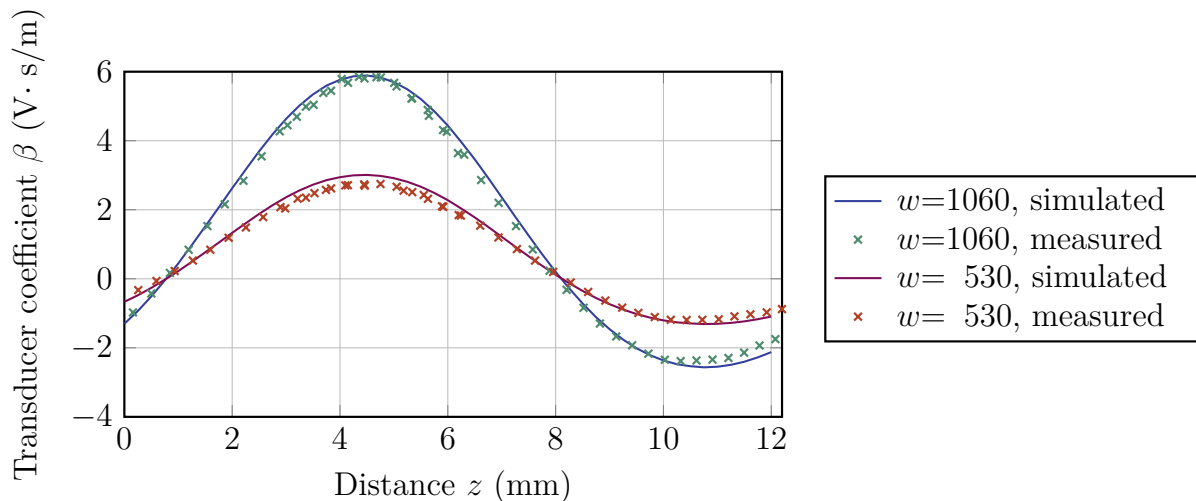


Figure 7.16: Position dependent transducer coefficient $\beta(z)$ - simulation (dashed line) and measurement (dots) for the two coil setups with respect to Tab. 7.3.

7.5.4 Repulsive Magnetic Force

Contrary to the aforementioned parameters, the repulsive magnetic force can be easily measured, using a tensile testing machine. The two different sized magnets were stuck on two non-ferromagnetic supports which were attached to the clamping jaws and to the force sensor of the tensile testing machine, respectively. The magnets were centered

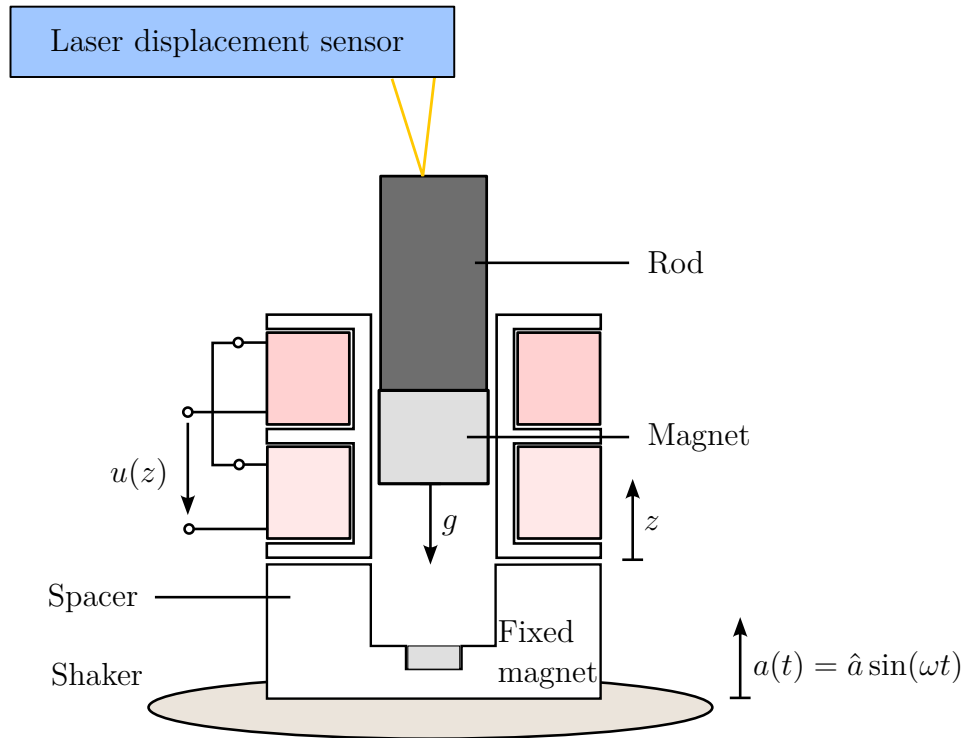


Figure 7.17: Experimental setup to determine the damping coefficient c

vertically and orientated to repel each other. Since the clamping jaws are ferromagnetic, a PMMA plate was used to reduce the effect of the ferromagnetic jaws on the magnetic field of the two permanent magnets. The experimental setup is shown in Fig. 7.18.

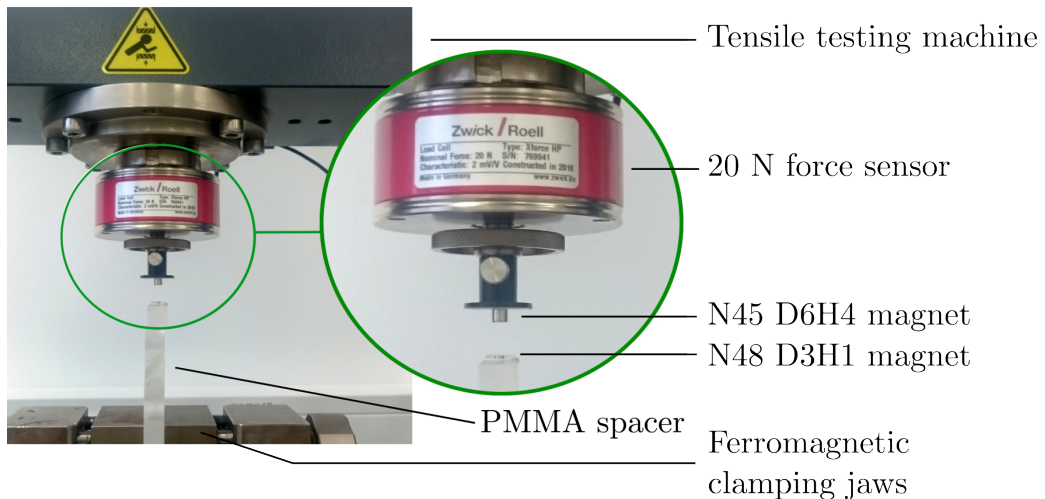
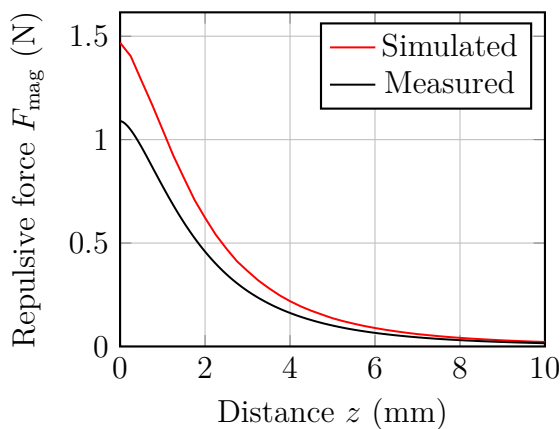


Figure 7.18: Tensile testing machine setup to measure the repulsive magnetic force

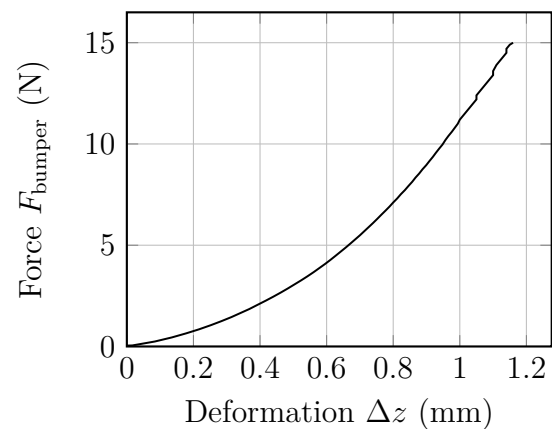
The initial point of the measurement was considered, when both magnets touched each other. The repulsive force was measured while the distance between the two magnets was continuously increasing. Figure 7.19a depicts both, simulated and measured values. The simulated magnetic force varies from the measured force by about 25%, which is within an acceptable range of accuracy to preselect an appropriate fixed magnet. Reasons for this variation rely on an overestimation of the coercivity of grade N45 and N48 magnets as explained earlier, as well as the magnets were not perfectly centrally aligned inside the tensile machine. As the measured magnetic force is used instead of the simulated force in the network simulation, the variations do not present an issue.

7.5.5 Elastic Bumper Force

The elastic force of the bumpers had been determined similarly with a tensile testing machine and fed to the model: the bumper was attached on a support and the sensor was moved slowly downwards and compressed the bumper. For sensor protection reasons, the tensile machine stopped, when the force $F = 15\text{ N}$ was reached, which is equivalent to the excitation force \hat{F}_{ex} at $v = 230\text{ km/h}$. The measurement resulted in a force-position relation, shown in Fig. 7.19b.



(a) Simulated and measured repulsive magnetic force between the two magnets as a function of distance



(b) Measured deformation-force relation of an elastic bumper element of diameter $d = 5\text{ mm}$ and height $h = 2\text{ mm}$

Figure 7.19: Tensile testing measurements to characterize the repulsive magnetic force between two magnets as a function of distance and the deformation-force relation of the elastic bumper

7.6 Network Simulation

Both the parameters from the FEM and the experimental data are implemented as concentrated network parameters and functions in the network simulator LTspice. Based on the nodal analysis, the network simulation is used to calculate all across and flow quantities. The network can be easily varied, expanded and resimulated. The strength of a network simulator for energy harvesting is, that nonlinear interface circuits can be implemented easily, modified and compared quickly. Their analysis is part of the next chapter.

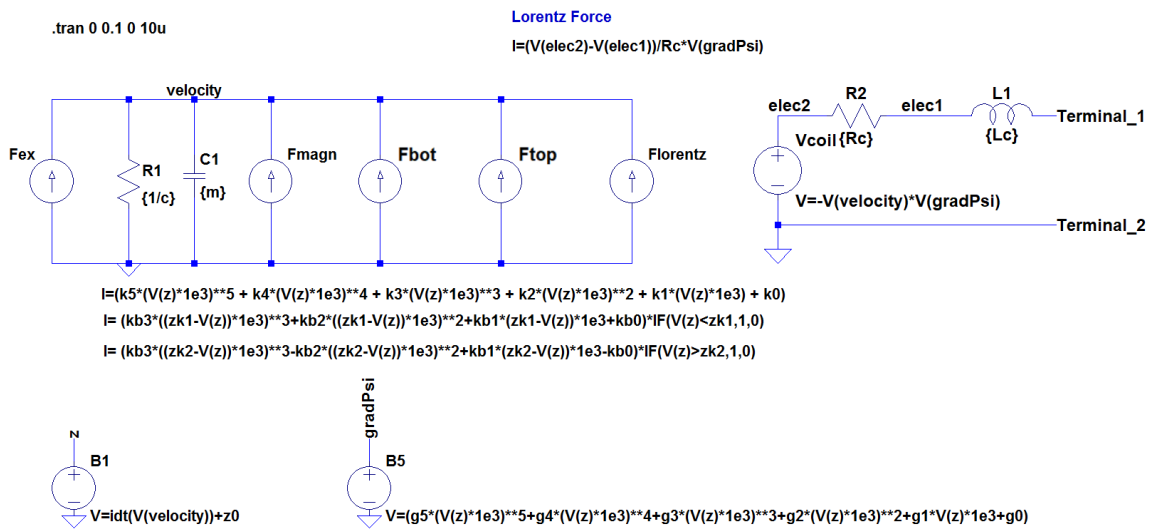


Figure 7.20: LTspice schematic of the nonlinear electromagnetic energy harvester

Figure 7.20 shows the implementation of the electromechanical network from Fig. 7.4. The position z is obtained through numerical integration in time-space as a separate part of the circuit description. Three behavioral current sources represent the compliant relations of the two bumpers and of the magnetic repulsive force (see Eqns. 7.11-7.13). Further, two behavioral sources, controlled by the velocity in the mechanical domain and the current in the electrical domain, represent the electro-magneto-mechanical transducer.

The presented network model is used hereinafter to estimate the output voltage at different velocities as well as the dynamical behavior of the movable magnet and its interaction with the top and bottom bumpers. The simulation parameters and the polynomial coefficients for the nonlinear functions can be found in App. E.

For simulations, Continental provided an acceleration signal, measured inside the innerliner of a vehicle tire at different velocities. The force applied on the tire was approximated to be $F = 4170$ N. For the given signal, the electromechanical network equations were solved in the time domain and selected quantities such as the magnetic force, the elastic bumper forces, the position of the magnet as well as the open-circuit voltage are plotted in Fig. 7.21 for one tire revolution. The magneto-magnetic spring, being preloaded by the centrifugal acceleration, is released in the area of tire ground contact (gray colored

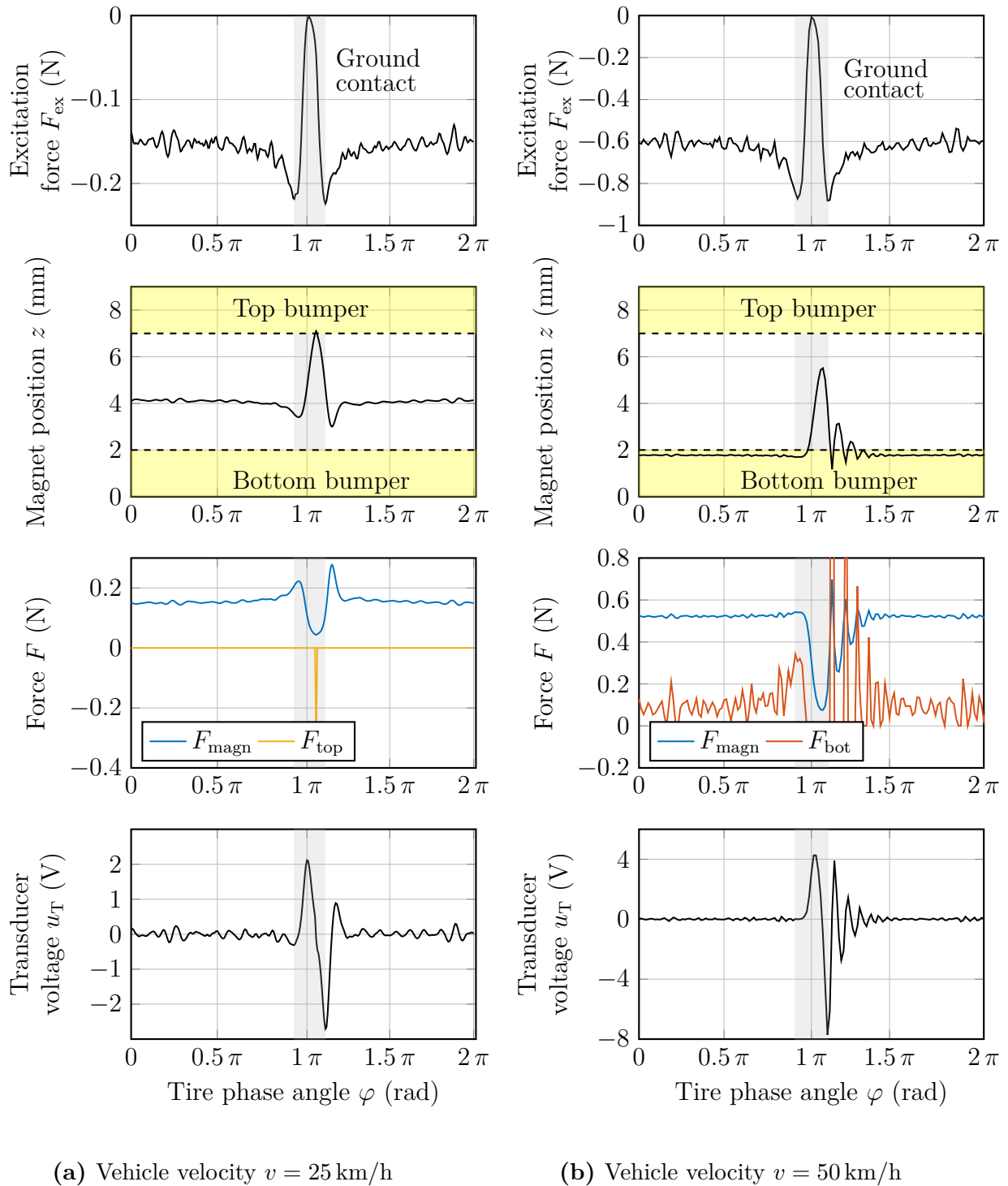


Figure 7.21: Network simulations of the electromagnetic energy harvester with $N = 1060$ for one revolution. The energy harvester is excited by the force $F_{\text{ex}} = m \cdot a_{\text{ex}}$, deduced from the measured acceleration signal a_{ex} . The movable magnet collides with the top bumper in the 25 km/h simulation and with the bottom bumper permanently in the 50 km/h scenario. The gray colored area designates the area of tire ground contact.

area). That is why for the case of $v = 25$ km/h, that the magnet moves from its equilibrium position at $z \approx 4$ mm upwards (towards the center of the wheel) and induces a positive voltage. When the magnet collides with the top bumper it changes the direction of moving and descends. Shortly after, when the entire transducer system is leaving the area of ground contact and the magnet is accelerated additionally downwards (towards the tire) which induces a negative voltage. The negative voltage peak represents the end of the contact patch.

The dashed lines and yellow colored areas in the Figures represent the beginning of the top and bottom bumper. While the magnet is well centered between the two bumpers at 25 km/h, it is already in contact with the bottom bumper at 50 km/h, in equilibrium. An instantaneous contact with one of the bumpers evokes a strong increase of the bumper force. This appears shortly after $\varphi = \pi$ at both 25 km/h and 50 km/h scenarios with the top and bottom bumper, respectively.

In the following, the objective is to describe the electrical energy E_{elec} and to find an upper bound. An electromagnetic energy harvesters is typically characterized by the induced open-circuit voltage at a specific excitation and the source impedance. As explained in Sec. 7.1, two coupled second order differential equations are used to describe the electromagnetic energy harvester. The equivalent circuit of the electrical domain is depicted in Fig. 7.22. Due to the electromechanical coupling, the electrical current impacts the motion of the magnet in the mechanical domain and vice versa. According to Lenz law, the electric current induced in a conductor (here the coil) is always directed such that it counteracts the initial magnetic field. Consequently, the higher the current, the stronger the counteracting magnetic field is and the more the velocity v of the movable magnet is reduced. As a result, both the velocity v and the absorbed mechanical energy E_{mech} are smaller and finally the electrical energy is lower, too. Calculating the electrical energy E_{elec} stored in the system is difficult especially for non-harmonic signal excitations.

However, the problem can be simplified, supposing that the mechanical domain only affects the electrical one, but not vice-versa. The system is considered as unidirectionally coupled, which means, that the electromagnetic feedback due to the Lorentz Force is neglected. In this case an upper limit of the electrical energy can be calculated. In general, the electrical energy transferred to any load at the terminals is

$$E_{\text{elec}}(t) = \int_{t'=0}^t P dt' = \int_{t'=0}^t u \cdot i dt'. \quad (7.22)$$

For the circuit of Fig. 7.22, the voltage u is

$$u = u_{\text{T}} - R_{\text{c}}i - L_{\text{c}} \frac{di}{dt} \quad (7.23)$$

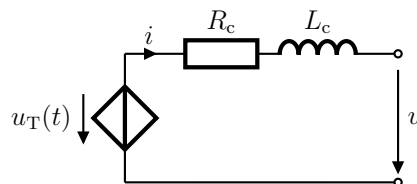


Figure 7.22: Equivalent circuit of a unidirectionally coupled electromagnetic transducer

and consequently the energy is

$$E_{\text{elec}}(t) = \int_{t'=0}^t \left(u_{\text{T}} - R_{\text{c}}i - L_{\text{c}} \frac{di}{dt'} \right) \cdot i dt'. \quad (7.24)$$

An upper bound can be easily calculated if the voltage drop across the inductance is neglected, which is reasonable since $R_{\text{c}} \cdot i \gg L_{\text{c}} \cdot di/dt$. The upper bound of the maximal energy is then

$$E_{\text{elec}}(t) = \int_{t'=0}^t \left(u_{\text{T}} - R_{\text{c}}i \right) \cdot i dt'. \quad (7.25)$$

An optimal load R_{L} with $R_{\text{L}} = R_{\text{c}}$ at the terminals is known for maximal power transfer as shown in Fig. 7.23. Replacing the current by $i = u_{\text{T}}/(R_{\text{c}} + R_{\text{L}})$ follows in

$$E_{\text{elec,max}}(t) \leq \int_{t'=0}^t \frac{u_{\text{T}}^2}{4R_{\text{c}}} dt', \quad (7.26)$$

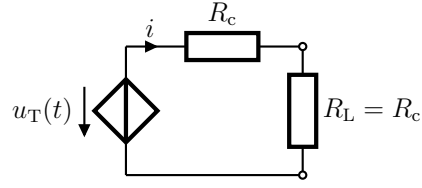


Figure 7.23: Maximal power transfer to the load resistance R_{L}

with $E_{\text{elec,max}}$ the maximal electrical energy. Since the voltage u_{T} of the unidirectionally coupled system equals the voltage of the bidirectionally coupled system under open-circuit conditions $u_{\text{T}}|_{i=0}$, the measured open-circuit voltage can be used to determine the maximal available electrical energy.

The amount of mechanical energy being absorbed by the system is expressed as

$$E_{\text{mech}}(t) = \int_{t'=0}^t F_{\text{ex}} \cdot v dt'. \quad (7.27)$$

Depending on the signs of force and velocity, in some cases a portion of the already absorbed energy is returned to the source of excitation. Dividing the electrical energy by the mechanical energy results in the efficiency of the energy harvester. After one period $t = T$, it is

$$\eta_{\text{eh}}(t = T) \leq \frac{E_{\text{elec}}(T)}{E_{\text{mech}}(T)} \quad (7.28)$$

Applying Eqns. 7.26 and 7.27 to the network simulation provides the mechanical and electrical energy during one tire revolution, presented in Fig. 7.24 for the unidirectional coupled case. The electrical energy is limited by 68 μJ and 220 μJ at 25 km/h and 50 km/h, respectively. Additionally, the optimal load case for the bidirectionally coupled system has been simulated and is represented, too, and summarized in Tab. 7.4.

While in a linear electromechanical network the optimal load is $R_{\text{L}} = R_{\text{c}} + \beta^2/c$, and results from the transformation of the damping element to the electrical domain, in a nonlinear network model it ranges from $R_{\text{c}} < R_{\text{L}} < R_{\text{c}} + \max(\beta^2)/c$. The optimal load

resistance was identified to be $R_L \approx 300 \Omega$ through parameter study.

Table 7.4: Mechanical energy, electrical energy and total efficiency for the unidirectionally and bidirectionally coupled network at 25 km/h and 50 km/h vehicle velocity.

		unidirectionally coupled	bidirectionally coupled
	Optimal load R_L	262 Ω	300 Ω
25 km/h	Energy $E_{\text{mech,max}}(t = T)$	630 μJ	660 μJ
	Energy $E_{\text{elec,max}}(t = T)$	68 μJ	60 μJ
	Efficiency $\eta_{\text{eh}}(t = T)$	11 %	9 %
50 km/h	Energy $E_{\text{mech,max}}(t = T)$	3000 μJ	2800 μJ
	Energy $E_{\text{elec,max}}(t = T)$	220 μJ	175 μJ
	Efficiency $\eta_{\text{eh}}(t = T)$	7 %	6 %

Although the energy harvester efficiency η_{eh} is low, the electrical energy of 60 μJ (bidirectionally coupled network) is much higher than the required 7.9 μJ . An interface circuit with an average efficiency of 16 % would be sufficient. As the output voltage of approximately 2.7 V at 25 km/h is smaller than the desired capacitor voltage of 3.9 V, an up-conversion is required. Therefore, suitable interface circuits will be considered in the next chapter.

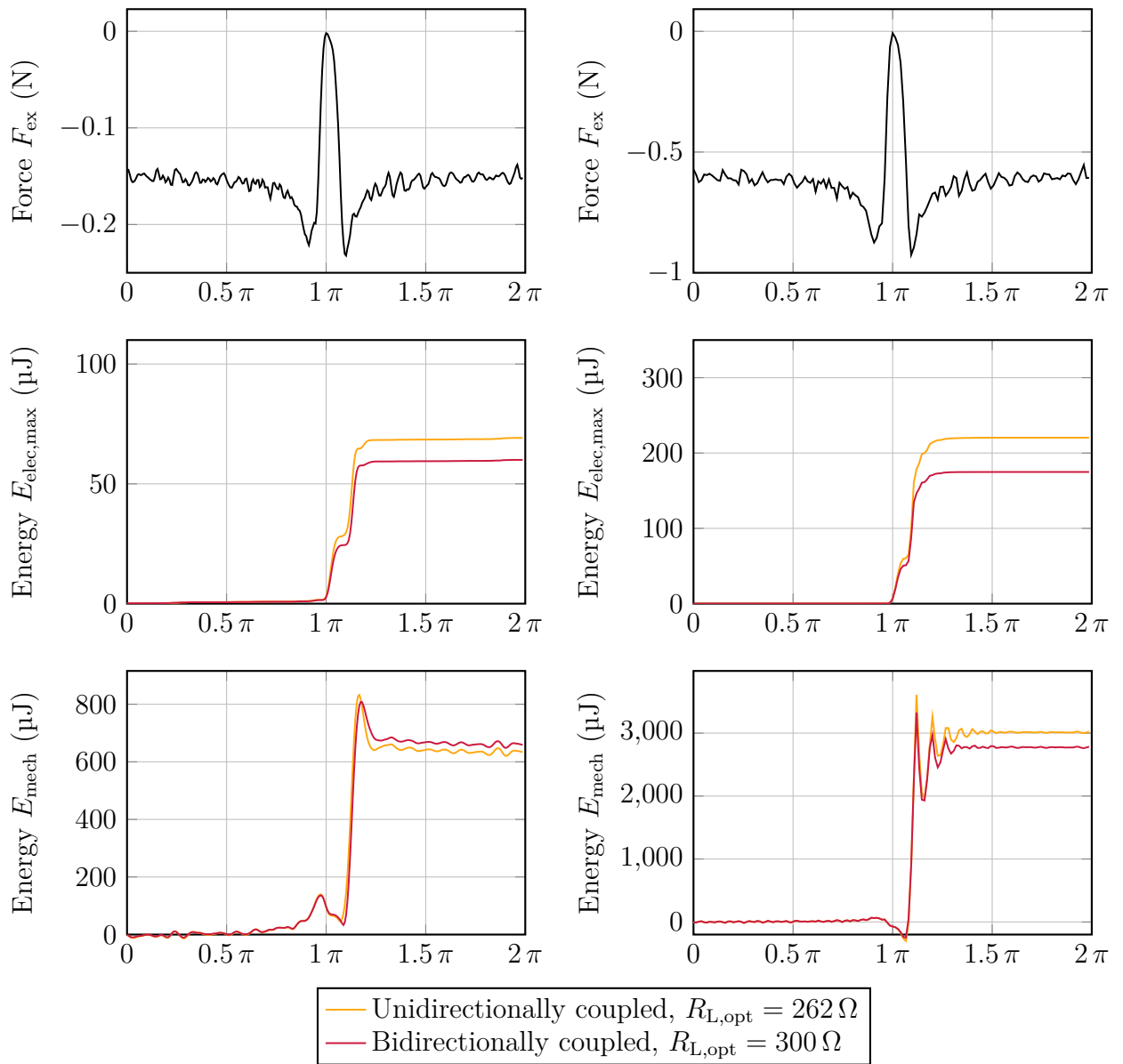
(a) Vehicle velocity $v = 25$ km/h(b) Vehicle velocity $v = 50$ km/h

Figure 7.24: Simulated electrical and mechanical energy of the electromagnetic energy harvester with $N = 1060$ with parameters based on force measurements for one revolution at 25 km/h and 50 km/h of the bidirectionally coupled network (red line) opposed to the maximal electrical energy of the unidirectionally coupled network (yellow line).

7.7 Summary

Electromagnetic Energy Harvester Prototypes

System

- Cylindrical system with two magnets and two symmetric coils
- Movable magnet: $d = 6 \text{ mm}$, $h = 4 \text{ mm}$, $m = 0.85 \text{ g}$
- Fixed magnet: $d = 3 \text{ mm}$, $h = 1 \text{ mm}$, $m = 0.05 \text{ g}$
- System dimensions: $d = 9 \text{ mm}$, $h_h = 13 \text{ mm}$
- Coil design: ($N = 530$, $d_{w1} = 0.1 \text{ mm}$) & ($N = 1060$, $d_{w2} = 0.07 \text{ mm}$)

Features

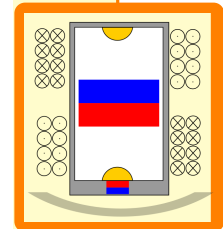
- Series coil connection with opposite sense of winding
- Elastic bumpers to reduce hard bounces
- Contactless magneto-mechanical springs
- Air-channels for reduced damping
- System tuned for low velocities ($v = 25 \text{ km/h}$)
- $E_{\text{elec,max}} = 60 \mu\text{J}$ with load $R_{L,\text{opt}} = 300 \Omega$ and velocity $v = 25 \text{ km/h}$

Advantages

- Easy integration in a TPMS
- System reusability
- Intrinsically robust

Disadvantages

- Thin wire diameter required to obtain high number of turns
- Low output voltage at 25 km/h



8 Electromagnetic Energy Harvesting Interface Circuits

Similar to piezoelectric interface circuits, electromagnetic energy harvesting interface circuits play a key role in the energy harvesting chain. According to the results of Sec. 7.6, the electromagnetic energy harvester with 1060 turns provides at most $60 \mu\text{J}/\text{rev}$ and a voltage magnitude of 2.7 V . This system is used in this chapter as reference system. The voltage signal needs to be up-converted to at least 3.9 V , while the energy $E_{\text{rev,charged}} = 7.9 \text{ V}/\text{rev}$ must be transferred to the storage, in average. Consequently, the purpose of this chapter is to study typical interface principles and to characterize circuit properties such as maximal output voltage and efficiency to charge the storage capacitor C_s . Furthermore, the analysis goes beyond the traditional resistive maximal power transfer analysis of [174–176] and the demands on an implementation are discussed.

Electromagnetic interface circuits are well known in the world of power electronics, where first, the energy from the grid is much larger than the energy required by a system, second, the system size is not generally crucial and third, the very efficient transfer of the electrical energy to the system is important. Contrary, energy harvesting interface circuits are developed with the desire of being compact and applied with the focus of maximal power transfer, where at least 50% of the energy is dissipated through the source resistance. If the energy and provided power is not instantly used by an energy harvester, it can not be used later. One well known interface circuit is the Standard Energy Harvesting (SEH), which will be studied at first. Although, remarkably high efficiencies can be obtained with SEH, the open-circuit voltage of an electromagnetic transducer is much lower than the one of a piezoelectric system. To up-convert the output voltage, efficient buck-boost interface circuit concepts are investigated.

Voltage multipliers such as voltage doublers or voltage triplers raise the open-circuit voltage multiple times. Inspired by the efficient piezoelectric Synchronous Electric Charge Extraction (SECE), Arroyo et al. [177, 178] developed the analogical counterpart: the Synchronized Magnetic Flux Extraction (SMFE) circuit. The main advantages of this circuit are the nearly load-independent energy transfer and the achievement of high output voltages. However, because of significant resistive losses, the efficiency is very low.

Bonisoli et al. [179] presented an active buck-boost converter which open-circuited and short-circuited an electromagnetic transducer to raise the output voltage. They obtained efficiencies higher than 50% with a complex control logic. However, this logic was designed

for only one specific transducer and needs to be recalculated for different transducers. To overcome this limitation, Germer et al. [168] extended the buck-boost concept from [179] and studied the optimal timing of the switch for a maximal efficiency η_{ic} . As it will be deduced in Sec. 8.4, the optimal timings of the switch solely depends on the inductance L_c and the parasitic resistance R_c of the electromagnetic transducer. Once determined, no complex algorithm as described in [179] is required anymore, but only a pulse-width-modulation (PWM)-signal with predefined on and off times.

For comparison reasons and to provide analytical estimates of the efficiency η_{ic} , the following calculations suppose a unidirectionally coupled network as explained in Sec. 7.6. The modified equivalent circuit with interface circuit and capacitor is depicted in Fig. 8.1.

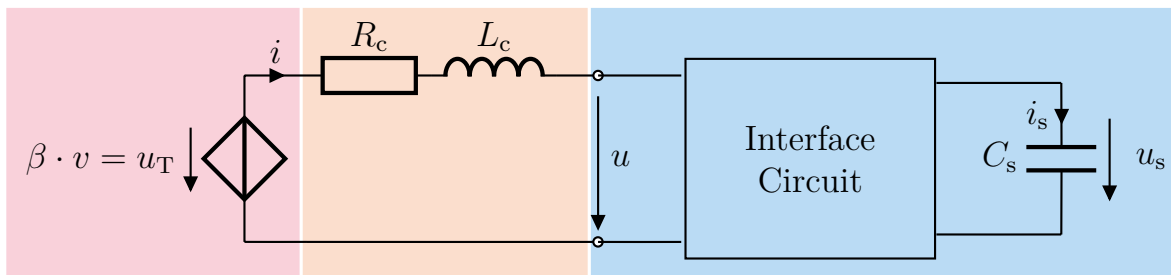


Figure 8.1: Equivalent circuit of a unidirectionally coupled electromagnetic energy harvester with interface circuit and storage.

8.1 Standard Energy Harvesting and Stochastic Signal Analysis

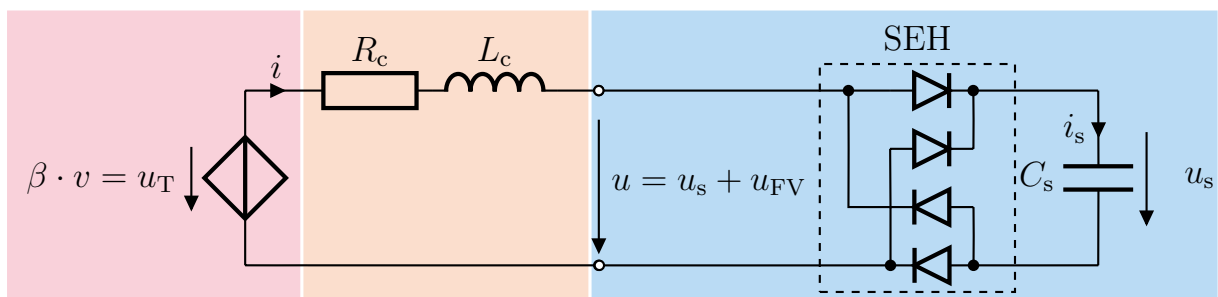


Figure 8.2: Equivalent circuit of a unidirectionally coupled electromagnetic energy harvester with with standard interface and storage.

Standard Energy Harvesting of a harmonic signal with piezoelectric transducers as presented in Sec. 6.2 is strongly dependent on the ratio $b = u_{s,0}/u_0$ between initial capacitor voltage $u_{s,0} = u_s(t = 0)$ and open-circuit voltage magnitude u_0 . The efficiency η_{SEH} is limited by 25% and very low efficient at smaller voltage ratios. In contrast, an SEH connected to an electromagnetic energy harvester can reach much higher efficiencies even

at low voltage ratios b , but only under ideal conditions in which the diode losses are neglected. Hereinafter, the efficiency $\eta_{\text{SEH}} = \eta_{\text{ic}}$ is deduced for the electromagnetic transducer. According to Eqn. 6.1 the efficiency has been defined as

$$\eta_{\text{ic}} = \frac{\Delta E_{\text{stored}}}{E_{\text{elec}}}. \quad (8.1)$$

The maximal available electrical energy $E_{\text{elec,max}}$ has been deduced in Sec. 7.6 under load matching conditions to be

$$E_{\text{elec,max}} = \int_{t=0}^T \frac{u_{\text{T}}^2(t)}{4R_{\text{c}}} dt. \quad (8.2)$$

The added energy to the capacitor $\Delta E = \Delta E_{\text{stored}}$ is defined as

$$\Delta E = \frac{(Q_{\text{s},0} + \Delta Q_{\text{s}})^2 - Q_{\text{s},0}^2}{2C_{\text{s}}} = \Delta Q_{\text{s}} \cdot \frac{2Q_{\text{s},0} + \Delta Q_{\text{s}}}{2C_{\text{s}}}, \quad (8.3)$$

where ΔQ_{s} and $Q_{\text{s},0}$ are the added charge and the initial charge of the capacitor C_{s} . Replacing the charge in the fraction term by the general relation $Q = C \cdot u$ results in

$$\Delta E = \Delta Q_{\text{s}} \cdot \frac{2C_{\text{s}}u_{\text{s},0} + C_{\text{s}}\Delta u_{\text{s}}}{2C_{\text{s}}} \quad (8.4)$$

$$\Delta E = \Delta Q_{\text{s}} \cdot \left(u_{\text{s},0} + \frac{1}{2}\Delta u_{\text{s}} \right). \quad (8.5)$$

With $\Delta u_{\text{s}} = u_{\text{s}} - u_{\text{s},0}$ the difference of voltage after and before the energy transfer, follows

$$\Delta E = \Delta Q_{\text{s}} \cdot \frac{1}{2} \cdot (u_{\text{s}} + u_{\text{s},0}). \quad (8.6)$$

If the capacitor C_{s} is large such that the transferred charge ΔQ_{s} causes only a small increase of the capacitor voltage $u_{\text{s}} \approx u_{\text{s},0}$, Eqn. 8.6 can be rewritten to

$$\Delta E \leq \Delta Q_{\text{s}} \cdot u_{\text{s},0}. \quad (8.7)$$

The charge ΔQ_{s} is only transferred, if $u_{\text{T}}(t) > u_{\text{s},0}$, expressed by the current

$$i_{*}(t) = \frac{u_{*}(t)}{R_{\text{c}}} \quad \text{with} \quad (8.8)$$

$$u_{*}(t) = \begin{cases} |u_{\text{T}}(t)| - u_{\text{s},0} & |u_{\text{T}}(t)| > u_{\text{s},0} \\ 0 & \text{else.} \end{cases} \quad (8.9)$$

The corresponding charge of the rectified signal is

$$\Delta Q_{\text{s}} = \int_{t=0}^T |i_{*}(t')| dt'. \quad (8.10)$$

With the relation $i_*(t) = u_*(t)/R_c$ follows

$$\Delta Q_s = \frac{1}{R_c} \int_{t=0}^T |u_*(t')| dt'. \quad (8.11)$$

Equation 8.11 represents the average rectified value of the voltage $u_*(t)$, weighted by the factor $1/R_c$. When Eqn. 8.11 is extended by the period T , it can be rewritten to

$$\Delta Q_s = \frac{T}{R_c} \cdot \frac{1}{T} \int_{t=0}^T |u_*(t')| dt' = \frac{T}{R_c} \overline{|u_*|}. \quad (8.12)$$

The average rectified voltage can be expressed by the mean value $\mathbb{E}(|u_*(t)|)$, defined as

$$\mathbb{E}(|u_*(t)|) = \frac{1}{T} \int_{t=0}^T |u_*(t')| dt'. \quad (8.13)$$

With the definition of the mean, value the added charge is rewritten to

$$\Delta Q_s = \frac{T}{R_c} \mathbb{E}(|u_*|). \quad (8.14)$$

Consequently, the voltage u_* determines the charge and hence the amount of energy transferred to the capacitor C_s .

The relative portion of the voltage signal $u_T(t)$ with $|u_T(t)| \geq u_{s,0}$ cannot be directly read neither from a voltage-time diagram nor from a voltage-frequency diagram. Therefore, a new concept of signal representation using stochastic signal analysis was presented by the author of this thesis in [167]. In that work, the common signal analysis in the time domain and frequency domain was extended by the representation with the amplitude distribution. The main idea is to estimate which part of the signal is above a voltage u_b , called barrier voltage subsequently, and thus contributes to the energy transfer, and which part is omitted due to the barrier imposed by the voltage $u_{s,0}$ (and later by the forward voltage of the rectifier u_{FV}). This new description is useful for comparing the voltage signals of harmonic and non-harmonic electromagnetic transducers, and to estimate the circuit efficiency of charge based interface circuits such as SEH and voltage multipliers.

In the stochastic signal analysis, the voltage signal $u_T(t)$ is considered as a realization of an ergodic, stationary process \mathbf{U}_T in which the time t is regarded as a random variable, equally distributed [180]. While in the time domain and in the frequency domain signal amplitudes are described as a function of time t and frequency f , respectively, the stochastic signal analysis represents the probability of occurrence as a function of signal amplitude. The corresponding domain is therefore called the amplitude domain in the following. The fundamental signal characterization is the probability density function (PDF) of the rectified voltage $|u_T|$ expressed by $h(|u_T(t)|)$. The probability density function is deduced from the absolute frequency distribution $H(|u_T|)$.

The function values are divided into equidistant intervals and counted with respect to

their absolute frequency. In Fig. 8.3a, the voltage signal $u_T(t)$ of the energy harvester at 25 km/h, which has already been presented in Fig. 7.24, is depicted for one period. The voltage signal has been divided exemplarily into intervals with the width $\Delta u_T = 0.5 \text{ V}$ from $-3 \text{ V} \leq u_T < 2.5 \text{ V}$ and the time has been divided into intervals with the width $\Delta t/T = 0.033$ from $0 \leq t < T$. The absolute frequency of the discretized signal is shown in Fig. 8.3b.

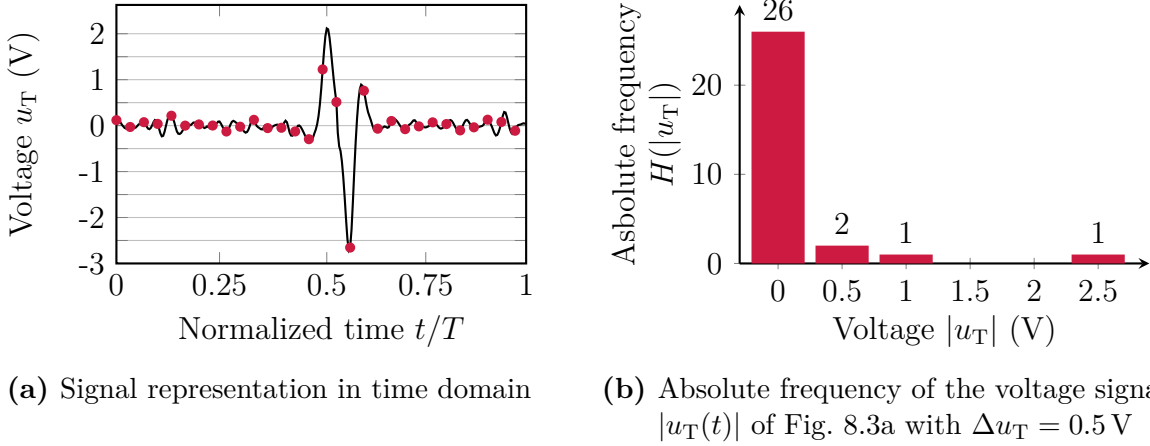


Figure 8.3: Voltage signal in the time domain and derived absolute frequency. For the specific signal $u_T(t)$, small voltages u_T are very likely to occur.

The normalization of the absolute frequency H by the number of values $n = \sum H$ and by the interval width Δu_T , where the interval width becomes infinitesimal small, leads to the PDF $h(|u_T(t)|)$ as

$$h(|u_T|) = \lim_{\Delta u_T \rightarrow 0} \frac{H(|u_T(t)|)}{\sum H(|u_T(t)|) \cdot \Delta u_T}. \quad (8.15)$$

The PDF is depicted in Fig. 8.4. The signal of the electromagnetic transducer consists mainly of low amplitudes and only a small part is attributed to high amplitudes. In contrast to the analyzed piezoelectric interface circuits, the specific voltage signal of an electromagnetic transducer strongly impacts the amount of energy being transferred.

Based on the introduced PDF, the mean value from Eqn. 8.13 is rewritten as a function of the voltage $u_{s,0}$ by

$$\mathbb{E}(u_*) = \mathbb{E}(|u_T| \geq u_{s,0}) = \int_{u_T=u_{s,0}}^{u_0} h(|u_T|) \cdot (|u_T| - u_{s,0}) du_T. \quad (8.16)$$

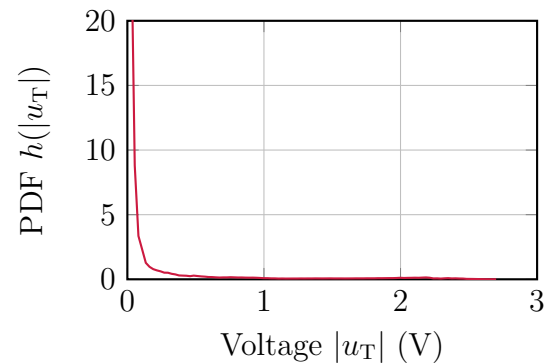


Figure 8.4: Probability density function of the voltage from Fig. 8.3a

with the maximal transducer voltage

$$u_0 = \max(|u_T|). \quad (8.17)$$

Inserting Eqn. 8.16 in Eqn. 8.14 leads to the charge as a function of voltage as

$$\Delta Q_s(u_*) = \Delta Q_s(|u_T| \geq u_{s,0}) = \frac{T}{R_c} \int_{u_T=u_{s,0}}^{u_0} h(|u_T|) \cdot (|u_T| - u_{s,0}) du_T. \quad (8.18)$$

As voltages are integrated in the interval $u_{s,0} \leq u_T \leq u_0$ and refer to a charge, the quantity $\Delta Q_s(|u_T| \geq u_{s,0})$ is introduced as the interval charge. Figure 8.5b shows the interval charge of the signal illustrated in Fig. 8.5a for $T = 298$ ms and $R_c = 262 \Omega$. For a better understanding, diode forward losses are neglected at this point.

In Fig. 8.5a, a part of the voltage signal is gray colored and represents the amount of voltage related charge which can be transferred to the storage, if the storage capacitor has been already precharged to $u_{s,0} = 0.6$ V. Multiplying the remaining voltage with T/R_c is equivalent to the available charge. The corresponding value can be easily read from the interval charge in Fig. 8.5b. At the voltage of $u_{s,0} = 0.6$ V a charge of $90 \mu\text{C}$ is still available. In contrast, when the capacitor is discharged ($u_{s,0} = 0$ V), a charge of $245 \mu\text{C}$ can be transferred.

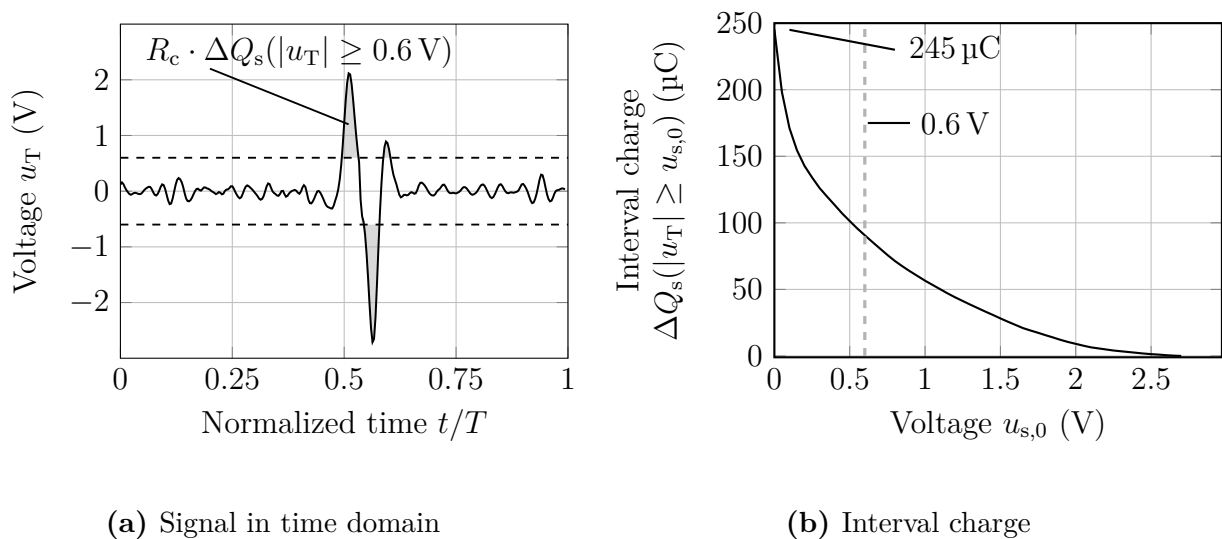


Figure 8.5: Voltage signal u_T and corresponding interval charge $\Delta Q_s(|u_T|)$ with respect to Eqn. 8.18. The charge of $90 \mu\text{C}$ can be transferred, when the storage capacitor is precharged to 0.6 V.

Knowing the interval charge ΔQ_s , the added energy ΔE can be estimated as stated in Eqn. 8.7. The normalization to the maximal available electrical energy $E_{\text{elec,max}}$, described in Eqn. 8.1 leads, according to Eqn. 8.2 to the efficiency, which is

$$\eta_{\text{SEH}}(u_T \geq u_{s,0}) \approx \frac{\Delta E}{E_{\text{elec}}} = \frac{\Delta Q_s(|u_T| \geq u_{s,0}) \cdot u_{s,0}}{E_{\text{elec,max}}}. \quad (8.19)$$

However, this relation only considers the voltage $u_{s,0}$ as charge barrier, preventing the current to flow to the capacitor, whereas diode losses have not been considered, yet. If they are incorporated, the amount of accumulated charge is reduced to $\Delta Q_s(|u_T| \geq u_b)$ with

$$u_b = u_{s,0} + u_{FV} \quad (8.20)$$

where u_{FV} is the total forward voltage of the rectifying circuit. It is e.g. $u_{FV} = 0.6$ V for an SEH composed of Schottky diodes.

Consequently, the efficiency with diode forward voltage losses is

$$\eta_{SEH}(|u_T| \geq u_b) \approx \frac{\Delta Q_s(|u_T| \geq u_b) \cdot u_{s,0}}{E_{elec,max}}. \quad (8.21)$$

The efficiency as a function of $u_{s,0}$ is depicted in Fig. 8.6, deduced for the voltage signal at 25 km/h and 50 km/h shown in Fig. 7.21. Maximal efficiencies of 38 % at $u_{s,0} = 0.7$ V and 61 % at $u_{s,0} = 1.9$ V can be reached at 25 km/h and 50 km/h, respectively.

Similarly to the interval charge, the interval energy can be defined as

$$E(u_T \geq u_{FV}) = \frac{T}{R_c} \int_{u_T=u_{FV}}^{u_0} h(|u_T|) (|u_T| - u_{FV})^2 du_T. \quad (8.22)$$

This quantity is helpful to characterize the maximal signal energy before and after rectification. The corresponding values can be directly determined from the function $E(u_T \geq u_{FV})$ at $u_T \geq 0$ V and $u_T \geq 0.6$ V, respectively. Again, the main advantage is to compare the signal energy of different signals (harmonic, non-harmonic) and how much energy is lost due to rectification. The interval energy is depicted in Fig. 8.7 for the transducer voltage signals at 25 km/h and 50 km/h. As shown, the energies of $30 \mu\text{J}$ and $160 \mu\text{J}$ can be provided at $v = 25$ km/h and 50 km/h, respectively, when an SEH with Schottky diodes ($u_{FV} = 0.6$ V) is applied.

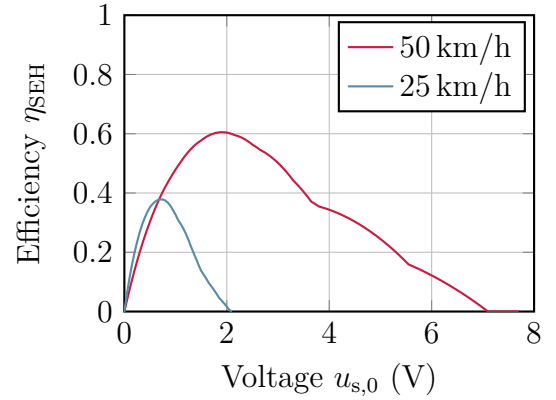


Figure 8.6: SEH efficiency as a function of voltage $u_{s,0}$ for the forward voltage $u_{FV} = 0.6$ V deduced from simulated signals.

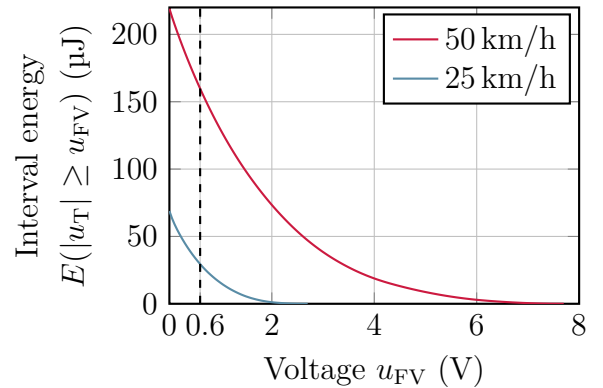


Figure 8.7: Interval energy as a function of the forward voltage u_{FV} .

The available energy is even lower for silicon diodes ($u_{FV} = 1.4 \text{ V}$).

Although the peak efficiency of the SEH is acceptable, a significant amount of energy is lost due to the diode voltage drop. In [181–183] full-wave rectifiers with very low voltage drop were developed and studied. But even reducing the diode forward voltage theoretically from $u_{FV} = 0.6 \text{ V}$ to 0 V would not lead to an output voltage of $u_{\text{charged}} = 3.9 \text{ V}$ at $v = 25 \text{ km/h}$. Therefore, further solutions will be explored.

8.2 Voltage Multipliers

To overcome the drawback of a limited output voltage u_T , voltage multipliers constitute a reasonable way to increase the voltage [184–186]. Figure 8.8 illustrates both a Voltage Doubler (VD) and a Voltage Tripler (VT). Exemplarily, the operating principle of a voltage doubler as the smallest voltage multiplier, shown in Fig. 8.8a, is explained.

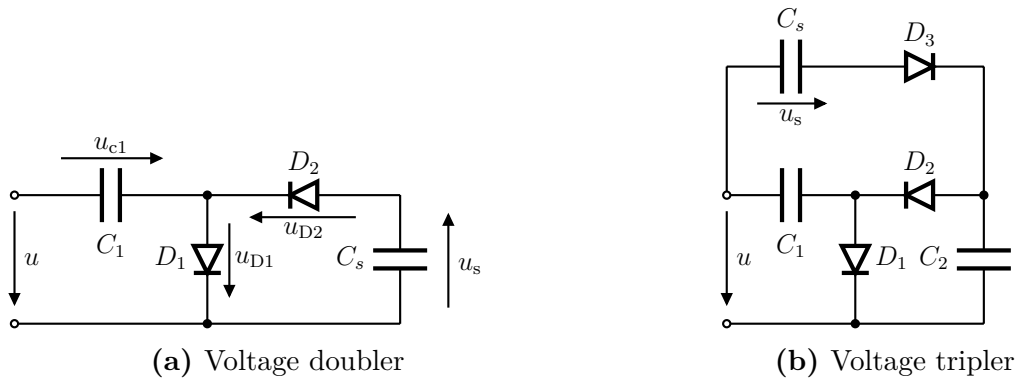


Figure 8.8: Electrical circuit of a voltage doubler and voltage tripler to double and triple the input voltage u

A harmonic sinusoidal voltage $u_T = u_0 \sin(\omega t)$ is supposed. During the positive half-wave, diode D_1 is conductive and the current charges the capacitor C_1 . The capacitor can reach a maximum voltage of $u_0 - u_d$, where u_d is the forward voltage of one diode and $u_0 = \max(u_T)$. When the polarity of the voltage signal is changing, Diode D_1 is reverse biased and Diode D_2 becomes conductive. Then, both voltage source u and capacitor voltage u_{c1} have the same polarity, are summed and lead to the maximal voltage $u_{D1} = -(u_0 + (u_0 - u_d))$. Due to the voltage drop of diode D_2 , the maximal voltage u_s is limited by

$$u_s \leq 2 \cdot (u_0 - u_d). \quad (8.23)$$

A voltage multiplier with n -stages generally limits the voltage to

$$u_s \leq n \cdot (u_0 - u_d). \quad (8.24)$$

The voltage magnitude at 25 km/h is $u_0 = 2.7 \text{ V}$. Supposing a forward voltage of the

Schottky diodes $u_d = 0.3 \text{ V}$, a voltage doubler and a voltage tripler provide a maximal voltages of $u_s = 4.8 \text{ V}$ and $u_s = 7.2 \text{ V}$, respectively. To calculate the efficiency of a voltage multiplier Eqn. 8.21 is applied. From Eqn. 8.24 follows the efficiency of a voltage multiplier η_{VM} with

$$\eta_{\text{VM}}\left(\left(|u_{\text{T}}| \geq \frac{u_{\text{s},0}}{n} + u_{\text{d}}\right)\right) \approx \frac{Q\left(\left|u_{\text{T}}\right| \geq \frac{u_{\text{s},0}}{n} + u_{\text{d}}\right) \cdot u_{\text{s},0}}{E_{\text{elec,max}}}. \quad (8.25)$$

Based on Eqn. 8.25, the efficiency has been calculated for the voltage signal at $v = 25 \text{ km/h}$. It is depicted for the VD and VT in Fig. 8.9 and opposed to the one of the SEH. On the one hand, the efficiency is wider and the peak efficiency is shifted towards a higher capacitor voltages $u_{\text{s},0}$. On the other hand, since the forward voltage drop is reduced by the voltage multiplier to u_d instead of $2u_d$, the peak efficiency raises from 38 % (SEH) to 56 % (VD, VT).

To evaluate the analytical results, obtained with the stochastic signal analysis, the storage capacitor voltage of the electromagnetic energy harvester with connected SEH, VD and VT was numerically calculated using LTspice and the bidirectionally coupled network model, presented in Fig. 7.20. From the voltage-time signal, the efficiency as a function of voltage $u_{\text{s},0}$ has been deduced and is depicted in Fig. 8.9 with densely dotted lines.

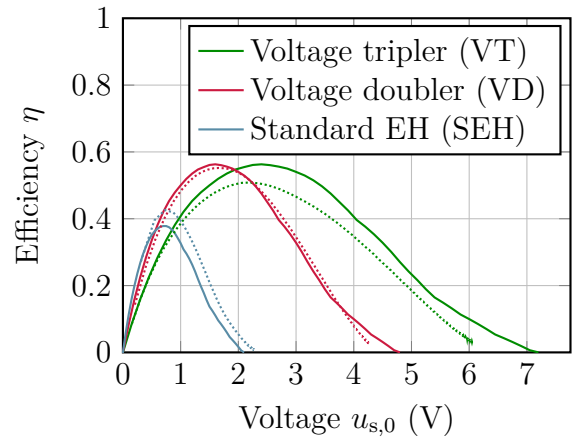


Figure 8.9: Analytically calculated efficiencies (solid lines) opposed to the efficiencies deduced from LTspice simulations (densely dotted lines) as a function of voltage $u_{\text{s},0}$ at 25 km/h

In the circuits, presented in Fig. 8.8, the capacitors C_1, C_2 with $47 \mu\text{F}$ were chosen from the E6-series because they lead to the highest capacitor voltage u_s for both VD and VT in the simulation compared to other intermediate capacitors. Comparing the efficiencies deduced from the LTspice simulation with the ones calculated, applying the stochastic signal analysis, shows that both results are in good accordance. The efficiency of the SEH and VT are slightly underestimated and overestimated, respectively, using the stochastic signal analysis. For the SEH, the forward voltage drop decreased in the LTspice simulation from $u_d = 300 \text{ mV}$ down to $u_d = 250 \text{ mV}$ with increasing voltage $u_{\text{s},0}$ since the current $i(t)$ was decreasing, whereas in the analytical model $u_d = 300 \text{ mV}$ was supposed as fixed diode voltage. For the VT, losses attributed to the capacitor C_2 were not incorporated in the stochastic model, leading to an overestimation of the efficiency.

In spite of the deviations, the stochastic analysis can be used as a tool for a quick estimation of the maximal electrical energy, the transferred energy and the corresponding efficiency for interface circuits, which transfer charges, such as SEHs and voltage multipliers.

Finally, both VD and VT provide a maximal voltage of 4.8 V and 7.2 V. The efficiency depends on the storage capacitor voltage $u_{s,0}$. As the efficiency is higher than 20 % over a wide range of initial capacitor voltages $u_{s,0}$, both circuits are worthwhile to investigate, experimentally.

8.3 Synchronized Magnetic Flux Extraction (SMFE)

The efficiency of the aforementioned interface circuits are strongly dependent on and limited by the storage voltage $u_{s,0}$. A new concept similar to the SECE as presented in Sec. 6.5 was developed by Arroyo et al. [178] to provide a nearly load-independent and voltage-independent energy transfer.

Inspired by the analogies between electrostatic and magnetic field energy, presented in Tab. 8.1, Arroyo et al. [178] adapted the Synchronous Electric Charge Extraction (SECE) concept (see Sec. 6.5), to electromagnetic transducers. Their goal was to accumulate a maximum of magnetic field energy in the inductor before the energy is transferred. Due to the duality of the electric charge in a piezoelectric energy harvester and the magnetic flux in an electromagnetic transducer, this method was called.

The unidirectionally coupled energy harvester with interface circuit is depicted in Fig. 8.10. In analogy to the SECE concept, where the terminal of a piezoelectric transducer is kept open (open-circuited) until the voltage is maximal, the terminal of an electromagnetic transducer is kept close (short-circuited) until the inductor current is maximal. The maximal inductor current is related to the maximal field energy stored in the inductor. Once the current is maximal, the switch is opened. Then, a series resonance circuit is set up with the storage C_s . Consequently, the inductor energy is transferred to the electrical load. To understand the circuit principle and the following calculations more easily, a sinusoidal voltage excitation is supposed. The corresponding waveforms of the source voltage u_T and current i are depicted in Fig. 8.11, for the most interesting case that $|u_T| \leq u_s$, exemplarily. The current i_0 is introduced as maximal current with

Table 8.1: Analogies between Electrostatics and Magnetics

	Electrostatics	Magnetics
Storage	Capacitor C	Inductor L
Relation	$Q = C \cdot u$	$\Psi = L \cdot i$
Energy	$\frac{Q^2}{2C}$	$\frac{\Psi^2}{2L}$

$$i_0 = \frac{u_0}{R_c}. \quad (8.26)$$

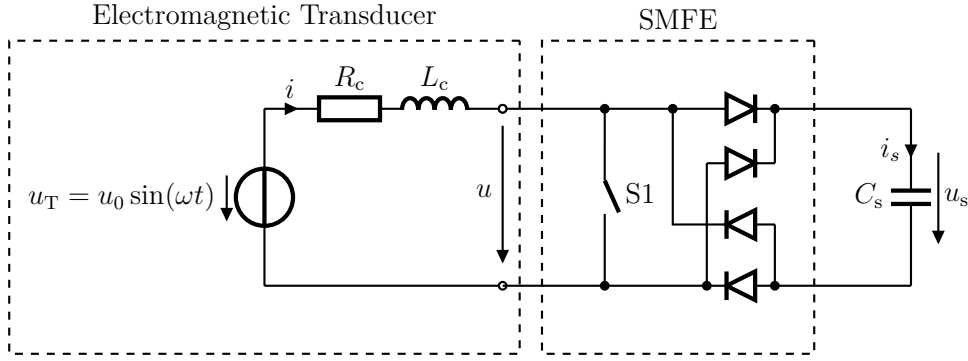


Figure 8.10: SMFE interface circuit connected to electromagnetic energy harvester with harmonic voltage source. Switch S1 is initially closed. When the current $i(t)$ reaches its maximum, switch S1 is opened and enables the energy transfer from the inductor L_c to the load/capacitor

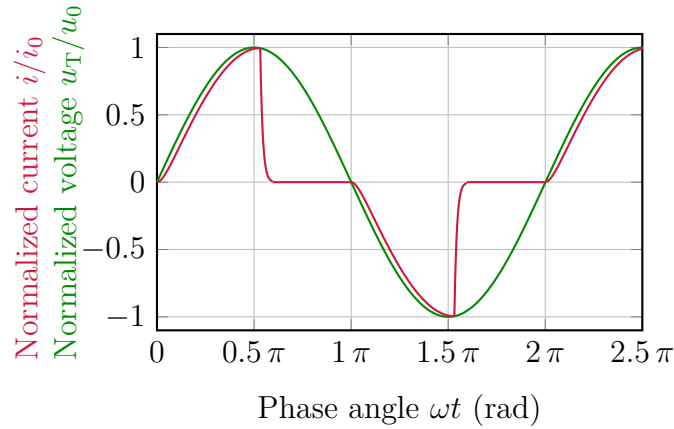


Figure 8.11: SMFE transducer voltage u_T and current i for the case that the source voltage is smaller than the capacitor voltage ($u_T < u_s$). When the current maximum is reached, S1 is opened (here shortly after 0.5π) and the inductor L_c drives the current to the load, until it is discharged ($i \rightarrow 0$).

The main advantage of this circuit is that the capacitor voltage u_s is not limited by the voltage u_T . To evaluate the circuit performance, the efficiency is deduced subsequently for the sinusoidal signal. The general results can be applied to the electromagnetic energy harvester voltage signal of the tire.

Similar as for the SECE for piezoelectric systems, the SMFE efficiency is characterized in two steps, and depends first on the energy being stored in the inductance L_c and second, on the energy transferred from the inductance L_c to the capacitor C_s . Generally, the energy being stored in the inductor is

$$E_L = \frac{1}{2} L_c i^2. \quad (8.27)$$

The following calculation aims at finding the maximal energy stored in the inductance E_L . Since the energy depends on both the inductance and the current, and since the current

$i(t)$ is a function of the voltage $u_T(t)$, resistance R_c and inductance L_c , the calculation is presented in several steps.

At first, the short-circuit current is expressed during the time, when the switch is closed. It is described by the differential equation

$$\frac{di(t)}{dt} + \frac{1}{\tau}i(t) = \frac{u_T(t)}{L_c} \quad \text{with} \quad (8.28)$$

$$\tau = L_c/R_c \quad (8.29)$$

the time constant. Solving Eqn. 8.28 for the harmonic excitation $u_T(t) = u_0 \sin(\omega t)$ and with the initial condition $i(t = 0) = 0$ results in

$$i(t) = \frac{u_0}{R_c} \frac{\tau\omega \cdot \left(\exp(-t/\tau) - \cos(\omega t) \right) + \sin(\omega t)}{\tau^2\omega^2 + 1}. \quad (8.30)$$

The next step is to find the current maximum i_{\max} , which is a function of the three parameters t , τ and ω . For every parameter set (τ, ω) there is one time t at which the current $i(t)$ is maximal. To incorporate this dependency, the three parameters will be expressed by the two dependable parameters

$$\gamma = \omega\tau = \frac{\omega L_c}{R_c}, \quad (8.31)$$

$$\varphi = \omega t, \quad (8.32)$$

where φ is the phase angle and γ is known from the complex impedance \underline{Z} of the series circuit in the stationary case

$$\underline{Z} = \sqrt{(\omega L_c)^2 + R_c^2} \cdot e^{j \cdot \text{atan}\left(\frac{\omega L_c}{R_c}\right)} \quad (8.33)$$

as tangent of the phase shift (between voltage and current). With the current amplitude from Eqn. 8.26, Eqn. 8.30 is rewritten to

$$i(\varphi, \gamma) = i_0 \cdot \frac{\gamma \left(\exp(-\varphi/\gamma) - \cos(\varphi) \right) + \sin(\varphi)}{(\gamma^2 + 1)}. \quad (8.34)$$

The transient current behavior is visualized in Fig. 8.12. The current maximum is shifted towards higher phase angles φ with increasing inductance L_c . The meaning and impact of γ is explained as followed: The case $\gamma \ll 1$ expresses that the resistance R_c is much greater than the impedance ωL_c . Consequently, the current follows the voltage almost without any phase shift and the current maximum is reached at $\varphi = \pi/2$. The opposite case is obtained when $\gamma \gg 1$ ($R_c \ll \omega L_c$) and occurs when the inductive behavior is dominant.

The result is a phase shift between voltage and current approaching $\Delta\varphi = \pi/2$ and the current maximum is reached at the phase angle $\varphi = \pi$.

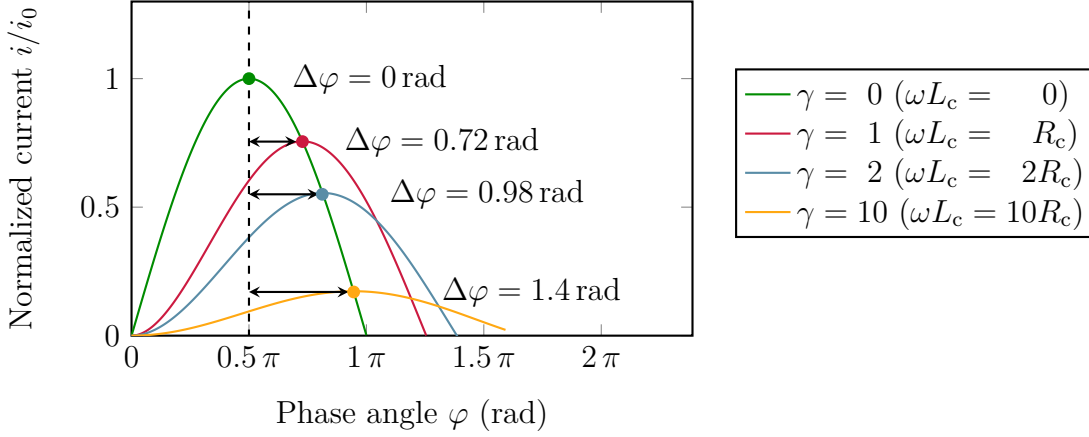


Figure 8.12: Transient normalized current i/i_0 as a function of phase angle φ for the first driving half-wave and for different ratios γ . With an increasing impedance ωL_c , the current maximum decreases and is reached at greater phase angles, leading to phase shifts $\Delta\varphi$ with respect to the current maximum in a purely resistive circuit at $\varphi = 0.5\pi$.

To calculate the current maximum as a function of φ and γ , the extreme value problem

$$\left. \frac{\partial i(\varphi, \gamma)}{\partial \gamma} \right|_{\varphi=\varphi_e, \gamma=\gamma_e} = 0 \quad (8.35)$$

is solved and leads to the following characteristic equation

$$-\exp(-\varphi_e/\gamma_e) + \cos(\varphi_e) + \gamma_e \sin(\varphi_e) = 0. \quad (8.36)$$

The pairs (φ_e, γ_e) span a solution set and describe the relation between phase angle φ and γ to maximize the current. The maximal current as a function of γ is

$$i_{\max}(\gamma = \gamma_e) = i(\varphi_e, \gamma_e). \quad (8.37)$$

According to Fig. 8.12 an increasing inductance (increasing γ) leads to a decreasing current maximum. The maximal inductor energy, which is directly proportional to the product of squared current maximum i_{\max} and inductance L_c , is calculated by

$$E_{L,\max} = \frac{L_c}{2} \cdot i_{\max}^2(\gamma). \quad (8.38)$$

Replacing R_c in Eqns. 8.26 by Eqn. 8.31 leads to the expression $L_c = \gamma R_c/\omega$. Substituting L_c in Eqn. 8.38 results in

$$E_{L,\max}(\gamma) = \frac{R_c}{2 \cdot \omega} \cdot \gamma \cdot i_{\max}^2(\gamma). \quad (8.39)$$

According to Eqn. 8.2, the maximal energy $E_{\text{elec,max}}$, dissipated by an impedance matched

load ($R_c = R_L$) during $0 < t < T/2$, is limited by

$$E_{\text{elec,max}} = \int_{t=0}^{T/2} \frac{(u_0 \sin(\omega t))^2}{4R_c} dt \quad (8.40)$$

$$E_{\text{elec,max}} = \frac{\pi}{8} \cdot \frac{u_0^2}{\omega R_c} = \frac{\pi}{8} \cdot i_0^2 \frac{R_c}{\omega}. \quad (8.41)$$

Dividing Eqn. 8.39 by Eqn. 8.41 leads to the expression of the efficiency

$$\eta_{\text{SMFE}} = \frac{E_{L,\text{max}}(\gamma)}{E_{\text{elec,max}}} = \frac{4}{\pi} \cdot \gamma \cdot \left(\frac{i_{\text{max}}(\gamma)}{i_0} \right)^2. \quad (8.42)$$

The efficiency as a function of γ is presented in Fig. 8.13. The maximal efficiency is

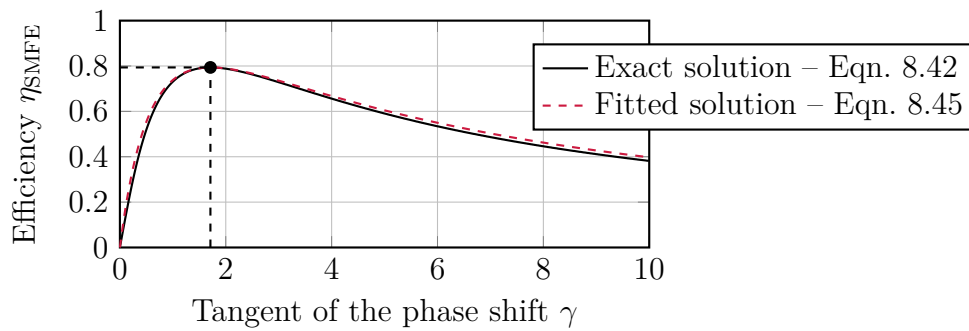


Figure 8.13: Normalized maximal energy E_{max} of the SMFE as a function of γ

obtained for $\gamma_{\text{opt}} \approx 1.71$. With respect to Eqn. 8.36, the corresponding phase angle is $\varphi_{\text{opt}} = 2.49$ rad, which is equivalent to

$$t_{\text{opt}} = 0.79 \cdot \frac{T}{2}. \quad (8.43)$$

The optimal inductance, corresponding to $\gamma_{\text{opt}} \approx 1.71$, is

$$L_{\text{opt}} = \frac{\gamma_{\text{opt}} \cdot R_c}{\omega}. \quad (8.44)$$

Remarkably is, that the curve in Figure 8.13 is similar to the curve of power transfer of a voltage source to a resistive load. The function

$$E_{\text{fit}} = \|E_{\text{max}}\|_{\infty} \cdot \frac{6.84 \cdot \gamma}{(\gamma + 1.71)^2} \quad (8.45)$$

can be used to approximate the energy curve and appears as a fit function in Figure 8.13. The maximal relative error is 1.8% in the interval $0 \leq \gamma \leq 10$. Finally, the former modeling steps of this section ends up in predicting the maximal efficiency of the SMFE

under ideal conditions (resistive losses, but no diode losses) to be

$$\eta_{\text{SMFE,max}} = 0.79 = 79\%. \quad (8.46)$$

The efficiency is strongly dependent on the parameters resistance R_c , inductance L_c and the angular frequency ω . Whether the SMFE circuit is a suitable circuit for the studied electromagnetic energy harvester is now discussed.

The angular frequency of the basic oscillation of the electromagnetic energy harvester is $\omega_0 = 210 \text{ rad/s}$. Relevant SMFE parameters for the two coil setups with $N = 530$ and $N = 1060$ turns from Sec. 7 are listed in Tab. 8.2

Table 8.2: Electromagnetic energy harvester parameters and attainable SMFE efficiency at 25 km/h of the two studied systems

Number of turns	N	(1)	530	1060
Total resistance	R_c	(Ω)	62	262
Total inductance	L_c	(mH)	3.2	13.5
Phase shift tangent	γ	(1)	0.011	0.011
Fundamental angular frequency	ω	(rad/s)	210	210
Maximal efficiency (if $u_T \leq u_{s,0}$)	η_{max}	(%)	2	2

With the given setups, the SMFE circuit, connected to the developed electromagnetic energy harvester, would provide a maximal efficiency of 2% when the voltage $u_T \leq u_{s,0}$. For the less interesting case $u_T > u_{s,0}$, not only the inductor drives the current to the storage but also the voltage source (which is deactivated when $u_T \leq u_{s,0}$). Only in this case, when the capacitor is only slightly charged, the efficiency would be higher than 2% and close to the one of an SEH.

With increasing vehicle speed the fundamental angular frequency of the transducers is increased and leads to a higher efficiency. At 50 km/h, it is still very low at 5%. An option is to tune the efficiency by increasing the total inductance, while the total resistance must remain unaffected. For example, to obtain an efficiency of 30% with the given data, an ideal inductor of 60 mH is required, while its parasitic resistance must be much smaller than the coil resistance R_c . Inductors in the range of a few tens of millihenry with negligible resistance possess a high permeable core, are large in size and increase both system mass and costs significantly. Consequently, this interface circuit does not present a meaningful alternative to reach both a higher efficiency and a higher output voltage.

To sum up, under optimal conditions a maximal efficiency of $\eta = 79\%$ can be attained. The efficiency is limited, because the circuit extracts the magnetic field energy after $t = 0.79T/2$ and waits, as depicted in Fig. 8.11, until $t = T/2$ before the next extraction cycle starts. In the time interval $0.79T/2 < t < T/2$ no energy is extracted. If the energy was extracted in that interval, theoretically, a slightly higher efficiency could be reached.

In practice, the case $\gamma \ll 1.71$ is more relevant and leads to small efficiency. As the time

constant is small compared to the oscillation period ($\tau \ll T$), the inductor L_c reaches almost instantaneously the actual current $i(t) = u(t)/R$ with negligible retardation. The voltage drop u_L across the inductance is then zero. As a result, the energy provided by the voltage source is mostly dissipated across the resistance R_L instead of being provided to the inductor. However, a large improvement can be reached if the inductor is regularly charged and discharged and if the energy is extracted several times within the same time period instead of only ones. This idea leads to the following new boost concept for electromagnetic energy harvesters.

8.4 Energizing and Transferring Circuit – EaT

Instead of charging the inductor L_c and transferring its energy once per half cycle, an interface circuit can terminate the process multiple times within the same time interval. Such a circuit resembles the Synchronized Magnetic Flux Extraction scheme. However, the switch is not controlled by a peak current detector but by PWM-like signal that connects and disconnects the circuit more often, as presented in Fig. 8.14. This kind of circuit is a step-up converter.

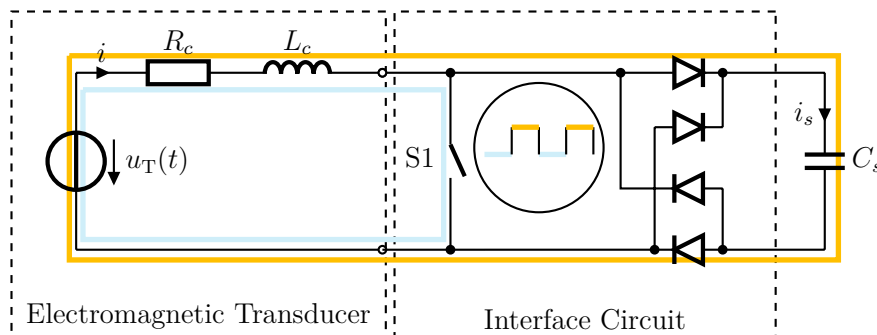


Figure 8.14: Energizing and Transferring circuit - The PWM controlled switch enables an efficient energy transfer towards the capacitor C_s

In 2017, Bonisoli et al. [179] presented such an active boost converter, with switching times greater than 20 kHz for a low-frequency transducer with a fundamental frequency of $f_0 < 100$ Hz. In the following, it is called Energizing and Transferring (EaT). Bonisoli et al. developed a through-out logic, that closes and opens the switch based on two conditions. First, the actual current level has to exceed a minimum threshold current level. Second, a fixed time delay has to be elapsed. In addition, in each step the threshold current level is adapted, based on both an interface dependent coefficient and on the last obtained current value, before the energy is transferred. Therefore, the circuit concept requires monitoring the current.

Extensive simulations in [179] of different coefficients revealed the best parameter setup for one specific system, but have the drawback to be repeated for every single energy harvester setup again. More desirable would be a universal approach, without the requirement

of a synchronization between switch and transducer current. Therefore, the next objective is to deduce analytically and numerically optimal switching parameters for a high circuit efficiency over a wide voltage range, independently of the specific electromagnetic energy harvester, as presented by Germer et al. in [168].

The interface principle exploits the inherent inductive nature of the electromagnetic transducer and relies on periodically switching between a short-circuited and open-circuited energy harvester to charge and discharge the inductor, respectively. During the energizing phase with the duration t_E , the inherent inductance is charged, while during the transferring phase t_T , the inductor energy E_L moves from the inductance L_c to the storage C_s . Figure 8.15 shows exemplarily the current evolution of the RLC network and the amount of transferred energy ΔE , being charged during t_E and entirely transferred during t_T once and twice within the same time interval, with $\tau = L_c/R_c$.

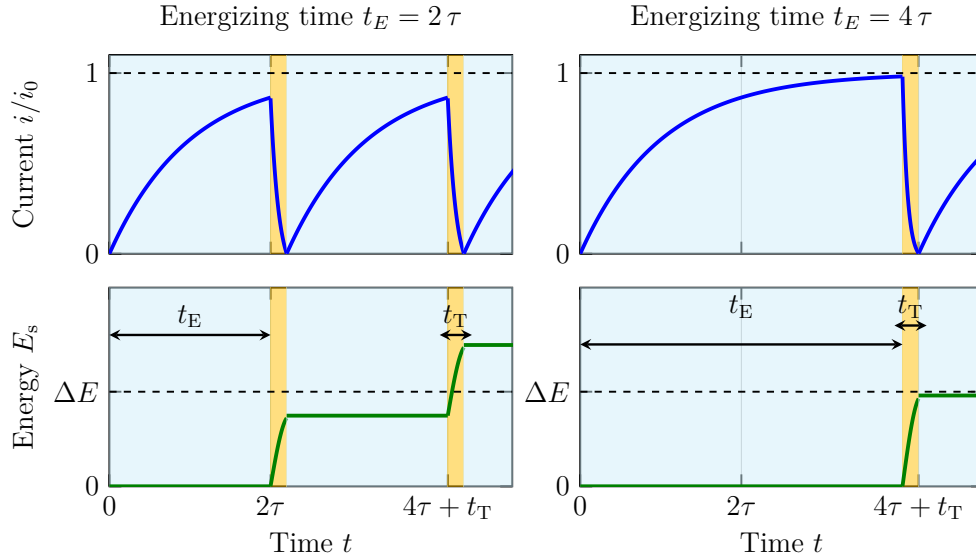


Figure 8.15: Current i and capacitor energy E_s for energizing times $t_E = 2\tau$ and $t_E = 4\tau$, supposing that $u_0 < u_{s,0}$. Since the switching times are much smaller than the signal period ($t_E, t_T \ll T$), the voltage u_T can be considered constant in the interval $0 < t < t_E + t_T$. After $t = 4\tau$, more energy is transferred with the energizing time $t_E = 2\tau$ despite of the lower current.

As illustrated, after $t = 4\tau + t_T$, an energizing time with $t_E = 2\tau$ leads to a higher capacitor energy E_s than with $t_E = 4\tau$. Therefore, the question arises, how long should the inductor be charged before the energy is transferred. To find the best switching time t_E and t_T , a quasi-stationary oscillation is supposed, which implies that the inductor conducts almost instantaneously the current $i(t)$, compared to the oscillation period ($\tau \ll T$). This is generally the case and specifically valid for the studied energy harvesters from the previous chapter, since $\tau = 47 \mu\text{s} \ll T = 30 \text{ ms}$. For the sake of simplicity, in the following two subsections only the energizing phase is illustrated and analyzed, while in Sec. 8.4.3 the transferring phase is incorporated in the analysis.

8.4.1 Discontinuous Current Mode – DCM

The amount of energy per time interval is calculated in the following. Let $u(t) = u_0$ be the voltage source of the electrical circuit branch, which can be considered constant, since $\tau \ll T$. A switch closes and opens the transducer terminal periodically after t_E and after $t_E + t_T$, respectively. In this scenario, the transferring time is assumed to be long enough, that the inductor energy is fully transferred, and the inductor current decreases down to zero (discontinuous current mode (DCM)) as shown in Fig. 8.16. The starting point to deduce the efficiency is the solution of the differential equation when the switch is closed, which is

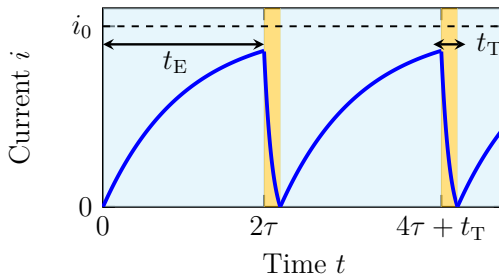


Figure 8.16: Current over time of the discontinuous current mode

As in the DCM the initial condition is always $i(t = 0) = 0$, the current $i(t)$ is

$$\frac{di(t)}{dt} + \frac{1}{\tau}i(t) = \frac{u_0}{L} \quad \text{with} \quad \tau = L_c/R_c \quad \text{and} \quad i_0 = u_0/R_c. \quad (8.47)$$

As in the DCM the initial condition is always $i(t = 0) = 0$, the current $i(t)$ is

$$i(t) = i_0 \cdot (1 - \exp(-t/\tau)), \quad (8.48)$$

and when the switch is opened at $t = t_E$ the current is

$$i(t_E) = i_0 \cdot (1 - \exp(-t_E/\tau)). \quad (8.49)$$

Repeating this process k times in the interval $[0, T]$ and supposing an immediate energy transfer for the moment, the total energy after k energizing phases, is

$$E_{\text{DCM}} = k \cdot \frac{1}{2} L_c i_0^2 \cdot (1 - \exp(-t_E/\tau))^2. \quad (8.50)$$

Replacing k by $k = \frac{T}{t_E}$ leads to the following expression of the energy

$$E_{\text{DCM}} = \frac{T}{t_E} \frac{L_c}{2} i_0^2 (1 - \exp(-t_E/\tau))^2. \quad (8.51)$$

According to Eqn. 8.2, the maximal energy with the voltage source $u_T = u_0$ is

$$E_{\text{elec,max}} = \int_{t=0}^T \frac{u_0^2}{4R_c} dt = \frac{TR_c i_0^2}{4}, \quad (8.52)$$

with $i_0 = u_0/R_c$. Normalizing the energy E_{DCM} by $E_{\text{elec,max}}$ results in the efficiency

$$\eta_{\text{DCM}} = \frac{E_{\text{DCM}}}{E_{\text{elec,max}}} = \frac{\frac{T}{t_E} \frac{L_c}{2} i_0^2 (1 - \exp(-t_E/\tau))^2}{\frac{TR_c i_0^2}{4}}. \quad (8.53)$$

Introducing the energizing time ratio x as the normalized energizing time with

$$x = \frac{t_E}{\tau} = t_E \cdot \frac{R_c}{L_c} \quad (8.54)$$

leads finally to

$$\eta_{\text{DCM}} = 2 \frac{(1 - \exp(-x))^2}{x}. \quad (8.55)$$

The efficiency η_{DCM} over x is depicted in Fig. 8.17. To determine the optimal parameter x , that maximizes the efficiency η_{DCM} , its derivative is calculated and set to zero ($\partial\eta_{\text{DCM}}/\partial x|_{x=x_e} = 0$), leading to the characteristic equation

$$\exp(x_e) - 2x_e - 1 = 0. \quad (8.56)$$

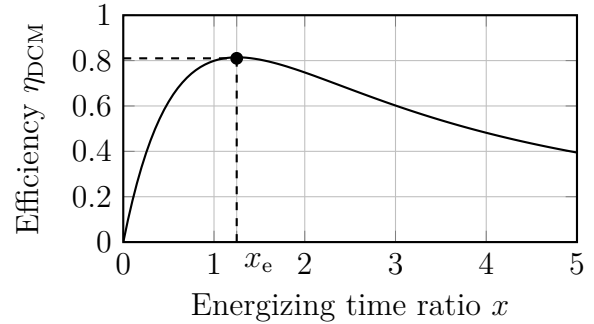


Figure 8.17: Maximal efficiency as a function of x for the DCM

The maximal efficiency is limited by $\eta_{\text{DCM,max}} = 81\%$ and necessitates the switch opening periodically at $x_e = 1.25$.

Even if the maximal efficiency is similar to the highest efficiency of a tuned SMFE, no tuning inductor is needed anymore. Further, no complex algorithm such as maximum peak detection or zero crossing detection have to be embedded. In addition, the optimal switching time $t_{E,e} = x_e \cdot \tau$ is only dependent on the time constant τ of the inductor.

A switch with defined energizing and transferring times is enough to increase the storage capacitor voltage u_s efficiently to a higher voltage than the electromagnetic output voltage u_T . Similar to the SFME circuit, ideal conditions were supposed but still 19% of the energy will be lost. To understand why still a part of the energy is dissipated, the derivative of E_{DCM} with respect to x is calculated and normalized. It describes the infinitesimal energy difference dE_{DCM} , which is added, as a function

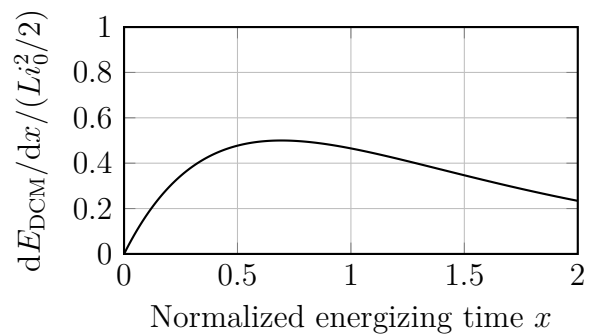


Figure 8.18: Infinitesimal energy difference that is stored in the inductor over normalized energizing time

of the normalized time ratio x . The relation is plotted in Fig. 8.18. As the normalized current $i(x)/i_0 = 1 - \exp(-x)$ increases for small x almost linearly, more energy can be added to the inductor when the inductor is charged in the same time interval e.g. from $0.1 i_0$ to $0.2 i_0$ ($\Delta E = 0.015 Li_0^2$) instead of from $0 i_0$ to $0.1 i_0$ ($\Delta E = 0.005 Li_0^2$). Moreover, dE_{DCM} is maximal for $x = 0.7$, which is related to the current $i(x) = 0.5 i_0$. Consequently, the current should not return to zero but maintain an initial value, ideally $i(x)/i_0 = 0.5$. This consideration leads to the continuous current mode (CCM), generally described in [187].

8.4.2 Continuous Current Mode – CCM

The continuous current mode (CCM) describes the more general situation, in which the inductor energy is not entirely removed, and an initial current $i_{L,0}$ remains. Figure 8.19 shows the current evolution of the CCM. To determine the maximal efficiency, the differential equation of the circuit, described by Eqn. 8.47 is solved similarly to the former section, with the difference that the initial condition now is

$$i(t = 0) = i_{L,0}. \quad (8.57)$$

Then, the solution is

$$i(t = t_E) = i_0 (1 - \exp(-t_E/\tau)) + i_{L,0} \exp(-t_E/\tau). \quad (8.58)$$

As demonstrated in Sec. 8.4.1, the energy E_{CCM} can be expressed as

$$E_{\text{CCM}} = \frac{T}{t_E} \frac{L_c}{2} (i^2(t_E) - i_{L,0}^2). \quad (8.59)$$

The initial current ratio

$$n = i_{L,0}/i_0 \quad (8.60)$$

is introduced and together with the energizing time ratio $x = t_E/\tau$ the current can be expressed as

$$i(t = t_E) = i_0 (1 - \exp(-x) + n \exp(-x)). \quad (8.61)$$

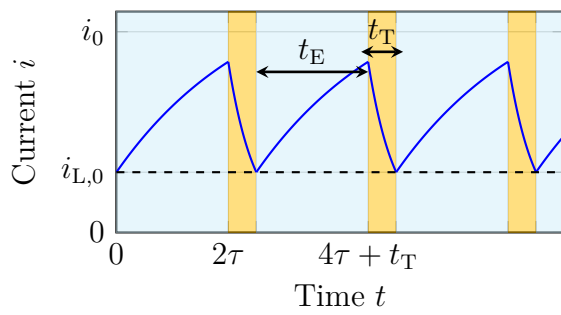


Figure 8.19: Current evolution over time of the continuous current mode. During the inductor discharge, the current does not drop to zero.

Similarly, the energy is rewritten as

$$E_{\text{CCM}}(x, n) = \frac{L_c T}{2 \tau} i_0^2 \cdot \frac{n^2 [\exp(-2x) - 1] - 2n [\exp(-x) - 1] \exp(-x) + [\exp(-x) - 1]^2}{x}. \quad (8.62)$$

Through normalization to $E_{\text{elec,max}}$ the efficiency is expressed by

$$\eta_{\text{CCM}}(x, n) = 2 \frac{n^2 [\exp(-2x) - 1] - 2n [\exp(-x) - 1] \exp(-x) + [\exp(-x) - 1]^2}{x}. \quad (8.63)$$

Setting the derivative of the efficiency with respect to the normalized initial current and with respect to the normalized energizing time to zero will lead to the set of solution pairs (x_e, n_e) fulfilling the conditions, first,

$$\left. \frac{\partial \eta_{\text{CCM}}}{\partial n} \right|_{x=x_e, n=n_e} = 0 \iff n_e = \frac{1 - \exp(-x_e)}{2 \sinh(x_e)}, \quad (8.64)$$

and second,

$$\begin{aligned} \left. \frac{\partial \eta_{\text{CCM}}}{\partial x} \right|_{x=x_e, n=n_e} = 0 \iff \\ n_e (\exp(2x_e) - x_e - 1) - 2 \exp(x_e)(x_e + 1) + 2x_e + \exp(2x_e) + 1 = 0. \end{aligned} \quad (8.65)$$

Substituting n_e in Eqn. 8.65 by Eqn. 8.64 and simplifying leads to

$$\sinh(x_e) - x_e = 0. \quad (8.66)$$

Inserting Eqns. 8.64 and 8.66 in Eqn. 8.63 results in the expression of the maximal efficiency as a function of $x = x_e$

$$\boxed{\eta_{\text{CCM,max}} = 2 \frac{\exp(x) - 1}{x (\exp(x) + 1)}}. \quad (8.67)$$

The efficiency as a function of the normalized energizing time $x = x_e$ is illustrated for the optimal pairs (x_e, n_e) in Fig. 8.20 with the related optimal initial current ratio n_e and opposed to the DCM results. Since the maximal efficiency is reached with the pair $(x, n) = (0, 0.5)$, the initial current should always be $i_{L,0} = 0.5 i_0$, which is identical to the optimal load case, where the current is half of the short-circuit current i_0 . However, a normalized time ratio $x = 0$ for charging the inductor is not physically meaningful. In practice, time is needed to charge and discharge the inductor. In addition, the formerly ignored transferring time t_T affects the amount of energy removed from the inductor. Therefore, the process of transferring energy to the capacitor is subsequently investigated.

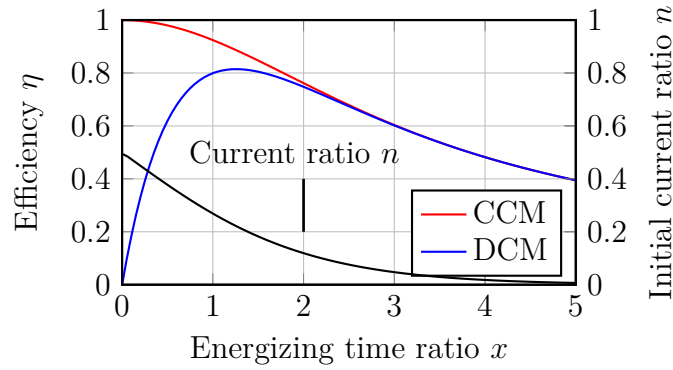


Figure 8.20: Efficiency η_{CCM} for the optimal pair (x, n) and the corresponding initial current ratio n opposed to the efficiency η_{DCM} as a function of energizing time ratio $x = t_E/\tau$.

8.4.3 Transferring Phase

While in the previous analytical description the time to transfer the energy was neglected, it is now incorporated. When the switch S1 of Fig. 8.14 is opened and the diodes are ideally conductive, the electrical circuit can be simplified to the one, depicted in Fig. 8.21. The math to describe the system is similar to the one of a SECE circuit as presented in Sec. 6.5, with the difference, that during the transferring phase the voltage source $u_T = u_0$ is in series with the components R_c , L_c , C_s .

The system is described by the inhomogeneous second order differential equation of an electrical resonator with

$$\frac{d^2u}{dt^2} + 2\delta\frac{du}{dt} + \omega_0^2u = \omega_0^2u_0, \quad (8.68)$$

where $u = u_s$, $\delta = R_c/(2L_c)$ and $\omega_0^2 = 1/(L_cC_s)$ are the voltage across the capacitor, the decay rate and the fundamental angular frequency, respectively. The initial conditions are

$$\begin{aligned} i_L(t=0) &= i_{L,0} \\ u(t=0) &= u_{s,0}. \end{aligned} \quad (8.69)$$

The solution of the inhomogeneous differential equation has the general form

$$u(t) = u_h(t) + u_p(t) \quad (8.70)$$

where $u_h(t)$ and $u_p(t)$ are the homogeneous and particular solution, respectively. With the data of the considered energy harvester from Tab. 8.2 the decay rate ($\delta = 262\Omega/(2 \cdot 13\text{mH}) = 10\text{kHz}$) is much larger than the fundamental angular frequency

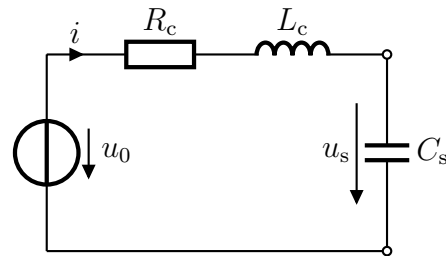


Figure 8.21: Electrical resonator in the transferring phase

($\omega_0 = 210$ Hz). Consequently, the homogeneous solution represents a creeping oscillation (heavily damped) with the angular frequency

$$\omega_e^2 = \delta^2 - \omega_0^2. \quad (8.71)$$

The homogeneous solution is a linear combination of hyperbolic functions, expressed as

$$u_h = \exp(-\delta t) \cdot \left(A \cosh(\omega_e t) + B \sinh(\omega_e t) \right). \quad (8.72)$$

The initial conditions of Eqn. 8.69 are inserted and the voltage is expressed as

$$u(t) = u_0 + \exp(-\delta t) \cdot \left((u_{s,0} - u_0) \cdot \cosh(\omega_e t) + \left(\frac{i_{L,0} + \delta C_s (u_{s,0} - u_0)}{\omega_e C_s} \right) \cdot \sinh(\omega_e t) \right). \quad (8.73)$$

After several reformulation steps, described in App. F, follows the efficiency η_{EaT} with

$$\eta_{\text{EaT}} = 2 \frac{u_N^2(x, y, n, q, b) - b^2}{q^2 \cdot (x + y)}, \quad (8.74)$$

where u_N is the normalized function $u_N = u(t)/u_0$. The efficiency of the circuit depends on the dimensionless parameters of the quintuple (x, y, n, q, b) . Although the quality factor q is generally given for an energy harvester, the quadruple (x, y, n, b) still remains to vary the efficiency. The numerical calculation of the best parameters for a given voltage ratio b is very sensible to the accuracy of the studied parameters. For the general continuous current mode, the highest efficiencies were calculated as a function of b . There is one pair (x, y) that correspond to each capacitor voltage ratio b , maximizing the efficiency. Both the optimal pair (x, y) and the related maximal efficiency are depicted in Fig. 8.22, for a capacitor $C_s = 220 \mu\text{F}$ and for the quality factor $q = 1/(262 \Omega) \cdot \sqrt{13 \text{ mH}/220 \mu\text{F}} = 0.03$, which is linked to the energy harvester parameters. Additionally, the efficiency of an ideal SEH interface circuit of the constant voltage signal $u_T = u_0$ is presented in Fig. 8.22.

Corresponding to Fig. 8.22, in the interval $0 < b < 0.5$ the transferring time ratio $y = t_T/\tau$ raises with the voltage ratio $b = u_s/u_0$ and tends towards infinity when $b = 0.5$. Accordingly, at this capacitor voltage ratio, the switch S1 is open most of the time ($y \gg x$), which means that the inductor should not be charged, but the energy should be directly transferred from the voltage source to the capacitor. In the interval $0 \leq b < 0.7$ the circuit behavior resembles an SEH. At higher capacitor voltage ratios $b \geq 0.7$, the impact of switching becomes more important and enables a high efficient energy transfer, when the storage voltage u_s becomes closer to the voltage of the voltage source u_0 . In the most interesting area, when $b \geq 1$, the transferring time ratio y continuously decreases, while the energizing time x increases to $x = 1.25$. The efficiency η_{EaT} slightly decreases but stays above $\eta = 0.8 = 80\%$ for $0.25 < b < 2$.

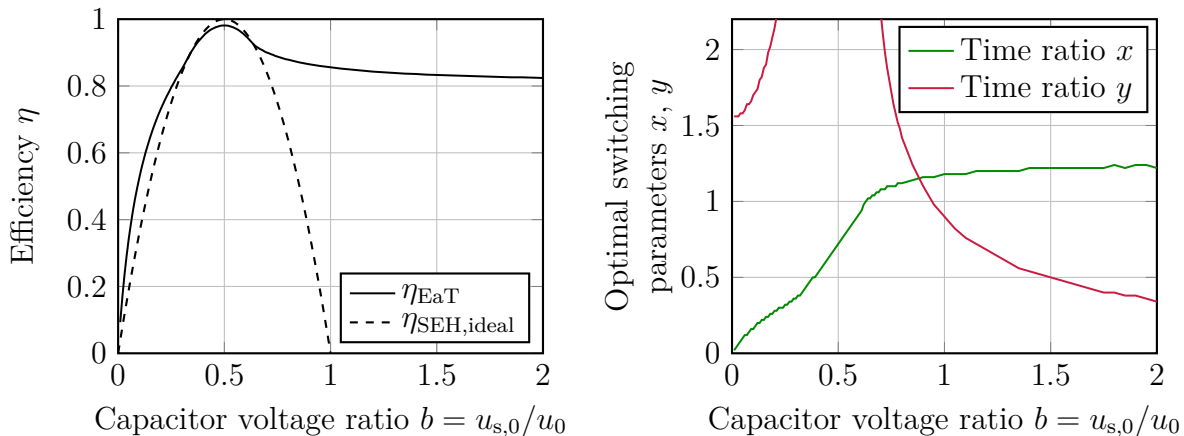


Figure 8.22: Maximal efficiency $\eta_{\text{EaT,max}}(x, y)$ (solid line) and corresponding optimal switching parameters as a function of capacitor voltage ratio b according to Eqn. 8.74 for the CCM and for a quality factor $q = 0.03$. The efficiency of the EaT interface circuit is opposed to the one of an ideal SEH circuit (dashed line).

As to each capacitor voltage ratio b different optimal parameter x and y exist, and as the energy harvester signal $u_{\text{T}}(t)$ is not constant but varies over time, an ideal implementation would require additional electronics to monitor both input voltage and storage capacitor voltage. However, acceptably high efficiencies can be reached, if the time ratios x and y are not modified as a function of voltage ratio b but chosen to be fixed. The impact will be analyzed numerically for the developed energy harvester.

8.4.4 Simulation and System Performance

LTspice simulations of the bidirectionally coupled energy harvester with 1060 turns, being excited at 25 km/h as explained in Sec. 7.6, were conducted to evaluate the analytical results, numerically. The interesting case, in which the capacitor voltage is $u_{\text{s},0} = u_0 = 2.7 \text{ V}$, is studied exemplarily and corresponds to $b = u_{\text{s},0}/u_0 = 1$. The corresponding optimal parameters deduced from Fig. 8.22 are $x = 1.2$ and $y = 0.9$. As the time constant of the system is $\tau = L/R = 13 \text{ mH}/262 \Omega = 50 \mu\text{s}$, the corresponding time parameters are $t_{\text{E}} = x \cdot \tau = 60 \mu\text{s}$ and $t_{\text{T}} = y \cdot \tau = 45 \mu\text{s}$.

Different switching times ($t_{\text{E}}, t_{\text{T}}$) were studied with regard to their efficiencies. The efficiencies were deduced from simulations with lossy rectifying Schottky diodes (BAT54) but without switching losses. The efficiencies are listed in Tab. 8.3.

According to the simulation data, the highest efficiency is obtained for $(t_{\text{E}}, t_{\text{T}}) = (45, 25) \mu\text{s}$ which corresponds to $(x, y) = (0.9, 0.5)$. A slightly smaller efficiency is reached with the predicted parameter constellation $(x, y) = (1.2, 0.9)$. There are also other parameter pairs, leading to efficiencies $\eta \geq 65\%$. They are highlighted in green in Tab. 8.3. The reason, why the analytically predicted parameters does lead to a high efficiency but not to the highest, is mainly related to the rectifying diodes. Their forward voltages reduce the

Table 8.3: Interface circuit efficiency η of the energy harvester at 25 km/h for different energizing and transferring parameters t_E , t_T , for the initial capacitor voltage $u_{s,0} = 2.7$ V, corresponding to $b = 1$ and with Schottky diodes.

t_T (μs) \backslash t_E (μs)	25	45	60
10	0.69	0.57	0.49
25	0.65	0.70	0.65
45	0.47	0.63	0.63
60	0.39	0.56	0.59

effectively available voltage u_0 by about 0.6 V in total. In addition, while the analytical results are valid for one fixed voltage ratio b , the energy harvester generates a signal with varying voltage $u_T(t)$, whereas most of the time $u_T(t) < u_0$, resulting in $b > 1$.

Since in practice switching losses appear, which are proportional to the switching frequency, the parameter set $(t_E, t_T) = (45, 25)$ μs is preferred over the parameter set $(25, 10)$ μs .

Additionally to the numerical parameter study for a fixed capacitor voltage $u_{s,0}$, the impact of a varying capacitor voltage was studied. The efficiency is investigated as a function of initial capacitor voltage $u_{s,0}$ for the fixed switching times $(t_E, t_T) = (45, 25)$ μs and is illustrated in Fig 8.23. The efficiency increases until $u_{s,0} = 3.4$ V and remains at a high level of 65 % until $u_{s,0} \leq 8$ V.

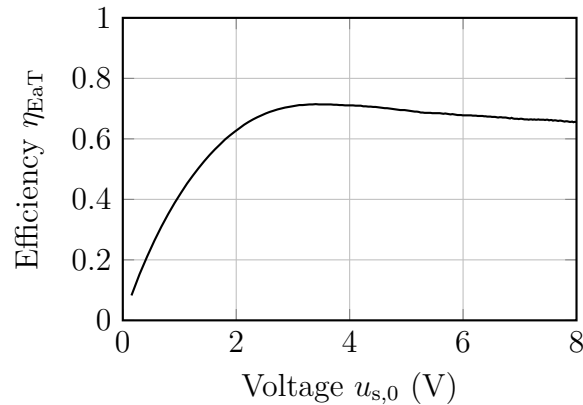


Figure 8.23: Efficiency η_{EaT} as a function of initial capacitor voltage $u_{s,0}$ deduced from the network simulation in LTspice with $(t_E, t_T) = (45, 25)$ μs and considering Schottky diodes. The efficiency is 65 % at $u_{s,0} \geq 2$ V.

While the previously studied interface circuits SEH, VD and VT no longer supply energy to the capacitor at $u_{s,0} = 2.4$ V, 4.8 V and 7.2 V, respectively, the EaT circuit adds energy with more than 65 % to the capacitor at even higher voltages. Therefore, this circuit is therefore highly recommended. However, the strongest challenge is to implement a self-powered, low-loss switch circuit.

8.5 Numerical Validation

To finally choose a suitable interface circuit, LTspice simulations of the bidirectionally coupled network of the electromagnetic energy harvester with 1060 turns, depicted in Fig. 7.20, were performed with the interface circuits SEH, VD, VT and EaT with $(t_E, t_T) = (45, 25) \mu\text{s}$. The intermediate capacitors of the voltage doubler and tripler were $47 \mu\text{F}$. As the amount of energy is critical at low velocities, the capacitor C_s was studied at 25 km/h for 60 s, which are imposed by OEMs. From the capacitor voltage signal the added energy was calculated, and the efficiency was obtained through normalization to the maximal energy being transferred under load matching conditions. Both the voltage-time evolution of the storage capacitor $C_s = 220 \mu\text{F}$ and the efficiency as a function of initial capacitor voltage are depicted in Fig. 8.24. The dashed line in the voltage-time diagram indicates the required capacitor voltage $u_{\text{charged}} = 3.9 \text{ V}$ for signal transmission.

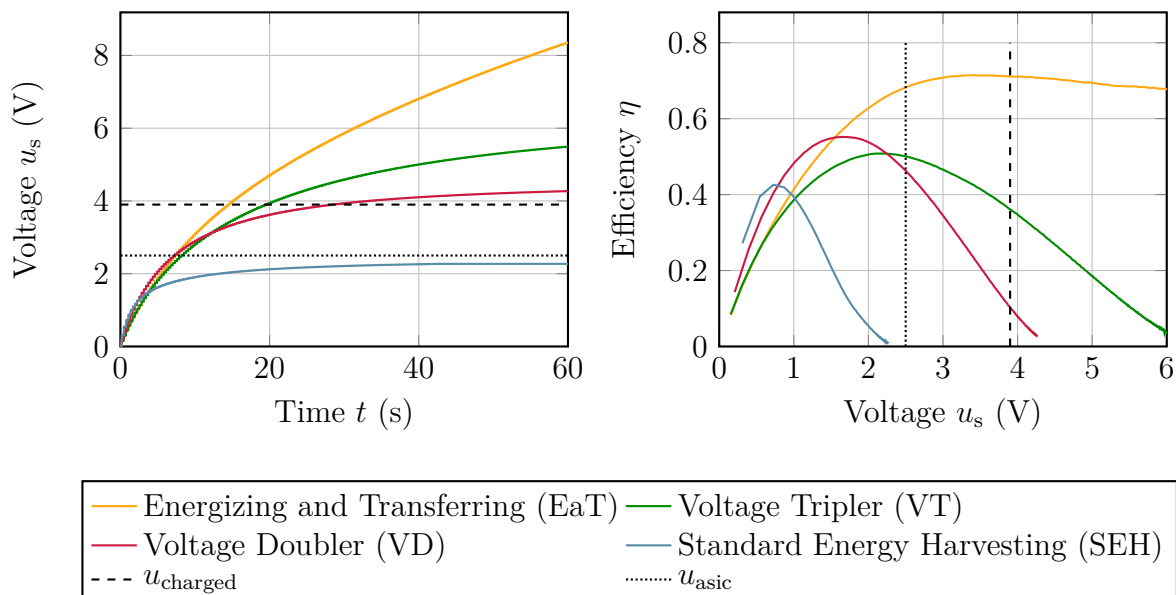


Figure 8.24: LTspice simulation of the electromagnetic energy harvester with 1060 turns at 25 km/h, connected to different interface circuits. The efficiency was derived from the capacitor voltage evolution over time. The dashed and densely dotted lines indicate the required capacitor voltage.

Obviously, all interface circuits, except of the SEH, fulfill the energy requirements and charge the capacitor in less than 60 s. Due to the high efficiency, the EaT circuit needs the least amount of time, followed by the VT and the VD. As the charging voltage is not limited, the efficiency of an EaT circuit remains high, also at voltages higher than the required voltage of 3.9 V. However, since the VD and VT are very easy to build and use in experimental tests in a tire, they were preferred for the experimental validation, described in the next chapter, while implementing an EaT in combination with an electromagnetic transducer for experimental verification inside the tire would have exceeded the scope of this work.

8.6 Summary

Electromagnetic Energy Harvester Interface Circuits

An overview of electromagnetic energy harvesting interface circuits have been provided. The performance was evaluated based on both a stochastic signal analysis and with LTspice simulations. As described in Sec. 7.20, the interface circuits SEH, VD, VT, SMFE and EaT were connected to the network model of the electromagnetic energy harvester with 1060 turns. The simulation was conducted for an input acceleration signal, corresponding to $v = 25$ km/h while a force $F = 4170$ N was applied to the tire. In the following, the quantity $u_0 = \max(|u_T(t)|)$ represents the maximal voltage of the electromagnetic transducer .

Interface Circuit	SEH	VD	SMFE
EMEH voltage u_0	☹ $u_0 - 2u_d = 2.4$ V	☺ $2(u_0 - u_d) = 4.8$ V	☺ $u \gg u_0$
Efficiency at $u_s = u_0$	☹ 0 %	☺ 42 %	☹ < 2 %
Efficiency at $u_s = 3.9$ V	☹ 0 %	☹ 10 %	☹ < 2 %
Circuit complexity	☺ easy	☺ easy	☹ elevated
Large components	☺ no	☹ small C_1	☺ no
Cold start	☺ yes	☺ yes	☹ no

Interface Circuit	VT	SMFE (tuned) ^a	EaT (new)
Output voltage u	☺ $3(u_0 - u_d) = 7.2$ V	☺ $u \gg u_0$	☺ $u \gg u_0$
Efficiency at $u_s = u_0$	☺ 49 %	☺ 70 %	☺ 70 %
Efficiency at $u_s = 3.9$ V	☺ 36 %	☺ 70 %	☺ 71 %
Circuit complexity	☺ easy	☹ elevated	☹ medium
Large components	☹ small C_1, C_2	☹ ☹ bulky L	☺ no
Cold start	☺ yes	☹ no	☹ no

The EaT has an excellent performance. Since the well-known circuits VD and VT are easy to build and sufficient to fulfill the energy requirements, they are preferred for experimental validation inside the tire.

^aIn the efficiency analysis of the tuned SMFE, only the energizing phase has been considered. Since losses appear due to the rectifying diodes and in the transferring phase, it can be concluded, that the efficiency is identical or smaller than the one of the EaT.

9 Tire Prototype Testing and Experimental Results

Following the prior analytical and numerical modeling, energy prediction of common wheel energy harvesting mechanisms inside the tire, prototype development, and investigations of performant interface circuits, the developed prototypes are evaluated in this chapter. For this purpose, the prototypes are combined with suitable interface circuits and studied, experimentally .

An experimental setup with constant, repeatable and comparable test conditions appropriate to validate the presented system concepts was designed and manufactured. The main objectives were to characterize the prototypes as a function of the two main parameters the vehicle velocity v and the force F with which a tire is pressed against the road surface. Another goal was to find out whether the systems were robust and could withstand the hostile conditions. Since an energy harvester needs to be operational both at low velocities and at high velocities, the energy transducers were tested in a wide velocity range of $20 \text{ km/h} < v < 200 \text{ km/h}$. Furthermore, it was tested which of the systems would provide enough energy and perform better than a coin cell battery in terms of energy. With the mentioned objectives, an experimental study of the transferred energy from the transducer to the storage capacitor C_s across different interface circuits is associated. The interface circuits Standard Energy Harvesting, Electronic Breaker, Voltage Doubler and Voltage Tripler were tested because they could be easily assembled using discrete components. More advanced low-loss circuits such as integrated SECE circuits for piezoelectric energy harvesters or the presented EaT circuit for electromagnetic energy harvesters were not part of the test series inside the tire. However, the knowledge of the experimentally validated electromechanical system description by the measured voltage or current signal under open-circuit and short-circuit conditions, respectively, enables to predict the performance of any interface circuits, reliably.

This chapter is divided into four parts. First, the experimental setup, the measurement methods and constellations of the energy harvesters are presented. Then, one part is dedicated to the experimental validation of each energy harvester principle (tire wave based piezoelectric energy harvesting, strain based piezoelectric energy harvesting, tire wave based electromagnetic energy harvesting). Measurement data will be presented, compared with analytical predictions and rated. At the end, an overview will be given that summarizes the experimental results.

9.1 Experimental Setup

The experimentation necessitates the following preparation steps for gathering data:

1. Tire inner liner laser cleaning
2. Adhesive joint of the prototypes with the inner liner
3. Tire mounting on a special rim with holes for wire feedthrough
4. Wire feedthrough
5. Solder connection between prototype wires and slip ring wires
6. Wheel sealing and signal testing
7. Airproof verification of the wheel
8. Mounting the wheel on a tire test machine
9. Wire connection with measurement setup

The specific test devices, measurement tools and their properties are listed in Tab. 9.1. Selected preparation steps are illustrated in Fig. 9.1.

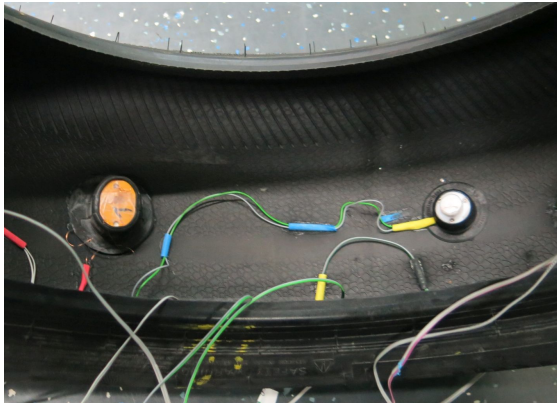
Table 9.1: Properties of test devices and measurement tools

Tire type	Continental PremiumContact 6 205 55 R16		
Tire setup	Tire pressure	2.3	bar
	Tire radius R at $F = 3000$ N load	0.31	m
Tire test bench	Drum diameter	1.9	m
	Minimal velocity v	20	km/h
	Minimal tire load F	1000	N
Signal recording	Bruel&Kjaer 6 Channel Signal Transmitter, Type 3050		
	Input impedance	1	M Ω
	Voltage range	± 31.6	V

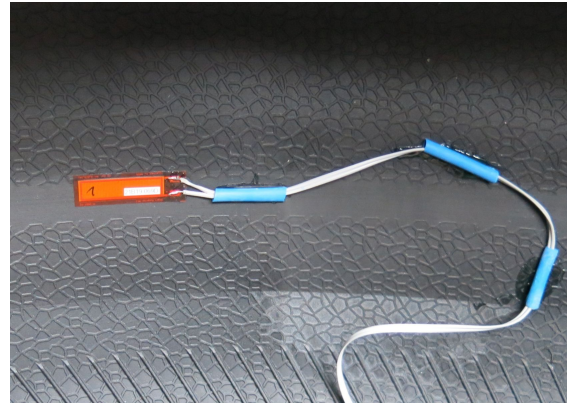
As listed in Tab. 9.1, a Bruel&Kjaer channel transmitter was used to measure the open-circuit voltage $u_{oc} = u_T$ of the electromagnetic transducers as illustrated in Fig. 9.2a. The signal recorder has a limited voltage range of ± 31.6 V, which is not sufficient to monitor the entire expected voltage of a piezoelectric transducer. Additionally, the input impedance of the measurement system with 1 M Ω is not significantly larger than the piezoelectric output impedance.¹ If the input impedance is in the range of the transducer's output impedance, systematic errors will occur. To decrease these errors and to extend the voltage measurement range, a voltage divider was placed between the piezoelectric terminal output and the signal transmitter input, as illustrated in Fig. 9.2b, and raised the input impedance to 10.5 M Ω and the voltage range to $21 \cdot (\pm 31.6) = \pm 663$ V. The voltage divider was used to measure the open-circuit voltage of piezoelectric transducers in one setup.

In a second setup, the voltage evolution of the storage capacitor was measured during 60 s. The input impedance of the signal transmitter and the storage capacitor build an

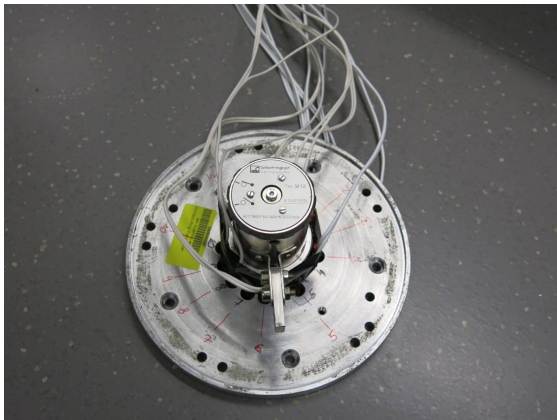
¹The impedance of a 10 nF capacitance at the fundamental angular frequency of 210 rad/s corresponding to the velocity $v = 25$ km/h is 480 k Ω .



(a) Inner liner with an acceleration based EH



(b) Inner liner with a strain based EH



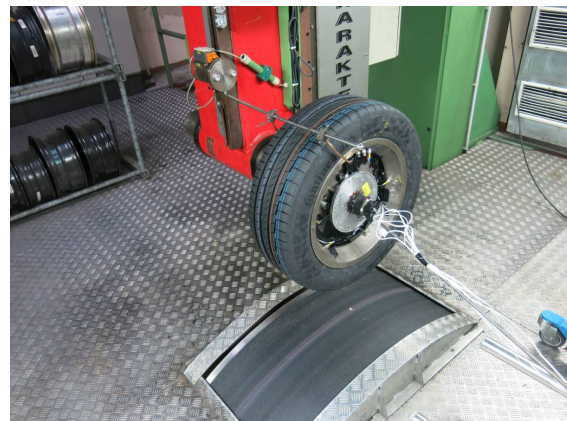
(c) Slip ring with electrical connections



(d) Tire before being mounted on the rim



(e) Airproof verification of the entire wheel



(f) Tire test machine with the mounted wheel

Figure 9.1: Devices installed in the tire and preliminary steps for the experiments

RC -network with a relatively low time constant $\tau = RC_s = 1 \text{ M}\Omega \cdot 220 \mu\text{F} = 220 \text{ s}$ compared to the measurement time of 60 s. As they would lead to a non-negligible capacitor storage discharge of 24 % after 60 s, the voltage divider was also used to raise the input impedance from 1 M Ω to 10.5 M Ω as depicted in Fig. 9.2c, in order to increase the time constant to 2310 s. The discharge after 60 s can be reduced to 3% with this modification.

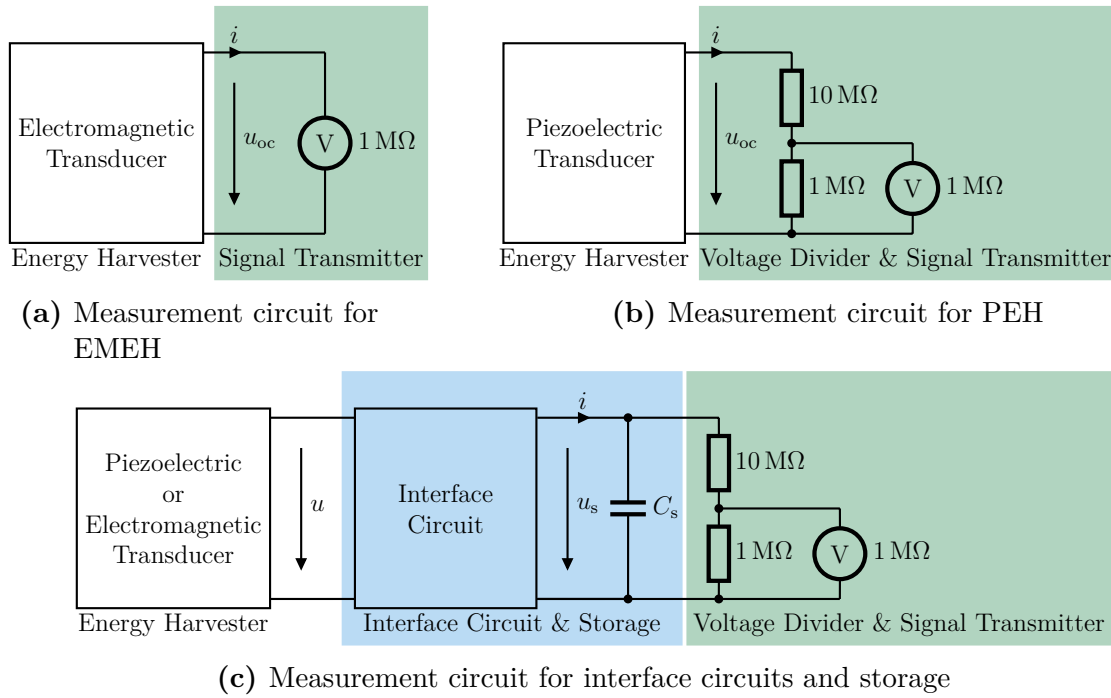


Figure 9.2: Measurement circuits for the characterization of the open-circuit voltage of the EMEH (a), PEH (b) and of interface circuits connected to the energy harvesters (c)

Three tires were equipped with various samples and prepared to be evaluated on the tire test bench. All presented harvesters - four tire wave based EMEHs, six strain based PEH and eight tire wave based PEH were embedded in one of the tires. The redundancy of the prototypes ensured that sufficient measurement data could be generated experimentally. Thereby, the impact of the tire load F and velocity v on the producible electrical energy E_{elec} and on the robustness were studied for different parameters as listed in Tab. 9.2. In addition to the different parameter studies, the orientation of the strain based PEH was investigated. The most significant results are explained subsequently.

Table 9.2: Parameter constellation for EMEH and PEH prototype testing

Velocity v (km/h)	Tire load F (N)	Measured voltage
20, 25, 30, 40, ..., 200	3000	open-circuit voltage u_{oc}
50	1000, 2000, ..., 9000	open-circuit voltage u_{oc}
50	3000	storage voltage u_s

9.2 Tire Wave Based Piezoelectric Energy Harvester

To evaluate tire wave based PEH, each piezoelectric transducer depicted in Fig. 5.9 was embedded in a metal housing, before being placed in a plastic housing, originally made for truck TPMSs, as shown in Fig. 9.3. The rubber containers were tightly adhered to the innerliner of the tire both in circumferential and lateral direction, as depicted in Fig. 9.4.

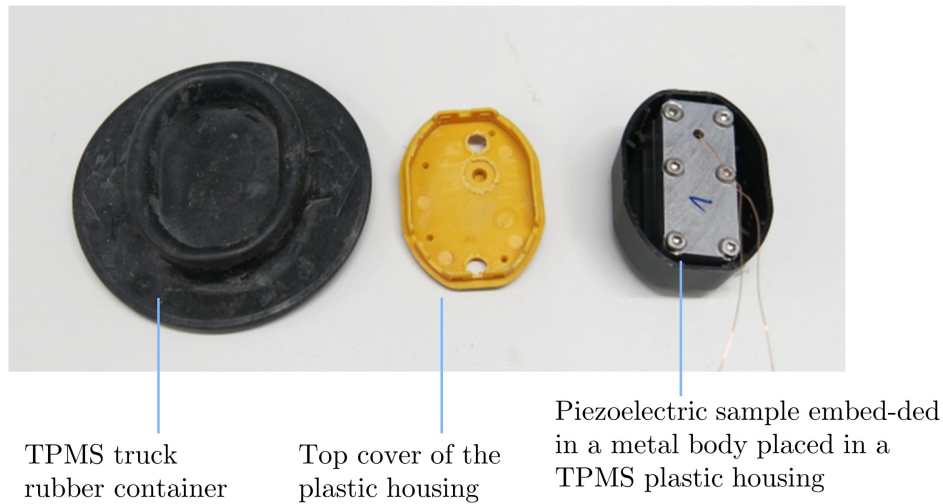


Figure 9.3: Pre-assembled tire wave based piezoelectric energy harvester embedded in a metal housing, placed in a truck TPMS plastic housing (right), before being mounted in the TPMS truck rubber container (left)

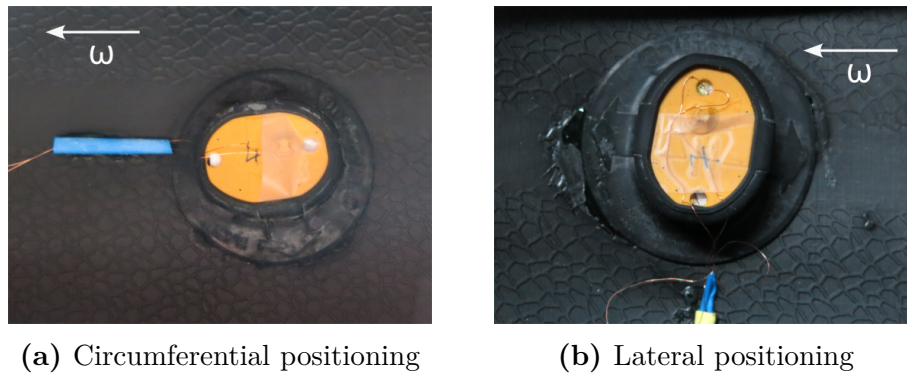


Figure 9.4: Tire wave based piezoelectric prototype embedded in a TPMS truck plastic housing and rubber container in a) circumferential direction and b) lateral direction. The arrow indicates the direction of the tire rotation.

9.2.1 Open-Circuit Voltage and Corresponding Energy

The open-circuit voltage $u_{oc}(t)$ and the corresponding piezoelectric energy

$$E_p = \frac{1}{2} C_p u_{oc}^2 \quad (9.1)$$

of a piezoelectric sample (tip mass $m = 3$ g and beam width $w = 3$ mm), placed in circumferential direction, were measured and are illustrated in Fig. 9.5 for the velocities $v = 20, 30, 50$ km/h and for the applied tire load $F = 3000$ N. According to Fig. 9.5, the voltage signal at 20 km/h exhibits voltages due to vibrational noise outside the contact-patch being with 8 V almost as high as the voltages in the area of ground contact with 11 V. However, the corresponding piezoelectric energy E_p does not exceed $1 \mu\text{J}/\text{rev}$ at all.

Already at $v = 30$ km/h, the centrifugal acceleration a_c is much stronger than the vibrational noise, leading to a smaller deflection of the piezoelectric beam tip outside the area of ground contact. Consequently, the voltage amplitudes caused by the noise are negligible compared to the voltage in the contact patch, where a maximum voltage of 18 V was measured. This voltage corresponds to an energy of $1.4 \mu\text{J}/\text{rev}$.

At 50 km/h, the open-circuit voltage reached 24 V which corresponds to an energy of $2.4 \mu\text{J}$. Although the velocity was increased from 30 km/h to 50 km/h by factor 1.67, the voltage raised only by factor 1.33. In addition, according to Sec. 5.2.1, a piezoelectric open-circuit voltage of 60 V was expected at 50 km/h and differs from the measured voltage of 24 V significantly. A smaller voltage was measured experimentally, because the gap between attached mass and elastic bumper was not exactly 1 mm. Both material processing and system assembly led to a beam curvature, resulting in a misalignment of 200–300 μm . This misalignment reduced the range of free oscillation of the piezoelectric generator to less than 1 mm and caused deviation between the measured and predicted voltage. While the electrical results were not satisfying and could be improved, other observations made during the test series concerning reliability are of greater interest.

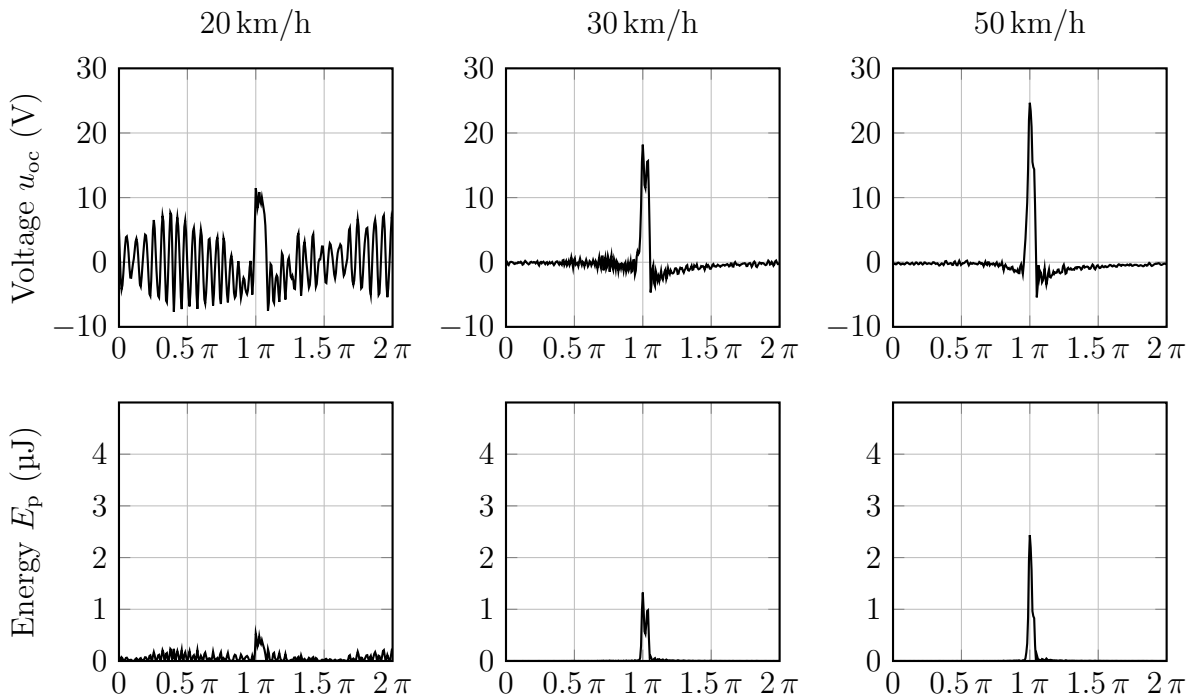


Figure 9.5: Open-circuit voltage u_{oc} at $v = 20$ km/h, 30 km/h and 50 km/h of tire wave based piezoelectric energy harvesters and corresponding energy E_p .

9.2.2 Robustness

All systems were tested from 20 km/h up to 200 km/h at $F = 3000$ N. Measuring the voltage of all studied tire wave based PEH revealed reliability problems. Two of the eight piezoelectric samples ($m = 3$ g and $w = 3$ g) were evaluated in the first test series and failed at 90 km/h ($F = 3000$ N). To figure out the reason of failure, the piezoelectric transducers were disassembled. Figure 9.6 shows a disassembled sample after testing.

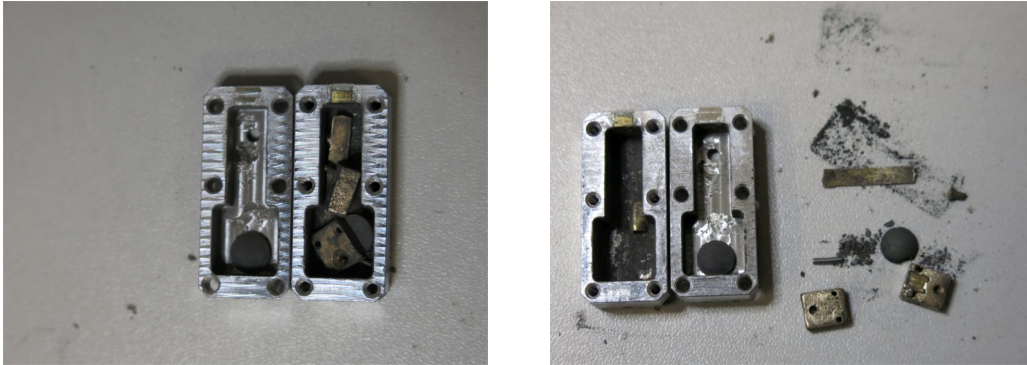


Figure 9.6: Disassembled tire wave based piezoelectric energy harvester after being tested in a tire. The brass support beam broke at the clamping. The piezoelectric beam detached from the brass beam and was converted into powder. The system failed at 90 km/h.

From the disassembly could be observed, that the support beam broke at the clamping, the initially screwed mass was detached from the beam and the piezoelectric beam was converted back to powder. To improve the system stability of subsequently tested samples, glue had been added to reinforce both the attachment of seismic mass at the beam tip and the clamped beam at the metal housing. These modifications lead to a slightly better reliability: one sample ($m = 2$ g, $w = 3$ mm) failed at 90 km/h whereas one sample ($m = 2$ g, $w = 4$ mm) failed at 130 km/h. In a third test series, all remained samples were placed inside the tire without wiring and checked after prototype testing. None of the eight systems with widths of 3 mm and 4 mm and tip masses of 2 g and 3 g survived the tests up to 200 km/h.

Although the prototypes built on elastic bumpers as compliant limit stops to restrict the tip mass deflection, the robustness has been still the main issue of the studied systems. If a smaller tip mass or a wider beam had been used, a smaller centrifugal force would occur, however the already low electrical energy generation, would be even lower. The systems suffered from strong robustness issues at medium velocities, while the energy generation was not sufficient at low and medium velocities. Consequently, the studied and improved piezoelectric tire wave based systems performed similarly bad as many other PEH presented in the literature. Based on these results, tire wave based piezoelectric energy harvester are therefore not recommended for TPMS energy harvesting.

9.3 Strain Based Energy Harvesters

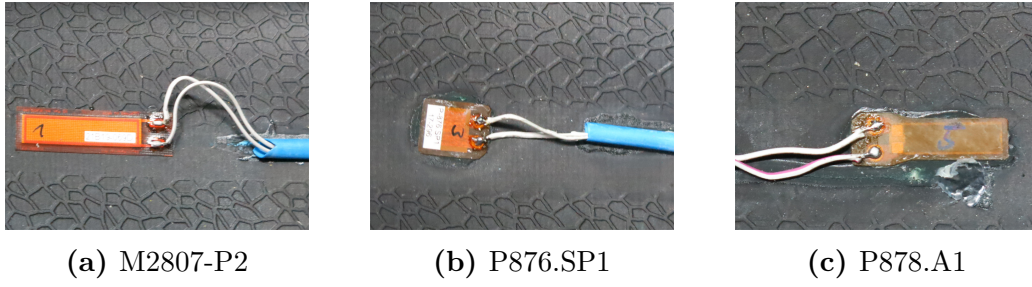


Figure 9.7: Strain based prototypes attached to the tire with soldered cables

With respect to Sec. 5.3, three piezoelectric composites from *SmartMaterials* and *Physik Instrumente* with a thickness of 300 μm and 500 μm were glued directly on the tire inner liner and are shown in Fig. 9.7. Electrical wires were soldered to the electrical pads of the specimens. Based on the measured open-circuit voltage u_{oc} at $v = 50 \text{ km/h}$ and at a wheel load $F = 3000 \text{ N}$, the amount of accumulated charge ΔQ , calculated by

$$\Delta Q(t) = \int_{t'=0}^t |i(t')| dt' = C \int_{t'=0}^t \left| \frac{du(t')}{dt'} \right| dt' \quad (9.2)$$

and the piezoelectric energy E_p

$$E_p(t) = \frac{C_p}{2} \cdot u_{oc}^2(t), \quad (9.3)$$

stored on the piezoelectric capacitance C_p were deduced for one tire revolution. The measured data are illustrated in Fig. 9.8 with a solid line and opposed to the simulated data from Sec. 5.3.3 (dashed lines). Following the assumptions of Lee et al. in [19], in the network simulations of Sec. 5.3.4, it was supposed, that 25% of the tire strain are applied to the piezoelectric samples. However, comparing the simulated with measured data reveals, that the measured piezoelectric open-circuit voltage is much smaller than expected. The most obvious explanation is, that less strain is transferred from the tire to the sample. In addition the transferred strain depends on the sample.

Applying Eqn. 5.25 on the measured open-circuit voltage leads to a maximal average strain $\bar{S} = 1/l \int_0^l S(x) dx$ over the entire transducer length l at $\varphi = \pi$ listed in Tab. 9.3. Normalizing the calculated strain to the supposed maximal tire strain of 3200 ppm leads to the strain portion of Tab. 9.3.

The difference in the transferred strain can be explained by the flexibility and the geometry. The M2807-P2 is the most compliant and flexible transducer among the samples. Consequently, the sample experiences most of the tire strain compared to the two other samples, which are both thicker and have a greater elasticity modulus, leading to a higher stiffness. Due to their higher stiffness, the strain portion is much lower than 25% leading to a much lower output voltage. Although the P878.A1 sample is 0.1 mm thicker than

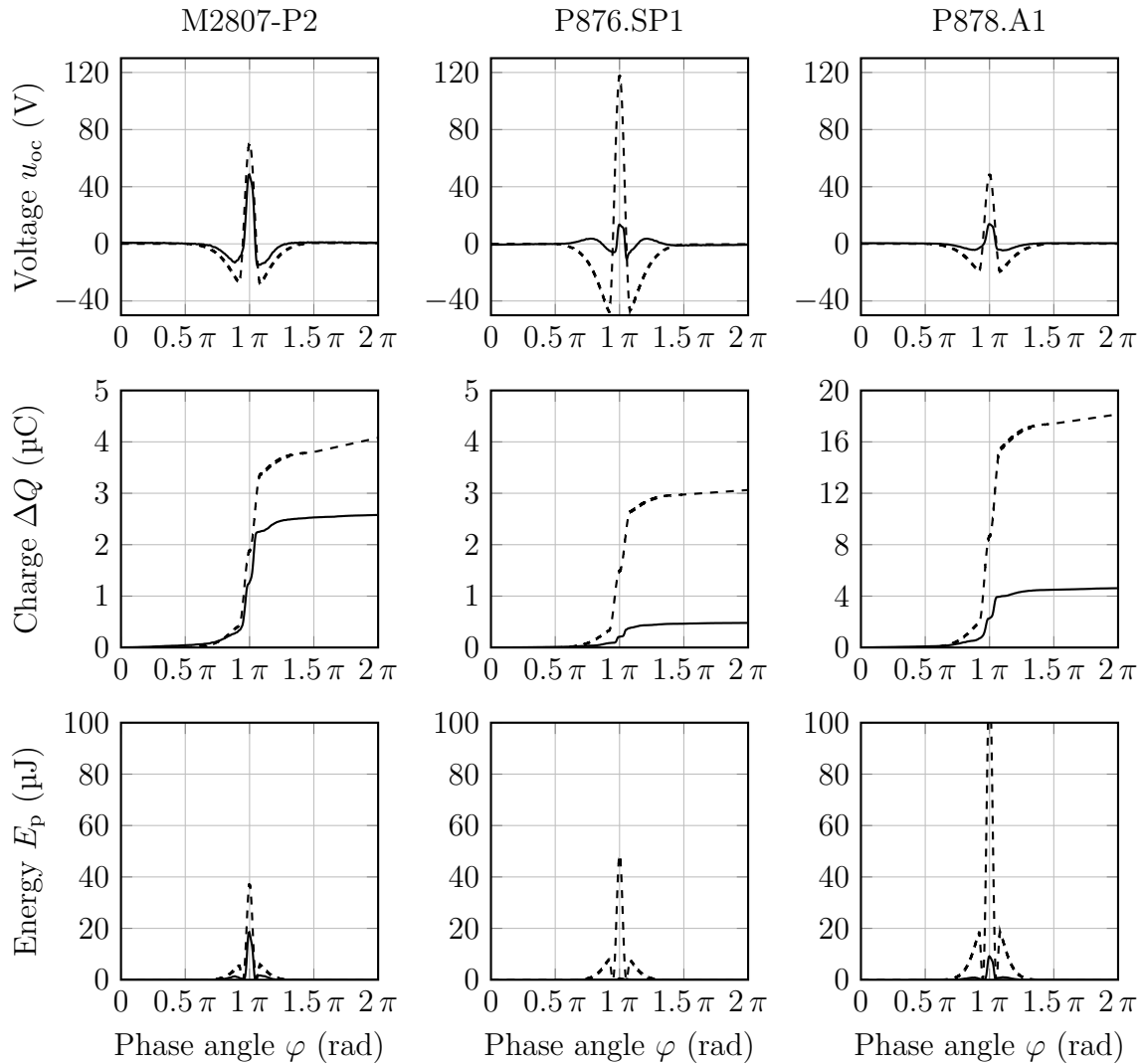


Figure 9.8: Strain PEH prototypes at 50 km/h and 3000 N - measured (solid line) and simulated (dashed line) voltage, accumulated charge and piezoelectric energy stored in the piezoelectric capacitance for one tire turn.

the P876.SP1 sample, it is longer, which presumably leads to more bending during the tire ground contact, which results in a higher transferred strain.

The piezoelectric energy $E_p(t)$, depicted in Fig. 9.8, represents a coarse figure of merit of the available energy. The harvestable energy is in the range of $2 \max(E_p)$ with an ideal SECE. The open-circuit measurements indicate, that the samples M2807-P2 and P878.A1 theoretically provide sufficient energy to supply a TPMS. Contrary, the sample P876.SP1 is not suitable for TPMS harvesting.

9.3.1 Velocity Dependency

After a general characterization, the effect of different velocities on the piezoelectric transducers are investigated. In two out of three measurement series, wire ruptures limited the data acquisition from 20 km/h to 70 km/h. To study precisely the impact of different

Table 9.3: Average strain \bar{S} at $\varphi = \pi$ experienced by different piezoelectric transducers in the measurements

	M2807-P2	P876.SP1	P878.A1
Average transferred strain \bar{S}	520 ppm	120 ppm	210 ppm
Strain portion	16 %	3.8 %	6.5 %

vehicle velocities on the deformation, the accumulated charge ΔQ is considered as figure of merit. To reduce the influence of signal variations and noise, the accumulated charge ΔQ was calculated, according to Eqn. 9.2, based on the data of 20 revolutions and normalized to one revolution. The accumulated charge as a function of velocity is plotted in Fig. 9.9 at 3000 N load for different velocities and samples.

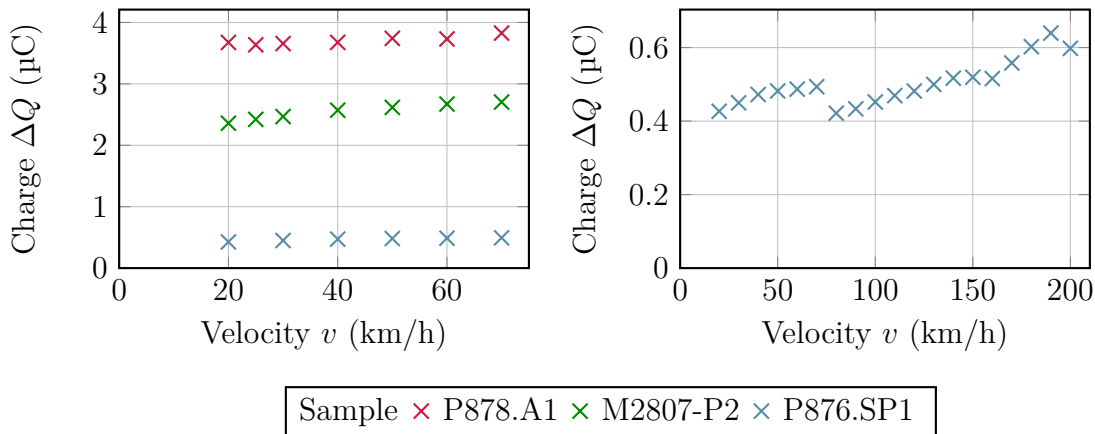


Figure 9.9: Accumulated charge as a function of velocity v at $F = 3000$ N in circumferential direction

From the considered velocities from 20 km/h to 70 km/h the accumulated charge per revolution only slightly increases with increasing velocity but can be considered as constant. Due to the wire rupture of the P878.A1 and M2807-P2, data at velocities higher than 70 km/h are not available. However the data of P876.SP1 can be analyzed for the general trend. Considering the data from 20 km/h to 200 km/h in Fig. 9.9 (right) indicates that the total accumulated charge generally increases with the velocity. However it decreases between 70 km/h and 80 km/h as well as between 190 km/h and 200 km/h. The corresponding measured voltage-time signals are illustrated in Fig. 9.10. As depicted at 190 km/h and 200 km/h, the strain related voltage signal waveform differs from the ideal signal waveform. Vibrational noise is superimposed and leads to an increasing charge generation with increasing velocity. The decrease after 70 km/h and 190 km/h can be presumably explained with eigenmodes of the tire, being excited at specific velocities and leading to a different tire deformation.

The described behavior can also be observed with samples, which were placed in the tire with lateral orientation. They are presented in App. G in Fig. G.1.

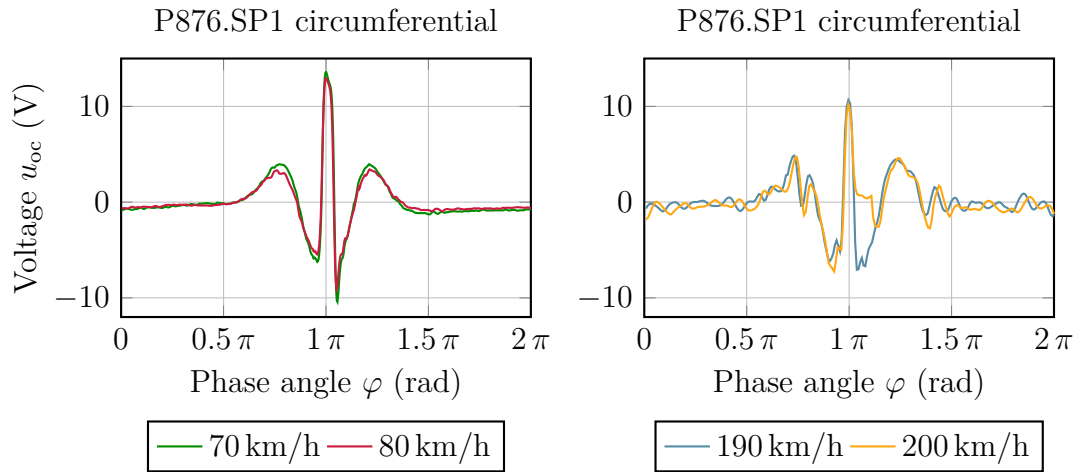


Figure 9.10: Open-circuit voltage signal for one tire revolution at different velocities. The strain related voltage signal waveform differs from the ideal signal shape at low velocities and is superimposed by vibrational noise.

9.3.2 Orientation Dependency

The circumferential sample orientation exhibits higher tensile strains than compressive strains. In contrast, a lateral sample orientation as illustrated in Fig. 9.11 exhibits similar tensile and compressive strain amplitudes as stated by Lee et al. [17]. The open-circuit voltage of two M2807-P2 samples each in one orientation and at 50 km/h and 3000 N is presented in Fig. 9.12 and confirms the recent observations.

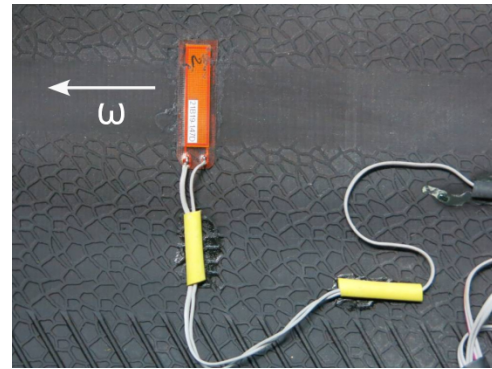


Figure 9.11: M2807-P2 strain transducer in lateral direction

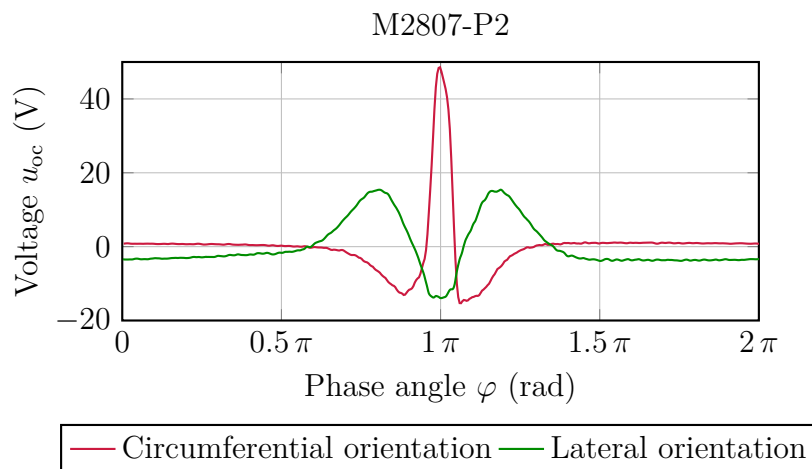


Figure 9.12: Open-circuit voltage of M2807-P2 sample in circumferential and lateral orientations at 50 km/h and 3000 N for one tire turn

As the strain amplitude in circumferential orientation is twice the strain amplitude in lateral orientation, much more energy is generated in the first case. Although the circumferential orientation allows harvesting more energy, the lateral sample orientation benefits from a similar tensile and compressive strain amplitude. This is advantageous since piezoelectric devices tolerate higher compressive than tensile strain, which might be beneficial for a better long-term behavior. Long-term tests of many thousands of kilometer were not part of this work but the tendency will be evaluated in Sec. 9.3.4 based on former studies from the literature in which the piezoelectric transducers experienced comparable strains over many million cycles.

9.3.3 Tire Force Dependency

The tire load (force) applied to the tire determines the tire's ground contact area and thus its strain. The impact of the force was measured at 50 km/h. The accumulated charge is illustrated in Fig. 9.13 for different forces, samples and orientations. Similarly, Fig. 9.14 depicts the open-circuit voltage waveform for one revolution at different forces.

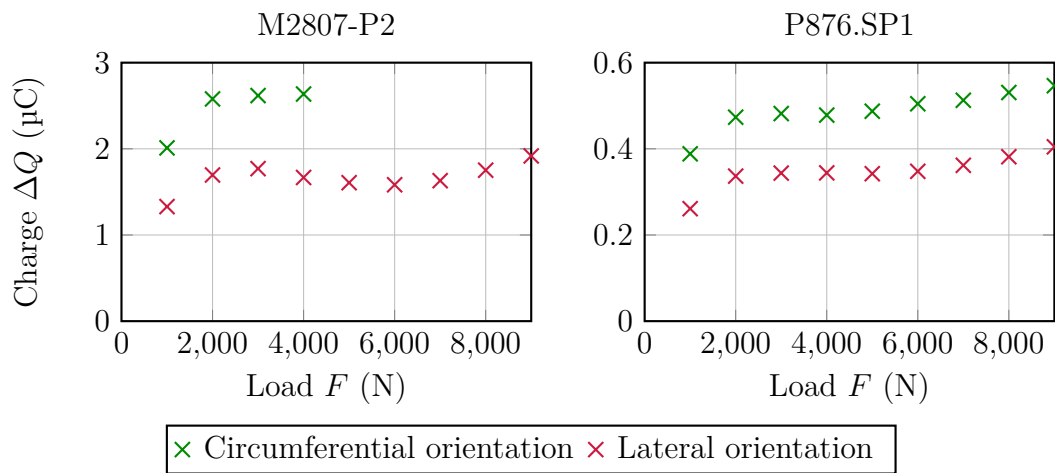


Figure 9.13: Accumulated charge for different forces at 50 km/h

The accumulated charge ΔQ increases significantly with the force F from 1000 N to 2000 N. Above, a continuous but small raise can be observed. For practical application the range from 3000 N up to 9000 N is representative and corresponds to a vehicle mass, including passengers and luggage, of about 1220 kg up to 3670 kg². The small increase in charge ΔQ above 2000 N indicates a similarly small increase in strain. According to Fig. 9.14, the reason is a higher compressive strain while the tensile strain decreases with increasing force F . Consequently, the reliability of the strain based energy harvesting system is marginally positively affected by higher vehicle loads (forces). As a force for a given tire pressure is equivalent to a lower tire pressure for a given force, the reliability of a strain based transducer is marginally affected by slowly decreasing pressures in leaky tires.

²It is supposed that the entire mass of the vehicle is evenly distributed on all four wheels

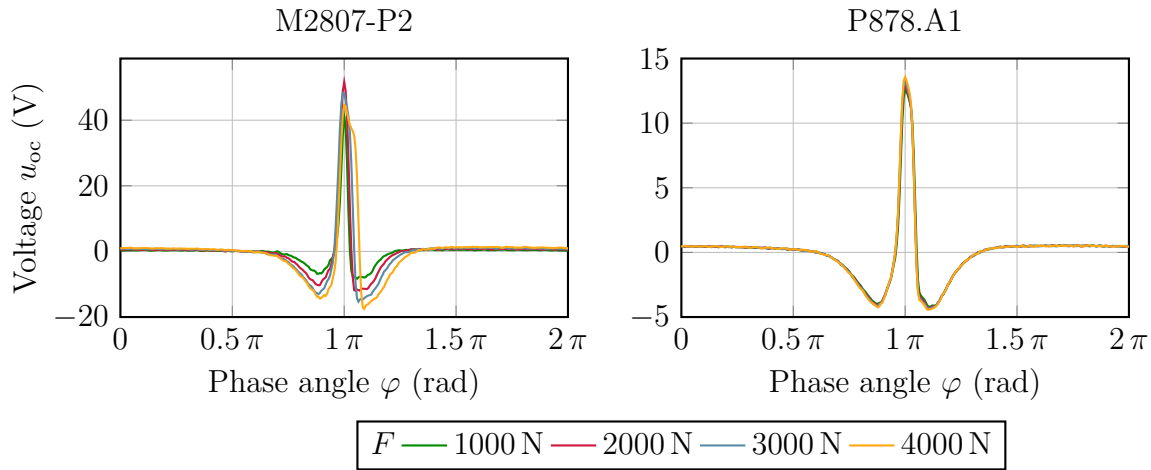


Figure 9.14: Open-circuit voltage signal for one tire revolution with different loads

9.3.4 Robustness

Short-Term Robustness



(a) Connected wires before testing



(b) Ruptured wires after testing

Figure 9.15: Strain based prototype wire connection before and after testing

During manifold driven test series, the main issue of strain based energy harvesters was related to signal connection losses. The wires of the first prototypes, which were connected to the slip ring transmitter, were not placed ideally. The wire did not possess enough clearance to compensate the tension, experienced by the wire, due to the change in centrifugal acceleration. The weakest point, the solder connection, broke at velocities between 50 km/h and 70 km/h as documented in Fig. 9.15. The problem was solved by creating a larger wire clearance during the second and third test. To identify whether the piezoelectric transducer suffered from destruction, the transducer capacitance was measured before and after testing. If an energy harvester had been damaged because of broken electrodes, the area A of the piezoelectric capacitance, covered by the electrodes, would have been decreased noticeably and consequently the capacitance $C = \varepsilon A/h$, too. The capacitance of all embedded strain based transducers remained constant, though. Neither elevated forces of 9000 N nor velocities up to 200 km/h had any impact on the

system robustness during short term tests of a few tens of kilometers.

Long-Term Robustness

The long-term behavior of the M2807-P2 samples is now evaluated based on long-term test results, using the data from two MFC studies, published by Daue et al. [49] and by Upadrashta et al. [106].

Daue et al. [49] attached M2814-P2 transducers³ to a much larger support, which was strained harmonically. They connected three different resistances ($R_L = 6\text{ k}\Omega$, $600\text{ k}\Omega$ and $6\text{ M}\Omega$) to the piezoelectric transducer, monitored the root mean square (RMS) voltage across the resistors and deduced the output power. The specimens were harmonically strained over 30 million oscillations with a strain amplitude of 1500 ppm at a frequency of 10 Hz. Their measurement results are depicted in Fig. 9.16.

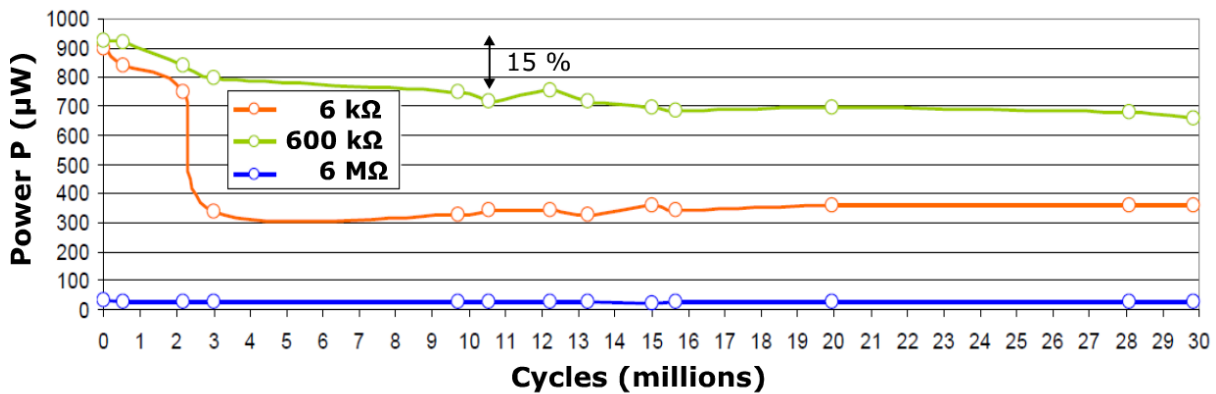


Figure 9.16: Long-term evaluation of M2814-P2 transducers with respect to the electrical power across different load resistances. The transducers were harmonically excited by strains with an amplitude of 1500 ppm. The figure is adapted from [49].

Daue et al. observed a strong power drop after 3 million oscillations of about 65% with the $6\text{ k}\Omega$ resistance. The $6\text{ k}\Omega$ resistance represents a short-circuit, compared to the impedance of the M2807-P2 transducer at 10 Hz of $Z_c = 600\text{ k}\Omega$. Under optimal load conditions ($R_L = 600\text{ k}\Omega$), the power decreased by 15% after 10 million oscillations and remained constant afterwards. After 30 million oscillations, a power drop smaller than 10% was measured with the high resistor $R_L = 6\text{ M}\Omega$, which represents almost an open-circuit. As the authors analyzed the piezoelectric material with an electric impedance spectroscopy after every 100.000 cycles, they concluded that the piezoelectric material depolarized which led to the power drop.

Noticeably in Fig. 9.16 is, that the low resistor ($6\text{ k}\Omega$) and the optimal resistor ($600\text{ k}\Omega$) exhibit the same output power at the beginning of the measurement. However, it can be demonstrated that if a 100 times smaller resistor than the optimal load resistor is

³The M2814-P2 transducers are made of the same material as the M2807-P2, with the only difference that the active width is 14 mm instead of 7 mm.

connected, the power should lead to a 50 times smaller power across the resistor. As this is not the case in Fig. 9.16, it is assumed that the absolute value of the electrical power was not calculated correctly in the publication. If the electrical power is only subject to scaling errors which is very probable, the relative power drop measured with the three different load resistances for 30 million cycles can be used for long-term evaluation. Contrary to the results at 1500 ppm, Daue et al. stated that no depolarization was observed at 500 ppm strain over 100 million cycles.

In the second study, Upadrashta et al. [106] analyzed the long-term behavior of M2807-P2 samples. Each piezo-ceramic was attached to a fixed-free aluminum beam that was deflected at 30 Hz, which was close to the natural frequency of the system. The authors monitored the strains with strain gauges attached on the M2807-P2 specimens and measured the RMS voltage under optimal load conditions for different strains and during 20 million oscillations. Their measurements are depicted in Fig. 9.17.

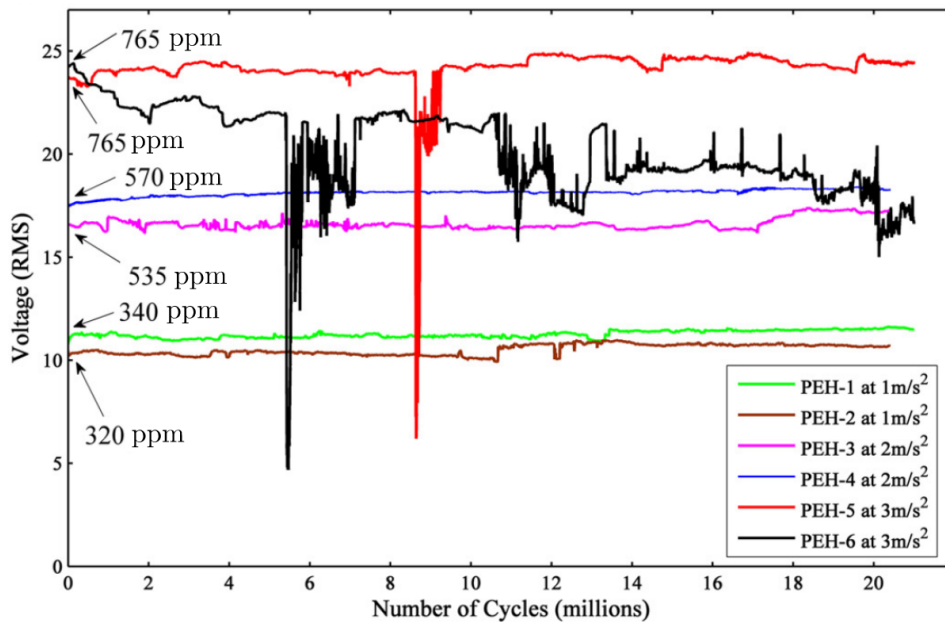


Figure 9.17: Reliability tests for performance evaluation of M2807-P2 transducers at different base accelerations at a low resonant frequency (30 Hz), adapted from [106]

From their data, they deduced a reversible and reliable system performance at strains less than or equal to 570 ppm. At strains of 765 ppm they observed a voltage drop by 30 % (black line in Fig. 9.17 after 5 million cycles), equivalent to a power drop of 50 % (because $P \propto u^2$). The authors explained this drop both with a shifting eigenfrequency of the system and smaller deflections due to inelastic deformations, while the excitation frequency stayed constant, and with possible cracks. However, after a few million oscillations the performance degradation recovered, which is a strong hint on an eigenfrequency shift. Upadrashta et al. also studied in a modified setup the RMS voltage over 60 million cycles and observed at 605 ppm no voltage drop and at 825 ppm a voltage decrease by

15 %, equivalent to a power drop of 28 %.

Table 9.4: Overview of Macro Fiber Composite long-term studies

Study	Cycles (million)	Strain (ppm)	Impedance	Normalized power after testing
Daue et al. [107] (M2814-P2)	30	1500	high	90 %
	30	1500	matching	85 %
	30	1500	low	30 %
	100	500	any	100 %
Upadrashta et al. [106] (M2814-P2)	20	570	matching	100 %
	60	605	matching	100 %
	55	825	matching	72 %

The relevant data of the two presented studies are summarized in Tab. 9.4. From the studies can be deduced, first, that strains in the range of 500 ppm do not lead to depolarization, no matter which electrical load is seen at the piezoelectric transducer output terminal. As the experienced strain of the M2807-P2 specimen installed in the tire is, according to Tab. 9.3 in the range of 500 ppm, neither depolarization nor cracks are expected.⁴

In addition, the studies based on harmonic excitations, whereas the strain in the tire is non-harmonic. Since the sample is strained inside the tire during 1/10 th of the tire revolution while the relaxation of the system occurs during 9/10 th, the non-harmonic excitation might be advantageous. Moreover, the curvature of the tire test bench with a drum diameter of 1.9 m provokes a higher tire deformation than a flat track or a typical road would do, resulting in a slightly overestimated strain in the experimentation.

To conclude, the applied strain on the piezoelectric M2807-P2 transducer inside the tire is sufficiently low that the transducers will neither suffer from depolarization nor from cracks under typical driving conditions. If the strain is large enough to provide sufficient energy to the storage will be investigated in the next subsection.

9.3.5 Interface Circuits and Harvested Energy

Interface circuits have a strong impact not only on the long-term behavior at elevated strains but also on the amount of energy that is extracted and transferred to the storage.

⁴If significant higher strains than 500 ppm are applied to this transducer, the connected electrical load is relevant for evaluating the long-term depolarization. A high impedance (open-circuit behavior) is more advantageous over impedance matching which in turn is better than a low impedance (short-circuit behavior). The input impedance of an SEH depends on the voltage ratio $b = u_s/u_0$ and varies between short-circuit behavior ($b = 0$), impedance matching ($b = 0.25$) and open-circuit behavior ($b = 0.5$) and corresponds to the analysis of Sec. 6.2. In contrast, the input impedance of an SECE is independent of the voltage ratio b as explained in Sec. 6.5. However, the SECE contains open-circuit and short-circuit phases to transduce all available energy. As all energy is transduced during one half wave, the SECE can also be regarded as matching impedance, in this interval. Which behavior dominates the long-term behavior needs to be investigated in future, when elevated strains appear.

Hereinafter, the SEH and the Electronic Breaker (EB) as implementation of the SECE (see Sec. 6.5) are studied experimentally. The full-wave rectifier (FWR) of the SEH was built with 1N4007 silicon diodes. The components of the EB are listed in Tab. 9.5.

Table 9.5: Electronic components of the electronic breaker

Functional group	Component	
AC/DC converter	FWR diodes	1N4007
Envelope detector	Resistor R_1	100 k Ω
	Diode D_1	1N4007
	Capacitor C_1	220 pF
Comparator	Resistor R_2	1 k Ω
	PNP transistor T_1	BC 557C
Controlled switch	Inductor L with R_L	1 mH, 3.8 Ω
	NPN transistor T_2	BC 547C
	Diode D_2	BAT54

As already mentioned, the voltage of an initially discharged 220 μ F storage capacitor was measured during 60 s for different velocities. To compare the harvested energy at different vehicle velocities v , the harvested energy is not illustrated as a function of time but of distance x with $x = v \cdot t$. The capacitor voltage over distance is shown in Fig. 9.18 for the most promising strain transducer, the M2807-P2 with SEH and with EB. The dashed and densely dotted lines indicate the voltage levels of $u_{\text{asic}} = 2.5$ V and $u_{\text{charged}} = 3.9$ V to precharge and to entirely charge the storage, respectively.

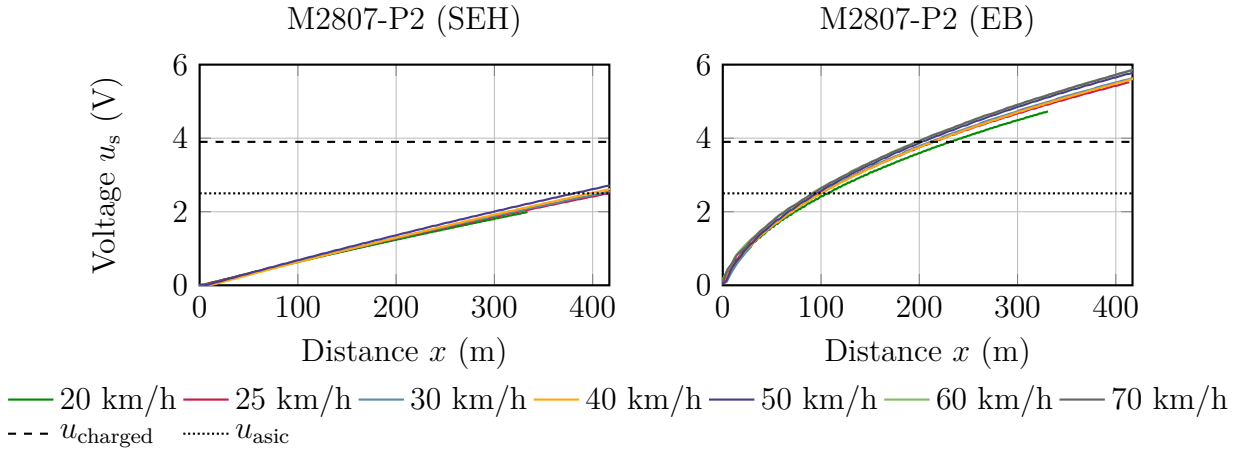


Figure 9.18: Storage voltage evolution of the M2807-P2 transducer at $F = 3000$ N. With an EB, the voltage of 3.9 V (dashed line) can be reached quickly.

According to the measurements, the M2807-P2 transducer with SEH is not able to charge the storage to the desired voltage $u_{\text{charged}} = 3.9$ V within 417 m (60 s at 25 km/h). Actually, a distance of more than 600 m is at least necessary. Contrary, the EB charges the storage to 3.9 V within 205 m to 230 m. The corresponding energy per revolution $E_{\text{rev,charged}}$ varies between 17 μ J/rev and 14 μ J/rev. If the capacitor C_s is precharged to

2.5 V as a result of an already moving vehicle, the driven distance decreases to less than 120 m to recharge the storage to 3.9 V, which corresponds to the energy $E_{\text{rev,add}} = 18 \mu\text{J}$.

LTspice network calculations, applied on the formerly measured open-circuit voltage $u_{\text{oc}}(t)$, revealed a maximum energy per revolution of $65 \mu\text{J}$ with an ideal SECE. The efficiency η_{EB} of the evaluated EB normalized to this maximal energy is illustrated as a function of storage voltage u_s in Fig. 9.19 for different velocities.

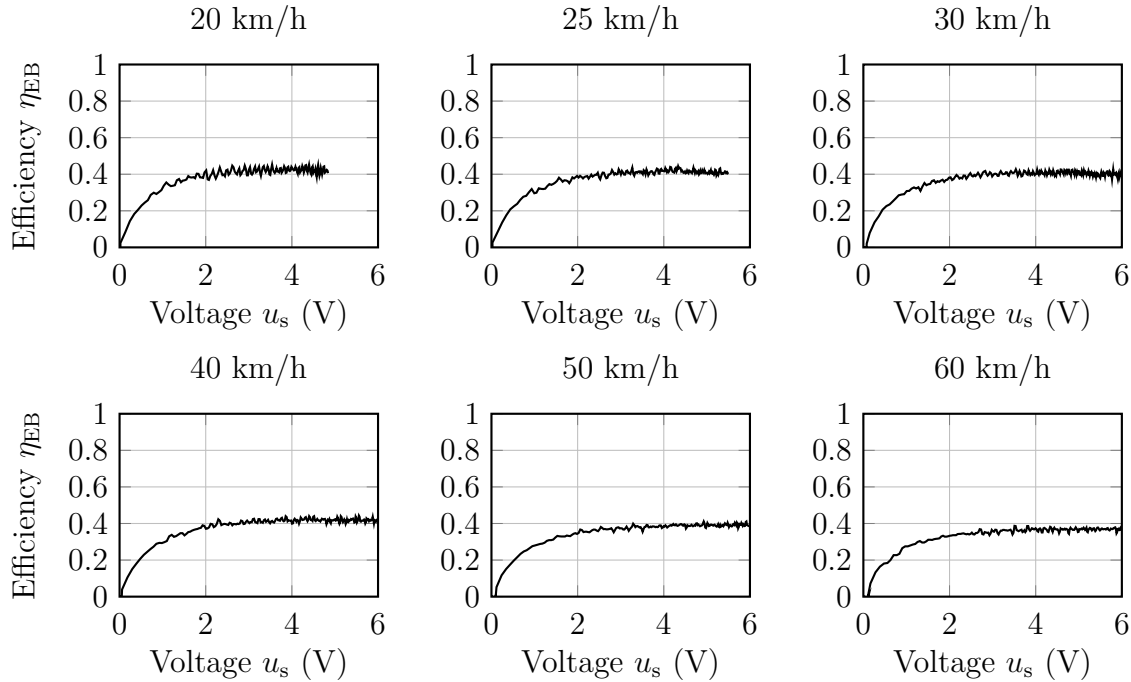


Figure 9.19: Efficiency of the electronic breaker for different velocities at $F = 3000 \text{ N}$. The efficiency of the interface circuit reaches 40% at $u_s \geq 2 \text{ V}$

At capacitor voltages above 2 V, the circuit efficiency reaches 40%.⁵ A smaller inductor (with similar $\tau = L/R_L$) or a better implementation of this principle e.g. as integrated circuit [160, 161] would even lead to a higher efficiency of up to 91%.

9.3.6 Summary

The generated electrical energy of strain based energy harvesters is almost independent of the vehicle velocity and only varies slightly. Furthermore, they the electrical energy slightly dependent on the applied tire load, which makes these transducers appropriate candidates to supply energy to TPMS. The investigation of M2807-P2 type energy harvesters showed excellent results in combination with an Electronic Breaker. Since the transferred strain from the tire to the M2807-P2 sample was of 520 ppm, a long lifetime is anticipated. In average, an energy between $14 \mu\text{J}$ and $17 \mu\text{J}$ were provided per tire

⁵The measured voltage-time signal of the capacitor was superimposed by an interfering 50 Hz noise, which become noticeably at voltages $u_s \geq 2 \text{ V}$, when the added energy ΔE does only lead to a very small increase of the capacitor voltage. Therefore, a Butterworth filter of second order with a cutoff frequency of 5 Hz was applied to the measured signal to reduce the noise, significantly.

revolution, which is almost twice as much as required. A comparison with experimentally validated strain transducer from other publications and under comparable test conditions is illustrated in Fig. 9.20, in which all results have been normalized to the surface of 1 cm^2 . Consequently, the obtained energy per revolution was divided by 1.96 for the M2807-P2 system.

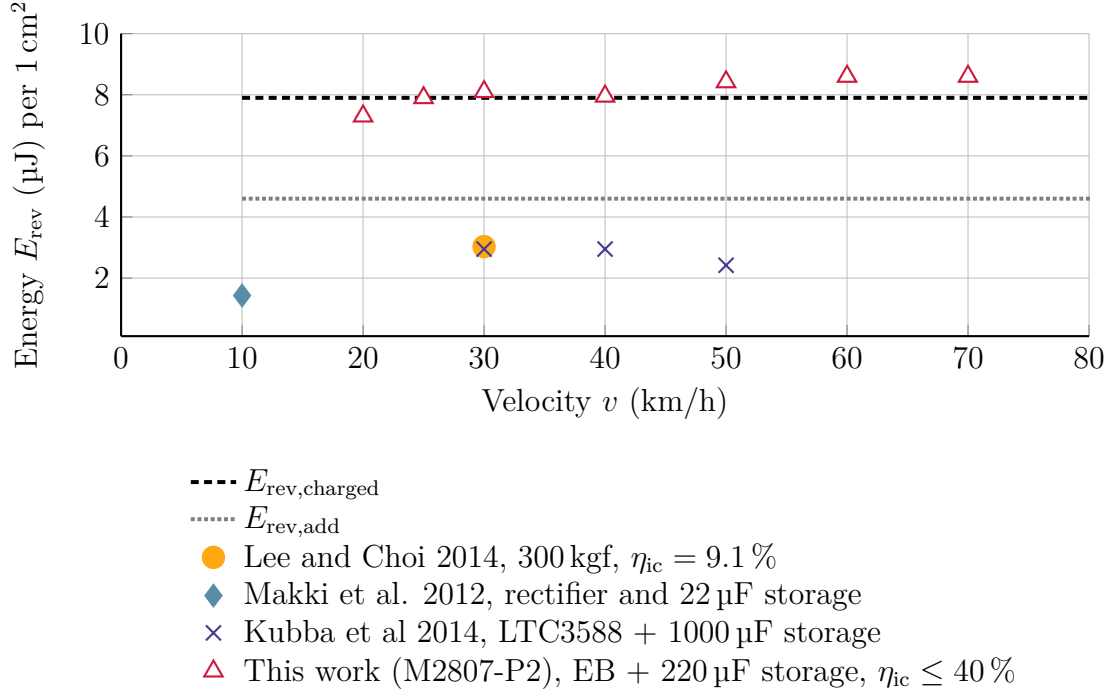


Figure 9.20: Comparison of different strain based energy harvesters. With an electronic breaker an efficiency of 40% could be reached in this work and lead to a much higher energy per revolution compared to the state-of-the-art systems.

Compared to other works, the herein studied strain energy harvester system generates the highest normalized energy per revolution by far. Compared to the best published strain based energy transducer, this system generates at least 180% more energy. Already an active piezoelectric area of 1 cm^2 in this setup is enough and fulfills the energy requirements from Sec. 2.2. As mentioned, the normalized energy can be further increased by using a more efficient interface circuit implementation.

As the energy harvester provides sufficient energy ($E_{\text{ref,charged}}$), to charge the entirely discharged capacitor due to a long parking period to $u_{\text{charged}} = 3.9 \text{ V}$, now the generated energy is considered in the driving mode. When the capacitor is already precharged to the minimal ASIC voltage of 2.5 V only the energy is required to charge the storage from 2.5 V to 3.9 V . Based on the voltage-time evolution of the storage as depicted in Fig. 9.18, the average time for one transmission of the full sized system with 1.96 cm^2 active surface is deduced and illustrated in Fig. 9.21. A remarkable outcome according to Fig. 9.21 is, that at most after 22s, sufficient electrical energy is harvested. The overall transducer system satisfies perfectly the imposed requirements.

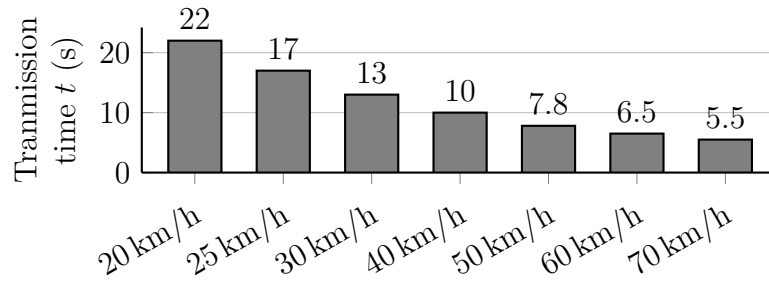


Figure 9.21: Estimated transmission time of the M2807-P2 (EB) system when the vehicle is in driving mode, deduced from the charging time from 2.5 V to 3.9 V of Fig. 9.19.

Finally, the flexibility and the low material price of soft and thin piezo-ceramic materials (≈ 0.1 Euro/cm², status: 2022) make M2807-P2 generators appropriate candidates for TPMS energy harvesting. A low-loss inductor in the range of a few hundred microhenry to 1 mH is required to build an efficient SECE circuit. While with the discrete component based EB efficiency of up to 40 % were reached in this work, an integrated circuit with low-loss rectifiers and with a tuned inductance might increase the efficiency up to 91 % [161]. Hence, the energy per revolution can still be more than doubled, and the transmission time more than halved.

The main disadvantage of this prototype relies on the reusability: once tightly attached to the tire, removing the piezoelectric generator from the tire without being damaged might be challenging. When the price of the generator is in the range of a few tens of euro-cents, it is not profitable to reuse the generator in the next tire.

9.4 Centrifugal Acceleration Based Electromagnetic Energy Harvester

Similar to the studied tire wave based piezoelectric transducers in Sec. 9.2, tire wave based electromagnetic energy harvesters were embedded in rubber containers which had been glued on the tire inner liner as depicted in Fig. 9.22. Four systems were studied experimentally, two of each with 530 turns and 1060 turns per coil. Their open-circuit voltage $u_{oc}(t)$ was measured. As demonstrated in Sec. 7.6 and according to Eqn. 7.26, the open-circuit voltage can be used to estimate the maximal available electrical energy of the electro-



Figure 9.22: Electromagnetic energy harvester embedded in a rubber container, which was glued on the tire inner liner

magnetic energy harvester $E_{\text{elec,max}}$ by

$$E_{\text{elec,max}}(t) \leq \int_{t'=0}^t \frac{u_{\text{oc}}^2}{4R_c} dt'. \quad (9.4)$$

Both, measured voltage $u_{\text{oc}}(t)$ and energy $E_{\text{elec,max}}(t)$ are depicted in Fig. 9.23 for one tire revolution (solid lines) and opposed to simulation results (red dashed lines). With respect to Sec. 7.5.3, the damping behavior of the simple PTFE tube had been estimated to be smaller than 0.23 kg/s. Based on the experimental result, the damping coefficient c was determined by matching the simulated energy after one revolution $E_{\text{elec,max}}(t = T)$ to the one, which results from the measurements. The calculated damping coefficients are listed in the title of each subplot. They vary from 0.14 kg/s to 0.19 kg/s. Correspondingly, the earlier estimated damping coefficient $c = 0.23$ kg/s is in acceptable accordance. Generally, the electromechanical network model and the predicted parameters are sufficiently precise to describe the system behavior and to estimate the energy limit per revolution. However, small variations occur and concern the first and second voltage peak as well as the oscillations after having left the area of ground contact.

The variations rely on slightly different test setups. On the one hand, the acceleration signal provided by Continental and fed to the network simulation in Sec. 7.6, was measured in a vehicle tire, rolling on a flat road (as the road is flat, the surface diameter d tends towards infinity ($d \rightarrow \infty$), and the force applied on the tire was equivalent to the gravitational force of 4170 N. On the other hand, the presented measurements in Fig. 9.23 were performed on a drum test rig with a drum diameter of $d = 1.9$ m and a force of 4000 N was applied to the wheel. The differences between the setups are distinguished in Fig. 9.24.

The curvature of the drum test rig leads to a stronger tire deformation than the flat track. With respect to Sec. 2.1.2, the drum test rig leads to a higher centrifugal acceleration before entering and after leaving the contact patch. The effect on the experimental measurements compared to the simulated results are both a higher voltage peak at $\varphi = \pi$ and a stronger signal attenuation once the system has left the area of ground contact at $\varphi \geq 1.1\pi$. In addition, the interaction between the bumper and the moving magnet is modeled in the simulation as ideal elastic collision. However, at each bumper contact a non-negligible fraction of energy is transformed into heat, which intensifies the attenuation of the damped oscillation. Both effects explain, why the magnet is still moving in the simulation when the system has already left the ground contact patch, whereas in the measurement, the magnet is at rest.

Until now the presented signals were mainly used to validate the simulation with measured data at $v = 50$ km/h and $F = 4000$ N. In the following, the behavior at different velocities and forces and the effect of different interface circuits will be studied.

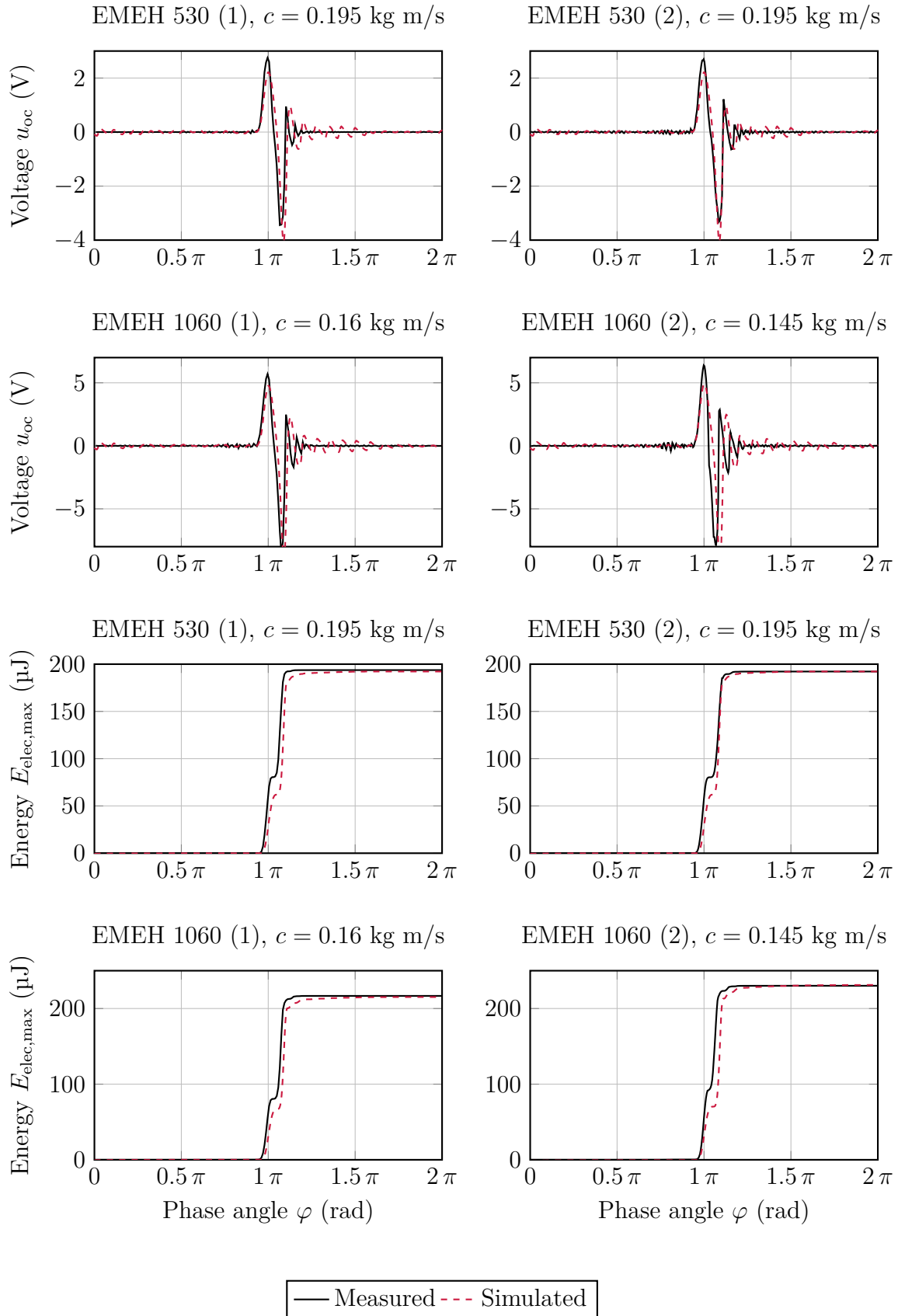


Figure 9.23: Open-circuit voltage u_{oc} and deduced maximal harvestable energy $E_{elec,max}$ for one tire revolution at $v = 50$ km/h and $F = 4000$ N.

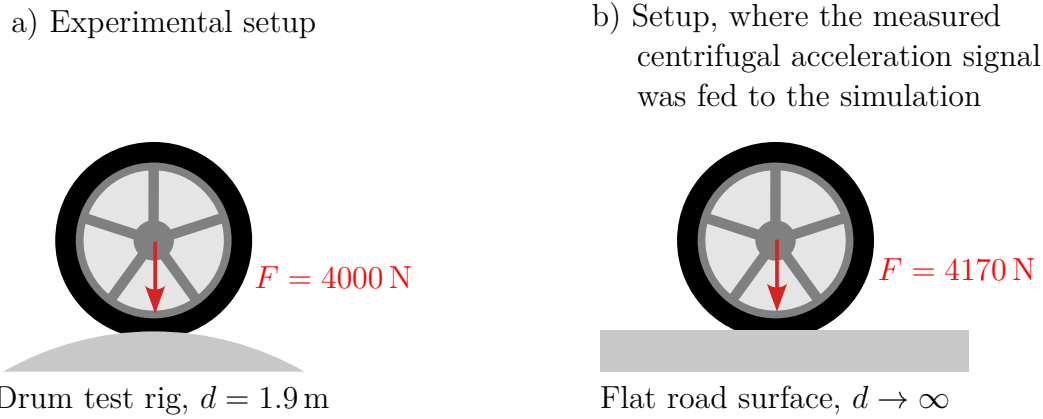


Figure 9.24: Test conditions in a) the experimental setup and b) the simulation

9.4.1 Velocity Dependency

According to Eqn. 8.22, the interval energy $E(u_{oc} \geq u_{FV})$ has been introduced to evaluate and classify the amount of energy above the voltage level u_{FV} imposed e.g. by the forward voltage of the rectifying circuit. Based on the open-circuit voltage signal u_{oc} of 30 tire

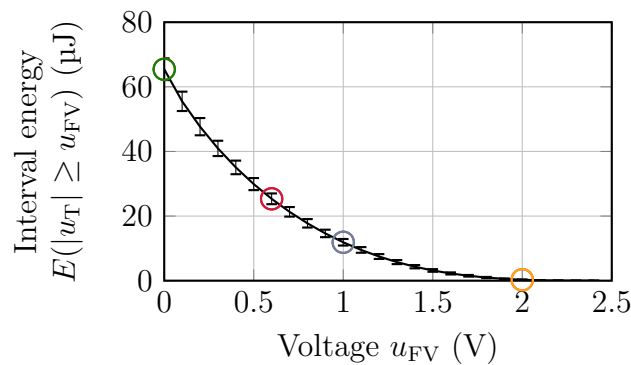


Figure 9.25: Interval energy $E(u_{oc} \geq u_{FV})$ as a function of forward voltage u_{FV} of EMEH 1060 (2) at $v = 25$ km/h at $F = 3000$ N

revolutions, the mean value of the interval energy as well as the standard deviation were calculated for one tire revolution for different voltages u_{FV} . Both the mean value (solid line) and the standard deviation (error bars) are depicted in Fig. 9.25 and were calculated for the EMEH 1060 (2) specimen at 25 km/h and at 3000 N.

Specific values of the interval energy were selected ($u_{FV} = 0$ V, 0.6 V, 1 V, 2 V) to compare the behavior of an energy harvester for different velocities. The selected values are highlighted with colored circles in Fig. 9.25 and opposed in Fig. 9.26 for various velocities, for $F = 3000$ N and for all four prototypes. Due to wire ruptures during the tests in the first and second measurement series, only high velocity data are available of the specimen EMEH 1060 (1). They are shown in Fig. 9.27.

From the definition of the interval energy, the interval energy at $u_{FV} = 0$ V refers to the maximal electrical energy theoretically available. According to Fig. 9.26, it ranges at 20 km/h between 20 μJ and 50 μJ and is consequently much higher than the required

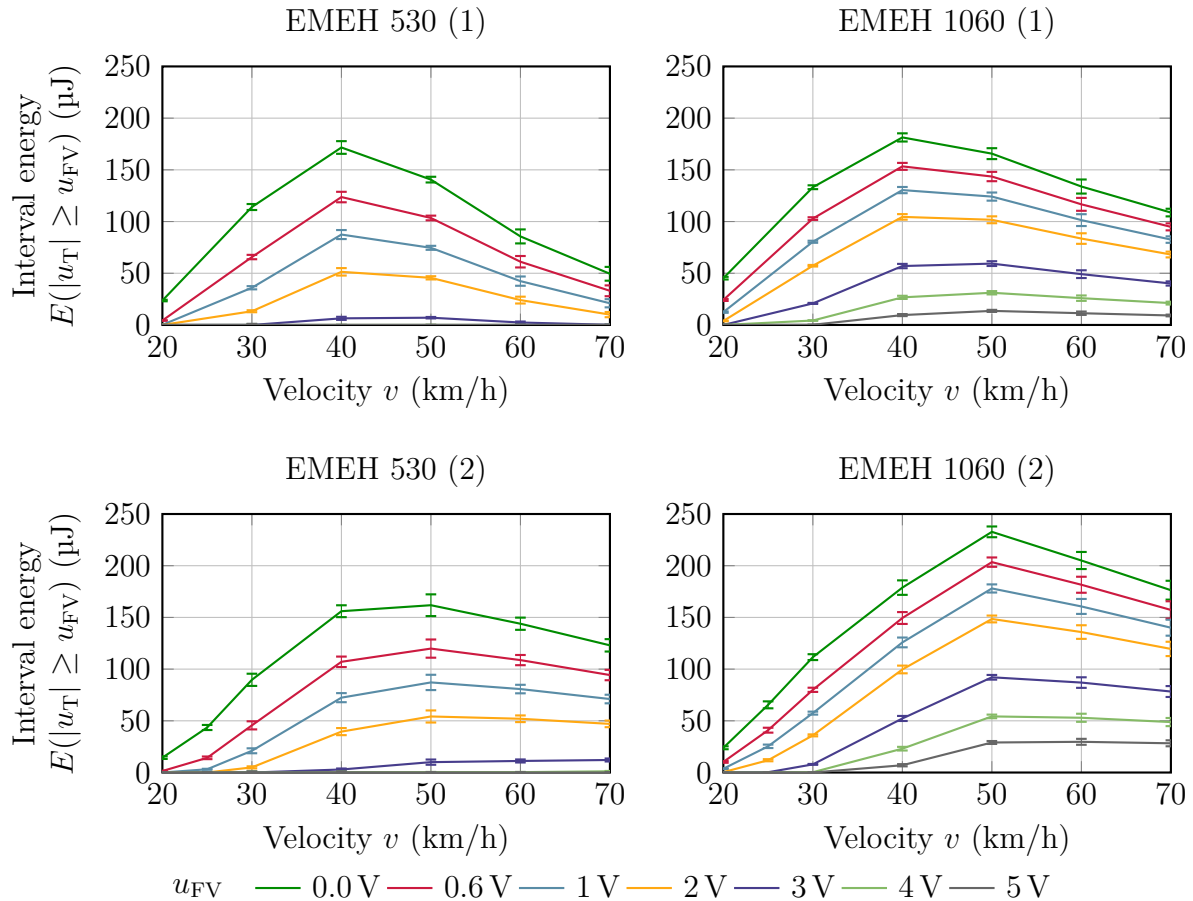


Figure 9.26: Interval energy of the four EMEH prototypes as a function of velocities for $F = 3000 \text{ N}$ and for different voltages u_{FV} .

$7.9 \mu\text{J}/\text{rev}$. As anticipated in Fig. 8.7, the effect of dissipated energy due to the diode forward voltage of 0.6 V is with at least 30% significant for $20 \text{ km/h} \leq v \leq 30 \text{ km/h}$ for all systems and in particular for the transducers EMEH 530 (1), EMEH 520 (2) with 530 turns per coil.

Generally, in all transducers, the energy per revolution rises from 20 km/h to 40 km/h or 50 km/h , which is caused by the quadratically increasing centrifugal acceleration. Although the centrifugal acceleration is increasing above 40 km/h , the amount of generated electrical energy decreases. Corresponding to Fig. 9.27, the energy per revolution decreases even until $v = 110 \text{ km/h}$. Above this velocity, the amount of energy alternates, but with a rising trend. To explore the reason why the electrical energy decreases above 40 km/h , the voltage-time signal of the harvester EMEH 1060 (1) normalized to one tire revolution is presented in Fig. 9.28 for selected velocities ranging from 20 km/h to 180 km/h .

Several effects, partially contrary, contribute to the aforementioned behavior:

1. In Eqn. 2.14, the energy per revolution has been defined as $E = \bar{P} \cdot T = \bar{P} \cdot 2\pi R/v$. As the period of one tire revolution $T = 2\pi R/v$ decreases with increasing velocity (see Fig. 2.5a), the energy per revolution decreases proportionally with the velocity.

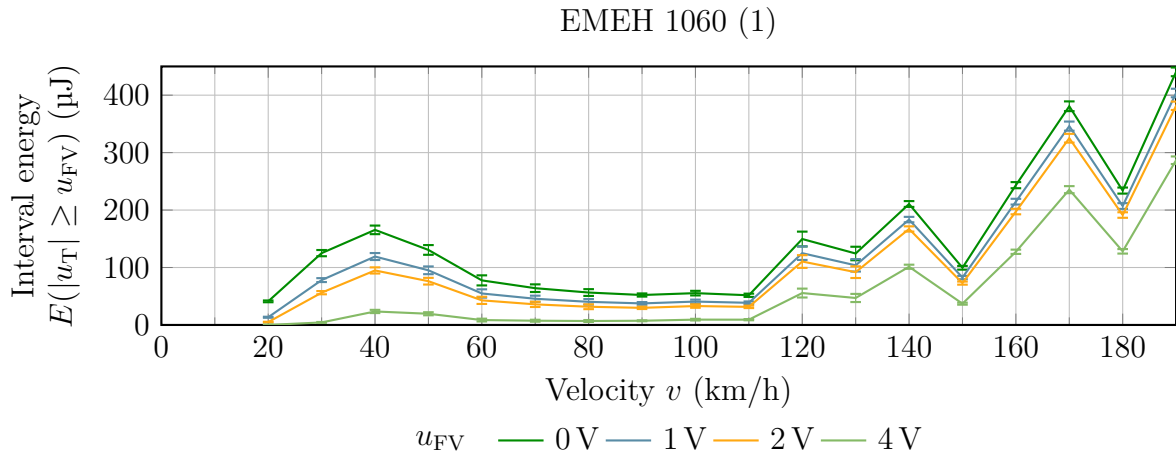


Figure 9.27: Interval energy as a function of velocity for $F = 3000$ N and for different voltages u_{FV}

2. A higher velocity results in a higher centrifugal acceleration, which causes a stronger compression of the magneto-mechanical compliance and of the bumper. Once released, more potential energy will be transformed into kinetic energy and into electrical energy. The energy increases with the velocity.
3. The shorter the time window of ground contact patch is, the shorter the time is, in which the magnet is accelerated towards the top of the housing, before it is decelerated by the centrifugal force towards the bottom. Therefore, neither u_{\max} nor u_{\min} increase quadratically with the velocity.
4. The transducer coils were designed and connected such that a high transducer coefficient $\beta(z)$ is reached at the equilibrium position at 25 km/h, which is obtained at $z \approx 4$ mm (see Fig. 7.13, 7.16). At higher vehicle velocity, the equilibrium position is shifted to smaller z . The result is, that the maximal velocity of the movable magnet $v(z)$ does not necessarily correspond with the position of maximal transducer coefficient $\beta(z)$.
5. Although the bumper is compressed like a spring, most of the energy is dissipated via material damping into heat, which is why the voltages amplitudes do not significantly increase in the range between 50 km/h and 110 km/h.

The enumerations explain the behavior of the transducers between 40/50 km/h to 110 km/h but do not provide an explanation why at velocities above 110 km/h, the voltage amplitudes rise and tremendously vary.

A deeper analysis would be necessary and would require more information than the measured one. For example, data on the centrifugal acceleration inside the tire, on the position and on the velocity of the movable magnet inside the energy harvester would be helpful. This would also be useful to explain, why EMEH 530 (1) and EMEH 1060 (1)

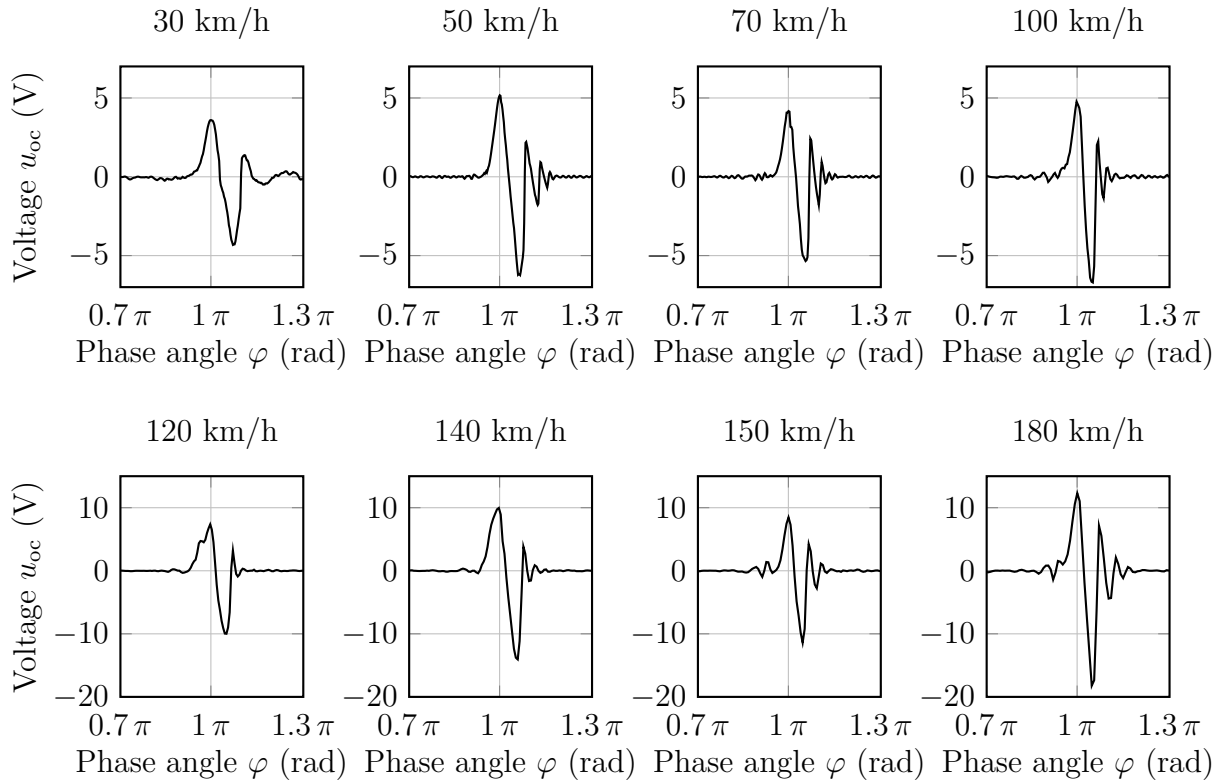


Figure 9.28: Open-circuit voltage signal u_{oc} as a function of phase angle φ of EMEH 1060 (1) for different velocities at $F = 3000$ N

possesses a local energy maximum at 40 km/h, whereas EMEH 530 (2) and EMEH 1060 (2) provide more energy at 50 km/h than at 40 km/h.

However, as the available energy in the tests is much greater than the required one at all velocities, a more in-depth analysis is outside the scope of this thesis.

9.4.2 Tire Force Dependency

The force F , with which the tire is pressed against the ground, influences the contact patch and consequently the time in which the movable magnet of the transducer is accelerated inside the housing from the "bottom" to the "top". Similarly to the former data representation, Fig. 9.29 depicts the interval energy per revolution for different forces F , which were measured at $v = 50$ km/h and at a constant pressure of $p = 2.3$ bar.

The interval energy increases monotonically from 1000 N to 4000 N, where the interval energy reaches a local maximum. At force $F \geq 4000$ N, the interval energy decreases slightly but remains at the same energy level. The reason can be found in the voltage-time signals, shown in Fig. 9.30 and 9.31 for $1000 \text{ N} \leq F \leq 4000 \text{ N}$ and $5000 \text{ N} \leq F \leq 9000 \text{ N}$, respectively

The area of ground contact (contact patch) continuously raises with increasing tire force F at a constant tire pressure p . Therefore, the time of free oscillation increases and the generated energy raises. In addition, the movable magnet has more time to be accelerated

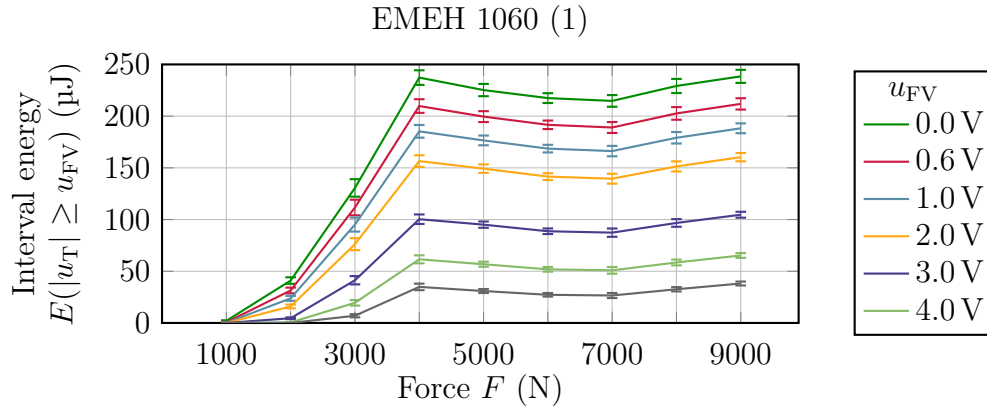


Figure 9.29: Interval energy as a function of force F at $v = 50$ km/h and for different voltages u_{FV} . The interval energy increases until $F = 4000$ N

towards the top of the housing, which is why the voltage amplitude at $\varphi = \pi$ rises to $u_{oc} = 6$ V, which is reached at 4000 N. At higher forces no significant further increase occurs as the movable magnet has already reached the maximal velocity and because it had enough time to perform half an oscillation where the centrifugal acceleration was $a_c \approx 0$. Furthermore, at $F \geq 6000$ N, the movable magnet collides with the top bumper, which is noticeable by the first local minimum of the open-circuit voltage, indicated by the dashed line in Fig. 9.31. At lower loads F at 50 km/h, there is no collision with the top bumper (see Fig. 9.30). Due to the lossy bumper impact, a part of the kinetic energy is dissipated into heat. This is why the energy per revolution is slightly decreasing at loads above 4000 N, whereas more attenuated oscillations lead to slightly more energy at forces $F \geq 7000$ N.

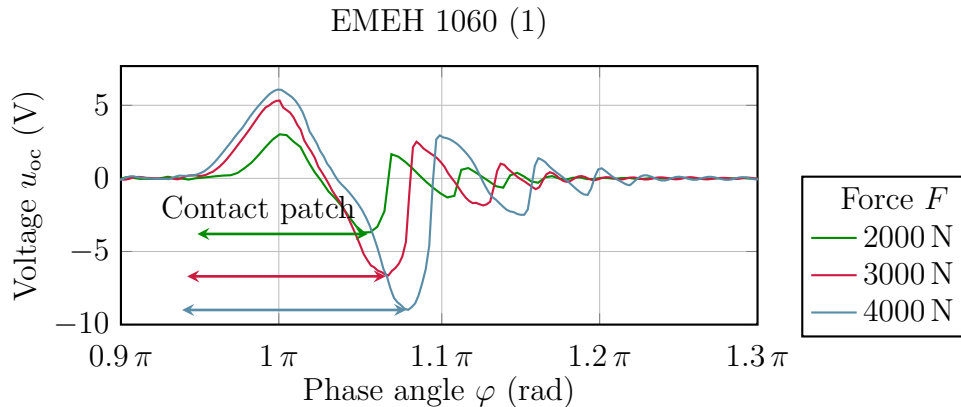


Figure 9.30: Open-circuit voltage over time for different force $F \leq 4000$ N. The colored arrows designate the area of ground contact. The negative voltage peak is sifted towards higher phase angles and indicates a rising area of ground contact.

To evaluate the impact of force, the recommended pressure and tire load are assessed. The inflated tire with a pressure of $p = 2.3$ bar is recommended for a tire load (force) of $F = 5600$ N [188] with the used Continental PremiumContact 6 205/55/R16 tires. This

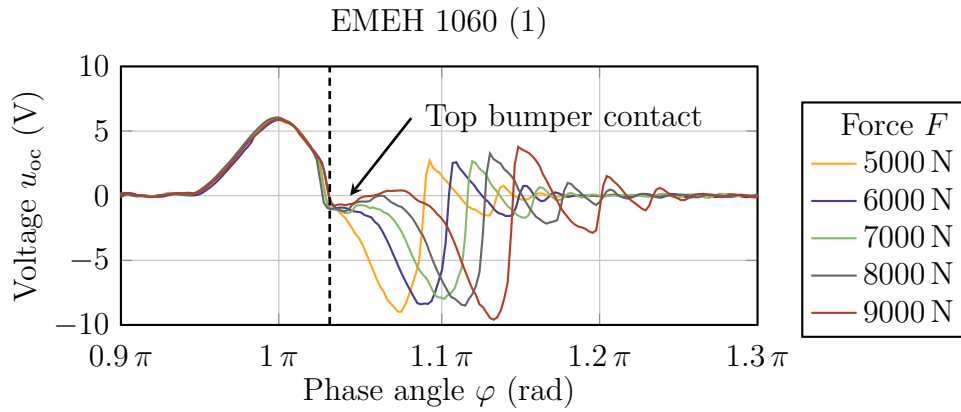


Figure 9.31: Open-circuit voltage over time for different forces $F \geq 5000$ N.

force is greater than the applied 3000 N in most of the measurement series. According to Fig. 9.29, if a load $F = 5600$ N rather than 3000 N is applied, 75 % more energy can be provided after one tire revolution.

Practically, the fact, that the interval energy remains almost constant in proximity of $F = 5600$ N is of advantage. When more passengers than usual with heavy luggages are inside the vehicle (e.g. on the way to the airport), the mass of the vehicle increases. As commonly the case for short trips, the air pressure is not adapted to the new vehicle mass. In this case, the interval energy and thus the system performance of the energy transducer will remain nearly constant.

The same behavior is presumed, if the tire loses air and the pressure decreases. A lower tire pressure corresponds to a larger ground contact area and is associated with a higher force at constant pressure. With this knowledge, it remains to verify if the energy harvester with one of the formerly presented interface circuits is able to fulfill the energy requirements.

9.4.3 Interface Circuits and Harvested Energy

The data analysis of the interval energy in Sec. 9.4.1 has shown, that multiples times of the necessary amount of energy can be provided even if diode losses are included. Providing sufficient energy at low output voltages remains challenging. As discussed in Sec. 8.4.4, the Voltage Doubler (VD) and the Voltage Tripler (VT) are easy to implement and might be suitable to transfer the energy from the transducer to the storage. The evolution of the capacitor voltage u_s as a function of distance is shown in Fig. 9.32 with a VD and a VT, respectively, for different velocities at 3000 N.

As deduced in Sec. 2.2, if the capacitor is charged to $u_{\text{charged}} \geq 3.9$ V, enough energy is available to transmit a signal and to fulfill the energy requirements. The system EMEH 530 (2) - VD, reaches this objective at velocities of 40 km/h and above. The system EMEH 530 (2) - VT charges the capacitor to 3.9 V, while driving slightly above 30 km/h (presumably 35 km/h). None of the two systems attains 3.9 V at 25 km/h within 417 m.

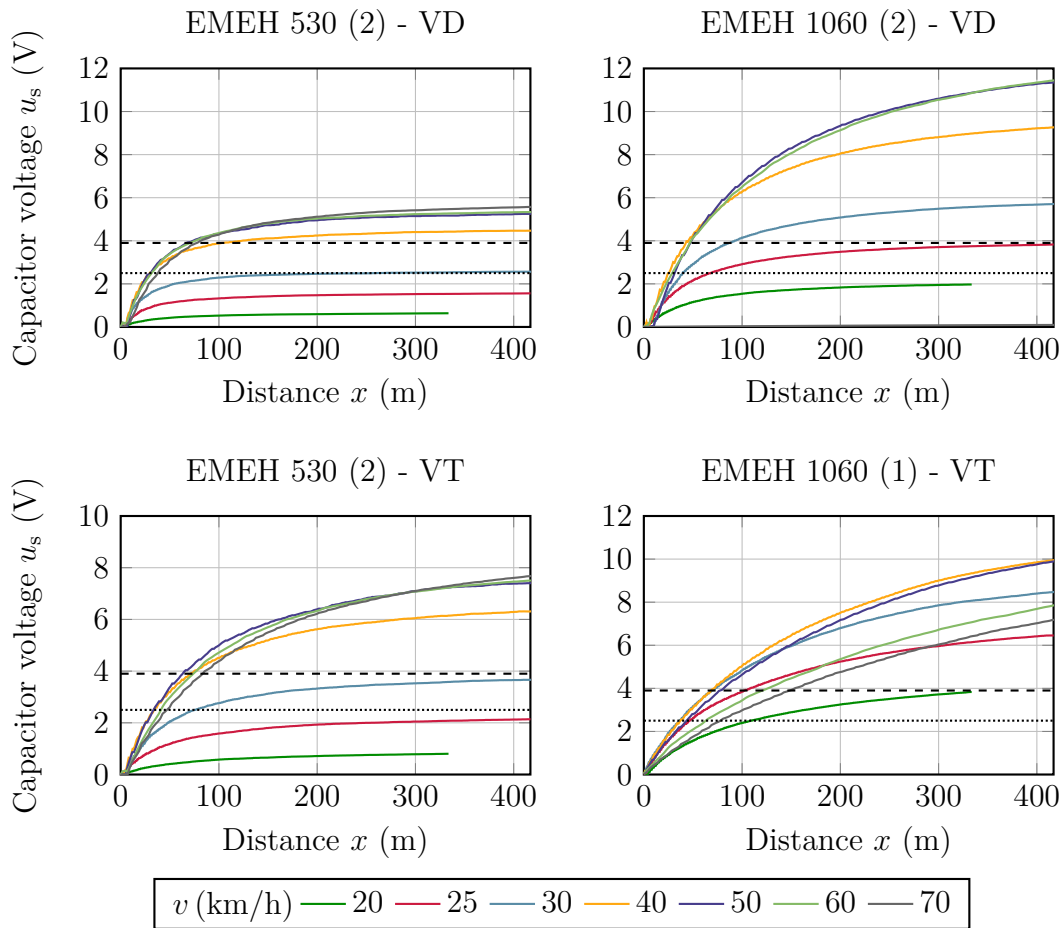


Figure 9.32: Voltage evolution of a $220 \mu\text{C}$ capacitor with connected Voltage Doubler (VD) and Voltage Tripler (VT) at $F = 3000 \text{ N}$. The dashed and densely dashed lines represent the required voltage $u_{\text{charged}} = 3.9 \text{ V}$ and $u_{\text{add}} = 2.5 \text{ V}$, respectively

In contrast, as predicted in Sec. 8.5, the systems EMEH 1060 (2) - VD and EMEH 1060 (1) - VT harvest enough energy while driving at $v \geq 25 \text{ km/h}$. At 50 km/h , five times more than the required energy is transferred to an empty capacitor. With the tested system EMEH 1060 (1) - VT less than 155 m are necessary to charge the storage to u_{charged} at 25 km/h . If the capacitor is already charged to 2.5 V , the distance x is reduced to less than 100 m .

These experimental results perfectly satisfy the energy requirements. Compared to the simulations of Fig. 8.24, in which the storage is charged with a voltage tripler to 5 V after 60 s ($= 417 \text{ m}$ at 25 km/h), the experimental data in Fig. 9.32 show a noticeably better result with 6.4 V . Reasons are the different acceleration input signal as highlighted in Fig. 9.24 and a smaller damping coefficient in the experimentation than assumed in the simulation.

The circuit efficiency is depicted in Fig. 9.33. Due to the normalization to a fixed energy value instead of the actual amount of electrical energy (which could not be measured in the tire at the same time), and due to partially filtered 50 Hz noise, as already explained

in Sec. 9.3.5, fluctuations of the calculated efficiency occur.

As the efficiency depends on the maximal open-circuit voltage, it only reaches 37% at 2 V and 20 km/h. It is significantly higher at higher velocities. This result is in good accordance with the initially calculated interface efficiency at 25 km/h (dashed line). Although the circuit efficiency is more than satisfying, the efficiency can be further increased, applying the optimal timed energizing and transferring circuit, presented in Sec. 8.4.

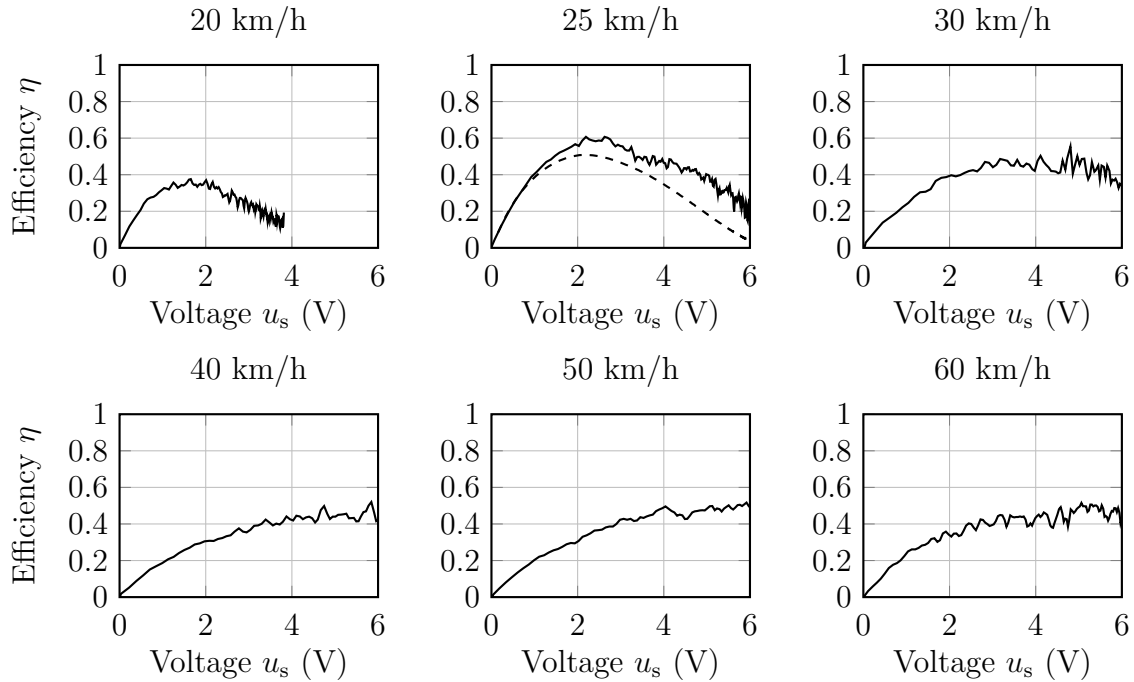


Figure 9.33: Efficiency of EMEH 1060 (1) - VT for different velocities at $F = 3000$ N. The dashed line at 25 km/h represents the initially calculated circuit efficiency of Sec. 8.5

Finally, the average energy per revolution as a function of velocity is compared with experimentally validated state-of-the-art solutions in Fig. 9.34. At each velocity, the designed tire wave based electromagnetic energy harvester EMEH 1060 with voltage tripler is widely better than formerly validated systems. Compared to the former systems, the herein presented system increases the energy per revolution by 400% and 1500% at the critical low velocities of 20 km/h and 30 km/h, respectively. The outstanding improvement compared to the best validated state-of-the-art system is maintained also at higher velocities.

From the capacitor voltage evolution and from the velocity, the average time to transmit a signal, while the vehicle is driving, is deduced and illustrated in Fig. 9.35. Accordingly, at 20 km/h, during 40 s the generate needs to accumulate energy before it can measure and transmit data. In contrast, at 25 km/h only 8 s are needed.

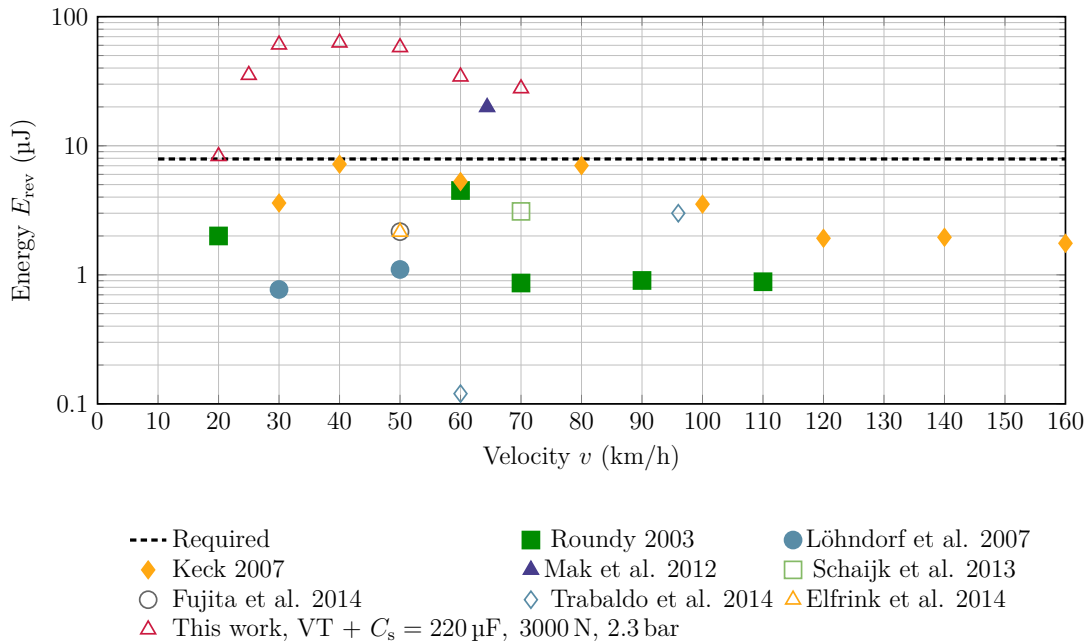


Figure 9.34: Comparison of different tire wave based energy harvesters on a semilogarithmic scale. This work increases the energy per revolution by 400 % and 1500 % at the critical velocities of 20 km/h and 30 km/h, respectively

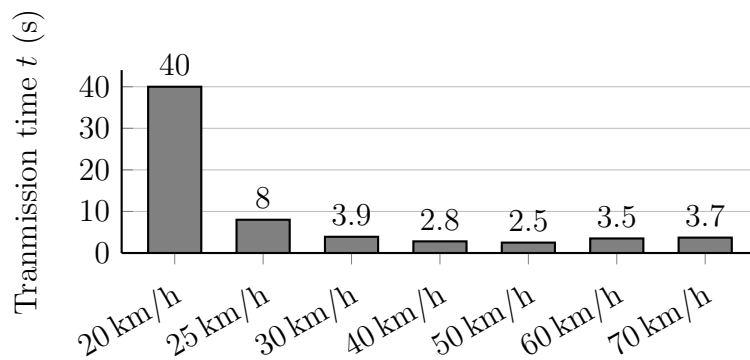


Figure 9.35: Estimated transmission time of EMEH 1060 (1) - VT, when the vehicle already moves, deduced from the charging time from 2.5 V to 3.9 V of the 220 μF capacitor.

9.4.4 Robustness

The electromagnetic energy harvester were tested at different velocities v from 20 km/h up to 200 km/h at $F = 3000$ N and for different forces $F = 1000$ N, ..., 9000 N at $v = 50$ km/h. The systems were in an excellent operational mode after testing and dismounting. After each tire test setup, the electrical parameters resistance and inductance of each coil were measured to assess damages, such as internal wire ruptures. Within the given tolerances of the multimeter, no changes were detected. Moreover, the transducers of the first tire tests were reevaluated in the third tire test, showing a similar performance.

Figure 9.36 shows the excellent state of the energy harvester after testing and dismounting. Only the top bumper did not hold on its initial adhesive position and stuck to the magnet. However, this had neither an important impact on the system performance nor on the reliability.

However, wire ruptures of the energy harvester coils occurred outside the transducer, at the location where the transducer was soldered to the wires of the measurement kit, as shown in Fig. 9.37a. During the first two measurement series, the wire were torn at 80 km/h, 140 km/h, 70 km/h and 130 km/h. The main reason relied on the thin and fragile coil wires, which had a large clearance. The clearance was a result of the wire leaving the top of the PTFE housing and being guided to the tire inner liner to be connected to the thicker wires for the measurement kit. Due to the clearance, the centrifugal acceleration catapulted the wire from the tire inner liner towards the center and backwards which led presumably to the rupture of the fragile solder connection.

To circumvent the failure, the wire was guided through the rubber container directly to the wire of the measurement kit, as illustrated in Fig. 9.37b. As a result, the wire connection did not tear before 190 km/h.

The mentioned issue is mainly related to the presented test setup, as the prototypes need to be connected to a slip ring unit to measure the amount of energy outside the tire. If the harvester is directly connected to the energy storage, embedded in the tire pressure monitoring system, in which all free space is filled with rubber, the described problem will not occur.

Finally, while the piezoelectric inertia energy harvester was destroyed at medium velocities, the electromagnetic energy harvesters withstood the studied test constellations. The observed behavior confirms the hypothesis that the sliding core of the electromagnetic energy harvester is intrinsically more robust than the bending beam in a piezoelectric transducer.



Figure 9.36: Electromagnetic transducer disassembled after testing

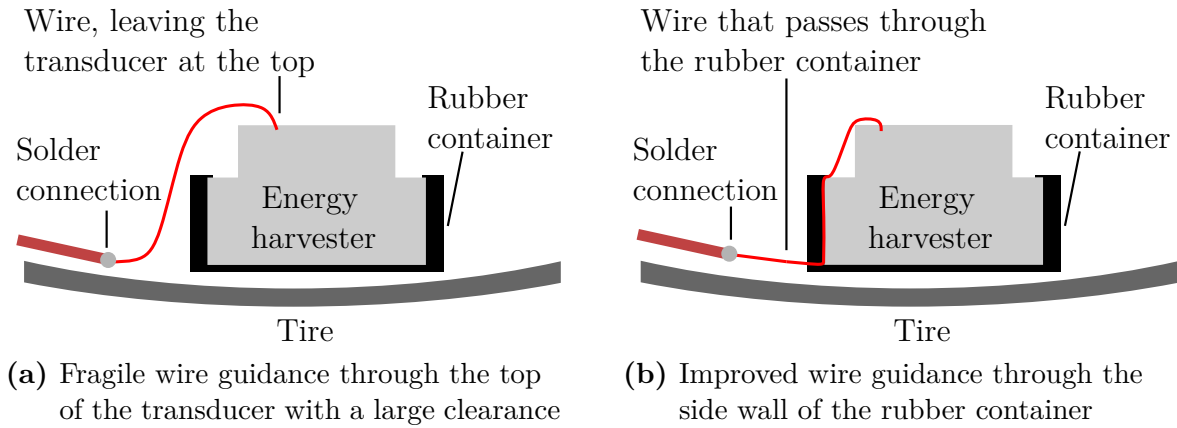


Figure 9.37: Electromagnetic energy harvester samples with a) fragile wire connection and b) improved wire connection

9.4.5 Optimization

The system can be optimized with respect to the provided energy and with respect to the system volume. The effect of selected parameters is rated:

1. Interface circuit

An integrated circuit (IC) that implements the concept of Energizing and Transferring (EaT) would significantly increase the amount of transferred energy. Ideas of the appearance of such an off-chip component IC can be taken from [189]. The additional capacitors required by a voltage tripler would not longer be necessary.

2. Transducer coil design

The combined finite element and network model presented in Chapter 7 and validated in Sec. 9.4 can be used to set up and solve a maximization problem of the generated electrical energy as a function of coil geometry (wire diameter, number of turns in r -direction and in z -direction) for a given volume constraint.

3. Flux concentrator

The use of a magnetic flux concentrator at the coil border can lead to an increased transducer coefficient.

4. Elastic bumpers

The effect of the elastic bumpers at the top and bottom is mainly to soften bounces which would otherwise occur between the movable magnet and the PTFE housing. The height of the bumpers, which were 2 mm can be decreased to 1 mm. Consequently, the system size can be either shrunk, or the open-circuit voltage at 25 km/h can be increased by 10% (which results from a simulation of the adapted network of Sec. 7.6). As the collision with the top bumper is much smaller (hundreds of millinewtons) than the one with the bottom bumper (a few newtons), an entire remove of the top bumper can be studied with respect to the long-term reliability.

9.5 Summary

TPMS Energy Harvester Systems

The three main energy harvester types with interface circuit have been experimentally validated. The most important results are characterized below. While all tire wave based piezoelectric energy harvester (PEH) were entirely damaged during the tests, the tire wave based electromagnetic energy harvester (EMEH) and the strain based PEH showed an outstanding system behavior.

Harvester	Tire wave based PEH	Tire wave based EMEH	Strain based PEH
Volume	☹ 1 cm ³	☺ 1.2 cm ³	☺ 0.11 cm ³
Mass m^a	☹ 3 - 4 g	☺ 1.5 g	☺ 0.16 g
Energy E_{rev} at 25 km/h ^b	☹ 2.0 μJ/cm ³	☺ 54 μJ/cm ³	☺ 20 μJ/cm ²
Energy E_{rev} at 30 km/h ^b	☹ 3.6 μJ/cm ³	☺ 93 μJ/cm ³	☺ 21 μJ/cm ²
Energy E_{rev} at 50 km/h ^b	☹ 10 μJ/cm ³	☺ 190 μJ/cm ³	☺ 24 μJ/cm ²
Interface circuit	Electronic breaker	Voltage tripler	Electronic breaker
Peak efficiency ^c	unknown	☺ 60 %	☺ 40 %
Charging time ΔT_{min} from (0 V to 3.9 V) ^d	☹ $\gg 60$ s	☺ 15 s	☺ 31 s
Charging time ΔT_{min} from (2.5 V to 3.9 V) ^e	☹ $\gg 60$ s	☺ 8 s	☺ 17 s
Velocity dependency	yes	yes	no
Force dependency	yes	yes, if $F \leq 3000$ N	no
System robustness	☹ poor	☺ robust	☺ robust, if $\bar{S} \leq 500$ pm
$E_{\text{rev}}/E_{\text{rev,charged}}$ at 25 km/h ^f	☹ $\ll 1$	☺ 4.5	☺ 2
$E_{\text{rev}}/E_{\text{rev,add}}$ at 50 km/h ^g		☺ 12.6	☺ 3.7
Reusability	☺ yes	☺ yes	☹ no
Recommendation	☹ no	☺ highly	☺ high

^aWithout housing

^bMaximal energy per revolution without interface circuit

^cThe peak efficiency corresponds to the implemented interface circuit at 25 km/h.

^dSignal transmission time at 25 km/h, when the storage capacitor is empty.

^eSignal transmission time at 25 km/h, when the storage capacitor is precharged to $u_{\text{asic}} = 2.5$ V.

^fRatio of harvested energy E_{rev} to required energy $E_{\text{rev,charged}}$, when the capacitor is empty

^gRatio of harvested energy E_{rev} to required energy $E_{\text{rev,add}}$, when the capacitor is precharged

10 Conclusions

State-of-the-art tire pressure monitoring systems (TPMSs) predict over- and under-inflated tires and warn immediately the driver about the tire pressure in a critical situation. Today, TPMSs suffer from limited energy and their lifetime is restricted by a coin cell battery. As the tire of a vehicle is the only physical connection to the road surface, the future tire has the potential to provide additional information to the control unit of the vehicle. Intelligent algorithms of tire based sensors enable monitoring friction, road surface conditions, tread depth, tire wear and aquaplaning situations, reduce the number of accidents, and are another piece of the puzzle that advances the development of autonomous driving vehicles. However, the new algorithms require more energy than a contemporary coin cell battery is able to provide.

Energy harvesting for TPMS has been considered as a promising alternative to replace the battery by a self-sufficient system, as the system converts mechanical energy from a seemingly infinite energy reservoir into electrical energy but requires several steps. In this thesis, the requirements of an energy harvester for TPMS have been analyzed. Different types of well-known transducers have been investigated. Complementary to the commonly stated maximum power of well-known transducers, the normalized energy density was studied and quantified. Among the studied transducer types, both piezoelectric and electromagnetic transducer were identified as most promising technologies for TPMS energy harvesting.

An extensive state-of-the-art analysis of the literature of TPMS energy harvesters has been presented and used to point out opportunities and problems. All in the literature stated centrifugal based piezoelectric energy harvesters were confronted with the unresolved problem of being simultaneously robust at high velocities and providing sufficient energy at low velocities. Contrary, the robustness issue was neither observed in the theoretical studies of a centrifugal based electromagnetic energy harvester nor in a few of many strain based systems. However, the generated electrical energy of the experimentally validated systems was generally not sufficient to meet the energy needs within the velocity range of $25 \text{ km/h} < v < 200 \text{ km/h}$. As most of the energy was lost during the energy transfer from the electrical transducer output to the storage, this thesis provided a deep analysis of common interface circuits. The typical characterization of the efficiency as a function of load resistance has been extended by a new description as a function of storage capacitor voltage, for both electromagnetic energy harvesting systems and piezoelectric energy harvesting systems.

Three common prototype concepts, namely strain based piezoelectric transducers, centrifugal acceleration based piezoelectric transducers and centrifugal acceleration based electromagnetic transducers have been studied and modeled. Preliminary laboratory experiments data replaced simulated FEM data and were fed to the nonlinear network model in order to precisely anticipate the system behavior and to develop prototypes, that meet the imposed energy constraints.

A comprehensive analysis of most common piezoelectric energy harvesting interface circuits, which were used in most TPMS piezoelectric energy harvesters, has demonstrated the efficiency limitation of the widely implemented Standard Energy Harvesting (SEH) interface to be no more than 25 %, but typically a few percent. Furthermore, the analysis revealed that the Synchronous Switch Harvesting on Inductor (SSHI), which has been the focus and recommendation of numerous scientific work, is not generally suitable for low voltage sensor systems, such as a TPMS. It is also as inefficient as the SEH if the piezoelectric open-circuit voltage is much higher than the storage capacitor voltage. In contrast, a Synchronous Electric Charge Extraction (SECE) circuit leads to a significant increase of the efficiency by multiple times compared to SEH and SSHI.

While piezoelectric energy harvesters provide a high open-circuit output voltage, electromagnetic transducers suffer from a low voltage. Electromagnetic systems are commonly characterized in the literature by the peak power and by the maximal average power. The maximal average power is typically deduced under load matching conditions. However, the maximal average power does not reveal how much energy is associated to noise and how much of the energy can be effectively used, if a rectifier reduces the low output voltage by a few hundreds of millivolts and how much energy can be transferred to a storage capacitor which is partially charged. Therefore, a new signal representation, based on stochastic methods, has been introduced and bases on the probability density function (PDF) of the open-circuit voltage signal of an electromagnetic energy harvester. An important outcome are the derived quantities interval charge and interval energy. They express the amount of charge and energy above a specific voltage level, respectively, and enable a quick system comparisons solely based on the open-circuit voltage signal.

Applying the new signal representation, different step-up converters were studied and compared with full-wave rectifiers. Voltage multipliers such as Voltage Doubler (VD) and Voltage Tripler (VT) are not only easy to build but also increase the open-circuit voltage of an electromagnetic energy harvester while driving at 25 km/h sufficiently. Moreover, it has been demonstrated that using the inherent inductor of the electromagnetic energy harvester in combination with a well-timed boost converter (energizing and transferring circuit) further rises the output voltage and the efficiency. An expression of the optimal timing of the converter has been analytically deduced and numerically verified. Switching times with $t_E = 0.9 \cdot L/R_L$ (charging time - switch is on) and $t_T = 0.5 \cdot L/R_L$ (transferring time - switch is off) result in an efficiency of more than 65 %, including rectifying losses of Schottky diodes. The efficiency of 65 % is provided at storage capacitor voltages where

SEH, VD or VT would have already reached the maximal storage voltage.

With the extensive preliminary analysis, different prototypes have been built and tested inside the tire, which has been mounted on a tire test bench. The overall available energy was identified for each prototype and for different velocities and tire loads. Among the prototypes, the centrifugal acceleration based piezoelectric energy harvesters have been damaged during all tests. Although elastic bumpers were installed, this outcome continues the findings from the literature, where it was observed that centrifugal acceleration based piezoelectric energy harvester are unreliable inside the tire. for TPMS, . Contrary, neither strain based piezoelectric transducers nor centrifugal based electromagnetic were damaged during the tests. Due to to a carefully-chosen efficient interface circuit for each transducer, not only the imposed energy requirements could be fulfilled but the provided energy could be improved by 400 % and 1500 % with an electromagnetic energy harvester connected to a voltage tripler at problematic low velocities of 20 km/h and 30 km/h compared to state-of-the-art solutions. Moreover, this system provides 350 % more energy at 25 km/h than is required, once the vehicle is moving continuously. The presented M2807-P2 strain-based piezoelectric system with Electronic Breaker (EB) provides at least 180 % more energy than the best strain based system of the literature. Furthermore it provides 100 % more energy than is required at 25 km/h. Consequently, both transducer systems deliver the energy which is needed for advanced data processing and communication in order to make the tire more intelligent, in the future.

No degradation was observed during short term tests of a few tens of kilometers. By comparing long-term tests of Macro Fiber Composite, the long-term behavior of the strain based energy harvester has been evaluated. Although degradation after millions of tire revolutions is not assumed, in future work, the prototypes should be subjected to long-term stress tests. Furthermore, the generated electrical energy can be significantly increased, if an improved SECE and an energizing and transferring circuit replace the EB and the VT of the piezoelectric system and electromagnetic system, respectively.

Finally, strain-based piezoelectric transducers and centrifugal acceleration based electromagnetic energy harvesters are suitable to replace commonly used coin cell batteries and enable to provide even more energy than batteries do today. A strong potential of optimization relies on the implementation of the proposed interface circuits as integrated circuits.

Appendices

A Voltage-Current-Relation of a Piezoelectric Transducer

The voltage-current relation of a DC voltage source is described by the series connection of an ideal voltage source U_0 connected to a source resistance R by the linear relation

$$U = U_0 - I \cdot R, \quad (\text{A.1})$$

where U , U_0 and I are the voltage, the open-circuit voltage and the current, respectively. In contrast, the voltage-current relation of a piezoelectric transducer forms an ellipse, which is caused by the phase shift between the current of the piezoelectric capacitance and the current of the resistance. The simplified circuit of the piezoelectric material as depicted in Fig. A.1 is the basis of the following calculations.

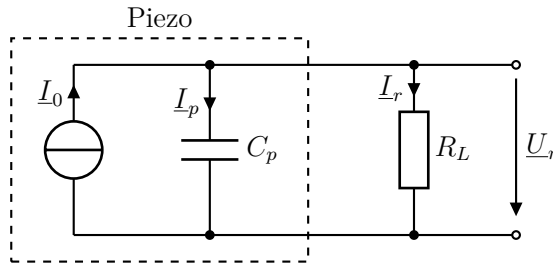


Figure A.1: Equivalent piezoelectric circuit with piezoelectric current source

The starting point is the expression of the current I_r in steady state with

$$I_r = I_0 - j\omega C_p U_r. \quad (\text{A.2})$$

The voltage U_r is given as

$$U_r = R_L \parallel \frac{1}{j\omega C_p} \cdot I_0 = \frac{R_L}{R_L j\omega C_p + 1} \cdot I_0. \quad (\text{A.3})$$

Replacing U_r in Eqn. A.2 with Eqn. A.3 leads to

$$I_r = I_0 \cdot \left(1 - \frac{R_L j\omega C_p}{R_L j\omega C_p + 1} \right) = I_0 \cdot \frac{1}{R_L j\omega C_p + 1}. \quad (\text{A.4})$$

Taking the absolute values of \underline{U}_r and \underline{I}_r results in

$$U_r = I_0 \cdot \frac{R_L \cdot \sqrt{(R_L \omega C)^2 + 1}}{(R_L \omega C)^2 + 1} \quad (\text{A.5})$$

$$I_r = I_0 \cdot \frac{\sqrt{(R_L \omega C)^2 + 1}}{(R_L \omega C)^2 + 1}. \quad (\text{A.6})$$

The maximal voltage and current are reached under open-circuit and short-circuit conditions as

$$I_0 = I_0 \quad \text{for } R_L \rightarrow 0 \quad (\text{A.7})$$

$$U_0 = \frac{I_0}{\omega C} \quad \text{for } R_L \rightarrow \infty. \quad (\text{A.8})$$

The normalization to the maximal voltage and current, respectively, and squaring the expressions to eliminate the root term leads to

$$\left(\frac{U_r}{U_0}\right)^2 = \frac{(R_L \omega C)^2}{(R_L \omega C)^2 + 1} \quad (\text{A.9})$$

$$\left(\frac{I_r}{I_0}\right)^2 = \frac{1}{(R_L \omega C)^2 + 1}. \quad (\text{A.10})$$

Noticeably is, that the sum of $(U_r/U_0)^2$ and I_r/I_0^2 equals 1.

$$\left(\frac{I_r}{I_0}\right)^2 + \left(\frac{U_r}{I_0/(\omega C_p)}\right)^2 = \frac{1}{(\omega C_p R_L)^2 + 1} + \frac{\omega C_p R_L}{(\omega C_p R_L)^2 + 1} \quad (\text{A.11})$$

$$\left(\frac{I_r}{I_0}\right)^2 + \left(\frac{U_r}{I_0/(\omega C_p)}\right)^2 = 1. \quad (\text{A.12})$$

Eqn. A.12 forms an ellipse that describes the relation between current and voltage of a resistor with the semi axis I_0 and $I_0/(\omega C_p)$ and the coordinates I_r and U_r .

The elliptical voltage-current relation can be demonstrated, when different load resistances are connected to the terminals of the piezoelectric transducer, while the deflection of the material is maintained constant and while current and voltage are measured. In the following, suitable resistances are calculated. Based on the elliptical equation Eqn. A.12 and on the standard ellipse described by

$$(x/a)^2 + (y/b)^2 = 1 \quad (\text{A.13})$$

$$\text{with } x = I_r, y = U_r \quad \text{and} \quad a = I_0, b = I_0/(\omega C_p) \quad (\text{A.14})$$

the coordinates U_r and I_r as functions of angle φ are

$$I_r = I_0 \cdot \cos(\varphi) \quad (\text{A.15})$$

$$U_r = U_0 \cdot \sin(\varphi). \quad (\text{A.16})$$

To determine the load resistance R_L that correspondence to the angle φ , the quotient y/x is calculated and expressed as

$$\frac{y}{x} = \frac{U_r}{I_r} = \frac{U_0 \cdot \sin(\varphi)}{I_0 \cdot \cos(\varphi)} = \tan(\varphi) \cdot \frac{U_0}{I_0} \quad (\text{A.17})$$

The resistance as a function of phase angle is

$$R_L = \tan(\varphi) \cdot \frac{1}{\omega C_p} \quad (\text{A.18})$$

$$R_L = \tan(\varphi) \cdot Z_C. \quad (\text{A.19})$$

The first quadrant of a diagram will be separated in n almost equidistant areas. For experimental measurements the parameters $n = 5$ and $\varphi = 18^\circ$ are selected. Table A.1 lists the coefficients $\tan(\varphi)$ corresponding to the angles φ .

Table A.1: Elliptical angle φ and corresponding load resistance ratio R_L/Z_C

φ ($^\circ$)	0	18	36	54	72	90
$U_r/U_0 = \sin(\varphi)$	0	0.31	0.59	0.81	0.95	1
$I_r/I_0 = \cos(\varphi)$	1	0.95	0.81	0.59	0.31	0
$R_L/Z_C = \tan(\varphi)$	0	0.32	0.73	1.38	3.07	∞ ¹

Both a load resistance R_L of 0 and ∞ are not realizable, practically. For good estimates of the open-circuit voltage and the short-circuit current, an error of less than 1% is acceptable. From $\sin(\varphi) > 0.99$ and $\cos(\varphi) < 0.01$ follows $\varphi > 81.9^\circ$ and $\varphi < 8.1^\circ$, respectively. Then, the load resistance are chosen such that $R_L/Z_C > 7.02$ and $R_L/Z_C < 0.14$, respectively.

B SSHI - Parasitic Effect

A parasitic piezoelectric resistance limits the piezoelectric voltage u_p and the efficiency η_{SSHI} of the Synchronous Switch Harvesting on Inductor (SSHI). The parasitic piezoelectric resistance is commonly modeled as resistance R_p , being in parallel to the capacitance C_p , as illustrated in Fig. B.1

The current flows through the parasitic resistance and is used to describe the self-discharge [151]. In steady state, the current entering and leaving C_p is constant. The

¹To be mathematically correct, the tangent of 90° is not defined.

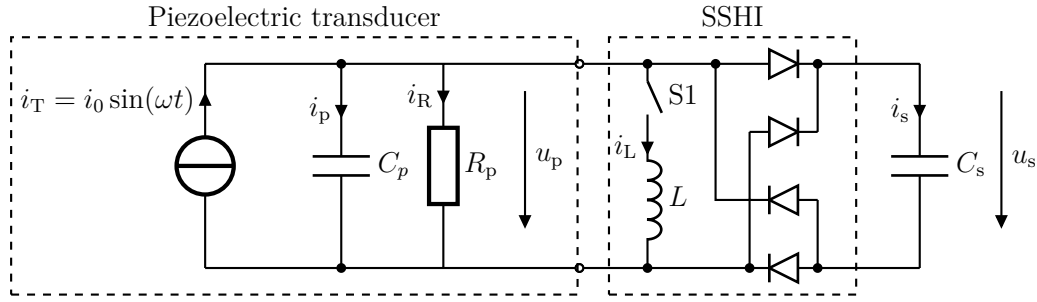


Figure B.1: Equivalent circuit of the piezoelectric transducer

charge balance of the circuit with parasitic resistance can be expressed as

$$Q_0 = \Delta Q_R + \Delta Q_s, \quad (\text{B.1})$$

where ΔQ_R is the accumulated current through the resistance R_p . With $\Delta Q_R = \int_{t=0}^{T/2} i_R dt$, with the current $i_R = u_s/R_p$ and with the capacitor voltage $u_s \approx \text{const}$ follows

$$Q_0 = \int_{t=0}^{T/2} \frac{u_s}{R_p} dt + \Delta Q_s = u_s \frac{T}{2R_p} + \Delta Q_s. \quad (\text{B.2})$$

Rearranging according to u_s results in

$$u_s = R_p \frac{2}{T} (Q_0 - \Delta Q_s). \quad (\text{B.3})$$

When no charge ΔQ_s can be transferred, the maximal capacitor voltage u_s is reached. Replacing Q_0 by

$$Q_0 = \int_{t=0}^{T/2} i_T(t) dt = \frac{T}{2} \overline{i_T(t)}, \quad (\text{B.4})$$

where $\overline{i_T(t)}$ is the average current leads to

$$u_{s,\text{max}} = R_p \cdot \overline{i_T(t)}. \quad (\text{B.5})$$

Consequently, both the parasitic resistance and the average source current determine the maximal voltage u_s . Real diodes further decrease the voltage u_s . If the resistance R_p is large, the parasitic effect plays a subordinated role.

C Average Efficiency of Piezoelectric Interface Circuits

In the following, the average efficiencies of common piezoelectric interface circuits are deduced. The piezoelectric system is approximated by an ideal harmonic current source in parallel to a piezoelectric capacitor C_p as depicted in Fig. C.1.

The average efficiency after n half waves is

$$\bar{\eta} = \frac{E_{\text{out}}}{E_0} = \frac{C_s u_{s,n}^2}{n \cdot \frac{C_p u_0^2}{2}} = \frac{C_s u_{s,n}^2}{n \cdot C_p u_0^2} \quad (\text{C.1})$$

$$\bar{\eta} = \frac{a \cdot u_{s,n}^2}{n \cdot u_0^2}, \quad (\text{C.2})$$

where $u_{s,n}$ is the capacitor voltage after the n -th half wave and $u_0 = 1/C \int_{t=0}^{T/2} i(t) dt$.

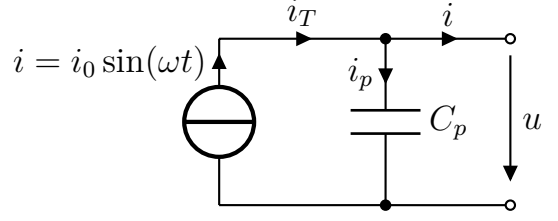


Figure C.1: Piezoelectric system with ideal harmonic current source

Standard Energy Harvesting

To analyze the efficiency of a SEH, an ideal full-wave rectifier is assumed with a diode voltage drop $u_d = 0$ V. From Eqn. 6.10, the capacitor voltage after the n -th half wave is

$$u_{s,n} = \frac{C_p u_0 + (C_s - C_p) \cdot u_{s,n-1}}{C_s + C_p}, \quad (\text{C.3})$$

which is rewritten with the ratios $a = C_s/C_p$ and $b_{n-1} = u_{s,n-1}/u_0$ as

$$u_{s,n} = u_0 \frac{1 + (a-1) \cdot b_{n-1}}{a+1}. \quad (\text{C.4})$$

The first three values of the voltage $u_{s,n}$ with $n = 1, 2, 3$ are

$$u_{s,1} = u_0 \frac{1}{a+1} \quad (\text{C.5})$$

$$u_{s,2} = u_0 \frac{1 + (a-1) \cdot \frac{1}{a+1}}{a+1} = u_0 \left(\frac{1}{a+1} + \frac{a-1}{(a+1)^2} \right) \quad (\text{C.6})$$

$$u_{s,3} = u_0 \frac{1 + (a-1) \cdot \left(\frac{1}{a+1} + \frac{a-1}{(a+1)^2} \right)}{a+1} = u_0 \left(\frac{1}{a+1} + \frac{a-1}{(a+1)^2} + \frac{(a-1)^2}{(a+1)^3} \right). \quad (\text{C.7})$$

Since the storage capacitor C_s is much greater than the piezoelectric capacitance C_p ($a \gg 1$), the expression of the storage capacitor voltage can be developed to the well known finite geometric series as

$$u_{s,n} = \frac{u_0}{a+1} \sum_{i=0}^{n-1} \left(\frac{a-1}{a+1} \right)^i. \quad (\text{C.8})$$

With the relation of the finite geometric series

$$\sum_{i=0}^{n-1} q = \frac{1 - q^n}{1 - q} \quad (\text{C.9})$$

follows

$$u_{s,n} = \frac{u_0}{a+1} \frac{1 - \left(\frac{a-1}{a+1}\right)^n}{1 - \frac{a-1}{a+1}} = \frac{u_0}{2} \left(1 - \left(\frac{a-1}{a+1}\right)^n\right). \quad (\text{C.10})$$

To figure out the amount of half waves n until the voltage $u_{s,n}$ reaches the desired voltage u_s , the equation

$$u_{s,n} - u_s = 0 \quad (\text{C.11})$$

$$\frac{u_0}{2} \left(1 - \left(\frac{a-1}{a+1}\right)^n\right) - u_s = 0 \quad (\text{C.12})$$

is solved and leads to

$$n = \frac{\ln\left(1 - 2\frac{u_s}{u_0}\right)}{\ln\left(\frac{a-1}{a+1}\right)} = \frac{\ln(1 - 2b)}{\ln\left(\frac{a-1}{a+1}\right)}. \quad (\text{C.13})$$

Inserting n from Eqn. C.13 and $u_{s,n}$ from Eqn. C.10 in Eqn. C.2 leads to

$$\bar{\eta}_{\text{SEH}} = \frac{au_s^2}{nu_0^2} = \frac{ab^2}{n} = b^2 \cdot \frac{a \cdot \ln\left(\frac{a-1}{a+1}\right)}{\ln(1 - 2b)}. \quad (\text{C.14})$$

Since $a \gg 0$, l'Hôpital's rule can be applied and the product $a \cdot \ln\left(\frac{a-1}{a+1}\right)$ tends towards -2 . Consequently, Eqn. C.14 is rewritten to the average expression of the efficiency as

$$\bar{\eta}_{\text{SEH}} = \frac{-2b^2}{\ln(1 - 2b)}. \quad (\text{C.15})$$

Switch Only Rectifier

Similarly as demonstrated beforehand, the average efficiency of the switch only rectifier is be deduced. Accordingly, the capacitor voltage after the n -th half wave is

$$u_{s,n} = \frac{C_p u_0 + C_s \cdot u_{s,n-1}}{C_s + C_p} = u_0 \frac{1 + a \cdot b_{n-1}}{a+1}. \quad (\text{C.16})$$

The first three values of the voltage $u_{s,n}$ are

$$u_{s,1} = u_0 \frac{1}{a+1} \quad (\text{C.17})$$

$$u_{s,2} = u_0 \frac{1 + a \cdot \frac{1}{a+1}}{a+1} = u_0 \left(\frac{1}{a+1} + \frac{a}{(a+1)^2} \right) \quad (\text{C.18})$$

$$u_{s,3} = u_0 \frac{1 + a \cdot \left(\frac{1}{a+1} + \frac{a}{(a+1)^2} \right)}{a+1} = u_0 \left(\frac{1}{a+1} + \frac{a}{(a+1)^2} + \frac{a^2}{(a+1)^3} \right) \quad (\text{C.19})$$

Since $a \gg 1$, the expression of the storage capacitor voltage can be developed to the finite geometric series

$$u_{s,n} = \frac{u_0}{a+1} \sum_{i=0}^{n-1} \left(\frac{a}{(a+1)} \right)^i. \quad (\text{C.20})$$

The series can be rewritten to

$$u_{s,n} = \frac{u_0}{a+1} \frac{1 - \left(\frac{a}{a+1} \right)^n}{1 - \frac{a}{a+1}} = u_0 \left(1 - \left(\frac{a}{a+1} \right)^n \right). \quad (\text{C.21})$$

To obtain the number of half waves n until the voltage $u_{s,n}$ is equal to the desired voltage u_s , the equation

$$u_{s,n} - u_s = 0 \quad (\text{C.22})$$

$$u_0 \left(1 - \left(\frac{a}{a+1} \right)^n \right) - u_s = 0 \quad (\text{C.23})$$

is solved and leads to

$$n = \frac{\ln(1-b)}{\ln\left(\frac{a}{a+1}\right)}. \quad (\text{C.24})$$

Inserting n and $u_{s,n}$ in Eqn. C.2 leads to

$$\bar{\eta}_{\text{SOR}} = b^2 \cdot \frac{a \cdot \ln\left(\frac{a}{a+1}\right)}{\ln(1-b)}. \quad (\text{C.25})$$

Since $a \gg 0$, l'Hôpital's rule can be applied to the product $a \cdot \ln\left(\frac{a}{a+1}\right)$ which tends towards -1 . Consequently, Eqn. C.14 is rewritten to

$$\bar{\eta}_{\text{SOR}} = \frac{-b^2}{\ln(1-b)}. \quad (\text{C.26})$$

Synchronized Switch Harvesting on Inductor

According to Sec. 6.4 the capacitor voltage after the n -th half wave is

$$u_{s,n} = \frac{C_p u_0 + (C_s + C_p) \cdot u_{s,n-1}}{C_s + C_p} = u_0 \frac{1 + (a + 1) \cdot b_{n-1}}{a + 1}. \quad (\text{C.27})$$

The first three values of the voltage $u_{s,n}$ with $n = 1, 2, 3$ are

$$u_{s,1} = u_0 \frac{1}{a + 1} \quad (\text{C.28})$$

$$u_{s,2} = u_0 \frac{2 + (a + 1) \cdot \frac{1}{a + 1}}{a + 1} = u_0 \left(\frac{2}{a + 1} \right) \quad (\text{C.29})$$

$$u_{s,3} = u_0 \frac{2 + (a + 1) \cdot \frac{2}{a + 1}}{a + 1} = u_0 \left(\frac{3}{a + 1} \right). \quad (\text{C.30})$$

Furthermore, $u_{s,n}$ can be rewritten as

$$u_{s,n} = u_0 \left(\frac{n}{a + 1} \right). \quad (\text{C.31})$$

From Eqn. C.31, n can be directly solved and is

$$n = (a + 1) \cdot b. \quad (\text{C.32})$$

Inserting n and $u_{s,n}$ in Eqn. C.2 leads to

$$\bar{\eta}_{\text{SSHI}} = \frac{a \cdot b^2}{(a + 1)b}. \quad (\text{C.33})$$

Since $a \gg 0$ follows

$$\bar{\eta}_{\text{SSHI}} = b. \quad (\text{C.34})$$

D SECE Efficiency Calculation

The transferred charge ΔQ_s is calculated in the steps below

$$\Delta Q_s = \int_0^t i(t) dt = \int_0^{\varphi_z} i(\varphi) \frac{d\varphi}{\omega_e} \quad (\text{D.1})$$

$$(\text{D.2})$$

With $i(t) = i_L(t)$ from Eqn. 6.54 follows

$$\Delta Q_s = \frac{i_0}{\omega_e} \cdot \left[\exp\left(-\frac{\varphi}{\kappa}\right) \cdot \frac{2bq_1\kappa \cos(\varphi) + (\kappa^2 + 2bq_1 + 1) \sin(\varphi)}{\kappa^2 + 1} \right]_0^{\varphi_z} \quad (\text{D.3})$$

$$\Delta Q_s = \frac{i_0\kappa}{\omega_e(\kappa^2 + 1)} \cdot \left(\exp\left(-\frac{\varphi_z}{\kappa}\right) \cdot \frac{2bq_1(2bq_1 + 1) + \kappa^2 + 2bq_1 + 1}{\sqrt{\kappa^2 + (2bq_1 + 1)^2}} - 2bq_1 \right) \quad (\text{D.4})$$

$$\Delta Q_s = \frac{i_0\kappa}{\omega_e(\kappa^2 + 1)} \cdot \left(\exp\left(-\frac{\varphi_z}{\kappa}\right) \cdot \sqrt{\kappa^2 + (2bq_1 + 1)^2} - 2bq_1 \right) \quad (\text{D.5})$$

Replacing κ in the first factor of Eqn. D.5 by $\kappa = \omega_e/\delta$ and ω_e^2 by $\omega_e^2 = \omega_0^2 - \delta^2$ leads to

$$\Delta Q_s = \frac{i_0\delta}{\omega_0^2} \cdot \left(\exp\left(-\frac{\varphi_z}{\kappa}\right) \cdot \sqrt{4q_2^2 + 4(bq_1)^2 + 4bq_1 - 2bq_1} \right) \quad (\text{D.6})$$

$$\Delta Q_s = \frac{2i_0\delta}{\omega_0^2} \cdot \left(\exp\left(-\frac{\varphi_z}{\kappa}\right) \cdot \sqrt{q_2^2 + (bq_1)^2 + bq_1 - bq_1} \right). \quad (\text{D.7})$$

The remaining k in the exponential term is replaced by the relation $\kappa = \sqrt{4q_2^2 - 1}$. The relation between the added energy to the capacitor in relation to the energy stored on the inductor returns the efficiency of the second phase:

$$\eta_{\text{SECE},2} = \frac{E_C}{E_L} = \frac{(\Delta Q_s + Q_{s,0})^2 - Q_{s,0}^2}{LC \cdot i_0^2} \quad (\text{D.8})$$

$$\eta_{\text{SECE},2} = \omega_0^2 \frac{\Delta Q_s(\Delta Q_s + 2Q_{s,0})}{i_0^2} \quad (\text{D.9})$$

$$\eta_{\text{SECE},2} = \frac{2 \exp\left(-\frac{\varphi_z}{\kappa}\right) \cdot \sqrt{q_2^2 + (bq_1)^2 + bq_1} - 2bq_1}{4q_2^2} \cdot \left(2 \exp\left(-\frac{\varphi_z}{\kappa}\right) \cdot \sqrt{q_2^2 + (bq_1)^2 + bq_1 + 2bq_1} \right) \quad (\text{D.10})$$

$$\eta_{\text{SECE},2} = \frac{4 \exp\left(-2\frac{\varphi_z}{\kappa}\right) \cdot \left(q_2^2 + (bq_1)^2 + bq_1 \right) - 4(bq_1)^2}{4q_2^2} \quad (\text{D.11})$$

$$\eta_{\text{SECE},2} = \frac{\exp\left(-2\frac{\varphi_z}{\kappa}\right) \cdot \left(q_2^2 + (bq_1)^2 + bq_1 \right) - (bq_1)^2}{q_2^2} \quad (\text{D.12})$$

$$\eta_{\text{SECE},2} = -\frac{(bq_1)^2}{q_2^2} + \left(1 + \frac{(bq_1)^2}{q_2^2} + \frac{bq_1}{q_2^2} \right) \cdot \exp\left(-2 \operatorname{atan}\left(\frac{\sqrt{4q_2^2 - 1}}{2bq_1 + 1}\right) \cdot \sqrt{4q_2^2 - 1}^{-1}\right). \quad (\text{D.13})$$

E Electromagnetic Energy Harvester Simulation Parameters

Both repulsive force and transducer coefficient are expressed as a polynomial function

$$f = a_n \cdot z^n + a_{n-1} \cdot z^{n-1} + \dots + a_1 \cdot z^1 + a_0 \cdot z^0. \quad (\text{E.1})$$

Accordingly, the parameters are listed in Tab. E.1

Parameter	a_5 (N/mm ⁵)	a_4 (N/mm ⁴)	a_3 (N/mm ³)	a_2 (N/mm ²)	a_1 (N/mm)	a_0 (N)
F_{mag}	0	$1.53 \cdot 10^{-4}$	$-5.84 \cdot 10^{-3}$	$8.06 \cdot 10^{-2}$	-0.491	1.17
β (1060)	$6.64 \cdot 10^{-4}$	$-2.70 \cdot 10^{-2}$	$3.31 \cdot 10^{-2}$	-1.20	-0.647	1.07
β (530)	$3.32 \cdot 10^{-4}$	$-1.35 \cdot 10^{-2}$	$1.65 \cdot 10^{-2}$	-0.60	-0.324	0.53

Table E.1: Polynomial coefficients of magnetic force F_{mag} and transducer coefficient β

The bumper force of the top bumper is represented with $z_0 = 7$ mm in the form of

$$f = a_3 \cdot (z - z_0)^3 + a_2 \cdot (z - z_0)^2 + a_1 \cdot (z - z_0)^1 + a_0, \quad (\text{E.2})$$

where z is the current position. The bottom bumper force is expressed as

$$f = a_3 \cdot (z - z_0)^3 - a_2 \cdot (z - z_0)^2 + a_1 \cdot (z - z_0)^1 - a_0, \quad (\text{E.3})$$

with $z_0 = 2$ mm. The coefficients are listed in Tab. E.2.

Parameter	a_3 (N/mm ³)	a_2 (N/mm ²)	a_1 (N/mm)	a_0 (N)
Bumper	3.03	5.65	2.41	$2.42 \cdot 10^{-2}$

Table E.2: Polynomial coefficients of elastic bumpers

F Energizing and Transferring Circuit - Efficiency Calculation

In this section the efficiency of the energizing and transferring circuit is calculated, introduced in Sec. 8.4.3. The general form of the homogeneous solution is composed of hyperbolic functions and expressed as

$$u_h = \exp(-\delta t) \cdot \left(A \cosh(\omega_e t) + B \sinh(\omega_e t) \right). \quad (\text{F.1})$$

The initial conditions of Eqn. 8.69 are inserted and the voltage is expressed as

$$u(t) = u_0 + \exp(-\delta t) \cdot \left((u_{s,0} - u_0) \cdot \cosh(\omega_e t) + \left(\frac{i_{L,0} + \delta C_s (u_{s,0} - u_0)}{\omega_e C_s} \right) \cdot \sinh(\omega_e t) \right). \quad (\text{F.2})$$

The current $i(t) = C_s \cdot du(t)/dt$ is

$$i(t) = \exp(-\delta t) \cdot \left(i_{L,0} \cosh(\omega_e t) - \left(\frac{C_s(u_{s,0} - u_0)(\delta^2 - \omega_e^2) + \delta i_{L,0}}{\omega_e} \right) \sinh(\omega_e t) \right), \quad (\text{F.3})$$

where $\delta = L_c/2/R_c$ and $i_{L,0} = i(t = t_E)$ as described in Eqn. 8.61. Both voltage and current are normalized to u_0 and can be expressed by the quality factor $q = \sqrt{L_c/C_s}/R_c$, the normalized transferring time ratio $y = t_T/\tau$ and the initial capacitor voltage ratio $b = u_{s,0}/u_0$. For $t = t_T$ the following terms $\delta \cdot t_T$ and $\omega_e \cdot t_T$ can be calculated to

$$\delta \cdot t_T = \frac{R_c}{2L_c} t_T = \frac{y}{2} \quad (\text{F.4})$$

and to

$$\omega_e \cdot t_T = \sqrt{\delta^2 - \omega_0^2} t_T = \sqrt{\frac{y^2}{2} - \frac{R_c^2}{L_c^2} \cdot \frac{L_c}{C_s R_c^2} t_T^2} \quad (\text{F.5})$$

$$\omega_e \cdot t_T = \sqrt{\frac{y^2}{2} - q^2 y^2} = \frac{y}{2} \sqrt{1 - 4q^2}. \quad (\text{F.6})$$

The normalized voltage $u_N(t) = u(t)/u_0$ at $t = t_T$ is

$$u_N(x, y) = \frac{u(x, y)}{u_0} = 1 + \exp(-y/2) \cdot \left[(b-1) \cosh\left(\frac{y\sqrt{1-4q^2}}{2}\right) + \left(\frac{2q^2(1 - \exp(-x) + n \exp(-x)) + (b-1)}{\sqrt{1-4q^2}} \right) \sinh\left(\frac{y\sqrt{1-4q^2}}{2}\right) \right] \quad (\text{F.7})$$

and the normalized current $i_N = i(t)/i_0$ at $t = t_T$ is

$$i_N(x, y) = \frac{i(x, y)}{i_0} = \exp(-y/2) \cdot \left[(1 - \exp(-x) + n \exp(-x)) \cosh\left(\frac{y\sqrt{1-4q^2}}{2}\right) - \left(\frac{2(b-1) + (1 - \exp(-x) + n \exp(-x))}{\sqrt{1-4q^2}} \right) \sinh\left(\frac{y\sqrt{1-4q^2}}{2}\right) \right]. \quad (\text{F.8})$$

Equations F.7 and F.8 describe the circuit, shown in Fig. 8.21. They are used to calculate the overall efficiency of the energizing and transferring circuit as below.

The energy ΔE that is added to the storage capacitor C_s is

$$\Delta E = \frac{C_s}{2} (u^2(t) - u(t=0)^2) = \frac{C_s u_0^2}{2} \left(\frac{u^2(t)}{u_0} - \frac{u(t=0)^2}{u_0} \right). \quad (\text{F.9})$$

With the initial voltage $u(t = 0) = u_{s,0}$ from Eqn. 8.69 and with Eqn. F.7 follows

$$\Delta E = \frac{C_s u_0^2}{2} \left(u_N^2(x, y, n) - b^2 \right). \quad (\text{F.10})$$

According to Eqn. 8.3, the available energy E_{elec} in the interval $[0, t_E + t_T]$ is

$$E_{\text{elec}} = \frac{u_0^2 \cdot (t_E + t_T)}{4R_c} \quad (\text{F.11})$$

Replacing the times t_E and t_T by the time ratios $x = t_E/\tau$ and $y = t_T/\tau$ results in

$$E_{\text{elec}} = \frac{L_c u_0^2 \cdot (x + y)}{4R_c^2}. \quad (\text{F.12})$$

Dividing the added energy from Eqn. F.10 by the available energy from Eqn. F.12 leads to the efficiency of the energizing and transferring circuit η_{EaT} with

$$\eta_{\text{EaT}} = \frac{\Delta E}{E_{\text{elec}}} = \frac{4C_s R_c^2 u_0^2}{2L_c u_0^2} \cdot \frac{u_N^2(x, y, n, q, b) - b^2}{x + y} \quad (\text{F.13})$$

Finally, replacing $L_c/C_s/R_c^2 = q^2$ results in

$$\eta_{\text{EaT}} = 2 \frac{u_N^2(x, y, n, q, b) - b^2}{q^2 \cdot (x + y)}. \quad (\text{F.14})$$

G Strain Based Energy Harvester Results

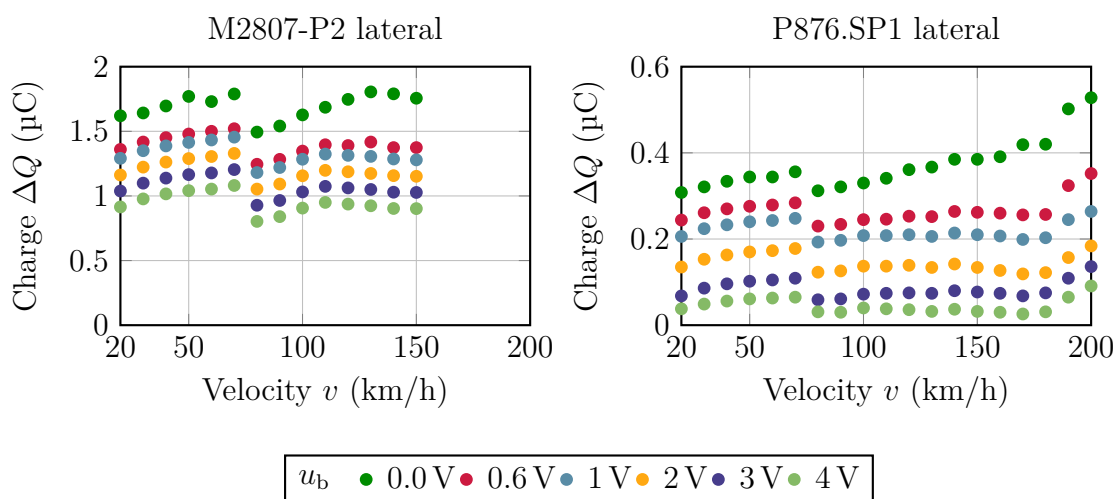


Figure G.1: Accumulated charge ΔQ as a function of velocity at $F = 3000$ N for different voltages u_b . The sample were placed in lateral direction.

Bibliography

- [1] S. Beeby and N. White, eds. *Energy Harvesting for Autonomous Systems*. Artech House, 2010.
- [2] P. Barron et al. *2011 Tire Pressure Monitoring Systems Special Study, User's Coding Manual*. Tech. rep. 2017.
- [3] Council of the European Union. *Regulation (EC) No 661/2009 of the European Parliament*. July 31, 2009.
- [4] R. MATSUZAKI et al. "Analysis of Applied Load Estimation Using Strain for Intelligent Tires". In: *Journal of Solid Mechanics and Materials Engineering* 4.10 (2010), pp. 1496–1510. DOI: 10.1299/jmmp.4.1496.
- [5] G. Erdogan, L. Alexander, and R. Rajamani. "Estimation of Tire-Road Friction Coefficient Using a Novel Wireless Piezoelectric Tire Sensor". In: *IEEE Sensors Journal* 11.2 (Feb. 2011), pp. 267–279. DOI: 10.1109/jsen.2010.2053198.
- [6] P. Behroozinia, S. Taheri, and R. Mirzaeifar. "Tire health monitoring using the intelligent tire concept". In: *Structural Health Monitoring* 18.2 (Feb. 2018), pp. 390–400. DOI: 10.1177/1475921718756602.
- [7] RoadCloud. *Aquaplaning and the dangers of driving in bad weather*. [Online; 2021-12-21]. 2021. URL: <https://roadcloud.com/news/aquaplaning-and-the-dangers-of-driving-in-bad-weather/>.
- [8] The Insurance Institute for Highway Safety. *Fatality Facts 2019 - State by state*. [Online; 2021-12-21]. 2021. URL: <https://www.iihs.org/topics/fatality-statistics/detail/state-by-state>.
- [9] EUROSTAT. *Road accident fatalities - statistics by type of vehicle*. [Online; 2021-12-21]. 2021. URL: https://ec.europa.eu/eurostat/statistics-explained/index.php?title=Road_accident_fatalities_-_statistics_by_type_of_vehicle.
- [10] A. J. Niskanen and A. J. Tuononen. "Three 3-axis accelerometers fixed inside the tyre for studying contact patch deformations in wet conditions". In: *Vehicle System Dynamics* 52.sup1 (Mar. 2014), pp. 287–298. DOI: 10.1080/00423114.2014.898777.

- [11] O. B. Akan et al. “Internet of Hybrid Energy Harvesting Things”. In: *IEEE Internet of Things Journal* 5.2 (Apr. 2018), pp. 736–746. DOI: 10.1109/jiot.2017.2742663.
- [12] S. Chen et al. “A Vision of IoT: Applications, Challenges, and Opportunities With China Perspective”. In: *IEEE Internet of Things Journal* 1.4 (Aug. 2014), pp. 349–359. DOI: 10.1109/jiot.2014.2337336.
- [13] N. Kumar, D. Acharya, and D. Lohani. “An IoT-Based Vehicle Accident Detection and Classification System Using Sensor Fusion”. In: *IEEE Internet of Things Journal* 8.2 (Jan. 2021), pp. 869–880. DOI: 10.1109/jiot.2020.3008896.
- [14] A. Hentati et al. “Analysis of the Interdelivery Time in IoT Energy Harvesting Wireless Sensor Networks”. In: *IEEE Internet of Things Journal* 8.6 (Mar. 2021), pp. 4920–4930. DOI: 10.1109/jiot.2020.3032537.
- [15] M. Germer and U. Marschner. “Energy Harvesting for TPMS from an Energy Point of View”. In: *9th National Days on Energy Harvesting and Storage*. June 2019.
- [16] M. Germer, U. Marschner, and A. Richter. “Energy Harvesting for Tire Pressure Monitoring Systems from a Mechanical Energy Point of View”. In: *IEEE Internet of Things Journal* (2022), pp. 1–1. DOI: 10.1109/jiot.2022.3152547.
- [17] J. Lee et al. “Strain-based piezoelectric energy harvesting for wireless sensor systems in a tire”. In: *Journal of Intelligent Material Systems and Structures* 26.11 (Nov. 2014), pp. 1404–1416. DOI: 10.1177/1045389x14544138.
- [18] *Intelligent Tyre for Accident-free Traffic*. Tech. rep. VTT Technical report IST-2001–34372, 2005.
- [19] J. Lee and B. Choi. “Development of a piezoelectric energy harvesting system for implementing wireless sensors on the tires”. In: *Energy Conversion and Management* 78 (Feb. 2014), pp. 32–38. DOI: 10.1016/j.enconman.2013.09.054.
- [20] Varta. *Lithium Manganese Dioxide*. Tech. rep. Accessed: 2021-03-08. Geneva, CH, Mar. 2014. URL: https://products.varta-microbattery.com/applications/mb_data/documents/data_sheets/DS6032.pdf.
- [21] *Road vehicles — Safety enhancement in conjunction with tyre inflation pressure monitoring*. Standard ISO_21750. Geneva, CH: International Organization for Standardization, Mar. 2006.
- [22] S. J. Roundy. “Energy scavenging for wireless sensor nodes with a focus on vibration to electricity conversion”. PhD thesis. University of California, Berkeley Berkeley, CA, 2003, pp. 129–154.
- [23] M. Löhndorf et al. “Evaluation of energy harvesting concepts for tire pressure monitoring systems”. In: *Proceedings of Power MEMS* (2007), pp. 331–334.

-
- [24] S. J. Roundy. “Energy harvesting for tire pressure monitoring systems: design considerations”. In: *Proceedings of Power MEMS+ microMEMS, Sendai, Japan* (2008), pp. 9–12.
- [25] T. Herndl. “Remote Sensing of Car Tire Pressure”. In: *Energy Harvesting Systems*. Ed. by T. J. Kazmierski and S. Beeby. New York, NY: Springer New York, Oct. 2010, pp. 141–159. ISBN: 978-1-4419-7566-9. DOI: 10.1007/978-1-4419-7566-9_4. URL: https://doi.org/10.1007/978-1-4419-7566-9_4.
- [26] T. Zimmermann et al. “MEMS-based piezoelectric energy harvesting modules for distributed automotive tire sensors”. In: *International Multi-Conference on Systems, Signals & Devices*. IEEE, Mar. 2012. DOI: 10.1109/ssd.2012.6198097.
- [27] Y.-J. Wang, S.-C. Shen, and C.-D. Che. “Wideband Electromagnetic Energy Harvesting from a Rotating Wheel”. In: *Small-Scale Energy Harvesting*. InTech, Oct. 2012. DOI: 10.5772/50739.
- [28] A. Frey et al. “Systementwurf eines MST basierten piezoelektrischen Versorgungsmoduls für energieautarke Anwendungen”. In: *tm - Technisches Messen* 80.2 (Feb. 2013), pp. 53–60. DOI: 10.1524/teme.2013.0007.
- [29] R. van Schaijk et al. “Energy harvesting for self powered sensor systems”. In: 2012, pp. 141–146.
- [30] A. E. Kubba et al. “Modeling of Strain Energy Harvesting in Pneumatic Tires Using Piezoelectric Transducer”. In: *Tire Science and Technology* 42.1 (Jan. 2014), pp. 16–34. DOI: 10.2346/tire.14.420102.
- [31] S. Roundy and J. Tola. “Energy harvester for rotating environments using offset pendulum and nonlinear dynamics”. In: *Smart Materials and Structures* 23.10 (Sept. 2014), p. 105004. DOI: 10.1088/0964-1726/23/10/105004.
- [32] T. Guo et al. “Compressible hexagonal-structured triboelectric nanogenerators for harvesting tire rotation energy”. In: *Extreme Mechanics Letters* 18 (Jan. 2018), pp. 1–8. DOI: <https://doi.org/10.1016/j.eml.2017.10.002>.
- [33] V. I. Meshcheryakov et al. “Solid-state thin film hybrid electrochemical cell”. US10734674B2. Aug. 2020.
- [34] Thinika. *MICRO ENERGY STORAGE DEVICES FOR ELEVATED TEMPERATURE APPLICATION*. Tech. rep. THINIKALIMITED LIABILITY COMPANY, 2021. URL: https://thinika.com/wp-content/uploads/2021/11/Micro_Energy_Storage_Devices.pdf.
- [35] Thinika. *Thin Film Energy Storage Devices*. Tech. rep. THINIKALIMITED LIABILITY COMPANY, 2019. URL: https://thinika.com/down/thinika_print_160819.pdf.

- [36] S. Roundy, P. K. Wright, and J. M. Rabaey. *Energy Scavenging for Wireless Sensor Networks*. Springer US, 2003. DOI: 10.1007/978-1-4615-0485-6.
- [37] B. Calhoun et al. “Design Considerations for Ultra-Low Energy Wireless Microsensor Nodes”. In: *IEEE Transactions on Computers* 54.6 (June 2005), pp. 727–740. DOI: 10.1109/tc.2005.98.
- [38] J. D. Clayton. “Dielectrics and Piezoelectricity”. In: *Nonlinear Mechanics of Crystals*. Springer Netherlands, Oct. 2010, pp. 481–542. DOI: 10.1007/978-94-007-0350-6_10.
- [39] S. KATZIR. “THE DISCOVERY OF THE PIEZOELECTRIC EFFECT”. In: *BOSTON STUDIES IN PHILOSOPHY OF SCIENCE*. Springer Netherlands, pp. 15–64. DOI: 10.1007/978-1-4020-4670-4_2.
- [40] R. G. Ballas, G. Pfeifer, and R. Werthschützky. *Elektromechanische Systeme der Mikrotechnik und Mechatronik*. Springer Berlin Heidelberg, 2009. DOI: 10.1007/978-3-540-89320-2.
- [41] U. Marschner and R. Werthschützky. *Aufgaben und Lösungen zur Schaltungsdarstellung und Simulation elektromechanischer Systeme*. Springer Berlin Heidelberg, 2015. DOI: 10.1007/978-3-642-55169-7.
- [42] NASA. ‘NASA Invention of the Year’ Controls Noise and Vibration. Accessed: 2021-05-09. URL: https://spinoff.nasa.gov/Spinoff2007/ip_9.html.
- [43] A. J. Schoenecker et al. “Piezocomposite transducers for smart structures applications”. In: ed. by A. B. Flatau. SPIE, May 2005. DOI: 10.1117/12.599444.
- [44] M. E. Ceramics. *Properties of Piezoelectricity Ceramics*. [Online; 2021-02-11]. 2021. URL: [http://www.ultrasonic-resonators.org/misc/references/articles/Berlincourt_27Properties_of_Morgan_Electro_Ceramic_Ceramics27_\(Morgan_Technical_Publication_TP-226\).pdf](http://www.ultrasonic-resonators.org/misc/references/articles/Berlincourt_27Properties_of_Morgan_Electro_Ceramic_Ceramics27_(Morgan_Technical_Publication_TP-226).pdf).
- [45] P. C. GmbH. *PI Werkstoffdaten*. Accessed: 2021-02-08. URL: https://www.physikinstrumente.de/fileadmin/user_upload/physik_instrumente/files/datasheets/PI_Ceramic_Werkstoffdaten.pdf.
- [46] J. Matthey. *JM Piezoceramic Masses*. Accessed: 2021-02-08. URL: https://www.piezoproducts.com/wp-content/uploads/2020/03/JM_Piezo_Products-Data-Sheet-Piezoceramic-Masses-v2.00.0004.pdf.
- [47] E. Schrüfer, ed. *Lexikon Meß- und Automatisierungstechnik*. Springer Berlin Heidelberg, 1992. DOI: 10.1007/978-3-642-95752-9.
- [48] iPolymer. *PVDF*. [Online; 2021-02-11]. 2021. URL: <https://www.ipolymer.com/pdf/PVDF.pdf>.

-
- [49] T. P. Daue, J. Kunzmann, and A. Schönecker. “Energy harvesting systems using piezo-electric macro fiber composites”. In: *IEEE International Symposium on Electrets (ISE13)*, paper 27. 2008.
- [50] V. N. Kestelman, L. S. Pinchuk, and V. A. Goldade. *Electrets In Engineering*. Springer US, 2000. DOI: 10.1007/978-1-4615-4455-5.
- [51] S. Boisseau, G. Despesse, and B. Ahmed. “Electrostatic Conversion for Vibration Energy Harvesting”. In: *Small-Scale Energy Harvesting*. InTech, Oct. 2012. DOI: 10.5772/51360.
- [52] V. Leonov and R. V. Schaijk. “Patterning of inorganic electrets”. In: *IEEE Transactions on Dielectrics and Electrical Insulation* 17.4 (Aug. 2010), pp. 994–1000. DOI: 10.1109/tdei.2010.5539666.
- [53] C. Lagomarsini et al. “Outstanding performance of parylene polymers as electrets for energy harvesting and high-temperature applications”. In: *Journal of Applied Polymer Science* 137.23 (Dec. 2019), p. 48790. DOI: 10.1002/app.48790.
- [54] U. Mescheder et al. “Properties of SiO₂electret films charged by ion implantation for MEMS-based energy harvesting systems”. In: *Journal of Micromechanics and Microengineering* 19.9 (Aug. 2009), p. 094003. DOI: 10.1088/0960-1317/19/9/094003.
- [55] A. Küchler. “Elektrische Festigkeit”. In: *Hochspannungstechnik*. Springer Berlin Heidelberg, 2017, pp. 141–268. DOI: 10.1007/978-3-662-54700-7_3.
- [56] X. Qiu. “Ferroelectrets: heterogenous polymer electrets with high electromechanical response”. habilitation. Universität Potsdam, 2016.
- [57] S. Bauer, R. Gerhard-Multhaupt, and G. M. Sessler. “Ferroelectrets: Soft Electroactive Foams for Transducers”. In: *Physics Today* 57.2 (Feb. 2004), pp. 37–43. DOI: 10.1063/1.1688068.
- [58] X. Zhang et al. “Vibration-based energy harvesting with piezoelectrets having high d₃₁ activity”. In: *Applied Physics Letters* 108.19 (May 2016), p. 193903. DOI: 10.1063/1.4948649.
- [59] X. Zhang, J. Hillenbrand, and G. Sessler. “Thermally stable fluorocarbon ferroelectrets with high piezoelectric coefficient”. In: *Applied Physics A* 84.1-2 (Apr. 2006), pp. 139–142. DOI: 10.1007/s00339-006-3573-5.
- [60] P. Fang et al. “Cellular polyethylene-naphthalate ferroelectrets: Foaming in supercritical carbon dioxide, structural and electrical preparation, and resulting piezoelectricity”. In: *Applied Physics Letters* 90.19 (May 2007), p. 192908. DOI: 10.1063/1.2738365.

- [61] Z. Xia et al. “High surface-charge stability of porous polytetrafluoroethylene electret films at room and elevated temperatures”. In: *Journal of Physics D: Applied Physics* 32.17 (Aug. 1999), pp. L83–L85. DOI: 10.1088/0022-3727/32/17/102.
- [62] Z. Xia, A. Wedel, and R. Danz. “Charge storage and its dynamics in porous polytetrafluoroethylene (PTFE) film electrets”. In: *IEEE Transactions on Dielectrics and Electrical Insulation* 10.1 (Feb. 2003), pp. 102–108. DOI: 10.1109/tdei.2003.1176568.
- [63] D. Rychkov. “Stabilization of Positive Charge on FEP Electret Films Modified with Titanium-Tetrachloride Vapor: Formation of a Two-Dimensional Nanodielectric”. In: DOI: 10.1109/ICSD.2013.6619860.
- [64] J. Shi, S. Yong, and S. Beeby. “An easy to assemble ferroelectret for human body energy harvesting”. In: *Smart Materials and Structures* 27.8 (July 2018), p. 084005. DOI: 10.1088/1361-665x/aabdbc.
- [65] X. Zhang et al. “Ferroelectret nanogenerator with large transverse piezoelectric activity”. In: *Nano Energy* 50 (Aug. 2018), pp. 52–61. DOI: 10.1016/j.nanoen.2018.05.016.
- [66] Y. Wang, Y. Yang, and Z. L. Wang. “Triboelectric nanogenerators as flexible power sources”. In: *npj Flexible Electronics* 1.1 (Nov. 2017). DOI: 10.1038/s41528-017-0007-8.
- [67] F.-R. Fan, Z.-Q. Tian, and Z. L. Wang. “Flexible triboelectric generator”. In: *Nano Energy* 1.2 (Mar. 2012), pp. 328–334. DOI: 10.1016/j.nanoen.2012.01.004.
- [68] Z. L. Wang, T. Jiang, and L. Xu. “Toward the blue energy dream by triboelectric nanogenerator networks”. In: *Nano Energy* 39 (Sept. 2017), pp. 9–23. DOI: 10.1016/j.nanoen.2017.06.035.
- [69] X. Wen et al. “Applicability of triboelectric generator over a wide range of temperature”. In: *Nano Energy* 4 (Mar. 2014), pp. 150–156. DOI: 10.1016/j.nanoen.2014.01.001.
- [70] C. X. Lu et al. “Temperature Effect on Performance of Triboelectric Nanogenerator”. In: *Advanced Engineering Materials* 19.12 (Aug. 2017), p. 1700275. DOI: 10.1002/adem.201700275.
- [71] B. Meng et al. “Self-powered flexible printed circuit board with integrated triboelectric generator”. In: *Nano Energy* 2.6 (Nov. 2013), pp. 1101–1106. DOI: 10.1016/j.nanoen.2013.08.006.
- [72] S. Niu et al. “Theory of freestanding triboelectric-layer-based nanogenerators”. In: *Nano Energy* 12 (Mar. 2015), pp. 760–774. DOI: 10.1016/j.nanoen.2015.01.013.

- [73] Q. Zheng et al. “In Vivo Powering of Pacemaker by Breathing-Driven Implanted Triboelectric Nanogenerator”. In: *Advanced Materials* 26.33 (July 2014), pp. 5851–5856. DOI: 10.1002/adma.201402064.
- [74] A. Lenk et al. *Electromechanical Systems in Microtechnology and Mechatronics*. Springer Berlin Heidelberg, 2011. DOI: 10.1007/978-3-642-10806-8.
- [75] M. Germer, U. Marschner, and A. B. Flatau. “Combined Finite Element Method (FEM) and Network Simulation of a Nonlinear Electromagnetic Energy Harvester”. In: *ASME 2020 Conference on Smart Materials, Adaptive Structures and Intelligent Systems*. American Society of Mechanical Engineers, Sept. 2020. DOI: 10.1115/smasis2020-2407.
- [76] W. GmbH. *Maximal operational temperature*. [Online; 2021-02-12]. 2021. URL: <https://www.supermagnete.de/faq/Wie-heiss-duerfen-Magnete-werden>.
- [77] TDK. *Ferrite Magnets*. Accessed: 2021-02-08. URL: https://product.tdk.com/info/en/catalog/datasheets/magnet_fb_summary_en.pdf.
- [78] D. Meeker. *Finite Element Method Magnetics : NeoProperties*. Accessed: 2021-02-08. URL: <https://www.femm.info/wiki/NeoProperties>.
- [79] B. T. K. GmbH. *Eigenschaften und Kennzahlen von NdFeB-Magneten*. Accessed: 2021-02-08. URL: <https://www.magnetkontor.de/content/de/ueber-NdFeB-Magnete.html>.
- [80] J. Joule. “On a new class of magnetic forces”. In: *Ann. Electr. Magn. Chem* 8.1842 (1842), pp. 219–224.
- [81] E. Villari. “Intorno alle modificazioni del momento magnetico di una verga di ferro e di acciaio, prodotte per la trazione della medesima e pel passaggio di una corrente attraverso la stessa”. In: *Il Nuovo Cimento (1855-1868)* 20.1 (1864), pp. 317–362.
- [82] *IEEE Standard on Magnetostrictive Materials: Piezomagnetic Nomenclature*. DOI: 10.1109/ieeestd.1991.101048.
- [83] L. TdVib. *Galfenol*. Accessed: 2021-02-19. URL: <http://tdvib.com/terfenol-d/>.
- [84] L. TdVib. *Galfenol*. Accessed: 2021-02-19. URL: <http://tdvib.com/galfenol/>.
- [85] M. Germer, U. Marschner, and A. B. Flatau. “Design and experimental verification of an improved magnetostrictive energy harvester”. In: *Active and Passive Smart Structures and Integrated Systems 2017*. Ed. by G. Park. SPIE, Apr. 2017. DOI: 10.1117/12.2263971.
- [86] M. Germer et al. “Equivalent Electromechanical Circuit Analysis for Electrical Tuning of Magnetostrictive Unimorph System Dynamics”. In: *Volume 2: Modeling, Simulation and Control; Bio-Inspired Smart Materials and Systems; Energy Harvesting*. American Society of Mechanical Engineers, Sept. 2016. DOI: 10.1115/smasis2016-9274.

- [87] M. Germer. “Optimization Studies of a Magnetostrictive Energy Harvester”. MA thesis. 2016.
- [88] T. Ueno. “Performance of improved magnetostrictive vibrational power generator, simple and high power output for practical applications”. In: *J. Appl. Phys.* 117.17 (May 2015), 17A740. DOI: 10.1063/1.4917464. URL: <http://dx.doi.org/10.1063/1.4917464>.
- [89] Q. Zheng et al. “Vibration energy harvesting device based on asymmetric air-spaced cantilevers for tire pressure monitoring system”. In: *Proceedings of Power MEMS (2009)*, pp. 403–406.
- [90] S. J. Roundy and J. Tola. “An energy harvester for rotating environments using offset pendulum dynamics”. In: *2013 Transducers & Eurosensors XXVII: The 17th International Conference on Solid-State Sensors, Actuators and Microsystems (TRANSDUCERS & EUROSENSORS XXVII)*. IEEE, June 2013. DOI: 10.1109/transducers.2013.6626860.
- [91] M. Keck. “A new approach of a piezoelectric vibration-based power generator to supply next generation tire sensor systems”. In: *2007 IEEE Sensors*. IEEE, 2007, pp. 1299–1302. DOI: 10.1109/icsens.2007.4388648.
- [92] A. Frey et al. “Energy autonomous microsystems for automotive applications”. In: *Mikrosystemtechnik Kongress 2011, Darmstadt, Germany*. 2011, pp. 297–300.
- [93] A. Frey et al. “System modeling of a piezoelectric energy harvesting module for environments with high dynamic forces”. In: *SPIE Proceedings*. Ed. by U. Schmid, J. L. Sánchez-Rojas, and M. Leester-Schaedel. Vol. 8066. SPIE, May 2011, 80661P. DOI: 10.1117/12.886749.
- [94] A. Frey et al. “Piezoelectric MEMS energy harvesting module based on non-resonant excitation”. In: *2011 16th International Solid-State Sensors, Actuators and Microsystems Conference*. IEEE, June 2011. DOI: 10.1109/transducers.2011.5969849.
- [95] I. Kuehne et al. “Fluid-Structure Interaction Modeling for an Optimized Design of a Piezoelectric Energy Harvesting MEMS Generator”. In: *Proceedings of the COMSOL Users Conference*. 2011. URL: https://www.comsol.com/paper/download/83327/frey_paper.pdf.
- [96] M. Renaud et al. “Improved mechanical reliability of MEMS electret based vibration energy harvesters for automotive applications”. In: *Journal of Physics: Conference Series* 557 (Nov. 2014), p. 012071. DOI: 10.1088/1742-6596/557/1/012071.
- [97] G. Altena et al. “Design improvements for an electret-based MEMS vibrational electrostatic energy harvester”. In: *Journal of Physics: Conference Series* 476 (Dec. 2013), p. 012078. DOI: 10.1088/1742-6596/476/1/012078.

-
- [98] M. Renaud et al. “Shock reliability analysis and improvement of MEMS electret-based vibration energy harvesters”. In: *Journal of Micromechanics and Microengineering* 25.10 (Sept. 2015), p. 104010. DOI: 10.1088/0960-1317/25/10/104010.
- [99] T. Fujita et al. “Reliability Improvement of Vibration Energy Harvester with Shock Absorbing Structures”. In: *Procedia Engineering* 87 (2014), pp. 1206–1209. DOI: 10.1016/j.proeng.2014.11.384.
- [100] M. Renaud et al. “A high performance electrostatic MEMS vibration energy harvester with corrugated inorganic SiO₂-Si₃N₄ electret”. In: *2013 Transducers & Eurosensors XXVII: The 17th International Conference on Solid-State Sensors, Actuators and Microsystems (TRANSDUCERS & EUROSENSORS XXVII)*. IEEE, June 2013. DOI: 10.1109/transducers.2013.6626861.
- [101] S. Tornincasa et al. “Optimization of magneto-mechanical energy scavenger for automotive tire”. In: *Journal of Intelligent Material Systems and Structures* 23.18 (Dec. 2011). Ed. by D. S. Neild, pp. 2055–2064. DOI: 10.1177/1045389x11430741.
- [102] S. Tornincasa et al. “Energy harvester for vehicle tires: Nonlinear dynamics and experimental outcomes”. In: *Journal of Intelligent Material Systems and Structures* 23.1 (Jan. 2012), pp. 3–13. DOI: 10.1177/1045389x11430739.
- [103] E. Bonisoli et al. “Dynamic Simulation of an Electromechanical Energy Scavenging Device”. In: *IEEE Transactions on Magnetics* 46.8 (Aug. 2010), pp. 2856–2859. DOI: 10.1109/tmag.2010.2044156.
- [104] D. A. van den Ende et al. “Direct strain energy harvesting in automobile tires using piezoelectric PZT-polymer composites”. In: *Smart Materials and Structures* 21.1 (Dec. 2011), p. 015011. DOI: 10.1088/0964-1726/21/1/015011.
- [105] D. A. van den Ende, W. A. Groen, and S. van der Zwaag. “Robust piezoelectric composites for energy harvesting in high-strain environments”. In: *Journal of Intelligent Material Systems and Structures* 24.18 (Oct. 2012), pp. 2262–2269. DOI: 10.1177/1045389x12462646.
- [106] D. Upadrashta and Y. Yang. “Experimental investigation of performance reliability of macro fiber composite for piezoelectric energy harvesting applications”. In: *Sensors and Actuators A: Physical* 244 (June 2016), pp. 223–232. DOI: 10.1016/j.sna.2016.04.043.
- [107] T. P. Daue, J. Kunzmann, and A. Schönecker. “Energy harvesting systems using piezo-electric macro fiber composites”. In: *IEEE International Symposium on Electrets (ISE13)*, paper 27. 2008.
- [108] M. Germer, U. Marschner, and A. B. Flatau. “Electrical tuning of magnetostrictive applications: Equivalent electromechanical circuit analysis”. In: *Journal of Intelligent Material Systems and Structures* 30.9 (Feb. 2019), pp. 1435–1450. DOI: 10.1177/1045389x19828484.

- [109] M. E. Staley and A. B. Flatau. “Characterization of energy harvesting potential of Terfenol-D and Galfenol”. In: *Smart Structures and Materials 2005: Smart Structures and Integrated Systems*. Ed. by A. B. Flatau. Vol. 5764. SPIE, May 2005. DOI: 10.1117/12.604871.
- [110] G. Hatipoglu and H. Ürey. “FR4-based electromagnetic energy harvester for wireless sensor nodes”. In: *Smart Materials and Structures* 19.1 (Dec. 2009), p. 015022. DOI: 10.1088/0964-1726/19/1/015022.
- [111] G. Manla, N. M. White, and J. Tudor. “Harvesting energy from vehicle wheels”. In: *TRANSDUCERS 2009 - 2009 International Solid-State Sensors, Actuators and Microsystems Conference*. IEEE, June 2009. DOI: 10.1109/sensor.2009.5285831.
- [112] G. Manla. “Design, and characterisation of impact based and non-contact piezoelectric harvesters for rotating objects”. PhD thesis. University of Southampton, School of Electronics and Computer Science, 2010.
- [113] G. Manla, N. M. White, and M. J. Tudor. “Numerical Model of a Non-Contact Piezoelectric Energy Harvester for Rotating Objects”. In: *IEEE Sensors Journal* 12.6 (June 2012), pp. 1785–1793. DOI: 10.1109/jsen.2011.2175721.
- [114] R. Elfrink et al. “Shock induced energy harvesting with a MEMS harvester for automotive applications”. In: *2011 International Electron Devices Meeting*. IEEE, Dec. 2011. DOI: 10.1109/iedm.2011.6131639.
- [115] R. van Schaijk et al. “A MEMS vibration energy harvester for automotive applications”. In: *SPIE Proceedings*. Ed. by U. Schmid, J. L. S. de Rojas Aldavero, and M. Leester-Schaedel. Vol. 8763. SPIE, May 2013, pp. 876305–1. DOI: 10.1117/12.2016916.
- [116] R. Elfrink et al. “Fully autonomous Tire Pressure Monitoring System (TPMS) powered by a vibrational electrostatic energy harvester”. In: *Proc. Smart Systems Integration 2014* (2014), pp. 69–76.
- [117] Y. Hu et al. “A Nanogenerator for Energy Harvesting from a Rotating Tire and its Application as a Self-Powered Pressure/Speed Sensor”. In: *Advanced Materials* 23.35 (Aug. 2011), pp. 4068–4071. DOI: 10.1002/adma.201102067.
- [118] N. Makki and R. Pop-Iliev. “Piezoelectric power generation for sensor applications: design of a battery-less wireless tire pressure sensor”. In: *Smart Sensors, Actuators, and MEMS V*. Ed. by U. Schmid, J. L. Sánchez-Rojas, and M. Leester-Schaedel. SPIE, May 2011. DOI: 10.1117/12.887112.
- [119] N. Makki and R. Pop-Iliev. “Battery-and wire-less tire pressure measurement systems (TPMS) sensor”. In: *Microsystem Technologies* 18.7-8 (Mar. 2012), pp. 1201–1212. DOI: 10.1007/s00542-012-1480-6.

- [120] K. B. Singh et al. “Piezoelectric vibration energy harvesting system with an adaptive frequency tuning mechanism for intelligent tires”. In: *Mechatronics* 22.7 (Oct. 2012), pp. 970–988. DOI: 10.1016/j.mechatronics.2012.06.006.
- [121] E. R. Westby and E. Halvorsen. “Design and Modeling of a Patterned-Electret-Based Energy Harvester for Tire Pressure Monitoring Systems”. In: *IEEE/ASME Transactions on Mechatronics* 17.5 (Oct. 2012), pp. 995–1005. DOI: 10.1109/tmech.2011.2151203.
- [122] K. H. Mak. “Vibration modelling and analysis of piezoelectric energy harvesters”. PhD thesis. University of Nottingham, 2011.
- [123] K. H. Mak, S. McWilliam, and A. A. Popov. “Piezoelectric energy harvesting for tyre pressure measurement applications”. In: *Proceedings of the Institution of Mechanical Engineers, Part D: Journal of Automobile Engineering* 227.6 (Nov. 2012), pp. 842–852. DOI: 10.1177/0954407012463849.
- [124] L. Gu and C. Livermore. “Compact passively self-tuning energy harvesting for rotating applications”. In: *Smart Materials and Structures* 21.1 (Dec. 2011), p. 015002. DOI: 10.1088/0964-1726/21/1/015002.
- [125] Q. Wang et al. “High power density energy harvester with high permeability magnetic material embedded in a rotating wheel”. In: *Nondestructive Characterization for Composite Materials, Aerospace Engineering, Civil Infrastructure, and Homeland Security 2012*. Ed. by A. L. Gyekenyesi. SPIE, Apr. 2012. DOI: 10.1117/12.916980.
- [126] Q. C. Tang, X. Y. Xia, and X. X. Li. “Non-contact frequency-up-conversion energy harvester for durable & broad-band automotive TPMS application”. In: *2012 IEEE 25th International Conference on Micro Electro Mechanical Systems (MEMS)*. IEEE, Jan. 2012. DOI: 10.1109/memsys.2012.6170389.
- [127] S. Lee and D.-H. Kim. “Durable and Sustainable Strap Type Electromagnetic Harvester for Tire Pressure Monitoring System”. In: *Journal of Magnetism* 18.4 (Dec. 2013), pp. 473–480. DOI: 10.4283/jmag.2013.18.4.473.
- [128] E. Trbaldo et al. “Simulation of a Novel Bridge MEMS-PZT Energy Harvester for Tire Pressure System”. In: *Journal of Physics: Conference Series* 557 (Nov. 2014), p. 012041. DOI: 10.1088/1742-6596/557/1/012041.
- [129] D.-W. L. Xuan Wu Mitesh Parmar. “A Seesaw-Structured Energy Harvester With Superwide Bandwidth for TPMS Application”. In: *IEEE/ASME Transactions on Mechatronics* 19.5 (Oct. 2014), pp. 1514–1522. DOI: 10.1109/tmech.2013.2286637.
- [130] Y.-J. Wang et al. “A Nonlinear Suspended Energy Harvester for a Tire Pressure Monitoring System”. In: *Micromachines* 6.3 (Feb. 2015), pp. 312–327. DOI: 10.3390/mi6030312.

- [131] O. J. Jousimaa et al. “Energy harvesting system for intelligent tyre sensors”. In: *2016 IEEE Intelligent Vehicles Symposium (IV)*. IEEE, June 2016, pp. 578–583. DOI: 10.1109/ivs.2016.7535445.
- [132] W. Yu-Jen, C. Tsung-Yi, and Y. Jui-Hsin. “Design and kinetic analysis of piezoelectric energy harvesters with self-adjusting resonant frequency”. In: *Smart Materials and Structures* 26.9 (Aug. 2017), p. 095037. DOI: 10.1088/1361-665x/aa7ad6.
- [133] L. Deng et al. “Design and optimization of a trapezoidal beam array energy harvester with operating wide speed rang for TPMS application”. In: *Microsystem Technologies* 25.7 (Nov. 2018), pp. 2869–2879. DOI: 10.1007/s00542-018-4243-1.
- [134] X. Liu et al. “An Innovative Design of In-Tire Energy Harvester for the Power Supply of Tire Sensors”. In: *SAE Technical Paper Series*. SAE International, Apr. 2018. DOI: 10.4271/2018-01-1115.
- [135] R. Esmaceli et al. “Design, modeling, and analysis of a high performance piezoelectric energy harvester for intelligent tires”. In: *International Journal of Energy Research* 43.10 (Mar. 2019), pp. 5199–5212. DOI: 10.1002/er.4441.
- [136] P. C. GmbH. *PI Werkstoffdaten*. Accessed: 2021-03-30. URL: <https://www.physikinstrumente.de/de/produkte/piezoelektrische-wandler-transducer-piezoaktoren/p-878-duraact-power-flaechenwandler-101795/>.
- [137] U. Marschner et al. “Equivalent circuit models of two-layer flexure beams with excitation by temperature, humidity, pressure, piezoelectric or piezomagnetic interactions”. In: *Journal of Sensors and Sensor Systems* 3.2 (Sept. 2014), pp. 187–211. DOI: 10.5194/jsss-3-187-2014.
- [138] J. P. D. Hartog and G. Mesmer. *Mechanische Schwingungen*. Springer Berlin Heidelberg, 1952. DOI: 10.1007/978-3-662-12444-4.
- [139] S. Roundy et al. “Improving Power Output for Vibration-Based Energy Scavengers”. In: *IEEE Pervasive Computing* 4.1 (Jan. 2005), pp. 28–36. DOI: 10.1109/mprv.2005.14.
- [140] C. Mo, L. J. Radziemski, and W. W. Clark. “Analysis of piezoelectric circular diaphragm energy harvesters for use in a pressure fluctuating system”. In: 19.2 (Jan. 2010), p. 025016. DOI: 10.1088/0964-1726/19/2/025016.
- [141] D. Kupferinstitut. *CuZn37*. Accessed: 2021-10-15. URL: <https://www.kupferinstitut.de/wp-content/uploads/2019/11/CuZn37-1.pdf>.
- [142] X. Gao, W.-H. Shih, and W. Y. Shih. “Induced voltage of piezoelectric unimorph cantilevers of different nonpiezoelectric/piezoelectric length ratios”. In: *Smart Materials and Structures* 18.12 (Oct. 2009), p. 125018. DOI: 10.1088/0964-1726/18/12/125018.

- [143] S. Material. *Smart Material - Home of the MFC*. Accessed: 2021-10-19. URL: <https://www.smart-material.com/MFC-product-mainV2.html>.
- [144] R. R. Knight, C. Mo, and W. W. Clark. “MEMS interdigitated electrode pattern optimization for a unimorph piezoelectric beam”. In: 26.1-4 (Oct. 2010), pp. 14–22. DOI: 10.1007/s10832-010-9621-8.
- [145] P. C. GmbH. *DuraAct Piezoelektrische Flächenwandler*. [Online; 2021-05-13]. 2021. URL: https://www.physikinstrumente.de/fileadmin/user_upload/physik_instrumente/files/BR0/PI-BR007D-R2-DuraAct-Piezoelectric-Patch-Transducer.pdf.
- [146] A. Deraemaeker and H. Nasser. “Numerical evaluation of the equivalent properties of Macro Fiber Composite (MFC) transducers using periodic homogenization”. In: *International Journal of Solids and Structures* 47.24 (Dec. 2010), pp. 3272–3285. DOI: 10.1016/j.ijsolstr.2010.08.006.
- [147] P. C. GmbH. *Discussion with Alexander Conrad (Sales and Distribution)*. Apr. 2019.
- [148] D. Guyomar and M. Lallart. “Recent Progress in Piezoelectric Conversion and Energy Harvesting Using Nonlinear Electronic Interfaces and Issues in Small Scale Implementation”. In: *Micromachines* 2.2 (June 2011), pp. 274–294. DOI: 10.3390/mi2020274.
- [149] E. Lefeuvre et al. “Piezoelectric Material-Based Energy Harvesting Devices: Advance of SSH Optimization Techniques (1999-2009)”. In: *Piezoelectric Ceramics*. Sciyo, Oct. 2010. DOI: 10.5772/9945.
- [150] M. Lallart et al. “Synchronous inversion and charge extraction (SICE): a hybrid switching interface for efficient vibrational energy harvesting”. In: *Smart Materials and Structures* 26.11 (Oct. 2017), p. 115012. DOI: 10.1088/1361-665x/aa8d44.
- [151] Y. K. Ramadass and A. P. Chandrakasan. “An Efficient Piezoelectric Energy Harvesting Interface Circuit Using a Bias-Flip Rectifier and Shared Inductor”. In: *IEEE Journal of Solid-State Circuits* 45.1 (Jan. 2010), pp. 189–204. DOI: 10.1109/jssc.2009.2034442.
- [152] Lefeuvre. “Piezoelectric Energy Harvesting Device Optimization by Synchronous Electric Charge Extraction”. In: *Journal of Intelligent Material Systems and Structures* 16.10 (Oct. 2005), pp. 865–876. DOI: 10.1177/1045389x05056859.
- [153] S. J. Yun et al. “Asymmetric SECE Piezoelectric Energy Harvester Under Weak Excitation”. In: *IEEE Access* 8 (2020), pp. 99132–99140. DOI: 10.1109/access.2020.2997353.
- [154] X. Wang et al. “Multi-Input SECE Based on Buck Structure for Piezoelectric Energy Harvesting”. In: *IEEE Transactions on Power Electronics* 36.4 (Apr. 2021), pp. 3638–3642. DOI: 10.1109/tpel.2020.3022424.

- [155] A. Badel et al. “Piezoelectric Energy Harvesting using a Synchronized Switch Technique”. In: 17.8-9 (May 2006), pp. 831–839. DOI: 10.1177/1045389x06057533.
- [156] M. Lallart et al. “Low-cost capacitor voltage inverter for outstanding performance in piezoelectric energy harvesting”. In: 57.2 (Feb. 2010), pp. 281–291. DOI: 10.1109/tuffc.2010.1408.
- [157] T. Components. *Datasheet - TC-HBCC-102J-00203*. [Online; 2020-08-01]. 2021. URL: <https://asset.conrad.com/media10/add/160267/c1/-/en/001589002DS01/datenblatt-1589002-tru-components-tc-hbcc-102j-00203-induktivitaet-%20%5C%5C%20axial-bedrahtet-1000-h-02-a-1-st.pdf>.
- [158] A. Brenes et al. “Large-bandwidth piezoelectric energy harvesting with frequency-tuning synchronized electric charge extraction”. In: *Elsevier BV* 302 (Feb. 2020), p. 111759. DOI: 10.1016/j.sna.2019.111759.
- [159] P. Gasnier et al. “An Autonomous Piezoelectric Energy Harvesting IC Based on a Synchronous Multi-Shot Technique”. In: 49.7 (July 2014), pp. 1561–1570. DOI: 10.1109/jssc.2014.2325555.
- [160] T. Hehn et al. “A Fully Autonomous Integrated Interface Circuit for Piezoelectric Harvesters”. In: *IEEE Journal of Solid-State Circuits* 47.9 (Sept. 2012), pp. 2185–2198. DOI: 10.1109/jssc.2012.2200530.
- [161] A. Morel et al. “A Shock-Optimized SECE Integrated Circuit”. In: *IEEE Journal of Solid-State Circuits* 53.12 (Dec. 2018), pp. 3420–3433. DOI: 10.1109/jssc.2018.2868299.
- [162] A. Quelen et al. “A 30nA quiescent 80nW-to-14mW power-range shock-optimized SECE-based piezoelectric harvesting interface with 420% harvested-energy improvement”. In: *2018 IEEE International Solid - State Circuits Conference - (ISSCC)*. IEEE, Feb. 2018. DOI: 10.1109/isscc.2018.8310228.
- [163] C. Richard, D. Guyomar, and E. Lefeuvre. “Self-powered electronic breaker with automatic switching by detecting maxima or minima of potential difference between its power electrodes”. 2007.
- [164] M. Lallart and D. Guyomar. “An optimized self-powered switching circuit for non-linear energy harvesting with low voltage output”. In: *Smart Materials and Structures* 17.3 (May 2008), p. 035030. DOI: 10.1088/0964-1726/17/3/035030.
- [165] K. A. Singh, R. Kumar, and R. J. Weber. “A Broadband Bistable Piezoelectric Energy Harvester With Nonlinear High-Power Extraction”. In: *IEEE Transactions on Power Electronics* 30.12 (Dec. 2015), pp. 6763–6774. DOI: 10.1109/tpel.2015.2394392.
- [166] C. Cepnik et al. “Effective optimization of electromagnetic energy harvesters through direct computation of the electromagnetic coupling”. In: *Sensors and Actuators A: Physical* 167.2 (June 2011), pp. 416–421. DOI: 10.1016/j.sna.2011.01.023.

- [167] M. Germer, U. Marschner, and A. Richter. “Stochastic Signal Analysis and Processing of Non-Harmonic, Periodic Vibrational Energy Harvesters”. In: *ASME 2021 Conference on Smart Materials, Adaptive Structures and Intelligent Systems*. American Society of Mechanical Engineers, Sept. 2021. DOI: 10.1115/smasis2021-68310.
- [168] M. Germer, U. Marschner, and A. Richter. “High Efficient Boost Energizing and Transferring Circuit for Electromagnetic Energy Harvesting”. In: *10th National Days on Energy Harvesting and Storage*. Grenoble, France, June 2021. URL: <https://hal.archives-ouvertes.fr/hal-03313226>.
- [169] T. W. Blad and N. Tolou. “On the efficiency of energy harvesters: A classification of dynamics in miniaturized generators under low-frequency excitation”. In: *Journal of Intelligent Material Systems and Structures* 30.16 (July 2019), pp. 2436–2446. DOI: 10.1177/1045389x19862621.
- [170] D. Meeker. *Finite Element Method Magnetics Version 4.2 User’s Manual*. Oct. 2015.
- [171] A. Benhama. “Computation of electromagnetic forces from finite element field solutions”. In: *3rd International Conference on Computation in Electromagnetics (CEM 96)*. IEE, 1996. DOI: 10.1049/cp:19960193.
- [172] M. Mösch and G. Fischerauer. “A Comparison of Methods to Measure the Coupling Coefficient of Electromagnetic Vibration Energy Harvesters”. In: *Micromachines* 10.12 (Nov. 2019), p. 826. DOI: 10.3390/mi10120826.
- [173] A. Mohammed. “Electromagnetic Energy Harvester for the Energy Supply of Autonomous Systems”. MA thesis. TU Dresden, 2020.
- [174] E. Dallago et al. “A Self-Powered Electronic Interface for Electromagnetic Energy Harvester”. In: *IEEE Transactions on Power Electronics* 26.11 (Nov. 2011), pp. 3174–3182. DOI: 10.1109/tpel.2011.2146277.
- [175] S.-W. Wang et al. “Electromagnetic Energy Harvester Interface Design for Wearable Applications”. In: *IEEE Transactions on Circuits and Systems II: Express Briefs* 65.5 (May 2018), pp. 667–671. DOI: 10.1109/tcsii.2018.2820158.
- [176] X. Wang, X. Liang, and H. Wei. “A study of electromagnetic vibration energy harvesters with different interface circuits”. In: *Mechanical Systems and Signal Processing* 58-59 (June 2015), pp. 376–398. DOI: 10.1016/j.ymsp.2014.10.004.
- [177] E. Arroyo and A. Badel. “Electromagnetic vibration energy harvesting device optimization by synchronous energy extraction”. In: *Sensors and Actuators A: Physical* 171.2 (Nov. 2011), pp. 266–273. DOI: 10.1016/j.sna.2011.06.024.

- [178] E. Arroyo, A. Badel, and F. Formosa. “Synchronized switch harvesting technique applied to electromagnetic vibrations harvester”. In: *Proc. 10th Int. Workshop on Micro and Nanotechnology for Power Generation and Energy Conversion Applications (Power MEMS 2010), Tech. Dig.-Poster Sessions, Leuven, Belgium*. 2010, pp. 45–48.
- [179] E. Bonisoli et al. “Electromechanical and Electronic Integrated Harvester for Shoes Application”. In: *IEEE/ASME Transactions on Mechatronics* 22.5 (Oct. 2017), pp. 1921–1932. DOI: 10.1109/tmech.2017.2667401.
- [180] R. Hoffmann and M. Wolff. *Intelligente Signalverarbeitung 1*. Springer Berlin Heidelberg, 2014. DOI: 10.1007/978-3-662-45323-0.
- [181] A. Rahimi et al. “A vibration-based electromagnetic energy harvester system with highly efficient interface electronics”. In: *2011 16th International Solid-State Sensors, Actuators and Microsystems Conference*. IEEE, June 2011. DOI: 10.1109/transducers.2011.5969876.
- [182] M. Ghovanloo and K. Najafi. “Fully integrated wideband high-current rectifiers for inductively powered devices”. In: *IEEE Journal of Solid-State Circuits* 39.11 (Nov. 2004), pp. 1976–1984. DOI: 10.1109/jssc.2004.835822.
- [183] Y. Rao and D. P. Arnold. “An Input-Powered Active AC/DC Converter with Zero Standby Power for Energy Harvesting Applications”. In: *2010 IEEE Energy Conversion Congress and Exposition*. IEEE, Sept. 2010. DOI: 10.1109/ecce.2010.5618445.
- [184] M. Salauddin and J. Y. Park. “Design and experiment of human hand motion driven electromagnetic energy harvester using dual Halbach magnet array”. In: *Smart Materials and Structures* 26.3 (Feb. 2017), p. 035011. DOI: 10.1088/1361-665x/aa573f.
- [185] S. Bradai et al. “Electromagnetic Energy Harvester for Battery-Free IoT Solutions”. In: *2020 IEEE 6th World Forum on Internet of Things (WF-IoT)*. IEEE, June 2020. DOI: 10.1109/wf-iot48130.2020.9221051.
- [186] N. M. Roscoe and M. D. Judd. “Optimization of Voltage Doublers for Energy Harvesting Applications”. In: *IEEE Sensors Journal* 13.12 (Dec. 2013), pp. 4904–4911. DOI: 10.1109/jsen.2013.2278468.
- [187] U. Schlien. *Schaltnetzteile und ihre Peripherie*. Springer Fachmedien Wiesbaden, 2020. DOI: 10.1007/978-3-658-29490-8.
- [188] T. U. T. P. Resource. *205/55R16 Tire Pressure Chart*. Accessed: 2022-02-01. URL: <https://tirepressure.com/205-55r16-tire-pressure>.

- [189] A. Quelen et al. “32.3 Electromagnetic Mechanical Energy-Harvester IC with No Off-Chip Component and One Switching Period MPPT Achieving up to 95.9% End-to-End Efficiency and 460% Energy-Extraction Gain”. In: *2020 IEEE International Solid-State Circuits Conference - (ISSCC)*. IEEE, Feb. 2020. DOI: 10.1109/isscc19947.2020.9063023.
- [190] A. Richter et al. “System zur haptischen Interaktion mit virtuellen Objekten für Anwendungen in der virtuellen Realität”. DE102019106684B4. Mar. 15, 2019.
- [191] M. Germer. “Vorrichtung zum Erzeugen von elektrischer Energie aus Schwingungsenergie sowie Verwendung hierfür”. DE102019206567A1. May 7, 2019.
- [192] M. Germer, U. Marschner, and A. Richter. “High Efficient Energy Harvesting Interface Circuit for Tire Pressure Monitoring Systems”. In: *IEEE Wireless Power Week 2022*. Bordeaux, France, July 2022.
- [193] M. Germer, U. Marschner, and A. B. Flatau. “Magnetic flux analysis of a magnetostrictive unimorph energy harvester”. In: *IDTechExShow*. Apr. 2018.
- [194] S. Priya and D. J. Inman, eds. *Energy Harvesting Technologies*. Springer US, 2009. DOI: 10.1007/978-0-387-76464-1.
- [195] J. Davidson and C. Mo. “Recent Advances in Energy Harvesting Technologies for Structural Health Monitoring Applications”. In: *Smart Materials Research 2014 (2014)*, pp. 1–14. DOI: 10.1155/2014/410316.
- [196] T. Haas. “Intelligenter Reifen mit energieautarker Mikroelektronik (Intelligent Tire Using Energy-autarkic Microelectronics)”. In: *tm-Technisches Messen* 74.12/2007 (Jan. 2007), pp. 613–620. DOI: 10.1524/teme.2007.74.12.613.
- [197] S. D. Nguyen. “Wideband MEMS energy harvesters utilizing nonlinear springs”. PhD thesis. 2013.
- [198] X. Xie and Q. Wang. “A mathematical model for piezoelectric ring energy harvesting technology from vehicle tires”. In: *International Journal of Engineering Science* 94 (Sept. 2015), pp. 113–127. DOI: 10.1016/j.ijengsci.2015.05.004.
- [199] A. T. Eshghi et al. “Design optimization under uncertainty and speed variability for a piezoelectric energy harvester powering a tire pressure monitoring sensor”. In: *Smart Materials and Structures* 26.10 (Sept. 2017), p. 105037. DOI: 10.1088/1361-665x/aa8886.
- [200] C. R. Bowen and M. H. Arafa. “Energy Harvesting Technologies for Tire Pressure Monitoring Systems”. In: *Advanced Energy Materials* 5.7 (Dec. 2014), p. 1401787. DOI: 10.1002/aenm.201401787.
- [201] A. D. T. Elliott et al. “Which is better, electrostatic or piezoelectric energy harvesting systems?” In: *Journal of Physics: Conference Series* 660 (Dec. 2015), p. 012128. DOI: 10.1088/1742-6596/660/1/012128.

- [202] T. Makinen and H. Wunderlich. “Intelligent tyre promoting accident-free traffic”. In: *Proceedings. The IEEE 5th International Conference on Intelligent Transportation Systems*. IEEE, 2002. DOI: 10.1109/itsc.2002.1041287.
- [203] M. J. Guan and W. H. Liao. “On the efficiencies of piezoelectric energy harvesting circuits towards storage device voltages”. In: *Smart Materials and Structures* 16.2 (Mar. 2007), pp. 498–505. DOI: 10.1088/0964-1726/16/2/031.
- [204] Y.-J. Lin and S.-J. Hwang. “Temperature prediction of rolling tires by computer simulation”. In: *Mathematics and Computers in Simulation* 67.3 (Nov. 2004), pp. 235–249. DOI: 10.1016/j.matcom.2004.07.002.
- [205] Y. Liao and H. A. Sodano. “Model of a single mode energy harvester and properties for optimal power generation”. In: *Smart Materials and Structures* 17.6 (Nov. 2008), p. 065026. DOI: 10.1088/0964-1726/17/6/065026.
- [206] R. D’hulst and J. Driesen. “Power processing circuits for vibration-based energy harvesters”. In: *2008 IEEE Power Electronics Specialists Conference*. IEEE, June 2008. DOI: 10.1109/pesc.2008.4592325.
- [207] K. B. Singh and S. Taheri. “Estimation of tire–road friction coefficient and its application in chassis control systems”. In: *Systems Science & Control Engineering* 3.1 (Dec. 2014), pp. 39–61. DOI: 10.1080/21642583.2014.985804.
- [208] S. Ergen et al. “The Tire as an Intelligent Sensor”. In: *IEEE Transactions on Computer-Aided Design of Integrated Circuits and Systems* 28.7 (July 2009), pp. 941–955. DOI: 10.1109/tcad.2009.2022879.
- [209] S. W. Yoon et al. “Shock-Protection Improvement Using Integrated Novel Shock-Protection Technologies”. In: *Journal of Microelectromechanical Systems* 20.4 (Aug. 2011), pp. 1016–1031. DOI: 10.1109/jmems.2011.2148154.
- [210] S. P. Matova et al. “Effect of length/width ratio of tapered beams on the performance of piezoelectric energy harvesters”. In: *Smart Materials and Structures* 22.7 (June 2013), p. 075015. DOI: 10.1088/0964-1726/22/7/075015.
- [211] A. Doria et al. “An Impulsive Method for the Analysis of Piezoelectric Energy Harvesters for Intelligent Tires”. In: *Volume 3: 18th International Conference on Advanced Vehicle Technologies; 13th International Conference on Design Education; 9th Frontiers in Biomedical Devices*. American Society of Mechanical Engineers. ASME, Aug. 2016, V003T01A025–V003T01A025. DOI: 10.1115/detc2016-59105.
- [212] A. Doria et al. “On the performance of piezoelectric harvesters loaded by finite width impulses”. In: *Mechanical Systems and Signal Processing* 100 (Feb. 2018), pp. 28–42. DOI: 10.1016/j.ymsp.2017.07.030.
- [213] A. Niskanen. “Sensing the tyre-road contact by intelligent tyre”. PhD thesis. 2017.

- [214] A. Kubba and K. Jiang. “A Comprehensive Study on Technologies of Tyre Monitoring Systems and Possible Energy Solutions”. In: *Sensors* 14.6 (June 2014), pp. 10306–10345. DOI: 10.3390/s140610306.
- [215] T. Galchev, H. Kim, and K. Najafi*. “A Parametric Frequency Increased Power Generator for Scavenging Low Frequency Ambient Vibrations”. In: *Procedia Chemistry* 1.1 (Sept. 2009), pp. 1439–1442. DOI: 10.1016/j.proche.2009.07.359.
- [216] N. Makki and R. Pop-Iliev. “Piezoelectric power generation in automotive tires”. In: *Proceedings of the Smart Materials & Structures/NDT in Aerospace/NDT in Canada* (2011).
- [217] W. Hall, J. T. Mottram, and R. P. Jones. “Finite element simulation of a rolling automobile tyre to understand its transient macroscopic behaviour”. In: *Proceedings of the Institution of Mechanical Engineers, Part D: Journal of Automobile Engineering* 218.12 (Dec. 2004), pp. 1393–1408. DOI: 10.1243/0954407042707722. eprint: <https://doi.org/10.1243/0954407042707722>.
- [218] X. Yang. “Finite element analysis and experimental investigation of tyre characteristics for developing strain-based intelligent tyre system”. PhD thesis. University of Birmingham, 2011.
- [219] J. Gardner and B. Queise. “Introduction to Tire Safety, Durability and Failure Analysis”. In: *The Pneumatic Tire* (2005), pp. 618–640.
- [220] F. Khameneifar and S. Arzanpour. “Energy Harvesting From Pneumatic Tires Using Piezoelectric Transducers”. In: *Smart Materials, Adaptive Structures and Intelligent Systems, Volume 1*. ASME, 2008, pp. 333–339. DOI: 10.1115/smasis2008-426.
- [221] D. S. Nguyen et al. “Fabrication and characterization of a wideband MEMS energy harvester utilizing nonlinear springs”. In: *Journal of Micromechanics and Microengineering* 20.12 (Nov. 2010), p. 125009. DOI: 10.1088/0960-1317/20/12/125009.
- [222] Y.-J. Wang, C.-D. Chen, and C.-K. Sung. “Design of a frequency-adjusting device for harvesting energy from a rotating wheel”. In: *Sensors and Actuators A: Physical* 159.2 (May 2010), pp. 196–203. DOI: 10.1016/j.sna.2009.12.007.
- [223] Q. Zheng. *Gapped cantilever for the enhancement of strain sensitivity and energy efficiency*. 2012.
- [224] A. Kubba and K. Jiang. “Efficiency Enhancement of a Cantilever-Based Vibration Energy Harvester”. In: *Sensors* 14.1 (Dec. 2013), pp. 188–211. DOI: 10.3390/s140100188.

- [225] K. S. Moon et al. “Tire tread deformation sensor and energy harvester development for smart-tire applications”. In: *Sensors and Smart Structures Technologies for Civil, Mechanical, and Aerospace Systems 2007*. Ed. by M. Tomizuka, C.-B. Yun, and V. Giurgiutiu. SPIE, Apr. 2007. DOI: 10.1117/12.721009.
- [226] J. Hand. “Modeling optimizes a piezoelectric energy harvester used in car tires”. In: *COMSOL Multiphysics, MEMS Energy Harvesters Special Advertising Section* (2012).
- [227] N. Makki and R. Pop-Iliev. “Piezoelectric power generation in tires”. In: *SPIE Newsroom* (May 2011). DOI: 10.1117/2.1201104.003702.
- [228] S. Li et al. “Dual resonant structure for energy harvesting from random vibration sources at low frequency”. In: *AIP Advances* 6.1 (Jan. 2016), p. 015019. DOI: 10.1063/1.4941353.
- [229] S. Li et al. “Dual resonant structure for energy harvesting from random vibration sources”. In: *2016 IEEE 11th Annual International Conference on Nano/Micro Engineered and Molecular Systems (NEMS)*. IEEE, Apr. 2016. DOI: 10.1109/nems.2016.7758245.
- [230] L. Gu and C. Livermore. “Passive self-tuning energy harvester for extracting energy from rotational motion”. In: *Applied Physics Letters* 97.8 (Aug. 2010), p. 081904. DOI: 10.1063/1.3481689.
- [231] E. Bonisoli et al. “Multi-physics optimisation of an energy harvester device for automotive application”. In: *COMPEL - The international journal for computation and mathematics in electrical and electronic engineering* 33.3 (Apr. 2014). Ed. by P. L. Dupré and D. G. Crevecoeur, pp. 846–855. DOI: 10.1108/compe1-10-2012-0208.
- [232] E. Zaouali et al. “Design and modelling of an energy harvester for tire pressure monitoring systems”. In: *MATEC Web of Conferences* 16 (2014). Ed. by M. Belhaq, p. 01009. DOI: 10.1051/mateconf/20141601009.
- [233] C.-D. Chen, Y.-J. Wang, and C. Sung. “A novel energy harvesting device embedded in a rotating wheel”. In: *Proceedings of PowerMEMS2008+ microEMS2008, Dendai, Japan* (2008).
- [234] H. Zhang et al. “Single-Electrode-Based Rotating Triboelectric Nanogenerator for Harvesting Energy from Tires”. In: *ACS Nano* 8.1 (Dec. 2013), pp. 680–689. DOI: 10.1021/nn4053292.
- [235] L. Wu et al. “A Battery-less Tire Pressure Monitoring System”. In: *2012 International Conference on Connected Vehicles and Expo (ICCVE)*. IEEE, Dec. 2012. DOI: 10.1109/iccve.2012.49.

- [236] Y. Li et al. “Power recovery circuit for battery-less TPMS”. In: *2007 7th International Conference on ASIC*. IEEE, Oct. 2007. DOI: 10.1109/icasic.2007.4415665.
- [237] G. D. Szarka, B. H. Stark, and S. G. Burrow. “Review of Power Conditioning for Kinetic Energy Harvesting Systems”. In: *IEEE Transactions on Power Electronics* 27.2 (Feb. 2012), pp. 803–815. DOI: 10.1109/tpe1.2011.2161675.
- [238] J. Dicken et al. “Power-Extraction Circuits for Piezoelectric Energy Harvesters in Miniature and Low-Power Applications”. In: *IEEE Transactions on Power Electronics* 27.11 (Nov. 2012), pp. 4514–4529. DOI: 10.1109/tpe1.2012.2192291.
- [239] V. Annapureddy et al. “Magnetic energy harvesting with magnetoelectrics: an emerging technology for self-powered autonomous systems”. In: *Sustainable Energy Fuels* (2017). DOI: 10.1039/c7se00403f.
- [240] H. Liu et al. “Study on the giant magnetostrictive vibration-power generation method for battery-less tire pressure monitoring system”. In: *Proceedings of the Institution of Mechanical Engineers, Part C: Journal of Mechanical Engineering Science* 229.9 (Aug. 2014), pp. 1639–1651. DOI: 10.1177/0954406214545821.
- [241] V. Franzitta et al. “A Magnetostrictive Electric Power Generator for energy harvesting from traffic: Design and experimental verification”. In: *2015 IEEE Magnetics Conference (INTERMAG)*. IEEE, May 2015. DOI: 10.1109/intmag.2015.7157483.
- [242] S. W. Yoon. “Vibration isolation and shock protection for MEMS”. PhD thesis. 2009.
- [243] R. Elfrink et al. “Vacuum-packaged piezoelectric vibration energy harvesters: damping contributions and autonomy for a wireless sensor system”. In: *Journal of Micromechanics and Microengineering* 20.10 (2010), p. 104001. DOI: 10.1088/0960-1317/20/10/104001. URL: <http://stacks.iop.org/0960-1317/20/i=10/a=104001>.
- [244] S.-T. Chen et al. “Shock reliability enhancement for MEMS vibration energy harvesters with nonlinear air damping as a soft stopper”. In: *Journal of Micromechanics and Microengineering* 27.10 (Sept. 2017), p. 104003. DOI: 10.1088/1361-6439/aa82ed.
- [245] S.-T. Chen et al. “Utilising Nonlinear Air Damping as a Soft Mechanical Stopper for MEMS Vibration Energy Harvesting”. In: *Journal of Physics: Conference Series* 773 (Nov. 2016), p. 012098. DOI: 10.1088/1742-6596/773/1/012098.

- [246] R. J. M. Vullers et al. “MEMS based vibration harvesting: Facing the ugly facts”. In: *2013 Transducers & Eurosensors XXVII: The 17th International Conference on Solid-State Sensors, Actuators and Microsystems (TRANSDUCERS & EUROSENSORS XXVII)*. IEEE, June 2013. DOI: 10.1109/transducers.2013.6626859.
- [247] A. T. Eshghi et al. “Parameter study and optimization for piezoelectric energy harvester for TPMS considering speed variation”. In: *Smart Materials and Non-destructive Evaluation for Energy Systems 2016*. Ed. by N. G. Meyendorf, T. E. Matikas, and K. J. Peters. SPIE, Apr. 2016. DOI: 10.1117/12.2219567.
- [248] J. Eom, H. Lee, and B. Choi. “A study on the tire deformation sensor for intelligent tires”. In: *International Journal of Precision Engineering and Manufacturing* 15.1 (Jan. 2014), pp. 155–160. DOI: 10.1007/s12541-013-0319-0.
- [249] J. PÉRISSE. “A STUDY OF RADIAL VIBRATIONS OF A ROLLING TYRE FOR TYRE–ROAD NOISE CHARACTERISATION”. In: *Mechanical Systems and Signal Processing* 16.6 (Nov. 2002), pp. 1043–1058. DOI: 10.1006/mssp.2001.1432.
- [250] L. Gu and C. Livermore. “Impact-driven, frequency up-converting coupled vibration energy harvesting device for low frequency operation”. In: *Smart Materials and Structures* 20.4 (Mar. 2011), p. 045004. DOI: 10.1088/0964-1726/20/4/045004.
- [251] Y.-J. Wang, C.-D. Chen, and C.-K. Sung. “System Design of a Weighted-Pendulum-Type Electromagnetic Generator for Harvesting Energy From a Rotating Wheel”. In: *IEEE/ASME Transactions on Mechatronics* 18.2 (Apr. 2013), pp. 754–763. DOI: 10.1109/tmech.2012.2183640.
- [252] N. Chidambaram et al. “Comparison of lead Zirconate Titanate thin films for microelectromechanical energy harvester with interdigitated and parallel plate electrodes”. In: *IEEE Transactions on Ultrasonics, Ferroelectrics, and Frequency Control* 60.8 (Aug. 2013), pp. 1564–1571. DOI: 10.1109/tuffc.2013.2736.
- [253] L. Lin et al. “Transparent flexible nanogenerator as self-powered sensor for transportation monitoring”. In: *Nano Energy* 2.1 (Jan. 2013), pp. 75–81. DOI: 10.1016/j.nanoen.2012.07.019.
- [254] C. R. Bowen et al. “Piezoelectric and ferroelectric materials and structures for energy harvesting applications”. In: *Energy Environ. Sci.* 7.1 (2014), pp. 25–44. DOI: 10.1039/c3ee42454e.
- [255] H. Askari et al. “A Triboelectric Self-Powered Sensor for Tire Condition Monitoring: Concept, Design, Fabrication, and Experiments”. In: *Advanced Engineering Materials* (Aug. 2017), p. 1700318. DOI: 10.1002/adem.201700318.
- [256] Y. Zi et al. “Effective energy storage from a triboelectric nanogenerator”. In: *Nature Communications* 7 (Mar. 2016), p. 10987. DOI: 10.1038/ncomms10987.

- [257] X.-S. Zhang et al. “Frequency-Multiplication High-Output Triboelectric Nanogenerator for Sustainably Powering Biomedical Microsystems”. In: *Nano Letters* 13.3 (Feb. 2013), pp. 1168–1172. DOI: 10.1021/nl3045684.
- [258] G. Zhu et al. “A Shape-Adaptive Thin-Film-Based Approach for 50% High-Efficiency Energy Generation Through Micro-Grating Sliding Electrification”. In: *Advanced Materials* 26.23 (Apr. 2014), pp. 3788–3796. DOI: 10.1002/adma.201400021.
- [259] C. Mo, S. Kim, and W. W. Clark. “Theoretical analysis of energy harvesting performance for unimorph piezoelectric benders with interdigitated electrodes”. In: *Smart Materials and Structures* 18.5 (Apr. 2009), p. 055017. DOI: 10.1088/0964-1726/18/5/055017.
- [260] R. R. Knight, C. Mo, and W. W. Clark. “MEMS interdigitated electrode pattern optimization for a unimorph piezoelectric beam”. In: *Journal of Electroceramics* 26.1-4 (Oct. 2010), pp. 14–22. DOI: 10.1007/s10832-010-9621-8.
- [261] C. Jean-Mistral et al. “Modelling of soft generator combining electret and dielectric elastomer”. In: *2014 IEEE/ASME International Conference on Advanced Intelligent Mechatronics*. IEEE, July 2014. DOI: 10.1109/aim.2014.6878283.
- [262] C. Lagomarsini et al. “Coupling of electro-active polymers for energy harvesting applications”. In: *2016 IEEE International Conference on Dielectrics (ICD)*. IEEE, July 2016. DOI: 10.1109/icd.2016.7547638.
- [263] A. Kachroudi et al. “Towards an autonomous electrostatic generator for micropower vibration energy harvesting under inertial load”. In: *7ème Journées Nationales sur la Récupération et le Stockage d’Energie (JNRSE’17)* (2017).
- [264] T. Vu-Cong, C. Jean-Mistral, and A. Sylvestre. “Autonomous dielectric elastomer generator using electret”. In: *Electroactive Polymer Actuators and Devices (EAPAD) 2013*. Ed. by Y. Bar-Cohen. SPIE, Apr. 2013. DOI: 10.1117/12.2008793.
- [265] C. Jean-Mistral, T. V. Cong, and A. Sylvestre. “Advances for dielectric elastomer generators: Replacement of high voltage supply by electret”. In: *Applied Physics Letters* 101.16 (Oct. 2012), p. 162901. DOI: 10.1063/1.4761949.
- [266] R. Matsuzaki and A. Todoroki. “Wireless strain monitoring of tires using electrical capacitance changes with an oscillating circuit”. In: *Sensors and Actuators A: Physical* 119.2 (Apr. 2005), pp. 323–331. DOI: 10.1016/j.sna.2004.10.014.
- [267] M. J. Guan and W. H. Liao. “On the efficiencies of piezoelectric energy harvesting circuits towards storage device voltages”. In: *Smart Materials and Structures* 16.2 (Mar. 2007), pp. 498–505. DOI: 10.1088/0964-1726/16/2/031.
- [268] R. Matsuzaki et al. “Rubber-based strain sensor fabricated using photolithography for intelligent tires”. In: *Sensors and Actuators A: Physical* 148.1 (Nov. 2008), pp. 1–9. DOI: 10.1016/j.sna.2008.08.001.

- [269] S. Kaur and E. Halvorsen. “Parameter sensitivity of an in-plane gap closing electrostatic energy harvester with end-stop impacts”. In: *Journal of Intelligent Material Systems and Structures* 28.12 (Jan. 2017), pp. 1640–1650. DOI: 10.1177/1045389x16679287.
- [270] H. Park. “Vibratory electromagnetic induction energy harvester on wheel surface of mobile sources”. In: *International Journal of Precision Engineering and Manufacturing-Green Technology* 4.1 (Jan. 2017), pp. 59–66. DOI: 10.1007/s40684-017-0008-z.
- [271] T. Lange and T. Kvisterøy. “Intelligent Low-Power Management and Concepts for Battery-less Direct Tire Pressure Monitoring Systems (TPMS)”. In: *Advanced Microsystems for Automotive Applications 2007*. Ed. by J. Valldorf and W. Gessner. Springer Berlin Heidelberg, 2007, pp. 237–248. DOI: 10.1007/978-3-540-71325-8.
- [272] M. Löhndorf and T. Lange. “MEMS for automotive tire pressure monitoring systems”. In: *MEMS for Automotive and Aerospace Applications*. Ed. by M. Kraft and N. M. White. Woodhead Publishing Limited, 2013, pp. 54–77. DOI: 10.1533/9780857096487.1.54.
- [273] Wikipedia contributors. *Electret* — *Wikipedia, The Free Encyclopedia*. [Online; 2021-02-08]. 2021. URL: <https://en.wikipedia.org/w/index.php?title=Electret&oldid=999688235>.
- [274] T. LLC. *Galfenol*. Accessed: 2021-02-09. URL: <http://tdvib.com/terfenol-d/>.
- [275] T. LLC. *Galfenol*. Accessed: 2021-02-09. URL: <http://tdvib.com/galfenol/>.
- [276] R. Kressmann, G. Sessler, and P. Gunther. “Space-charge electrets”. In: *IEEE Transactions on Dielectrics and Electrical Insulation* 3.5 (1996), pp. 607–623. DOI: 10.1109/94.544184.
- [277] R. A. P. Altafim et al. “Template-based fluoroethylenepropylene piezoelectrets with tubular channels for transducer applications”. In: *Journal of Applied Physics* 106.1 (July 2009), p. 014106. DOI: 10.1063/1.3159039.
- [278] C. Zhang et al. “Surface charge density of triboelectric nanogenerators: Theoretical boundary and optimization methodology”. In: *Applied Materials Today* 18 (Mar. 2020), p. 100496. DOI: 10.1016/j.apmt.2019.100496.
- [279] F. T. Ulaby and U. Ravaioli. “Fundamentals of applied electromagnetics 7th Edition”. In: *Boston, Massachusetts: Prentice Hall* (2014).
- [280] Q. Zheng. “Gapped cantilever for the enhancement of strain sensitivity and energy efficiency”. PhD thesis. 2012.

- [281] I.-H. Ho et al. “A Battery-Less Tire Pressure Monitoring System”. In: *VTC Spring 2009 - IEEE 69th Vehicular Technology Conference*. IEEE, Apr. 2009. DOI: 10.1109/vetecs.2009.5073285.
- [282] G. Hatipoglu and H. Urey. “FR4-based electromagnetic energy harvester for wireless tyre sensor nodes”. In: *Procedia Chemistry* 1.1 (Sept. 2009), pp. 1211–1214. DOI: 10.1016/j.proche.2009.07.302.
- [283] L. Wu et al. “Battery-less piezoceramics mode energy harvesting for automobile TPMS”. In: *2009 IEEE 8th International Conference on ASIC*. IEEE, Oct. 2009. DOI: 10.1109/asicon.2009.5351190.
- [284] B. Zhu, J. Han, and J. Zhao. “M”. In: *Lecture Notes in Electrical Engineering*. Springer Singapore, Oct. 1994, pp. 971–978. DOI: 10.1007/978-981-10-8506-2_65.
- [285] R. Esmaeeli et al. “A Rainbow Piezoelectric Energy Harvesting System for Intelligent Tire Monitoring Applications”. In: *Journal of Energy Resources Technology* 141.6 (Jan. 2019). DOI: 10.1115/1.4042398.
- [286] R. Esmaeeli et al. “Optimization of a Rainbow Piezoelectric Energy Harvesting System for Tire Monitoring Applications”. In: *ASME 2018 12th International Conference on Energy Sustainability*. American Society of Mechanical Engineers, June 2018. DOI: 10.1115/es2018-7496.
- [287] M. Flatscher et al. “A robust wireless sensor node for in-tire-pressure monitoring”. In: *2009 IEEE International Solid-State Circuits Conference - Digest of Technical Papers*. IEEE, Feb. 2009. DOI: 10.1109/isscc.2009.4977420.
- [288] “Intelligent Low-Power Management and Concepts for Battery-less Direct Tire Pressure Monitoring Systems (TPMS)”. In: *Advanced Microsystems for Automotive Applications 2007*. Springer Berlin Heidelberg, pp. 237–249. DOI: 10.1007/978-3-540-71325-8_19.
- [289] F. Dell’Anna et al. “State-of-the-Art Power Management Circuits for Piezoelectric Energy Harvesters”. In: *IEEE Circuits and Systems Magazine* 18.3 (2018), pp. 27–48. DOI: 10.1109/mcas.2018.2849262.
- [290] M. V. Tholl et al. “An Intracardiac Flow Based Electromagnetic Energy Harvesting Mechanism for Cardiac Pacing”. In: *IEEE Transactions on Biomedical Engineering* 66.2 (Feb. 2019), pp. 530–538. DOI: 10.1109/tbme.2018.2849868.
- [291] G. Martin and V. P. S. A. EnOcean. “Wireless sensor solutions for home & building automation-the successful standard uses energy harvesting”. In: *EnOcean white paper* (2007).
- [292] C. Saha et al. “Electromagnetic generator for harvesting energy from human motion”. In: *Sensors and Actuators A: Physical* 147.1 (Sept. 2008), pp. 248–253. DOI: 10.1016/j.sna.2008.03.008.

- [293] L. Garbuio et al. “Mechanical Energy Harvester With Ultralow Threshold Rectification Based on SSHI Nonlinear Technique”. In: *IEEE Transactions on Industrial Electronics* 56.4 (Apr. 2009), pp. 1048–1056. DOI: 10.1109/tie.2009.2014673.
- [294] D. Guyomar et al. “Toward energy harvesting using active materials and conversion improvement by nonlinear processing”. In: *IEEE Transactions on Ultrasonics, Ferroelectrics and Frequency Control* 52.4 (Apr. 2005), pp. 584–595. DOI: 10.1109/tuffc.2005.1428041.
- [295] H. S. Dhadwal and J. Rastegar. *Energy Harvesting for Low-Power Autonomous Devices and Systems*. SPIE, Feb. 2017. DOI: 10.1117/3.2256429.
- [296] M. Deterre et al. “Energy harvesting system for cardiac implant applications”. In: *2011 Symposium on Design, Test, Integration & Packaging of MEMS/MOEMS (DTIP)*. IEEE, 2011, pp. 387–391.
- [297] C. Mo, L. J. Radziemski, and W. W. Clark. “Experimental validation of energy harvesting performance for pressure-loaded piezoelectric circular diaphragms”. In: *Smart Materials and Structures* 19.7 (June 2010), p. 075010. DOI: 10.1088/0964-1726/19/7/075010.
- [298] S. Mohammadi and M. Abdalbeigi. “Analytical Optimization of Piezoelectric Circular Diaphragm Generator”. In: *Advances in Materials Science and Engineering* 2013 (2013), pp. 1–10. DOI: 10.1155/2013/620231.
- [299] S. A. N. Prasad et al. “Analytical Electroacoustic Model of a Piezoelectric Composite Circular Plate”. In: *AIAA Journal* 44.10 (Oct. 2006), pp. 2311–2318. DOI: 10.2514/1.19855.
- [300] C. Mo et al. “Behaviour of a unimorph circular piezoelectric actuator”. In: *Smart Materials and Structures* 15.4 (July 2006), pp. 1094–1102. DOI: 10.1088/0964-1726/15/4/023.
- [301] D. Semiconductor. *Schottky Barrier Rectifiers*. Accessed: 2021-09-08. URL: <https://cdn-reichelt.de/documents/datenblatt/A400/sb5100.pdf>.
- [302] G. Semiconductor. *1N4001 THRU 1N4007*. Accessed: 2021-09-08. URL: <https://docs.rs-online.com/6307/0900766b8002659f.pdf>.
- [303] Y. Suzuki. “Electret based vibration energy harvester for sensor network”. In: *2015 Transducers - 2015 18th International Conference on Solid-State Sensors, Actuators and Microsystems (TRANSDUCERS)*. IEEE, June 2015. DOI: 10.1109/transducers.2015.7180856.
- [304] Z. Xia et al. “Thermal stability of piezoelectricity for porous polytetrafluoroethylene electret film”. In: *Journal of Electrostatics* 58.3-4 (June 2003), pp. 265–274. DOI: 10.1016/s0304-3886(02)00205-x.

- [305] M. Koca et al. “Empirical Feasibility Analysis for Energy Harvesting Intravehicular Wireless Sensor Networks”. In: *IEEE Internet of Things Journal* 8.1 (Jan. 2021), pp. 179–186. DOI: 10.1109/jiot.2020.3001992.
- [306] L. Buccolini and M. Conti. “An Energy Harvester Interface for Self-Powered Wireless Speed Sensor”. In: *IEEE Sensors Journal* 17.4 (Feb. 2017), pp. 1097–1104. DOI: 10.1109/jsen.2016.2635940.
- [307] J. Leicht et al. “20.6 Electromagnetic vibration energy harvester interface IC with conduction-angle-controlled maximum-power-point tracking and harvesting efficiencies of up to 90%”. In: *2015 IEEE International Solid-State Circuits Conference - (ISSCC) Digest of Technical Papers*. IEEE, Feb. 2015. DOI: 10.1109/isscc.2015.7063079.
- [308] TDK. *EFR32BG22 Series 2 Bluetooth® Wireless SoC*. Accessed: 2021-12-21. URL: <https://www.silabs.com/wireless/bluetooth/efr32bg22-series-2-socs#>.
- [309] T. Sanislav et al. “Energy Harvesting Techniques for Internet of Things (IoT)”. In: 9 (2021), pp. 39530–39549. DOI: 10.1109/access.2021.3064066.
- [310] A. Nozariasbmarz et al. “Review of wearable thermoelectric energy harvesting: From body temperature to electronic systems”. In: 258 (Jan. 2020), p. 114069. DOI: 10.1016/j.apenergy.2019.114069.
- [311] S. Boisseau et al. “An autonomous switch based on a rotating magnet driven by magnetic launchers”. In: 30.2 (Jan. 2021), 02LT01. DOI: 10.1088/1361-665x/abd7e8.
- [312] A. Richter et al. “Tunable interface for piezoelectric energy harvesting”. In: IEEE, Feb. 2014. DOI: 10.1109/ssd.2014.6808750.
- [313] D. A. Sanchez et al. “21.2 A $4\mu\text{W}$ -to-1mW parallel-SSHI rectifier for piezoelectric energy harvesting of periodic and shock excitations with inductor sharing, cold start-up and up to 681% power extraction improvement”. In: IEEE, Jan. 2016. DOI: 10.1109/isscc.2016.7418059.
- [314] Y. C. Shu and I. C. Lien. “Analysis of power output for piezoelectric energy harvesting systems”. In: 15.6 (Sept. 2006), pp. 1499–1512. DOI: 10.1088/0964-1726/15/6/001.
- [315] Y. C. Shu, I. C. Lien, and W. J. Wu. “An improved analysis of the SSHI interface in piezoelectric energy harvesting”. In: 16.6 (Oct. 2007), pp. 2253–2264. DOI: 10.1088/0964-1726/16/6/028.
- [316] J. Liang and W.-H. Liao. “Impedance Modeling and Analysis for Piezoelectric Energy Harvesting Systems”. In: 17.6 (Dec. 2012), pp. 1145–1157. DOI: 10.1109/tmech.2011.2160275.

- [317] Y. Liao and J. Liang. “Unified modeling, analysis and comparison of piezoelectric vibration energy harvesters”. In: 123 (May 2019), pp. 403–425. DOI: 10.1016/j.ymsp.2019.01.025.
- [318] K.-R. Cheng et al. “A 0.25 μ m HV-CMOS Synchronous Inversion and Charge Extraction (SICE) Interface Circuit for Piezoelectric Energy Harvesting”. In: IEEE, May 2018. DOI: 10.1109/iscas.2018.8351700.
- [319] G. Lombardi and M. Lallart. “Synchronous electric charge and induced current extraction (SECICE): a unified nonlinear technique combining piezoelectric and electromagnetic harvesting”. In: 30.2 (Jan. 2021), p. 025029. DOI: 10.1088/1361-665x/abd346.
- [320] E. Starke. “Kombinierte Simulation - eine weitere Methode zur Optimierung elektromechanischer Systeme”. In: *TUDpress* (Feb. 2010).
- [321] H. Ulasan et al. “An efficient integrated interface electronics for electromagnetic energy harvesting from low voltage sources”. In: *2013 Transducers & Eurosensors XXVII: The 17th International Conference on Solid-State Sensors, Actuators and Microsystems (TRANSDUCERS & EUROSENSORS XXVII)*. IEEE, June 2013. DOI: 10.1109/transducers.2013.6626800.
- [322] N. Stephen. “On energy harvesting from ambient vibration”. In: *Journal of Sound and Vibration* 293.1-2 (May 2006), pp. 409–425. DOI: 10.1016/j.jsv.2005.10.003.
- [323] E. Lefeuvre et al. “A comparison between several approaches of piezoelectric energy harvesting”. In: *Journal de Physique IV (Proceedings)* 128 (Sept. 2005), pp. 177–186. DOI: 10.1051/jp4:2005128027.
- [324] C. Broß et al. “Piezoelectric Crystals as an Example for Structure-Property-Relation”. In: *CHEMKON* (July 2021). DOI: 10.1002/ckon.202100024.
- [325] P. Hadley. *Advanced Solid State Physics*. Accessed: 2022-06-08. URL: <http://lampx.tugraz.at/~hadley/ss2/crystalphysics/piezo.php>.
- [326] S. R. Williams. “Magnetostriktion und ihre Bedeutung für die magnetischen Theorien”. In: *Theorien des Magnetismus*. Vieweg + Teubner Verlag, 1925, pp. 244–257. DOI: 10.1007/978-3-663-04515-1_5.
- [327] S.-W. Wang et al. “Electromagnetic Energy Harvester Interface Design for Wearable Applications”. In: *IEEE Transactions on Circuits and Systems II: Express Briefs* 65.5 (May 2018), pp. 667–671. DOI: 10.1109/tcsii.2018.2820158.
- [328] Thinika. *Thin Film Energy Storage Devices*. Tech. rep. Thinika Limited Liability Company, 2017.

- [329] Y. Yuan et al. “Different effects of monophasic pulses and biphasic pulses applied by a bipolar stimulation electrode in the rat hippocampal CA1 region”. In: *BioMedical Engineering OnLine* 20.1 (Mar. 2021). DOI: 10.1186/s12938-021-00862-y.
- [330] M. Germer, U. Marschner, and A. Richter. “Strain Based Tire Pressure Monitoring Systems (TPMS) With Synchronous Electric Charge Extraction (SECE)”. In: (Sept. 2022). DOI: 10.1115/smasis2022-91168.

List of Acronyms

ASIC	Application specific integrated circuit
AC	Alternating current
ABS	Anti-lock braking system
CAE	Computer aided engineering
CCM	Continuous current mode
DC	Direct current
DCM	Discontinuous current mode
DOF	Degree of freedom
EaT	Energizing and Transferring
EB	Electronic Breaker
EMEH	Electromagnetic energy harvester
ESC	Electronic stability control
FE	Finite element
FEM	Finite element method
FEP	Fluorethylenpropylen
FOM	Figure of merit
FWR	Full-wave rectifier
IC	Integrated circuit
IEEE	Institute of Electrical and Electronics Engineers
IOT	Internet of Things
IOV	Internet of Vehicles
ISO	International Organization for Standardization

MFC	Macro Fiber Composite
NASA	National Aeronautics and Space Administration
NHTSA	National Highway Traffic Safety Administration
OEM	Original equipment manufacturer
OC	Open-circuit
PDF	Probability density function
PEH	Piezoelectric energy harvester
PMMA	Polymethylmethacrylat
ppm	Parts per million
P-SSHI	Parallel Synchronous Switch Harvesting on Inductor
PTFE	Polytetrafluorethylen
PVDF	Polyvinylidene fluoride
PWM	Pulse-width-modulation
PZT	Lead zirconate titanate
RMS	Root mean square
RDKS	Reifendruckkontrollsystem
SC	Short-circuit
SECE	Synchronous Electric Charge Extraction
SEH	Standard Energy Harvesting
SMFE	Synchronized Magnetic Flux Extraction
SOR	Switch-Only Rectifier
SSHI	Synchronous Switch Harvesting on Inductor
S-SSHI	Series Synchronous Switch Harvesting on Inductor
TPMS	Tire pressure monitoring system
VD	Voltage Doubler
VT	Voltage Tripler

List of Symbols

α	Piezoelectric transducer coefficient
β	Electromagnetic transducer coefficient
ΔE_{stored}	Energy difference of storage
ΔQ_p	Charge added to the capacitor C_p
ΔQ_s	Charge added to the capacitor C_s
δ	Decay rate
\mathbb{E}	Mean value
ϵ_{11}	Piezoelectric permittivity in 11 direction
ϵ_{33}	Piezoelectric permittivity in 33 direction
η	Efficiency
η_{CCM}	Efficiency of the continuous current mode
η_{DCM}	Efficiency of the discontinuous current mode
η_{EaT}	Efficiency of the EaT
η_{eh}	Efficiency of the energy harvester
η_{ic}	Efficiency of the interface circuit
η_{max}	Maximal efficiency
η_{SECE}	Efficiency of the SECE
η_{SEH}	Efficiency of the SEH
η_{SMFE}	Efficiency of the SMFE
η_{SOR}	Efficiency of the SOR
η_{SSHI}	Efficiency of the SSHI
η_{tot}	Efficiency of the total energy harvesting system
η_{xy}	Poisson's rate
γ	Tangent of the phase shift between voltage and current
\hat{I}_r	Peak current amplitude
\hat{U}_r	Peak voltage amplitude
\hat{z}	Peak deflection
μ_r	Relative permeability
μ_0	Vacuum permeability
ω	Angular velocity
ω	Natural angular frequency
ω_0	Frequency of the undamped oscillator
ω_e	Frequency of the damped system

ω_e	Frequency of the damped oscillator
$\bar{\eta}$	Average efficiency to charge a capacitor from 0 V to u_s
$\bar{\eta}$	Average efficiency
\bar{P}	Average power
\bar{v}	Average velocity
Φ	Surface potential
Ψ	Linked magnetic flux
Ψ	Magnetic flux
σ	Mechanical stress
σ	Surface charge density
σ_c	Compressive strength
σ_t	Tensile strength
σ_c	Compressive stress
σ_t	Tensile stress
τ	Time constant of the inductor
\underline{I}_r	Complex current through the resistor R
\underline{U}_r	Complex voltage across the resistor R
ε^T	Dielectric permittivity at $T = 0$
ε_d	Relative permittivity of a dielectric
ε_e	Relative permittivity of an electret
ε_0	Vacuum permittivity
φ	Phase angle
\vec{A}	Oriented cross section
\vec{B}	Magnetic flux density
\vec{D}	Electric displacement field
\vec{E}	Electric field
\vec{F}_1	Lorentz force
\vec{F}_{mag}	Magnetic force
\vec{l}	Oriented wire length
\vec{s}	Oriented integration path
Ξ	Mechanical displacement
A	Area
a	Acceleration
a	Ratio between storage capacitance and piezoelectric capacitance
a_{ex}	Acceleration of the excitation
a_g	Gravitational acceleration
a_c	Centrifugal acceleration
b	Ratio between storage capacitor voltage and open-circuit voltage
B_r	Magnetic flux density component in r-direction
B_z	Magnetic flux density component in z-direction

c	Damping coefficient
c_M	Geometric parameter of a piezoelectric transducer
C_p	Piezoelectric capacitance of the blocked system
C_s	Storage capacitor
d	Piezoelectric stress constant
d_1	Diameter of the movable magnet
d_2	Diameter of the fixed magnet
d_{31}	Piezoelectric stress constant in 31-direction
d_{33}	Piezoelectric stress constant in 33-direction
d_w	Diameter of the wire
E	Energy
$E(u_T \geq u_{FV})$...	Interval energy
E_0	Available Energy
$E_{1,strike}$	Energy of one strike
$E_{2,strike}$	Energy of two strikes
E_{add}	Required energy to charge C_s from u_{asic} to $u_{charged}$
E_{asic}	Energy corresponding to u_{asic}
E_{bat}	Energy of the battery
E_{CCM}	Energy related to the continuous current mode
$E_{charged}$	Energy to transmit data
E_{DCM}	Energy related to the discontinuous current mode
E_{elec}	Electrical energy
$E_{harvested}$	Harvested electrical at the transducer output
$E_{inversion}$	Remaining energy after charge inversion
E_{in}	Incoming energy
E_L	Energy stored in the inductor
E_{mech}	Mechanical energy
E_{rev}	Energy per revolution
E_{stored}	Energy of the storage (capacitor)
E_b	Electric breakdown field strength
F	Force
$f(z)$	Polynomial approximation function
F_{bumper}	Force of the bottom bumper
F_{ex}	Force of the excitation
F_{top}	Force of the top bumper
F_T	Transducer force
H	Absolute frequency distribution
H	Magnetiv field
h	Probability density function
h	Thickness/height of the dielectric

h_b	Height of the bumper
H_c	Magnetic coercivity
h_e	Thickness/height of the electret
h_h	Height of the housing
h_p	Piezoelectric height
h_s	Substrate height
I	Second moment of inertia
i	Electric current
$i_{L,0}$	Initial inductor current
i_L	Inductance current
i_p	Piezoelectric current
i_T	Transducer current
i_N	Normalized current
i_R	Resistor current
k	Electromechanical coupling coefficient
k_{11}	Piezoelectric coupling coefficient in 11 direction
k_{33}	Piezoelectric coupling coefficient in 33 direction
l	Length
L_c	Coil inductance
l_p	Length of the piezoelectric beam
l_s	Length of the substrate beam
L_c	Coil inductance
m	Mass
N	Coil turns/windings
N	Tire revolutions
n	Compliance
n	Initial current ratio between charged inductor current i_{L0} and initial current i_0
n	Number of multiplier stages
n	Number of values
n_{oc}	Compliance for the electrical open-circuit case
n_{sc}	Compliance for the electrical short-circuit case
P	Power
p	Pressure
q	Quality factor
$Q(u_T \geq u_{FV})$...	Interval charge
Q_0	Available charge
Q_0	Initial charge
Q_{bat}	Charge of the battery
Q_d	Charge for data transmission

$Q_{p,0}$	Initial charge of the capacitor C_p
$Q_{s,0}$	Initial charge of the capacitor C_s
R	Tire radius
R_c	Coil resistance
r_i	Inner coil radius
$R_{L,opt}$	Optimal load resistance
R_L	Load resistor
R_L	Parasitic resistance of the inductor L
r_o	Outer coil radius
R_p	Parasitic piezoelectric resistance
R_r	Rim radius
S	Strain
s^E	Compliance when the electric field $E = 0$
S_{max}	Maximal strain
s_{11}	Compliance in 11 direction
s_{33}	Compliance in 33 direction
T	Maxwell stress tensor
T	Operation temperature
T	Period
T	Stress
T	Temperature
t	Time
T_{curie}	Curie temperature
t_E	Energizing time - time in which the switch is closed
T_{LC}	Period of LC network
T_{op}	Operation temperature
t_T	Transferring time - time in which the switch is open
u	Electric voltage
u_0	Maximal piezoelectric voltage
u_{asic}	Minimal voltage of the ASIC
u_b	Barrier voltage
u_b	Electric breakdown voltage
$u_{charged}$	Voltage level. when the capacitor is charged
u_d	Diode forward voltage
u_{FV}	Forward voltage
u_{oc}	Open-circuit voltage
$u_{p,0}$	Initial capacitor voltage of C_p
u_R	Voltage across load resistance
$u_{s,0}$	Initial capacitor voltage of C_s
u_T	Transducer voltage

u_b	Barrier voltage
u_N	Normalized voltage
u_s	Capacitor voltage
V	Volume
v	Velocity
w	Volumetric energy density
w	Width/beam width
w_{el}	Electrical energy density
w_{magn}	Magnetic energy density
w_{mech}	Mechanical energy density
x	Quotient of the energizing time the t_E and time constant τ
Y	Young's modulus
y	Quotient of the transferring time the t_T and time constant τ
z	Position
z_{c1}	Position of the bottom coil
z_{c2}	Position of the top coil

List of Figures

1.1	Smart tire pressure monitoring systems	2
1.2	Energy harvesting chain - from the source to the storage	3
1.3	Visualization of the structure of this thesis	5
2.1	Rim mounted energy harvester	8
2.2	Rim wave signal for one tire revolution at constant velocity	8
2.3	Tire inner liner mounted energy harvester	9
2.4	Tire wave signal for one tire revolution at constant velocity	9
2.5	Tire wave signal for different velocities and related centrifugal accelerations	10
2.6	Tire deformation at the tire inner liner and corresponding strain wave signal	10
2.7	Distribution of the available capacity of a CR2032 battery in a TPMS . . .	11
2.8	Current consumption of typical TPMS tasks	13
2.9	Charge Q that a capacitor C_s must store to provide the charge Q_d	16
2.10	Energy E_{asic} , E_{add} and $E_{charged}$ as a function of capacitance C_s	17
3.1	Overview of common electromechanical transducers for energy harvesting .	19
3.2	Simplified two-dimensional crystal lattice structure without point symmetry	21
3.3	Transducer element of a piezoelectric material	21
3.4	Schematic of an electret-based electrostatic transducer	23
3.5	Schematic of a ferroelectret transducer with polarized air cavities and altered center of charge due to an external force F	25
3.6	Schematic of the triboelectric transducer principle	27
3.7	Electromagnetic induction caused by the relative motion between permanent magnet and coil	28
3.8	Electrodynamic transducer element	29
4.1	Rim based piezoelectric energy harvester from Roundy et al.	34
4.2	Clamped piezoelectric bimorph converter with seismic mass and rigid stoppers	34
4.3	Piezoelectric unimorph with asymmetric motion stops and seismic mass . .	35
4.4	Nonlinear cylindrical electromagnetic energy harvester	36
4.5	Energy per revolution of TPMS energy harvesters distinguished with respect to the energy source	42
5.1	Electromechanical network model of a linear piezoelectric energy harvester	48
5.2	Mass-spring system inside the tire	49

5.3	Static deflection of a piezoelectric unimorph beam as static compliance . . .	51
5.4	Electrical and mechanical boundary conditions of the piezoelectric one-sided clamped beam with different substrate and piezo-ceramic length . . .	53
5.5	Coefficient c_M as a function of beam length ratio l_p/l_s	54
5.6	Relation between mass m and velocity v and beam width w to generate at least $E_{2,\text{strikes}} = 7.9 \mu\text{J}$	54
5.7	Schematic of the tire wave based piezoelectric energy harvester prototype .	55
5.8	Energy $E_{2,\text{strikes}}$ and deflection z for two beam widths w for two masses m .	56
5.9	Piezoelectric inertia energy harvester samples	56
5.10	Piezoelectric inertia energy harvester and metal housing	57
5.11	Network model of a piezoelectric strain energy harvester	58
5.12	Network model of a piezoelectric strain energy harvester after transformation	58
5.13	Flexibility test of an MFC by the manufacturer	59
5.14	Structure of the thin stacked transducer P878.A1	60
5.15	Flexible piezoelectric transducers attached to a 130 mm x 20 mm x 2 mm aluminum beam for material characterization on an electrodynamical shaker	61
5.16	Experimental setup of the clamped-free-end aluminum beam with attached piezoelectric sample mounted on an electrodynamical shaker	62
5.17	Equivalent piezoelectric circuit with a current source and a resistance R_L .	62
5.18	Relation between voltage amplitude \hat{U}_r and current amplitude \hat{I}_r four different piezoelectric transducers for different tip deflection amplitudes . . .	63
5.19	ANSYS static structural analysis of an aluminum beam with attached M2807-P2 piezoelectric sample	64
5.20	Energy E_{max} for different samples as a function of tip amplitude	66
5.21	Strain signal and deduced transducer current according to Eqn. 5.19 for one tire revolution used as input for the electromechanical network simulation .	67
5.22	Strain based piezoelectric energy harvester prototypes - voltage, accumulated charge and momentary energy for one tire turn.	68
6.1	Equivalent circuit of the piezoelectric transducer in the electrical domain with interface circuit and storage capacitor C_s	71
6.2	Equivalent circuit of the piezoelectric transducer	73
6.3	Piezoelectric transducer with connected capacitor C_s	74
6.4	Normalized charge and efficiency as functions of normalized capacitor voltage for an initially empty capacitance C_p with $u_{p,0} = 0$	76
6.5	SEH interface circuit with storage capacitor	76
6.6	Simulated SEH current i_T , piezoelectric current i_p , capacitor current i_s and piezoelectric voltage u_p for one period	77
6.7	SEH - normalized charge and efficiency as functions of normalized capacitor voltage for an initially precharged capacitance C_p with $u_{p,0} = -u_{s,0}$	78
6.8	SOR interface circuit with storage capacitor	78

6.9	Simulated SOR current i_T , piezoelectric current i_p , capacitor current i_s and piezoelectric voltage u_p for one period	79
6.10	SOR - normalized charge and efficiency as functions of normalized capacitor voltage $u_{s,0}/u_0$. Due to the short-circuited piezoelectric transducer after each half wave the piezoelectric capacitance C_p is discharged ($u_{p,0} = 0$). . .	80
6.11	Parallel-SSHI circuit with storage capacitor	80
6.12	SSHI source current i_T , piezoelectric current i_p , capacitor current i_s and piezoelectric voltage u_p for one period	81
6.13	SSHI - normalized charge and efficiency as functions of voltage ratio $u_{s,0}/u_0$	82
6.14	SECE circuit with storage capacitor	83
6.15	SECE currents i_T , i_p , i_s and voltage u_p for one period	84
6.16	SECE efficiency as a function of product of normalized capacitor voltage and quality factor bq_1 , depicted for different quality factors q_2	87
6.17	SECE - Efficiency η_{SECE} as a function of voltage ratio $b = u_{s,0}/u_0$ for the quality factors $q_1 = 79$ and $q_2 = 0.53$	88
6.18	Inductor related ratio \sqrt{L}/R_L for different inductors L of a series	89
6.19	Electronic Breaker (EB) circuit as an easy implementation of the SECE principle with discrete electronic components	90
6.20	Interface circuit efficiency deduced from LTspice simulation with diode forward losses and from analytical results	91
6.21	Analytical results: normalized efficiency of four basic piezoelectric interface circuits as a function of normalized voltage $b = u_{s,0}/u_0$	92
7.1	Schematic of the considered electromagnetic energy harvester	94
7.2	Equivalent circuit of a linear electromagnetic energy harvester	94
7.3	Magnetic flux lines of the movable magnet at the position $z = z_m$	96
7.4	Equivalent circuit for the nonlinear electromagnetic energy harvester with the nonlinear electromagnetic transducer coefficient $\beta(z)$	97
7.5	Different repulsive magnetic forces and corresponding equilibrium positions	99
7.6	Mesh and magnetostatic FE simulation of two magnets separated by 5 mm	100
7.7	Two method to calculate magnetostatic parameter with FEM	101
7.8	Movable magnet centered in cylindrical coordinate system	102
7.9	Radial magnet flux density B_r as a function of position z and radius r of the moving magnet in central position	102
7.10	Serial coil connections with same and opposite sense of winding	103
7.11	Simulated transducer coefficient as a function of distance z between the movable magnet and coil	104
7.12	Position dependent transducer coefficient - simulation for two different wire diameters and the same copper volume	105
7.13	Simulated repulsive force for a N45D6H4 movable neodymium magnet and different sized fixed N48 neodymium magnets	106

7.14	Electromagnetic energy harvester prototypes - support with coils, encapsulation and TPMS container	107
7.15	Experimental setup to determine the distance-dependent coefficient $\beta(z)$	109
7.16	Position dependent transducer coefficient $\beta(z)$ - simulation and measurement for the two coil setups	109
7.17	Experimental setup to determine the damping coefficient c	110
7.18	Tensile testing machine setup to measure the repulsive magnetic force	110
7.19	Tensile testing measurements to characterize the repulsive forces	111
7.20	LTspice schematic of the nonlinear electromagnetic energy harvester	112
7.21	Network simulations of the electromagnetic energy harvester	113
7.22	Equivalent circuit of a unidirectionally coupled electromagnetic transducer	114
7.23	Maximal power transfer to the load resistance R_L	115
7.24	Simulated electrical and mechanical energy of the electromagnetic energy harvester with $N = 1060$ for one revolution at 25 km/h and 50 km/h	117
8.1	Equivalent circuit of a unidirectionally coupled electromagnetic energy harvester with interface circuit and storage.	120
8.2	Equivalent circuit of a unidirectionally coupled electromagnetic energy harvester with with standard interface and storage.	120
8.3	Voltage signal in the time domain and derived absolute frequency	123
8.4	Probability density function of the voltage from Fig. 8.3a	123
8.5	Voltage signal u_T and corresponding interval charge $\Delta Q_s(u_T)$	124
8.6	SEH efficiency as a function of voltage $u_{s,0}$ for the forward voltage $u_{FV} = 0.6$ V	125
8.7	Interval energy as a function of the forward voltage u_{FV}	125
8.8	Electrical circuit of a voltage doubler and voltage tripler to double and triple the input voltage u	126
8.9	Analytically calculated efficiencies opposed to the efficiencies deduced from LTspice simulations as a function of voltage $u_{s,0}$	127
8.10	SMFE interface circuit connected to electromagnetic energy harvester with harmonic voltage source	129
8.11	SMFE transducer voltage u_T and current i for the case that the source voltage is smaller than the capacitor voltage	129
8.12	Transient normalized current i/i_0 as a function of phase angle φ for different ratios γ	131
8.13	Normalized maximal energy E_{\max} of the SMFE as a function of γ	132
8.14	Energizing and Transferring circuit	134
8.15	Current i and capacitor energy E_s for energizing times $t_E = 2\tau$ and $t_E = 4\tau$, supposing that $u_0 < u_{s,0}$	135
8.16	Current over time of the discontinuous current mode	136
8.17	Maximal efficiency as a function of x for the DCM	137

8.18	Infinitesimal energy difference that is stored in the inductor over normalized energizing time	137
8.19	Current evolution over time of the continuous current mode	138
8.20	Efficiency η_{CCM} for the optimal pair (x, n) opposed to the efficiency η_{DCM} .	140
8.21	Electrical resonator in the transferring phase	140
8.22	Maximal efficiency $\eta_{\text{EaT,max}}(x, y)$ (solid line) and corresponding optimal switching parameters as a function of capacitor voltage ratio b	142
8.23	Efficiency η_{EaT} as a function of initial capacitor voltage $u_{s,0}$ deduced from the network simulation in LTspice with $(t_E, t_T) = (45, 25) \mu\text{s}$	143
8.24	LTspice simulation of the electromagnetic energy harvester with 1060 turns at 25 km/h, connected to different interface circuits	144
9.1	Devices installed in the tire and preliminary steps for the experiments . . .	149
9.2	Measurement circuits for the characterization of the open-circuit voltage of the EMEH (a), PEH (b) and of interface circuits connected to the energy harvesters (c)	150
9.3	Pre-assembled tire wave based piezoelectric energy harvester embedded in a metal housing, placed in a truck TPMS plastic housing	151
9.4	Tire wave based piezoelectric prototype embedded in a TPMS truck plastic housing and rubber container.	151
9.5	Open-circuit voltage u_{oc} at $v = 20 \text{ km/h}$, 30 km/h and 50 km/h of tire wave based piezoelectric energy harvesters and corresponding energy E_p	152
9.6	Dissembled tire wave based piezoelectric energy harvester after tests in a tire.	153
9.7	Strain based prototypes attached to the tire with soldered cables	154
9.8	Strain PEH prototypes at 50 km/h and 3000N - voltage, accumulated charge and momentary energy for one tire turn.	155
9.9	Accumulated charge as a function of velocity v at a tire load of $F = 3000\text{N}$ in circumferential direction	156
9.10	Open-circuit voltage signal for one tire revolution at different velocities . .	157
9.11	M2807-P2 strain transducer in lateral direction	157
9.12	Open-circuit voltage of M2807-P2 sample in circumferential and lateral orientations at 50 km/h and 3000 N	157
9.13	Accumulated charge for different forces at 50 km/h	158
9.14	Open-circuit voltage signal for one tire revolution with different load	159
9.15	Strain based prototype wire connection before and after testing	159
9.16	Long-term evaluation of M2814-P2 transducers with respect to the electrical power across different load resistances	160
9.17	Reliability tests for performance evaluation of harvesters at different base accelerations at low resonant frequency (30 Hz)	161
9.18	Storage voltage evolution of the M2807-P2 transducer at $F = 3000\text{N}$	163

9.19	Efficiency of the electronic breaker for different velocities at $F = 3000$ N . . .	164
9.20	Comparison of different strain based energy harvesters.	165
9.21	Estimated transmission time of the M2807-P2 (EB) system	166
9.22	Electromagnetic energy harvester embedded in a rubber container, which was glued on the tire inner liner	166
9.23	Open-circuit voltage u_{oc} and deduced maximal harvestable energy $E_{elec,max}$ for one tire revolution at $v = 50$ km/h and $F = 4000$ N	168
9.24	Test conditions in a) the experimental setup and b) the simulation	169
9.25	Interval energy as a function of forward voltage u_{FV} at $v = 25$ km/h at $F = 3000$ N	169
9.26	Interval energy of the four EMEH prototypes as a function of velocity for $F=3000$ N and for different voltages u_{FV}	170
9.27	Interval energy as a function of velocity for $F = 3000$ N and for different voltages u_{FV}	171
9.28	Open-circuit voltage signal u_{oc} of EMEH 1060 (1) for different velocities at $F = 3000$ N	172
9.29	Interval energy as a function of force F at $v = 50$ km/h and for different voltages u_{FV}	173
9.30	Open-circuit voltage over time for different force $F \leq 4000$ N	173
9.31	Open-circuit voltage over time for different forces $F \geq 5000$ N	174
9.32	Voltage evolution of a 220 μ C capacitor with connected VD and VT	175
9.33	Efficiency of EMEH 1060 (1) - VT for different velocities at $F = 3000$ N . . .	176
9.34	Comparison of different tire wave based energy harvesters	177
9.35	Estimated transmission time of EMEH 1060 (1) - VT, when the vehicle already moves	177
9.36	Electromagnetic transducer disassembled after testing	178
9.37	Electromagnetic energy harvester samples with a) fragile wire connection and b) improved wire connection	179
A.1	Equivalent piezoelectric circuit with piezoelectric current source	185
B.1	Equivalent circuit of the piezoelectric transducer	188
C.1	Piezoelectric system with ideal harmonic current source	189
G.1	Accumulated charge ΔQ as a function of velocity at $F = 3000$ N for dif- ferent voltages u_b	196

List of Tables

2.1	Overview of published data concerning the energy consumption of a TPMS for one measuring and transmission cycle	14
2.2	Charge and ASIC voltage supposed in this thesis	16
2.3	Capacitances and corresponding energies normalized to 208 revolutions . .	17
3.1	Properties of selected piezoelectric materials	23
3.2	Maximal strain and calculated mechanical energy density of selected piezoelectric materials	23
3.3	Properties of common electrets	24
3.4	Properties of ferroelectret with large direct effect	26
3.5	Properties of ferroelectret with large transverse effect	26
3.6	Properties of selected magnetic materials	29
3.7	Properties of magnetostrictive materials	30
3.8	Calculated mechanical energy density of selected piezoelectric materials . .	30
4.1	TPMS energy harvesters - state of the art overview	40
4.2	TPMS energy harvesters - state of the art overview (contd.)	41
4.3	Energy density as a function of velocity for a PZT-5A piezoelectric energy harvester	44
5.1	Piezoelectric component assignment	47
5.2	Selected boundary conditions of a beam and corresponding compliances for a beam with a rectangular cross section	52
5.3	Material properties of the brass substrate layer	52
5.4	Geometry parameters of the inertia piezoelectric systems	55
5.5	Calculated system parameters of inertia based piezoelectric system deduced from ANSYS FEM simulations	57
5.6	Properties of commercially piezoelectric thin transducers	61
5.7	Geometry data of piezoelectric thin transducers	61
5.8	Simulated average strain corresponding to a tip deflection $\hat{z} = 1$ mm for studied piezoelectric samples	65
5.9	Network parameter estimation of strain based transducers	65
6.1	Parameters of the simplified electromechanical network of Fig. 6.1	90

7.1	Electromagnetic component assignment	95
7.2	Coil data corresponding to the simulation of Fig. 7.11	103
7.3	Prototyping coil data for two setups with different wire diameters.	106
7.4	Mechanical energy, electrical energy and total efficiency for the unidirectionally and bidirectionally coupled network at 25 km/h and 50 km/h vehicle velocity.	116
8.1	Analogies between Electrostatics and Magnetics	128
8.2	Electromagnetic energy harvester parameters and attainable SMFE efficiency at 25 km/h of the two studied systems	133
8.3	Interface circuit efficiency η of the energy harvester at 25 km/h for different energizing and transferring parameters t_E , t_T , for the initial capacitor voltage $u_{s,0} = 2.7 \text{ V}$, corresponding to $b = 1$ and with Schottky diodes.	143
9.1	Properties of test devices and measurement tools	148
9.2	Parameter constellation for EMEH and PEH prototype testing	150
9.3	Average strain \bar{S} at $\varphi = \pi$ experienced by different piezoelectric transducers in the measurements	156
9.4	Overview of Macro Fiber Composite long-term studies	162
9.5	Electronic components of the electronic breaker	163
A.1	Elliptical angle φ and corresponding load resistance ratio R_L/Z_C	187
E.1	Polynomial coefficients of magnetic force F_{mag} and transducer coefficient β	194
E.2	Polynomial coefficients of elastic bumpers	194

List of Publications

Journal Papers

1. **M. Germer**, U. Marschner, and A. Richter. “Energy Harvesting for Tire Pressure Monitoring Systems from a Mechanical Energy Point of View”. In: *IEEE Internet of Things Journal* (2022), pp. 1–1. DOI: 10.1109/jiot.2022.3152547
2. **M. Germer**, U. Marschner, and A. B. Flatau. “Electrical tuning of magnetostrictive applications: Equivalent electromechanical circuit analysis”. In: *Journal of Intelligent Material Systems and Structures* 30.9 (Feb. 2019), pp. 1435–1450. DOI: 10.1177/1045389x19828484

Patents and Patent Disclosure Documents

1. A. Richter, K. Henkel, G. Paschew, U. Marschner, R. Körbitz, and **M. Germer**. “System zur haptischen Interaktion mit virtuellen Objekten für Anwendungen in der virtuellen Realität”. DE102019106684B4. Mar. 15, 2019
2. **M. Germer**. “Vorrichtung zum Erzeugen von elektrischer Energie aus Schwingungsenergie sowie Verwendung hierfür”. DE102019206567A1. May 7, 2019

Conference Proceedings (peer reviewed)

1. **M. Germer**, U. Marschner, and A. Richter. “High Efficient Energy Harvesting Interface Circuit for Tire Pressure Monitoring Systems”. In: *IEEE Wireless Power Week 2022*. Bordeaux, France, July 2022
2. **M. Germer**, U. Marschner, and A. Richter. “High Efficient Boost Energizing and Transferring Circuit for Electromagnetic Energy Harvesting”. In: *10th National Days on Energy Harvesting and Storage*. Grenoble, France, June 2021. URL: <https://hal.archives-ouvertes.fr/hal-03313226>
3. **M. Germer**, U. Marschner, and A. Richter. “Stochastic Signal Analysis and Processing of Non-Harmonic, Periodic Vibrational Energy Harvesters”. In: *ASME 2021 Conference on Smart Materials, Adaptive Structures and Intelligent Systems*.

- American Society of Mechanical Engineers, Sept. 2021. DOI: 10.1115/smasis2021-68310
4. **M. Germer**, U. Marschner, and A. B. Flatau. “Combined Finite Element Method (FEM) and Network Simulation of a Nonlinear Electromagnetic Energy Harvester”. In: *ASME 2020 Conference on Smart Materials, Adaptive Structures and Intelligent Systems*. American Society of Mechanical Engineers, Sept. 2020. DOI: 10.1115/smasis2020-2407
 5. **M. Germer** and U. Marschner. “Energy Harvesting for TPMS from an Energy Point of View”. In: *9th National Days on Energy Harvesting and Storage*. June 2019
 6. **M. Germer**, U. Marschner, and A. B. Flatau. “Design and experimental verification of an improved magnetostrictive energy harvester”. In: *Active and Passive Smart Structures and Integrated Systems 2017*. Ed. by G. Park. SPIE, Apr. 2017. DOI: 10.1117/12.2263971
 7. **M. Germer**, U. Marschner, J. H. Yoo, and A. B. Flatau. “Equivalent Electromechanical Circuit Analysis for Electrical Tuning of Magnetostrictive Unimorph System Dynamics”. In: *Volume 2: Modeling, Simulation and Control; Bio-Inspired Smart Materials and Systems; Energy Harvesting*. American Society of Mechanical Engineers, Sept. 2016. DOI: 10.1115/smasis2016-9274

Conference Poster

1. **M. Germer**, U. Marschner, and A. B. Flatau. “Magnetic flux analysis of a magnetostrictive unimorph energy harvester”. In: *IDTechExShow*. Apr. 2018

Awards

1. **Outstanding Poster Award**

M. Germer, U. Marschner, and A. Richter. “High Efficient Boost Energizing and Transferring Circuit for Electromagnetic Energy Harvesting”. In: *10th National Days on Energy Harvesting and Storage*. Grenoble, France, June 2021. URL: <https://hal.archives-ouvertes.fr/hal-03313226>

2. **Student Best Paper Award Finalist**

M. Germer, U. Marschner, and A. Richter. “High Efficient Energy Harvesting Interface Circuit for Tire Pressure Monitoring Systems”. In: *IEEE Wireless Power Week 2022*. Bordeaux, France, July 2022